Stony Brook University

STUDIES OF GROWTH MECHANISM AND DEFECT ORIGINS IN 4H-SILICON CARBIDE SUBSTRATES AND HOMOEPITAXIAL LAYERS

A Dissertation Presented

by

Huanhuan Wang

to

The Graduate School

in Partial Fulfillment of the

Requirements

for the Degree of

Doctor of Philosophy

in

Materials Science and Engineering

Stony Brook University

December 2014

Stony Brook University

The Graduate School

Huanhuan Wang

We, the dissertation committee for the above candidate for the

Doctor of Philosophy degree, hereby recommend

acceptance of this dissertation.

Michael Dudley – Dissertation Advisor
Professor, Chair, Department of Materials Science and Engineering

Dilip Gersappe - Chairperson of Defense
Professor, Graduate Student Director, Department of Materials Science and Engineering

Balaji Raghothamachar
Research Assistant Professor, Department of Materials Science and Engineering

Darren Michael Hansen
Ph.D, Science and Technology Manager, Dow Corning Corporation, Midland, MI

This dissertation is accepted by the Graduate School

Charles Taber
Dean of the Graduate School

Abstract of the Dissertation

Studies of Growth Mechanism and Defect Origins in 4H-SiC

Substrates and Homoepitaxial Layers

by

Huanhuan Wang

Doctor of Philosophy

in

Materials Science and Engineering

Stony Brook University

2014

4H-Silicon Carbide (SiC) is a widely used semiconductor for high power devices due to its outstanding properties such as high thermal conductivity, high breakdown voltage and high saturated electron drift velocity. However, the detrimental effects of defects, e.g., dislocations and stacking faults, in 4H-SiC crystals require crystal growth scientists to gain knowledge of the formation mechanisms and behavior of the defects to develop strategies in order to lower the densities of these defects. The goal of this study is, therefore, to (i) understand the growth mechanism of 4H-SiC ----Physical Vapor Transport (PVT) for substrate growth and Chemical Vapor Deposition (CVD) for homoepitaxial growth, (ii) study the formation mechanism and behavior of defects according to changes in growth conditions and (iii) the influence of defects on device performance. The content is divided into two parts: the first part will discuss the growth mechanism and defect configurations in 4H-SiC substrates; the second part will be concentrate on growth mechanism and defect configurations in 4H-SiC homoepitaxial layers.

Various state-of-the-art experimental techniques have been applied to study the growth mechanism and defect origins in 4H-SiC substrates and homoepitaxial including (i) non-destructive Synchrotron X-ray Topography (XRT) mainly carried out in National Synchrotron Light Source (NSLS) and Advanced Photon Source (APS) synchrotron sources with additional experiments carried out at Cornell High Energy Synchrotron Source (CHESS) and Angströmquelle Karlsruhe (ANKA); (ii) Transmission Electron Microscopy (TEM) carried out at CFN; (ii) Scanning Electron Microscopy (SEM); (ii) Nomarski Optical Microscopy (NOM) and (iv) Selective Chemical Etching. Using these techniques, the following in-depth studies have been carried out:

1) Construction of the three-dimensional configuration of defects in 4H-SiC single crystals by the combined application of section and projection topography carried out using synchrotron white beam radiation. In this chapter, examples are presented of the application of this combination of techniques to the analysis of defect configurations in PVT-grown 4H-SiC wafers

cut perpendicular and parallel to the growth axis. Detailed correlation between section and projection topography of threading screw dislocations (TSDs) is presented with particular emphasis on the determination of the signs of the dislocations. Further, information regarding the position of the dislocations as a function of crystal depth can be obtained. In addition, similar correlation is presented for threading edge dislocations (TEDs) and basal plane dislocations (BPDs). The section topography images of dislocations can comprise direct, intermediary and dynamical contrast and all three types are observed. The application to the study of stacking faults will be also discussed in detail.

2) Comparison of dislocation density measurement using molten KOH selective etching and Synchrotron X-ray Topography. Both are well established as two of the major characterization techniques used for observing as well as analyzing the various crystallographic defects in both substrates and homo-epitaxial layers of silicon carbide. Regarding assessment of dislocation density in commercial wafers, though the two techniques show good consistency in threading dislocation density analysis, significant discrepancy is found in the case of basal plane dislocations (BPDs). In this chapter, measurements of BPD densities in 4-inch 4H-SiC commercial wafers will be assessed using both etching and topography methods. The ratio of the BPD density calculated from topographic images to that from etch pits is estimated to be larger than $1/\sin\theta$, where θ is the offcut angle of the wafer. Based on the orientations of the defects in the wafers, a theoretical model is put forward to explain this disparity and the two main sources of errors in assessing the BPD density using chemical etching are discussed.

3) Multiplication of basal plane dislocations in the primary slip system. Synchrotron white beam X-ray topography (SWBXT) observations are reported of single-ended Frank-Read sources in 4H-SiC. These result from inter-conversion between basal plane dislocations (BPDs) and threading edge dislocations (TEDs) brought about by step interactions on the growth interface resulting in a dislocation comprising several glissile BPD segments on parallel basal planes interconnected by relatively sessile TED segments. Under stress, the BPD segments become pinned by the TED segments producing single ended Frank-Read sources. This apparently is the dominant multiplication mechanism for BPDs in 4H-SiC and is referred to as the “Hopping” Frank-Read source mechanism.

4) Stacking fault formation mechanism in PVT-grown 4H-SiC substrates. The first part is the study of macrostep overgrowth of the surface outcrops of threading dislocations with Burgers vector **c** and **c**+**a**, which causes them to be deflected onto the basal plane. The second part is a review of different types of stacking faults observed in PVT-Grown 4H-SiC crystals. The strength of the contrast observed on different reflections and comparison with calculated phase shifts ($\delta=-2\pi\ \mathbf{g}\cdot\mathbf{R}$) for postulated fault vectors enables determination of the fault vectors and combined analysis of the observed fault morphologies has enabled us to develop models for their formation mechanisms. Three types of faults were observed and analyzed in this way: (a) Shockley Faults; (b) Frank Faults; (c) Combined Shockley + Frank Faults with fault vectors **s**+**c**/2;

5) Study of star shape faults nucleated from micropipes due to high nitrogen doping in 4H-SiC substrates. The pattern often consists of a six-pointed star comprised of rhombus-shaped stacking faults with three different fault vectors of the Shockley type bounded by 30° Shockley partial dislocations. Formation of the star fault is associated with a micropipe at its center which can act

as nucleation sites for dislocation half-loops belonging to the primary basal (1/3<11-20> (0001)) slip system and occasionally the secondary prismatic (1/3<11-20>{1-100}) slip systems. In this case, the nucleation of the rhombus-shaped Shockley type stacking faults on the basal plane involves the reaction of 60° dislocations of $1/3\langle\bar{2}110\rangle$ Burgers vector on the basal plane and pure screw dislocations of $1/3\langle11\bar{2}0\rangle$ Burgers vector on the prismatic plane and cross slip of the partial dislocation from prismatic plane to basal plane leading to the expansion of the faults. The formation mechanism involves the operation of a double-ended Frank-Read partial dislocation source. In the limit, this glide and cross-slip mechanism leads to 4H to 3C polytype transformation in the vicinity of the micropipe by a mechanism similar to that proposed by Pirouz (1993).

6) Study of prismatic slip and cross-slip of threading edge dislocations (TED) employing X-ray Topography and KOH etching. In X-ray topography, it is observed that dislocation slip emanates from the micropipes in the form of slipbands along <11-20> directions. These bands mainly comprise screw type dislocations of the 1/3<11-20> type. After KOH etching, rows of etch pits corresponding to dislocation arrays were also observed in vicinity of micropipes. In the early stages, the arrays consist of threading edge dislocations and later on, more and more BPD etch pits are observed mixing with the TED etch pits. The dislocation configurations in the slip bands are interpreted as initial prismatic slip of TEDs on <11-20> {-1100} of the hexagonal SiC structure during the growth process and when certain segments of TED loop adopt screw-orientation they cross-slip onto primary slip system. <11-20>{0001}.

7) Investigate of dislocation behavior during homoepitaxy of 4H-SiC on offcut substrates by Chemical Vapor Deposition (CVD). (1) Studies carried out before and after epilayer growth have revealed that, in some cases, short, edge oriented segments of basal plane dislocation (BPD) inside the substrate can be drawn towards the interface producing screw oriented segments intersecting the growth surface. In other cases, BPD half-loops attached to the substrate surface are forced to glide into the epilayer producing similar screw oriented surface intersections. Both processes are driven by thermal stress. These screw segments subsequently produce interfacial dislocations (IDs) and half-loop arrays (HLAs). (2) In addition, we show that IDs and HLAs can be formed from new BPDs generated in the epilayer from surface dislocation sources, 3C inclusions, micropipes, and substrate surface scratches. The HLAs are known to result in Shockley fault expansion within the epilayer which results in forward voltage drop and device failure. (3) During device operation or UVPL imaging, BPD segments of HLAs will dissociate into two inclined and two vertical segments of mobile, Si-core, 30^o partials via electron-hole recombination enhanced dislocation glide, which will expand in opposite directions and form Shockley faults on the basal plane, a phenomenon which leads to lifetime limiting forward voltage drop.

8) Nomarski optical microscopy, KOH etching and Synchrotron Topographic studies are presented of faint needle-like surface morphological features in 4H-SiC homoepitaxial layers. Grazing incidence synchrotron white beam x-ray topographs show V shaped features which transmission topographs reveal to enclose ¼[0001] Frank-type stacking faults. Some of these V-shaped features have a “tail” associated with them and are referred to as Y-shaped defects. Geometric analysis of the size and shape of the V-shaped faults indicates that they are fully contained within the epilayer and appear to be nucleated at the substrate/epilayer interface. Detailed analysis shows that the Y-shaped defects match well with the substrate surface

intersections of **c**-axis threading dislocations with Burgers vectors of **c** or **c**+**a** in the substrate which were deflected onto the basal plane during substrate growth, similarity, the positions of some V-shaped stacking faults in the center match with the positions of **c**-axis threading dislocations with Burgers vectors of **c** or **c**+**a** in the substrate and thus appear to result from the deflection of these dislocations onto the basal plane during epilayer growth. However, most V-shape stacking faults around the edge are not associated with any defects in the substrate and it appears that opposite sign of Frank partials generating from the interface. Based on the observed morphology of these defect configurations we propose a model for their formation mechanism.

Table of Contents

List of Tables xi
List of Figures xii
List of Abbreviations xviii
List of Symbols xix
Acknowledgments xx
Publications xxi
1. Introduction 1
1.1 Properties of Silicon Carbide 1
1.1.1 Application of Silicon Carbide Devices 1
1.1.2 SiC Crystallography 2
1.2 Defect Structure in Silicon Carbide 4
1.2.1 Fundamental Understanding of Defects in SiC 5
1.3 Motivation 7
1.4 Crystal Growth Techniques for SiC 8
2. Characterization Techniques 10
2.1 Synchrotron X-ray Topography 10
2.1.1 Introduction 10
2.1.2 Principles of XRT Method 11
2.1.3 Sample Geometry for Diffraction Imaging 12
2.1.4 Image Contrast in X-Ray Topography 15
2.1.5 Sample Preparation 18
2.2 Transmission Electron Microscopy (TEM) (JEOL-2100) 19
2.2.1 T-tool Wedging Polishing (TechCut 4, MultiPrep System) 20
2.2.2 Focused Ion beam (FIB) Dual SEM/FIB system 21
2.3 Scanning Electronic Microscopy (SEM) (FEG LEO1550) 21
2.4 Nomarski Optical Microscopy (Nikon Polarizing Microscope Eclipse E600W POL) 22
2.5 Selective Chemical Etching (melted KOH) 22
3. Combined Application of Section and Projection Topography for Defect Analysis in PVT-Grown 4H-SiC substrate 24
3.1 Outline 24

3.2 Introduction 24
3.3 Results and Discussion 25
3.3.1 Dislocations Parallel to the Entrance Surface 25
3.3.2 Dislocations Making an Angle with Entrance Surface 26
3.3.3 Dislocations being Perpendicular to the Entrance Surface 27
3.3.4 Application of Section Topography of Stacking Faults 28
3.4 Conclusion 28
4. Quantitative Comparison between Dislocation Densities in Offcut 4H-SiC Wafers Measured Using Synchrotron X-ray Topography and Molten KOH Etching 30
4.1 Outline 30
4.2 Introduction 30
4.3 Experimental Procedure 31
4.4 Results and Analysis 32
4.4 Conclusion 35
5. Basal Plane Dislocation Multiplication in (0001) Plane via the Hopping Frank-Read Source Mechanism in 4H-SiC Substrate 36
5.1 Outline 36
5.2 Introduction 36
5.3 Results and Discussion 37
5.4 Conclusion 41
6. Stacking Faults Created by the Combined Deflection of Threading Dislocations of Burgers Vector c and c+a during the PVT Growth of 4H-SiC 42
6.1 Outline 42
6.2 Introduction 42
6.3 Results and Discussion 43
6.3.1 Deflection of Threading Screw Dislocations 43
6.3.2 Shockley Faults 46
6.3.3 Frank Faults 48
6.3.4 Shockley + c/4 Frank Faults 50
6.3.5 Influence of Stacking Faults on Device Performance 52
6.4 Conclusion 53

7. Studies of the Operation of Double-Ended Frank-Read Partial Dislocation Sources in 4H-SiC with Heavily Nitrogen Doping 54
7.1 Outline 54
7.2 Introduction 54
7.3 Experimental 55
7.4 Result and Discussion 55
7.5 Conclusion 65
8. Prismatic Slip and Cross-Slip Behavior of Threading Edge Dislocations 66
8.1 Outline 66
8.2 Introduction 66
8.3 Result and Discussion 66
8.4 Conclusion 69
9. SiC Homoepitaxy on Off-cut (0001) Substrates 70
9.1 SiC Epitaxial Growth Processes 70
9.1.1 Step- Control Epitaxy and Substrate Surface Preparation 72
9.2 Dislocation Replication during Off-axis Homoepitaxial Growth 74
9.2.1 Conversion of BPDs into TEDs 75
9.3 Introduction of Interfacial Dislocation 76
9.3.1 Matthews-Blakeslee (M-B) Model for Interfacial Dislocation Formation 77
9.3.2 People and Bean Model 79
10. Studies of Relaxation Processes and Basal Plane Dislocations in CVD Grown Homoepitaxial Layers of 4H-SiC 80
10.1 Outline 80
10.2 Introduction 80
10.3 IDs and HLAs Resulting from BPDs Inherited from Substrate 81
10.3.1 Formation Mechanism of Half-loop Arrays 83
10.3.2 IDs and HLAs Generated by Half-loops from Substrate 85
10.3.3 Conclusions 90
10.4 Studies of Relaxation Processes 91
10.4.1 Critical Thickness Measurement 91
10.4.2 Conclusion 97

10.5 Different Nucleation Sources for Interfacial Dislocations and Half-loop Arrays. 98
10.5.1 Surface Sources 98
10.5.2 3C polytypes 98
10.5.3 Micropipes 103
10.5.4 Scratches 104
10.6 Study the Sign of Interfacial Dislocations and Half-loop Arrays. 107
10.6.2 Formation of Shockley Faults Associated with HLAs 109
10.6.3 Conclusion 111
11. Study of V and Y shape Frank-type Stacking Faults Formation in 4H-SiC epilayer 112
11.1 Outline 112
11.2 Introduction 112
11.3 Results and Discussion 113
11.4 Conclusion 119
Conclusions 118
Future work 121
Reference 122

List of Tables

Table 1 Properties comparison between 4H-SiC and other semiconductor materials[1] 1
Table 2 Properties of three major SiC polytypes [8,9] 3
Table 3 Characteristics of various dislocations in 4H-SiC substrate 6
Table 4 The influence of defects on device performance 7
Table 5. Milestones of the development of X-ray Topography [24] 10
Table 6 Contrast Behavior of Shockley Fault with R=1/3[10-10] 47
Table 7 Contrast Behavior of Frank Fault with R=1/2[0001] 49
Table 8 Contrast Behavior of two (S+C/4) Faults together 52
Table 9 The comparison of different SiC epitaxy growth 70
Table 10 various characters of different segments of misfit dislocations in 4H-SiC 82

List of Figures

Figure 1 (a) Untwinned and twinned SiC tetrahedra which are composed of one C atom (grey color) at the center and four Si atoms (blue color) bonded symetricaly around it. (b) The triangles produced by projection of the twinned variantof the SiC tetrahedra along the [1120] direction. 3

Figure 2 Projection of 4H-SiC (left) and 6H-SiC (right) structure into (11-20) plane. Small and large balls indicate C and Si atoms, respectively. The stacking sequences are "ABA'C'…"and "ABCB'A'C'…" for 4H and 6H-SiC, respectively 4

Figure 3. (a) A straight BPD in (0001) basal plane; (b) A TSD in SiC with line directions along [0001] and Burgers vector n<0001> (c) A TED in SiC with line direction along [0001] and burgers vector on basal plane. 6

Figure 4. Schematic of the SiC growth system [21] 9

Figure 5. (a) Schematic shows diffraction patterns from sample in transmission geometry (Laue case). (b)Laue pattern map in transmission geometry when surface plane (0001), side plane (11-20) and the red dot is direct beam. (c)Schematic shows diffraction patterns from sample in reflection geometry (Bragg case). (d) Laue pattern map in back-reflection geometry with surface plane (0001), side plane (11-20) 11

Figure 6. (a)-(d) schematic of transmission, back reflection, grazing and section geometry and X –ray topographs. 13

Figure 7 Orientation contrast (a) For the case of monochromatic incident beam, the diffracted beams are still parallel to each other when the misorientation of adjacent area is smaller than the beam divergence. (b) The diffracted beams are getting overlapped or separated from each other when the misorientation of adjacent area is bigger than the beam divergence. (c) When the incident beam is continuous, the diffracted beams can also give rise to the contrast of boundaries between misorientated adjacent regions. 15

Figure 8 (a) Diffraction contour mapping of a four inch 4H-SiC crystal recorded in grazing-geometry (g=11-28) by monochromatic X-ray beam. Bragg angle was rotated in 0.01^{o} step each time. At each angular position, an image was recorded to produce a multiple-exposure composite image of the strain in the sample. The strain is mainly positioned in the top and bottom of the wafer along [-1100] direction 16

Figure 9. Schematic of ray pass for bright field image(a) and dark field image(b) 19

Figure 10 Schematic of zone-axis alignment for HRTEM 20

Figure 11 A Nomarski Interference Contrast (NIC) optical image showing a selected area on etched Si-face of a commercial PVT-grown 8^{o} offcut 4H-SiC wafer (a). Three types of etch pits are observed—scallop-shell-like shaped etch pits corresponding to BPDs (b), large hexagonal etch pits to TSDs, small hexagonal etch pits to TEDs (c) 23

Figure 12 Side view of configuration for setting up X-ray section topography to record g= [0004] reflection of SiC axial slices. (b) The schematic diagram indicating the depth dependence of the direct image inside Bormann Fan. (c) Combined x-ray topography where transmission topography (g=0004) and several section topographs were recorded on the same film. (d) Section topographs were taken at the same position as (c). (e) The enlarged section topography of the rectangle part in (d) presents one pair of threading screw dislocations with opposite sign. (f) X-ray transmission topography showing dislocation 1 and 2 nucleate from one impurity. (g) Section topography of these two dislocations. The direct images are pointed out by black arrows. 25

Figure 13 (a) Dislocation AA' intersects the entrance surface at point A, exit surface at A'. a'c' is the direct image of dislocation AA', a'b'c': dynamic image with fringes due to the intermediary image. (b) TSDs got knocked off onto basal plane by advancing macrostep. Section topographs were recorded at the deflected TSDs. (c) The enlarged section topography of deflected TSDs. 26

Figure 14 (a) Schematic representations of the formation of mixed direct, intermediary and dynamic image from dislocations perpendicular to entrance surface [50]. (b) Grazing topography of 4H-SiC c-plane giving information of TSDs and TEDs distribution. The red line marks the position where section topography will be recorded. (c)Combined transmission and section topography. (d) The enlarged section topography where TSDs, TEDs and BPDs having distinguishable patterns. 27

Figure 15 (a) Combined transmission and section topography of 4H-SiC crystal with 15μm thickness epilayer. (b) The enlarged section topography of EF position from (a), and stacking faults expanding all the way from substrate to

epilayer along step flow direction. (c) Similar examples of stacking faults expanding into epilayer. (d) Schematically diagram showing the mechanism of stacking faults growing into epilayer as a “growth defect”. 28

Figure 16 A Nomarski Interference Contrast optical image showing a selected area on an etched Si-face of a commercial PVT-grown 4o offcut 4H-SiC wafer (a). Three types of etch pits are observed—scallop-shell-like shaped etch pits corresponding to BPDs (b), large hexagonal etch pits to TSDs, small hexagonal etch pits to TEDs (c).....31

Figure 17 SXRT image (a) and NIC image of etch pits (b) taken in the same area of a pre-etched 4H-SiC wafer. The illustration (c) demonstrates how threading dislocations (S1-S4: TSDs; E1-E4: TEDs.) and BPDs (B1-B3) are oriented in the sample.....33

Figure 18 Histograms showing the discrepancy of BPD densities obtained from etch pit counting and SXRT image line length measurement for eight 1.8 mm×2.3mm areas on each of the two commercial 4H-SiC wafers with different thickness.....33

Figure 19 Schematic diagrams giving a rough view showing the morphologies of (a) threading dislocations and (b) BPDs inside a wafer. The grey-shaded planes are (0001) basal planes that have an offcut angle of θ inclining towards the top surface. (c) Illustrates a simplified model where BPDs are considered as straight lines distributed uniformly in the selected volume. a and b refer to the dimensions of the selected etched area and t stands for the sample thickness.....34

Figure 20 Synchrotron White Beam X-ray Topography (SWBXT) transmission image (g=1120) recorded from a wafer cut with 4 degree offcut towards [1120] from a PVT-grown boule.....37

Figure 21 SWBXT images recorded from the same area of one 4H-SiC wafer show the various contrasts of the diamond shaped loops in different g vectors (a) g=-1-120, (b) g=10-10, (c) g=0-111, (d) g=-1101. The arrows in (b) and (c) indicate the location of jogs.....38

Figure 22 (a)-(d) Schematic cross-sectional view of the deflection on a TED onto the basal plane by a macrostep followed by re-deflection up into threading orientation through the encounter between macrostep and a TED spiral advancing in the opposite direction. 39

Figure 23 (a)-(c) Schematic of the formation of a single-ended Frank-Read Source through the deflection of a TED into a BPD and back again. The TED segments act as pinning points for the BPD glide; (d) the final configuration of the loops produced by the Hopping Frank-Read Source. “SP” indicates the starting point, and “EP” end point.....40

Figure 24 Schematic of two BPD arms on parallel basal planes separated by a jog comprising a segment of TED with the length of “y” (a) When y is small, the BPDs are locked as a dislocation dipole; (b) when y is sufficiently large, the BPDs can glide independently as single-ended Frank-Read sources.....40

Figure 25 SWBXT of an axial wafer cut parallel to the growth axis of a 4H-SiC boule confirming the existence of the double deflection process between TED and BPD segments. (b) Transmission SWBXT image (g=-1-120) recorded from a wafer cut perpendicular to the growth axis of 4H-SiC boule. Note the isolated Hopping Frank Read sources in the lower part of the image as well as many such sources superimposing in the upper part of the image. 41

Figure 26 Schematic of the deflections of threading edge dislocations with burgers vector **c** and **c+a** onto the basal plane form stacking fault. 42

Figure 27 Two ways of cutting crystals: (1) Perpendicular-cut, which is cut perpendicular to [0001] direction, with surface plane (0001). (2) Axial slice, which is cut parallel to [0001] direction.....44

Figure 28 SWBXT images of axial slices (a) g=0004; (b) g= $1\bar{2}1\bar{0}$.Threading screw dislocation a, b, d are visible on both g vectors, and c is only visible on (0004), out of contrast on ($1\bar{2}1\bar{0}$).....44

Figure 29 (a)-(d) Microscopic images of growth surface of wafer boule. The big steps called macrostep can be seen in the images. And the spiral loops shows the existence of threading screw dislocation (TSD). 45

Figure 30 Schematic mechanism of deflection of threading screw dislocation onto basal plane, and then re-deflected into threading direction.....46

Figure 31 (a)-(h) SWBXT images with various g vectors recorded at the same area from 4H-SiC wafer with 4^{o} offcut from the [11-20] direction.....46

Figure 32 (a) Schematic shows the deflected of **a**+**c** threading screw dislocation. The leading partial and the trailing partial are separated by **c**-height step which is caused by deflection of threading screw dislocation with Burgers vector **c**, and the leading partial can move under stress, while the trailing partial cannot, resulting the formation of Shockley faults. (b) Schematic shows the stacking sequence change after one step glide of the leading partial dislocation.....48

Figure 33 SWBXT Images recorded from a region near the edge of a 76mm wafer cut with 4 degrees offcut towards [1120]. One triangle stacking fault is visible on [10-11], [-1101] and [0-11], and out of contrast when the fourth number of the g vectors is zero.....49

Figure 34 (a)-(c) Schematic of macrostep overgrowth of the surface outcrop of a TSD with **g** vector "**c**". When **c** gets deflected onto the basal plane, it split into two **c**/2 steps. 49

Figure 35. (a)-(d), SWBXT Images recorded from a region near the edge of a 100 mm wafer cut with 4 degrees offcut towards [11-20]: (a) 10-10 reflection showing triangular faults; (b) -1101 reflection from same area showing stacking fault contrast from fault A only; (c) -1011 reflection from same area showing contrast from faults B only; (d) -12-10 reflection showing absence of all fault contrast. Dislocations *a*, *b*, and *c* are indicated. These can also be seen on (a) and (c) but not (b).....50

Figure 36 (a)-(c) Overgrowth of **c** + **a** dislocation with a c-height step converting it into a Frank dislocation plus two Shockley partials, one sessile (since its slip plane terminates) and one glissile; (d)-(f) Overgrowth of **c** + **a** dislocation 11' with c/4- and a 3c/4-height steps which has a second **c** + **a** dislocation, 22' with c-height spiral step protruding onto the terrace between these two step risers. Stacking sequences are indicated (normal 4H stacking sequence is ABA'C'). In (e) the "interfacial Shockley" converts the A layer into B', allowing overgrowth by the A' layer at the bottom of the macrostep. Following overgrowth in (f) the Shockley associated with the deflected 22' dislocation located at 23 glides under stress until it reaches the edge of the step 23' creating the fault of type B.....51

Fig. 37 (a) and (b) SWBXT images recorded on one 'bad' performance *pin* diode. (c) and (d) SEBXT images recorded on one 'good' performance *pin* diode.....52

Figure 38. (a) and (b) X-ray transmission topographs from a 4H-SiC substrate showing various configurations of rhombus-shaped stacking faults anchored to micropipes in groups forming rosette-like configurations; (c) Schematic showing <11-20> traces of the intersecting {1-100} type planes around a micropipe.....55

Figure 39 (a)-(c) Enlarged X-ray transmission topographs recorded from region A in Fig. 1(a). (a)-(c) {1-100} type reflections showing a rosette comprising five rhombus-shaped stacking faults (marked S1-S5) surrounding a micropipe (MP); (d)-(f) {11-20} type reflections where the stacking faults are not visible but dislocation lines bordering the faults are selectively visible. Dislocations bordering faults S1, S3 and S4 are visible on (d), those outlining S1, S2, S4 and S5 are visible on (e) while those outlining S2, S3 and S5 are visible on (f). 56

Figure 40 (a)-(c) Enlarged X-ray transmission topographs recorded from region B in Fig. 38(b). (a)-(c) {1-100} type reflections; (d)-(f) {11-20} type reflections where the stacking faults are not visible but dislocation lines bordering the faults are selectively visible. For this fault, the dislocations are out of contrast for g = -12-10 indicating that the Burgers vectors of the dislocations is 1/3[-1010]. 58

Figure 41 X-ray transmission topograph showing dislocation half loops are belonging to both basal (B) and prismatic slip systems (P) emanating from a micropipe. Prismatic slip appears as narrow bands aligned along the six {11-20} directions, corresponding to the traces of the 6 prismatic {1-100} planes on the wafer surface; Schematic representation of the nucleation of prismatic (b) and basal (c) dislocation half-loops from a micropipe showing pile up of prismatic dislocations.....58

Figure 42 Schematic representation of cross slip of a prismatic screw dislocation segment XX' on to the basal plane which is then pinned by the Shockley partial, YY', associated with a BPD in an adjacent basal plane.....59

Figure 43 Schematic representation of the operation of a double-ended partial Frank-Read source: (a) Screw dislocation segment XX' with Burgers vector AB is dissociated into two 30º partials: $AB \rightarrow A\sigma+\sigma B$; (b)-(e) Leading partial $A\sigma$ advances and rotates around pinning points XX' to form stacking fault loop. (f) The stacking fault expands form the rhombus shape observed.....60

Figure 44 (a) Modification of the stacking sequence of the 4H structure by glide, cross slip, and double cross slip of a Shockley partial as shown in Fig. 6 to form a 3C stacking sequence; (b) Illustration of the mechanism of

transformation from 4H polytype to 3C polytype through the sequential formation of faulted loops followed by double-cross slip to the next plane.....62

Figure 45 (a) Modification of the stacking sequence of the 4H structure by glide of double Shockley partials to form a six layer 3C stacking sequence; (b) TEM micrograph showing two double Shockley faults in low resolution. (c) HRTEM micrograph showing the predicted 3C stacking.....63

Figure 46 X-ray topographs from regions showing 3C inclusions. (a), (d) are transmission images (g=10-11); (b), (c) and (e), (f) are corresponding grazing incidence images (g=11-28) recorded from the two sides of the wafer. White contrast is the location of the 3C inclusion that diffracts to a different position on the X-ray film.....64

Figure 47 (a)-(c) SWBXT transmission images of axial slices recorded at various diffraction vector (a) g=01-10 (b) -12-10 (c) 0004. (e)- (f) Schematic mechanism of cross slip of threading edge dislocation. (f) and (g) threading edge dislocation cross glide in opposite directions due to the direction of shear stress.....67

Fig. 48 Analysis of basal plane dislocations: Dislocation morphology consists of concentric loops and pile-ups, indicating that they were clearly generated through deformation processes. This occurs at crystal edge and at micropipes under the action of thermal stress.....67

Figure 49 SWBXT images of dislocations emanating from an isolated micropipe in a 4H-SiC wafer. (a) g=0110. (b) g=1120. (c) g=1010 where the slip band is out of contrast. (d) Schematic of formation of threading edge dislocation slip band. 68

Figure 50 (a)-(b) etch pit patterns recorded at different wafers sliced from the same SiC ingot. The micropipes in (a) and (b) can be called the same one, as they locate at the same position on these two parallel wafer. Wafer (a) is closer to the seed than wafer (b).....69

Figure 51 Schematic of typical horizontal hotwall SiC CVD reactor ; (b) typical vertical hotwall SiC CVD reactor [133]. 71

Figure 52 Schematic show a substrate surface with 4 degree off cut along [11-20] direction, resulting a surface with terraces and growth steps. Growth steps contain the stacking sequence information. (b) Atom 'A' drop onto front terrace which has no growth step ahead resulting the appearance of 3C polytype. Atom 'B' drop onto other terraces and is incorporated into step risers replicating the stacking sequence information of 4H-SiC.....72

Figure 53 Schematic shows how defects (low angle grain boundaries, threading screw dislocations, threading edge dislocations, screw-oriented basal plane dislocation) are replicated from substrate into epilayer.....74

Figure 54 Schematic shows threading screw dislocations and non-screw oriented basal plane dislocations can be converted into other defects during epitaxial growth.....74

Figure 55 SMBXT image showing the conversion of BPDs into TEDs after 4H-SiC homoepitaxial growth.(a) BPD half-loop have two surface intersections with the interface which convert into two opposite-sign TEDs as shown in the magnified picture (b) straight BPD convert into TED in its downstep direction. 75

Figure 56 schematics of (a) after KOH etch on Si face, BPD line attached with one etch pit on the surface. Two growth directions (lateral and step-flow directions) can happen to fill the etch pit; (b) and (c) evolution of the basal plane during epitaxy if lateral growth dominates, and (d) evolution of the basal plane during epitaxy if step-flow growth dominates[160].....76

Figure 57 Schematic shows the different lattice parameters due to the nitrogen doping difference in substrate and epilayer, which leads to the formation of misfit dislocation with extra half plane in the bottom. 76

Figure 58 (a) White Beam x-ray topography with transmission-geometry g=11-20 recorded form 4H-SiC homoepitaxial wafer shows screw-oriented dislocation 'AB' gets replicated into epilayer and form interfacial dislocation 'BC'. (b)Schematic shows the formation process of the interfacial dislocations according to Matthews-Blakeslee model, where $hc$the critical thickness for interfacial dislocation formation is; $he$is the epilayer thickness; FL is the line tension exerted on threading BPD; $F\varepsilon$ is the stress caused by misfit between substrate and epilayer...77

Figure 59 (a)-(c) Transmission SWBXT images recorded from a substrate with a 12.5 micron epilayer grown on it. (d) Etch pits pattern of the same posi- tion on the wafer. (e) Schematic of the 3D geometry of configuration.....81

Figure 60 SWBXT showing two pairs of interfacial dislocations. (b) NOM image showing two pairs of half-loop arrays corresponding to the interfacial dislocation in (a). (c) The enlarged picture of half-loop arrays. (d) One BPD etch pit connected with the end of half-loop arrays. 83

Figure 61 Schematic showing the formation mechanism of a HLA. (a) – (g) sequential stages in the process; (h) Summary of process. 84

Figure 62 (a) and (c) transmission x-ray topographs with g=11-20 recorded at the same area before and after epitaxy growth. (b) and (d) are the enlarged pictures of the black frames in (a) and (c). 85

Figure 63 (a) and (b) transmission white-beam x-ray topographs with g=11-20 were recorded on the same area of 4H-SiC wafer before and after epilayer growth. (c) Grazing geometry mono-chromatic x-ray topography with g=11-28 recorded at the same area. (d) and (e) are the enlargement of area 'A' and 'B' in (c). 86

Figure 64 (a) A curved basal plane dislocation in substrate has two pinning points (red dots). (b) The short BPD component pinned by two ends is dragged towards interface under the combination of line tension, and thermal stress. (c) If the BPDs piecing into epilayer are slightly off screw-orientation, then BPDs will be converted into opposite sign TEDs. (d) If the BPDs piecing into epilayer are still in screw-orientation, then BPDs will convert into interfacial dislocations and half-loop arrays once critical thickness is exceeded. 87

Figure 65 (a) and (b) transmission white-beam x-ray topographs with g=11-20 were recorded on the same area of 4H-SiC wafer before and after epilayer growth. (c) Grazing geometry mono-chromatic x-ray topography with g=11-28 recorded at the area enclosed in the black frame in (b). (d)-(j) Schematic diagrams show the formation mechanism of pairs of interfacial dislocations and half-loop arrays. 89

Figure 66 (a) SMBXT image recorded in grazing geometry (g=11-28) on the homoepitaxy wafer with 12.5 μm; the nitrogen doping concentrate of the substrate and epilayer is 5 x 10^{18} cm^{-3} and 4.8 x 10^{15} cm^{-3} respectively. (b) SWBXT image recorded on the other wafer with the epilayer thickness around 30 μm; the nitrogen doping concentrate of the substrate and epilayer is 5 x 10^{18} cm^{-3} and 2 x 10^{15} cm^{-3} respectively 91

Figure 67 the bow shape of epilayer during epitaxial growth [178]. 94

Figure 68 (a) schematic shows gliding process of dislocation half-loop from 'a'→ 'b' → 'c' → 'd'. The line direction of dislocation 'a' is opposite to that of interfacial dislocation 'd'. 95

Figure 69 Monochromatic Beam X-ray topography with grazing-geometry g=11-28 shows expansion of a dislocation half-loop to form interfacial dislocations and half-loop arrays. (b) Schematic shows stages in the formation of a misfit dislocation by the nucleation and expansion of a half-loop on the surface. 98

Figure 70 Two different growth modes of CVD epitaxy on 4H-SiC. (a) 2D nucleation mode; (b) step-controlled growth mode. 99

Figure 71 (a), (c)-(e) white beam X-ray topographs with transmission geometries with different diffraction g vectos recorded at the same area on 4H-SiC wafer with 12.5 μm homo-epitaxial layer. (b) A Nomarski Interference Contrast optical image showing the etch pit pattern of the same area. (f)Monochromatic beam X-ray topography with grazing geometry g=11-28 recorded on a different area. (g) Schematic shows the formation stages of interfacial dislocations from 3C polytype. 100

Figure 72 (a) SWBXT grazing image g=11-28 shows the 3C polytypes and half-loop arrays emanating from the edge of the wafer. (b) the schematic shows how 3C polytypes and HLAs distributing at the upstep edge of the wafer. 101

Figure 73 (a)-(c) SWBXT images recorded at different g vectors on the same area of 4H-SiC epiwafer. (d) Microscopic images of HLA etch pit patterns coming out micropipes recorded on the same area as (a)-(c). (e) Schematic shows the formation of interfacial dislocations from a micropipes during epitaxy growth. 103

Figure 74 (a) and (c) A Nomarski Interference Contrast optical image showing two selected areas from Si face of KOH etched 4H-SiC homoepitaxial wafer. (b) and (d) Monochromatic x-ray topography with grazing geometry g=11-28 recorded on the same two areas. (a) and (b) are belonging to the same area, while (c) and (d) belongs to another area. 104

Figure 75 Schematic diagrams show (a) generation of dislocation loops near the substrate surface due to the scratch, and (b) Two possibilities for replication of the loop surface intersections during CVD epitaxial growth. 105

Figure 76 (a) A Nomarski Interference Contrast optical image recorded from Si face of KOH etched 4H-SiC homoepitaxial wafer. (b) – (c) SWBXT images with various diffraction g vector recorded on the same area. 106

Figure 77 (a) the simulated X–ray back-reflection topography of edge dislocation with extra half plane pointing downward (b) the simulated X-ray back-reflection topography of edge dislocation with extra half plane pointing upward [36]. 107

Figure 78 (a) untwinned and twinned SiC tetrahedras which are composed by one C atom at the center and bonded with four Si atoms symetricaly around it. (b) triangle variants obtained by the projection of SiC tetrahedra along <1120> direction. (c) The motion of partial dislocation belongs to 'glide' set. (d) The motion of 'shuffle' set. 108

Figure 79 Schematics showing Shockley partial dislocations of different core structures dissociated from a perfect BPD. (a) Partial dislocation core structure for various angles θ between the Burgers vector, **b**, and line direction, **u**, of the perfect BPD, defining regions I-IV; (b) Region I: $30^o<\theta<150^o$, the BPD is dissociated into two Si-core partials; (c) $210^o<\theta<330^o$, the BPD is dissociated into two C-core partials; (d) $-30^o<\theta<30^o$, one Si-core and one C-core; (e) $150^o<\theta<210^o$, one Si-core and one C-core. θ is defined in the inset of (a) {Zhang, 2009 #35}. 109

Figure 80 (a) The stacking sequence of 4H-SiC projected along <11-20> direction is as indicated by the tetrahedra ABA'B', and the interface is indicated by the dash line. (b) The magnified image of tretrahedra at the interface. The Si-core tetrahedron above the interface and C-core tetrahedron below the interface are marked out.....109

Figure 81 (a) UVPL image of a HLA (the array of dots along the line DC) before extended UV exposure. The HLA is connected to the mobile threading segment of the BPD at C. The interfacial segment of BPD is along AB. (b) Magnified view of boxed area in Fig. 1(a) after extended UV exposure. (c) HLA and ID configuration after longer UV exposure. (d) Schematic diagram showing the evolution of the rhombic shaped faults during dissociation [172]. 110

Figure 82 (a) and (c) examples of the mobile segments that interfacial dislocations are attached with can form stacking faults which are pointed out by arrows.....111

Figure 83 (a) and (b) Nomarski optical micrographs show the surface morphological features associated with the defects of interest. (c) Nomarski optical micrographs recorded on KOH etched Si face of 4H-SiC show Frank partials 'a', 'b', 'c' and 'd'.....113

Figure 84 (a) a white beam synchrotron topography image is recorded in grazing incidence (g=11-28) on the epilayer surface (Si-face) from a region near the edge containing many such features. (b) - (d) transmission topography images with different g vectors are recorded from the same region. 'A' indicates the stacking faults from the substrate and 'B' indicates the small triangle stacking fault inside the epilayer.(e) and (f) grazing geometry topographs recorded from another wafer with epilayer thickness around 30 μm with diffraction vectors are 1-109 and 11-28, respectively.....114

Figure 85The schematic in the middle shows how the V and Y shape defects distribute around the periphery of the wafer. (a)- (h) the grazing topographs of selected areas from point A-H on the edge of the wafer.....116

Figure 86 (a1), (b1), (c1) and (d1) are grazing topographs recorded on the epilayer surface after epilayer growth, while (a2), (b2), (c2) and (d2) are grazing topographs recorded on the substrate without epilayer. The open black dots in the images are threading screw dislocations. (a3), (b3), (c3) and (d3) are the schematic of the formation mechanism of Frank-type stacking faults. 117

Figure 87 (a) -(b) x-ray topographs with g=0004 of axial slice show how the deflected TSD and deflected TSD at the left and right edges of the wafer intersecting with the Si surface, which is similar to those shown schematical in (c). (c) Schematic cross-section of a SiC boule (grown on the C-face) showing as-grown TSDs which have been deflected onto the basal plane. Substrate wafers are then cut from the boule with a 4 degree offcut towards 11-20 as represented by the shaded region in between the black and red dashed lines. The Si-face of such wafers (shown pointing down in (c)) is then used for epilayer growth. The upturned substrate is shown in (d). The intersection point between TSD and Si face are marked as 'A', 'B', 'C' and 'D'. (d) The intersection of TSD and deflected TSD with the interface will grow Frank-type stacking fault on basal plane towards downstep direction . The red dash lines in (a) and (b) are corresponding to the red on in (c) 118

Figure 88 (a)-(c) the formation mechanism of V shape stacking fault during epitaxial growth; (d)-(f) the formation mechanism of Y shape stacking fault during epitaxial growth 119

List of Abbreviations

AFM	atomic force microscope
BPD	basal plane dislocation
BSE	back-scattered electrons
CVD	chemical vapor deposition
FR	Frank-Read
FWHM	full width at half maximum
HLA	half-loop arrays
HRXRD	high-resolution x-ray diffraction
ID	interfacial dislocation
LAGB	low angle grain boundary
MP	micropipe
NOM	Nomaski optical microscopy
PD	partial dislocation
PVT	physical vapor transport
REDG	recombination enhanced dislocation glide
SEM	scanning electron microscope
SF	stacking fault
SWBXT	synchrotron white beam x-ray topography
TED	threading edge dislocation
TEM	transmission electron microscope
TSD	threading screw dislocation
XRT	x-ray topography

List of Symbols

ν	Poisson's ratio
σ	stress (N/m^2)
ε	strain
$\boldsymbol{b}$	Burgers vector (m)
$\boldsymbol{l}$	line direction of the dislocation
$\boldsymbol{g}$	reflection vector
$\boldsymbol{R}$	stacking fault vector (m)
(uvw)	factional coordinates of atom in the unit cell
(hkl)	miller indices
F_{hkl}	structure factor of (hkl) reflection
f	atomic scattering factor
λ	wavelength (m)
V	unit cell volume (m^3)
ξ_g	extinction distance
S_x	source size in the incidence plane
E	incident X-ray energy
$\hbar$	Planck's constant
θ_B	Bragg angle
Φ_0	incident angle (angle between incidence beam and sample surface)
Φ_h	exit angle (angle between exit beam and sample surface)
μ	linear absorption coefficient
r_e	classical electron radius
τ_c	critical resolved shear stress
μ	shear modulus (J/m^2)

**Bold italic symbols are vectors*

Acknowledgments

First I would like to give my deep and sincere gratitude to Prof. Michael Dudley, my Ph.D. advisor, for providing me this opportunity to work in the crystal growth and characterization field. His wide knowledge and helpful guidance have been of great value for me. His understanding, encouragement and personal guidance have provided an excellent basis for my Ph.D. research.

Second, I would like to thank my parents, sister and brother in China who are always there for me and supporting me to finish my Ph.D. study.

I would also like to thank Prof. Balaji Raghothamachar for his instruction regarding both experiment and theory. I also thank him for being one of my committee members.

I would like to thank Prof. Dilip Gersappe and Dr. Darren Hansen of Dow Corning Company for being my dissertation committee members and their valuable advice on my thesis. Especially thanks to Dr. Hansen who came all the way from Michigan to attend my defense.

I would also like to thank my colleagues: Dr. Fangzhen Wu, Dr. Shayan Byrappa, Dr. Yu Zhang, Ms. Yu Yang, Mr. Jianqiu Guo, Mr. Ouloide Yannick Goue, Ms. Shun Sun, Ms. Gloria Chou, Ms. Hao Wang, Ms Ruifen Chen, Mr Zihao Ding, Mr. Zheyu Li, Ms. Mengnan Zou, Mr. Tianyi Zhou and Ms. Xuejing Wang for their help and discussion during my research.

Work financially supported under Dow Corning. And most of 4H-SiC wafers under investigation in this thesis were provided by Dow Corning Company.

Topography experiments were carried out at the Stony Brook Synchrotron Topography Facility, Beamline X-19C, at the National Synchrotron Light Source (NSLS) located at Brookhaven National Laboratory, which is supported by the U.S. Department of Energy, Office of Science, Office of Basic Energy Sciences, under Contract No. DE-AC02-98CH10886.

Monochromatic X-ray topography was carried out at 1-BM beamline at the Advanced Photon Source, Argonne National Laboratory, which is supported by the U. S. Department of Energy, Office of Science, Office of Basic Energy Sciences, under Contract No. DE-AC02-06CH11357.

We acknowledge the Synchrotron Light Source ANKA for provision of instruments at their beamlines and we would like to thank Andreas Danilewsky, Patrick McNally and Thorsten Muller for assistance in using TOPO-TOMO beamline.

Publications

1. M. Dudley, S. Byrappa, **H. Wang**, F. Wu, Y. Zhang, B. Raghothamachar, G. Choi, E. Sanchez, D. Hansen, R. Drachev, and M. Loboda, "Analysis of Dislocation Behavior in Low Dislocation Density, PVT-Grown, Four-Inch Silicon Carbide Single Crystals" in *Silicon Carbide 2010 — Materials, Processing, and Devices*, (S.E. Saddow, E. Sanchez, F. Zhao, M. Dudley (Eds.), Mater. Res. Soc. Symp. Proc., **1246**, 1246-B02-02, Warrendale, PA, (2010).

2. M. Dudley, S. Byrappa, **H. Wang**, F. Wu, B. Raghothamachar, G. Choi, S. Sun, E. K. Sanchez, D. Hansen, R. Drachev, S. Mueller, and M. J. Loboda, "Formation Mechanism of Stacking Faults in PVT 4H-SiC Created by Deflection of Threading Dislocations with Burgers Vector c+a," in Silicon Carbide, III-Nitrides, and Related Materials 2010, Edouard V. Monakhov, Tamás Hornos and Bengt. G. Svensson (Eds.), Materials Science Forum, 679-680, 269-272, (2011).

3. M. Dudley, F. Wu, **H. Wang**, S. Byrappa, B. Raghothamachar, G. Choi, S. Sun, E. K. Sanchez, D. Hansen, R. Drachev, S. G. Mueller, and M. J. Loboda, "Stacking Faults Created by the Combined Deflection of Threading Dislocations of Burgers Vector c and c+a During the Physical Vapor Transport Growth of 4H–SiC" Appl. Phys. Lett., 98, 232110-1 - 232110-1, (2011).

4. **H. Wang**, F. Wu, S. Byrappa, S. Sun, B. Raghothamachar, M. Dudley, E. K. Sanchez, D. Hansen, R. Drachev, S. G. Mueller, and M. J. Loboda, 'Basal plane dislocation multiplication via the Hopping Frank-Read source mechanism in 4H-SiC" Appl. Phys. Lett. 100, 172105 (2012)

5. **H. Wang**, S. Byrappa, F. Wu, B. Raghothamachar, M. Dudley, M. Dudley, E. K. Sanchez, D. Hansen, R. Drachev, S. G. Mueller, and M. J. Loboda, Materials "Basal Plane Dislocation Multiplication via the Hopping Frank-Read Source Mechanism and Observations of Prismatic Glide in 4H-SiC" , Science Forum Vols. 717-720 (2012) pp327

6. S. Byrappa, F. Wu, **H. Wang**, B. Raghothamachar, G. Choi, S. Sun, M. Dudley, E. K. Sanchez, D. Hansen, R. Drachev, S. G. Mueller and M. J. Loboda, "Deflection of Threading Dislocations with Burgers vector **c**/**c+a** observed in 4H-SiC PVT –Grown Substrates with associated Stacking faults", Materials Science Forum Vols. 717-720 (2012) pp 347-350

7. F. Wu, **H. Wang**, S. Byrappa, B. Raghothamachar, M. Dudley, E. K. Sanchez, D. Hansen, R. Drachev, S. G. Mueller and M. J. Loboda, "Synchrotron X-ray Topography Studies of the Propagation and Post-Growth Mutual Interaction of Threading Growth Dislocations with c-component of Burgers Vector in PVT-Grown 4H-SiC" Materials Science Forum Vols. 717-720 (2012) pp 343-346

8. F Wu., S. Byrappa., **H. Wang**, Y. Chen, B. Raghothamachar, M. Dudley, E.K. Sanchez, G. Chung,, D. Hansen, S. G. Mueller and M. J. Loboda, "Simulation of Grazing-Incidence Synchrotron X-ray Topographic Images of Threading c+a Dislocations in 4H-SiC", Mater. Res. Soc. Symp. Proc., Vol. 1433 (2012).

9. **H. Wang**, F Wu. S. Byrappa., S. Shun, B. Raghothamachar, M. Dudley, E.K. Sanchez, G. Chung,, D. Hansen, S. G. Mueller and M. J. Loboda, "Combined Application of Section and Projection

Topography to Defect Analysis in PVT-Grown 4H-SiC", Mater. Res. Soc. Symp. Proc., Vol. 1433 (2012).

10. M. Dudley, **H. Wang**, F. Wu., S. Byrappa, S. Shun, B. Raghothamachar, E. K Sanchez, G. Chung, D. Hansen, S. G. Mueller and M. J. Loboda, "Synchrotron Topography Studies of Growth and Deformation-Induced Dislocations in 4H-SiC", Mater. Res. Soc. Symp. Proc., Vol. 1433 (2012).

11. St. G. Müller, E. K. Sanchez, D. M. Hansen, R. D. Drachev, G. Chung, B. Thomas, J. Zhang, M. J. Loboda, M. Dudley, **H. Wang**, F. Wu, S. Byrappa, B. Raghothamachar, and G. Choi, "Volume production of high quality SiC substrates and epitaxial layers: Defect trends and device applications", J Cryst. Growth, 352, 39-42, (2012).

12. **H. Wang**, S. Sun, M. Dudley, S. Byrappa, F. Wu, B. Raghothamachar, G. Chung, E. K. Sanchez, S. G. Mueller, D. Hansen, and M. J. Loboda," Quantitative Comparison between Dislocation Densities in Offcut 4H-SiC Wafers Measured Using Synchrotron X-ray Topography and Molten KOH Etching" Journal of Electronic Materials, (March 2013).

13. F. Wu, **H. Wang**, S. Byrappa, B. Raghothamachar, M. Dudley, P. Wu, X. Xu, and I. Zwieback, "Characterization and Formation Mechanism of Six Pointed Star-Type Stacking Faults in 4H-SiC", Journal of Electronic Materials, (2013)

14. F. Wu, M. Dudley, **H. Wang**, S. Byrappa, S. Shun, B. Raghothamachar , E. K. Sanchez, G. Yong Chung, D. M. Hansen, S. G. Mueller, M. J. Loboda, "The Nucleation and Propagation of Threading Dislocations with c-Component of Burgers Vector in PVT-Grown 4H-SiC", in Silicon Carbide and Related Materials 2012, A.A. Lebedev, S. Y. Davidov, P.A. Ivanov and M. Levinshtein (Eds.), Materials Science Forum, 740-742, 217-220, (2013).

15. M. Dudley, B. Raghothamachar, **H. Wang**, F. Wu, S. Byrappa, G. Chung, E. K. Sanchez, S. G. Mueller, D. Hansen, M. J. Loboda, Synchrotron X-ray topography studies of the evolution of the defect microstructure in physics vapor transport growth on 4H-SiC single crystals., ECS Tranaction, 58(4) 315-324 (2013)

16. **H. Wang**, F. Wu, M. Dudley, B. Raghothamachar, G. Chung, J. Zhang, B. Thomas, E. K. Sanchez, S. G. Mueller, D. Hansen, and M. J. Loboda, "Measurement of Critical Thickness for the Formation of Interfacial Dislocations and Half Loop Arrays in 4H-SiC Epilayer via X-ray Topography" Materials Science Forum, Vols. 778-780 (2014) pp328-331.

17. **H. Wang**, F. Wu, S. Byrappa, Y. Yang, B. Raghothamachar, M. Dudley, ,G. Chung, J. Zhang, B. Thomas, E. K. Sanchez, S. G. Mueller, D. Hansen, and M. J. Loboda, "Study of V and Y shape Frank-type Stacking Faults Formation in 4H-SiC epilayer" Materials Science Forum, Vols. 778-780 (2014) pp332-337.

18. **H. Wang**, F. Wu, S. Byrappa, B. Raghothamachar, M. Dudley, P. Wu, I. Zwieback, A. Souzis, G. Ruland, and T. Anderson, "Synchrotron Topography Studies of the Operation of Double-Ended Frank-Read Partial Dislocation Sources in 4H-SiC", Journal of Crystal Growth (2014),

19. J. Zhang, D.M. Hansen, V.M. Torres, B. Thomas, G. Chung, H. Makoto, I. Manning, J. Quast, C. Whiteley, E.K. Sanchez, S. Mueller, M.J. Loboda, **H. Wang**, F. Wu and M. Dudley, "Defect Reduction Paths in SiC Epitaxy", MRS Proceedings, Volume 1693 (2014)

20. F. Wu, **H. Wang**, B. Raghothamachar, M. Dudley, S. G. Mueller, G. Chung, E. K. Sanchez, D. Hansen, M. J. Loboda, L. Zhang, D. Su, K. Kisslinger and E. Stach, Journal of Applied Physics 116, 104905 (2014)

21. **H. Wang**, F. Wu, Y. Yang, J. Guo, B. Raghothamachar, M. Dudley, J. Zhang, G. Chung, B. Thomas, E. K. Sanchez, S. G. Mueller, D. Hansen and M. J, Loboda, "Studies of Relaxation Processes and Basal Plane Dislocations in CVD Grown Homoepitaxial Layers of 4H-SiC" in "Gallium Nitride and Silicon Carbide Power Technologies 4", K. Shenai, M. Bakowski, M. Dudley, N. Ohtani (Eds.), ECS Transactions, 64 (7) 213-222 (2014)

22. **H. Wang**, F. Wu, Y. Yang, J. Guo, B. Raghothamachar, M. Dudley, J. Zhang, G. Chung, B. Thomas, E. K. Sanchez, S. G. Mueller, D. Hansen and M. J, Loboda. "Characterization of Defects in SiC Substrate and Epilayers", in "Gallium Nitride and Silicon Carbide Power Technologies 4", K. Shenai, M. Bakowski, M. Dudley, N. Ohtani (Eds.), ECS Transactions, 64 (7) 145-152 (2014)

23. **H. Wang**, F. Wu, Y. Yang, J. Guo, B. Raghothamachar, M. Dudley, J. Zhang, G. Chung, B. Thomas, E. K. Sanchez, S. G. Mueller, D. Hansen and M. J, Loboda. "Stacking Fault Formation during Homo-Epitaxy of 4H-SiC", in "Gallium Nitride and Silicon Carbide Power Technologies 4", K. Shenai, M. Bakowski, M. Dudley, N. Ohtani (Eds.), ECS Transactions, 64 (7) 125-131 (2014)

24. **H. Wang**, M. Dudley, F. Wu, Y. Yang, B. Raghothamachar, J. Zhang, G. Chung, B. Thomas, E. K. Sanchez, S. G. Mueller, D. Hansen and M. J, Loboda. "Studies of the Origins of Half-Loop Arrays and Interfacial Dislocations Observed in Homoepitaxial Layers of 4H-SiC", Journal of Electronic Materials (2014): 1-7.

1. Introduction

1.1 Properties of Silicon Carbide

Silicon carbide (SiC) grown by the physical vapor transport (PVT) technique is steadily replacing conventional semiconductor materials, e.g., silicon (Si) and gallium arsenide (GaAs), in certain extreme applications due to its outstanding properties such as a wide band-gap, high thermal conductivity, good chemical stability and high saturated electron drift velocity. However, while some applications have already been realized, issues relating to crystalline defects remain a barrier to the successful realization of several others. Compared with conventional semiconductor materials, e.g., Silicon (Si) and GaAs, SiC has ~3 times larger bandgap (3.2 eV) which is also comparable to GaN (3.4 eV), ~5 times higher breakdown voltage, ~2 times higher thermal conductivity, ~2 times higher saturated electron drift velocity. The comparison of some properties between SiC and other conventional semiconductor materials is presented in Table1.

Table 1 Properties comparison between 4H-SiC and other semiconductor materials[1]

Property	Silicon	GaAs	**4H-SiC**	GaN
Bandgap (eV)	1.1	1.42	**3.2**	3.4
Breakdown filed N_D=10^{17} cm-3 (MVcm^{-1})	0.6	0.6	**∥(0001) :3.0** **⊥(0001): 2.5**	2-3
Thermal Conductivity (W/cmK)	1.5	0.5	**3-5**	1.3
Electron mobility at N_D=10^{16} cm-3 (cm^{-2}V^{-1}s^{-1})	1200	6500	**∥(0001) :60** **⊥(0001): 400**	900
Saturated election velocity (10^7 cm^{-1})	1.0	1.2	**2**	2.5
Commercial wafer diameter (inch)	12	6	**6**	2

1.1.1 Application of Silicon Carbide Devices

SiC is also characterized by high hardness, good resistance in radiation environment, good mechanical and chemical stability, which render it able to function under extreme conditions *e.g.* high-temperature and high power conditions. Therefore SiC has a far-ranging variety of applications. These range from greatly improved high-voltage switching for energy savings in public electric power distribution and electric motor drives to more powerful microwave electronics for radar and communications to sensors and controls for cleaner-burning more fuel-efficient jet aircraft and automobile engines [2-7].

(1) LEDs

The first commercial LEDs were made by SiC which was demonstrated in 1907. Yellow LEDs were manufactured using 3C-SiC in the Soviet Union in the 1970s, and blue LEDs become worldwide in the 1980s. Recently, Gallium Nitride (GaN) began to replace SiC in LED

manufacturing due to its 10-100 times brighter emission. However, SiC is a very popular substrate for GaN growth. And SiC also serves as a heat spreader in high-power LEDs.

(2) Power Electronic Devices

Electronic devices and circuits which are made by Silicon carbide (SiC)-based semiconductor are presently being developed for use in extreme conditions such as high-temperature, high-power, and high-radiation conditions, while conventional semiconductors cannot adequately perform. The first and most popular SiC devices available were Schottky diodes, followed by Junction-gate FETs and MOSFETs for high-power switching, and Bipolar transistors and thyristors are currently being developed. The first commercial JFETs rated at 1200 V were introduced to the market in 2008, and the first commercial MOSFETs rated at 1200 V since 2011.

(3) Jewelry

6H-SiC can also be used in jewelry, which is called "synthetic moissanite" or just "moissanite" after the mineral name. Moissanite is similar to the conventional jewelry materials-diamond in several important respects: having good transparent, hardness (9–9.5 on the Mohs scale, compared to 10 for diamond), and a good refractive index between 2.65 and 2.69 (compared to 2.42 for diamond).

1.1.2 SiC Crystallography

SiC is a member of a family of materials which exhibit a one-dimensional polymorphism called polytypism. Approximately 200 polytypes of SiC have been observed. The first SiC structure discovered was 15R; the same Si-C bilayer repeats every 15 layers with a rhombohedral structure, which was labeled as type I; the second one was the hexagonal structure (6H) with six-layer repetition labeled as type II; the third one found was the 4-layer hexagonal structure (4H) labeled as type III. The cubic structure (3C) was the fourth one to be discovered, which was naturally labeled as type IV. 3C-SiC is a commonly observed polytype, but no large-size and high-quality 3C-SiC can currently be grown. The number in the polytypes' name indicates the number of bilayers in the repeat unit followed by a letter, which indicates the category of basic crystallographic type; cubic (C), hexagonal (H), and rhombohedral (R). SiC polytypes are differentiated by the stacking sequence of each tetrahedrally bonded Si-C bilayer as shown in Fig. 1(a). Note a carbon atom (grey color) is at the centroid of four silicon atoms (or vice versa) and is bonded to each of these atoms by a predominantly covalent bond and then a tetrahedron arises out of the tetrahedral bonding between silicon and carbon atoms. One of the Si-C bonds is parallel to the c-axis (0001), so the triangular base of the tetrahedron opposite to this bond is normal to the c-axis and defines a c-plane. The Si-C tetrahedron on the right in Fig.1 (a) is produced by rotating the tetrahedron on the left (untwinned) in Fig.1 (a) by 180^{O} around the c-axis. The former is called the twinned variant. The projection of the tetrahedron along the [11-20] direction is shown in Fig 1(b).

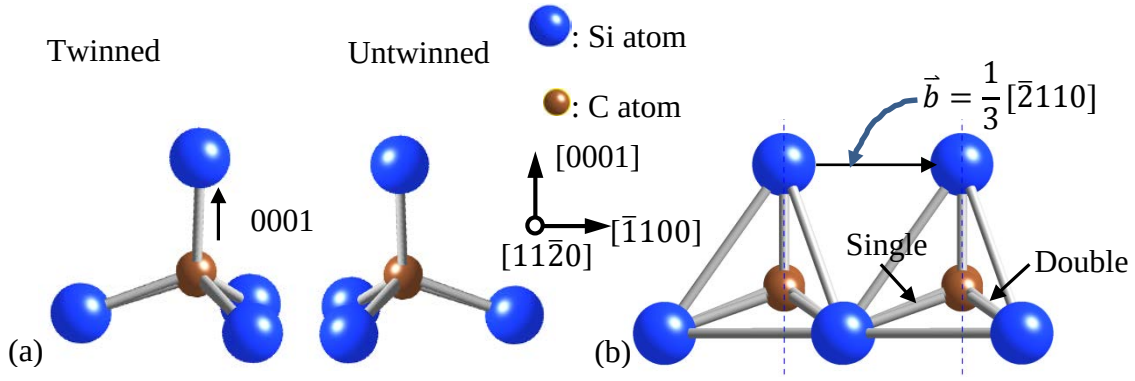

Figure 1 (a) Untwinned and twinned SiC tetrahedra which are composed of one C atom (grey color) at the center and four Si atoms (blue color) bonded symetricaly around it. (b) The triangles produced by projection of the twinned variantof the SiC tetrahedra along the $[11\bar{2}0]$ direction.

Table 2 Properties of three major SiC polytypes [8,9]

Polytype	3C	4H	6H
Crystal Structure	Cubic	Hexagonal	Hexagonal
Space Group	T^2_d-F43m	C^4_{6v}-P6$_3$mc	C^4_{6v}-P6$_3$mc
Lattice constants (a)	4.36	3.08	3.08
Lattice constants (c)	4.36	10.05	15.12
Stacking sequence	ABC	ABA'C'	ABCB'C' A'
Density (g/cm^3)	3.21	3.21	3.21
Bandgap (eV)	2.36	3.23	3.05
Bulk modulus (GPa)	250	220	220
Thermal conductivity (W cm^{-1}K^{-1})	3.6	3.7	4.9
Hole mobility at N_A=10^{16} cm-3 (cm^{2}V^{-1}s^{-1})	40	90	115

The polytypes we are primarily interested in are hexagonal 4H- and 6H-SiC, although 3C is the most common polytype. Fig.2 shows the projection of their structures onto the (11-20) plane. The stacking sequence is "ABA'C'…" for 4H-SiC and "ABCB'A'C'…" for 6H-SiC (where, for example, A' is twinned variant of A). SiC is a polar semiconductor along the c-axis, in that one surface normal to the c-axis is terminated with silicon atoms while the opposite normal c-axis surface is terminated with carbon atoms as shown in Fig 2. These surfaces are referred as 'silicon face' and 'carbon face', respectively. It should be noted that 4H- and 6H-SiC are only two of the many SiC polytypes with hexagonal crystal structure.

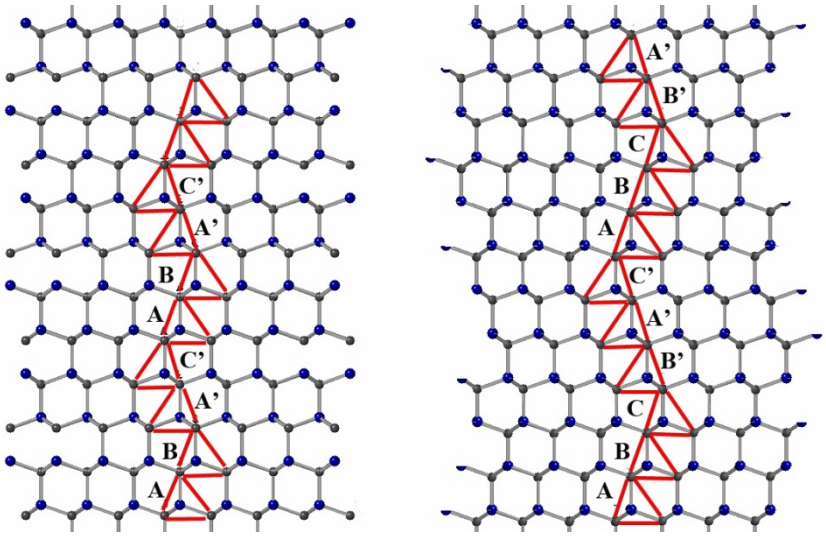

Figure 2 Projection of 4H-SiC (left) and 6H-SiC (right) structure into (11-20) plane. Small and large balls indicate C and Si atoms, respectively. The stacking sequences are "ABA'C'…"and "ABCB'A'C'…" for 4H and 6H-SiC, respectively

1.2 Defect Structure in Silicon Carbide

Dislocations in crystals can be divided into two general categories: Grown-in (or growth) dislocations and deformation- induced dislocations. The nucleation and behavior of these two categories of dislocations can correspondingly be distinguished according to phenomena occurring at the growth interface (growth dislocations) or behind the growth interface (deformation-induced dislocations).

Growth dislocations are observed in crystals grown from vapor, melt, solution and flux. They are formed *during growth* via replication of dislocations which thread the moving crystal-growth front/interface. The dislocations threading the growth interface can originate from the following processes: (1) the continuation of dislocations already present in the seed; (2) the relaxation of stresses from handling damage on the surface of the seed; and (3) the relaxation of stresses arising from the incorporation of inclusions of solvent or impurity which can occur on the seed surface or later during growth or equivalently imperfect lattice closure around such an inclusion.

Growth dislocations typically have the following characteristics: (1) they are long and straight; (2) they run in well-defined directions which correspond to the minimum elastic line energy per unit growth length. These directions depend on the degree of anisotropy of the elastic properties: for isotropic crystals, they run perpendicular to the growth face, i.e., parallel to the normal to the growth face, **n**; for highly anisotropic crystals they can deviate by up to 45º away from **n**, although in most cases they lie within ±20 º (dislocations can, in such cases, run along non-crystallographic directions). For cases where the elastic properties are unknown, three rules apply: (1) for a pure screw dislocation, **l** (line direction) is parallel to **n;** For a pure edge dislocation, provided **n** is parallel to a two-fold symmetry axis, **l** is parallel to **n**; For a mixed dislocation, **l** lies between **n** and **b**. In addition, if the growth dislocations have a screw component, they have growth spirals associated with them on the growth surface

Deformation-induced dislocations otherwise known as slip dislocations are dislocation configurations produced by plastic deformation, i.e., stress-induced slip/glide and/or multiplication of pre-existing dislocations. This process is characterized by the glide system, (hkl)[uvw] and the critical resolved shear stress required to activate it. The pre-existing dislocations can be: growth dislocations; dislocation loops surrounding inclusions/precipitates; surface dislocation loops, e.g. originating due to surface damage; or point defect condensates. The stresses can originate from thermal gradients in the growing crystal, thermal expansion mismatch between crystal and crucible or other crystal holding device, or thermal expansion mismatch between inclusions and surrounding crystal.

Deformation-induced or slip dislocations typically have the following characteristics: they have the appearance of loops bowing out from pinning points; they comprise configurations consisting of concentric loops, half-loops, or smaller fractions of loops emanating from a dislocation source; they comprise configurations consisting of dislocation pile-ups against a barrier; they are characterized by straight intersections of the slip bands to which they belong with the crystal surfaces in cases where the slip plane is inclined to these surfaces.

Generally one can distinguish growth dislocations from slip dislocations from their shape or general morphology as mentioned above. It should be noted that, subsequent to growth, the dislocation configuration may be changed by: (a) Movement of grown-in dislocations due to glide or climb; (b) propagation of new dislocations generated by glide processes, for example around inclusions or condensation of vacancies and self-interstitials.

1.2.1 Fundamental Understanding of Defects in SiC

For the case of 4H-SiC, growth dislocations in such crystals therefore are expected to have line directions parallel or close or parallel to the growth axis. Accordingly, dislocations with line directions approximately along [0001] have been commonly observed with the following Burgers vectors:

(1) **b**=n[0001] or n**c** as shown in Fig.3(b) ,
   a. when n=1or 2, these are the so-called threading screw dislocations (TSDs);
   b. when n>2, the dislocations have a hollow core and are known as micropipes (MP);
(2) **b**=1/3[11-20] or a, the so-called threading edge dislocations, TEDs as shown in Fig.3(c). the line direction is roughly parallel to c axis;

In addition, there have been several observations of growth dislocations with line direction parallel to [0001] with Burgers vector of 1/3[11-23], or **c** + **a**, (so called threading mixed dislocations, TMDs). Later in this thesis, deflection of such growth dislocations through overgrowth by macrosteps will be described.

The commonly observed deformation induced dislocations in 4H-SiC are basal plane dislocations (BPDs) which are glissile dislocations with both line directions and Burgers vectors in basal plane (0001), as shown in Fig. 3(a), as there is only one primary slip plane (0001) in SiC and the primary slip system is<11-20>(0001), Shockley partials are in c-plane with Burgers vectors 1/3<1-100> type and Frank partials have Burgers vector component out of c-plane and its dislocation lines is usually within c-plane. In addition to dislocations, other extended defects are also widely observed in SiC bulk crystals, epilayers and devices. In bulk crystals, the major

extended defects are Shockley type stacking faults (SFs), Frank-type SFs and large grain boundaries (LAGBs) which are composed by close-packed TEDs or aggregation of BPDs. The characters of the major dislocations are shown in Table 3.

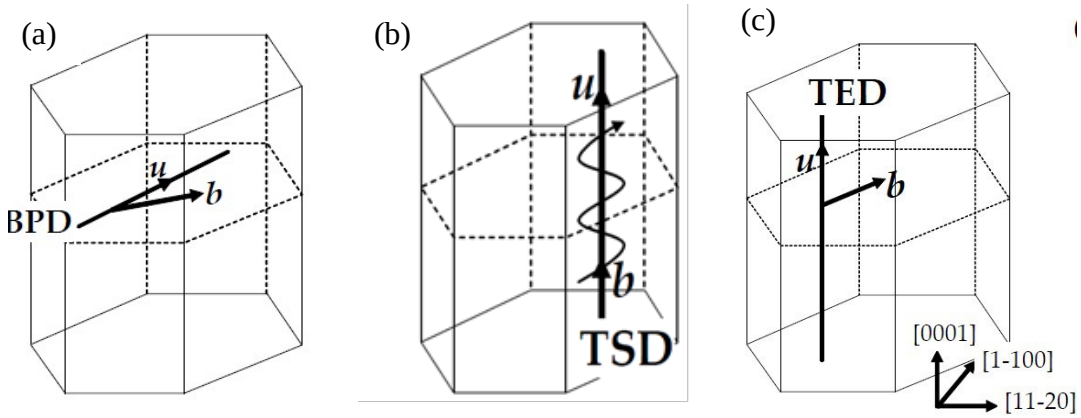

Figure 3. (a) A straight BPD in (0001) basal plane; (b) A TSD in SiC with line directions along [0001] and Burgers vector n<0001> (c) A TED in SiC with line direction along [0001] and burgers vector on basal plane.

Table 3 Characteristics of various dislocations in 4H-SiC substrate

	Dislocation line (**u**)	Burgers vector (**b**) (magnitude)
BPD	‖ (0001) plane	1/ <11-20> (3.08 Å)
TED	Roughly ‖ [0001] direction	1/ <11-20> (3.08 Å)
TSD	‖ [0001] direction	nc (10.05nÅ) n(integer) ≤2, or **c**+**a**
MP	‖ [0001] direction	nc (10.05nÅ) n(interger)>2
Shockley PD	‖ (0001) plane	1/3<1-100> (1.778Å)
Frank PD	‖ (0001) plane	1/2c, 1/4c

Micropipes have been shown to nucleate at inclusions of foreign material (either graphite particles or silicon droplets, or at polytype inclusions. The work of Dudley *et al* [10] showed that micropipes are hollow core screw dislocations. The work of Neudeck *et al* [11] showed that micropipes had a strong detrimental effect on device performance. As a result, an enormous effort to eliminate them was undertaken and this was achieved around 2007 [12]. It is believed that screw dislocations with smaller Burgers vector may also form from similar mechanisms.

Basal plane dislocations are usually produced by plastic deformation under internal or external stress. The stresses driving the BPD motion are thought to arise from radial temperature gradients or even non-linear axial temperature gradients. As a result there have been concerted efforts to reduce these gradients by intelligent hot-zone design. This resulted in the so-called “low stress” process announced by Dow Corning in 2009 [13] wherein the thermal, shear stress on the basal plane were reduced to around 0.5 MPa which is thought to be below the critical resolved shear stress 1MPa for glide at the growth temperature (value extrapolated from measurements made at lower temperatures by Samant *et al.*[14]). This enabled the BPD density to be driven down by several orders of magnitude to around a few hundred centimeters per cubic centimeter.

Simultaneously, when the thermal stress was reduced, the 1**c** screw dislocation densities also diminished significantly suggesting some relationship between the thermal stress and their densities also. While reducing the screw density is also desirable, it should be noted that the TSDs actually provide a useful service. The complex structure of SiC means that polytype reproduction cannot be achieved by 2D nucleation. Atom species experiencing 2D nucleation are unable to sense the stacking sequence more than one layer below the terrace surface. Such nucleation therefore inevitably produced the default 3C structure rather than reproducing the underlying 4H structure. In order to replicate the correct stacking sequence, growth much occurs in a low supersaturation mode that is mediated by step flow. This requires species to adsorb onto a flat terrace, and then surface diffuse to a step riser or kink in a step riser where they can stably attach. The correct stacking sequence is presented to the species at the step riser thereby enabling correct polytype replication. One could conceive using an offcut seed to provide such steps although eventually all such steps will grow out of the crystal. Inexhaustible supplies of steps are therefore required. These are provided by the growth surface intersection of the dislocation with screw component. Screw dislocations, therefore help with growth and enable maintenance of polytype.

1.3 Motivation

Table 4 The influence of defects on device performance

Defect	Density in Substrate (cm^{-2})	Density in Epilayer (cm^{-2})	Disadvantage
Micropipes MPs	$0\text{-}10^2$	$0\text{-}10^2$	Severe reduction in power device breakdown voltage and increase in off-state leakage
Threading screw dislocations (TSD)	$10^2\text{-}10^3$	$10^2\text{-}10^3$	Reduction in Device breakdown voltage by 5%~35%, increase in leakage current, reduction in carrier lifetime
Threading edge dislocations (TEDs)	$10^3\text{-}10^4$	$10^3\text{-}10^4$	Formation of LAGBs and providing pinning points for BPDs gliding.
Basal plane dislocations (BPDs)	$10^2\text{-}10^4$	$10^2\text{-}10^4$	Nucleation source of expanding sacking faults leading to bipolar power device degradation, reduction in carrier lifetime.
Low angle grain boundaries (LAGB)			Causing an area with high BPD density
Stacking faults (SFs)			Degrade bipolar power devices, reduce carrier lifetime

As we discussed earlier, SiC materials are facing serious issues related to various defects exiting in the substrates and epilayers, such as MPs, TSDs, TEDs, BPDs and SFs which are listed in Table 4. MPs are device-killing defects due to the hollow-core associated with them. TSDs play a critical role in maintaining the desired polytype promoting spiral step-flow growth. However, they have been found to degrade the device performance, reducing the breakdown voltage by 5-35% [15]. In addition, the forest of TEDs in the as-grown crystal poses a significant barrier which creates a pinning effect on the glide of BPDs either during growth or post-growth cooling, leading to localized higher densities of BPDs. Unconverted BPDs have been observed to be dissociated into partial dislocations (PDs) and degrade the device performance. The

interaction between the advancing PDs and threading dislocations can lead to complex webs of dislocations in SiC bipolar devices. Thus the goals of our studies are to understand the behavior and nucleation mechanisms of various defects and their mutual interactions SiC bulk crystals, and then facilitate the development of strategies to reduce the densities of defects so as to improve device performance.

1.4 Crystal Growth Techniques for SiC

Because SiC starts to decompose above 2830^{O}C, it is thus unfeasible to grow SiC from a stoichiometric melt. The best way to achieve the single SiC growth is based on vapor growth at high temperature. The earliest and simplest manufacturing production of SiC was using the Acheson Method in 1892 [16]. In 1959, Lely demonstrated the growth of SiC on a porous SiC cylinder by vapor condensation [17]. In the Lely process, SiC sublimed from polycrystalline SiC powder at temperatures near 2500°C is randomly condensed on the walls of a cavity forming small, hexagonally shaped platelets (size up to 2×2 cm). This original method was improved later by Hamilton [18] and Novikov and Ionov [19], and is commonly referred to as the Lely method. Because of the high growth temperature, the 6H-SiC polytype is predominantly produced by this method. The thin layer of platelet is due to the fact that 6H-SiC tends to grow faster in direction parallel to the basal plane rather than along the basal plane normal direction (usually less than 1mm in thickness)

The big breakthrough in SiC growth happened in 1978, when Tairov and Tsvetkov developed the seeded sublimation growth technique [20], which is commonly referred as the modified Lely method, which make it possible to achieve controlled growth of large size SiC wafers on seeds. In the modified Lely method also called the Physical Vapor Transport (PVT) growth technique, the seeds are usually held at the top of the chamber, and deposition of Si and C atoms occurs in an argon environment at 10^{-4} –760 Torr in the temperature range of 1800–2600 ℃ and the vapor transport is facilitated by a temperature differential, $\Delta T = T_2 - T_1$, between the seed and the source material. Because the seed temperature T_1 is maintained slightly lower than the source temperature T_2, the source vapor gets supersaturated near the seed, and then crystallizes onto the seed. This PVT growth method has spurred intense worldwide research activity in recent years and has become a standard method for growing SiC crystals. The first available commercial SiC wafers were made by Cree Research, Inc., in 1991. Scientists have made great efforts on studies for growing larger size and lower-defect- density SiC wafers. 4H-SiC wafers have gradually expanded from 2 inch, 4 inch and now even 6 inch wafers are commercially available.

There are three essential parameters for crystal growth which are growth temperature (T), temperature gradient, and pressure inside the reaction chamber. The growth temperature together with the Si/C ratio and the orientation of the seed crystal used mainly determines the polytype of the growing crystal. At the same time, the temperature gradient and gas pressure control the transport and hence the crystal growth velocity. The control of temperature is very crucial for 4H-SiC crystal growth. 4H-SiC crystals are grown in a narrow temperature range of 2350-2375 ℃ at 5 mbar using the (0001) C face of 4H seed plates [21]. Above 2300 ^{o}C, the 4H-SiC polytype transforms into 6H; below 2350 ^{o}C, crystal quality becomes a limiting factor.

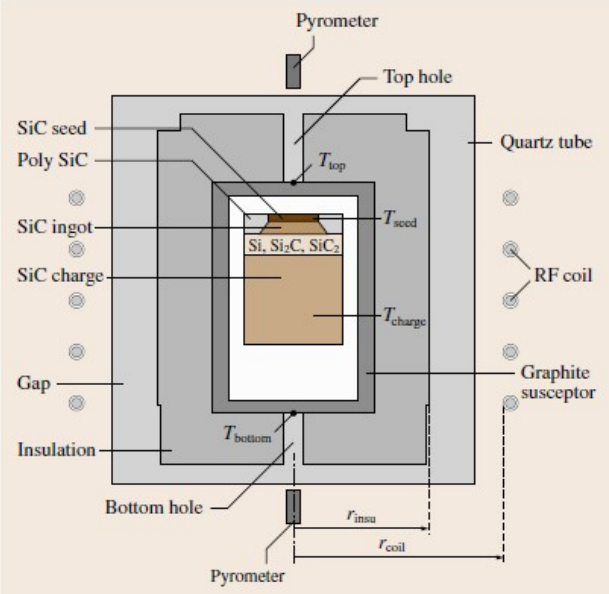

Figure 4. Schematic of the SiC growth system [22]

A new SiC growth technique called “repeated *a*-face’ method has been reported by Nakamura et al.[23]. The seeds required for conventional substrate growth is obtained by repeating a-face growth in order to eliminate the growth dislocations. Then the obtained seed is used to grow SiC ingots by conventional PVT growth method along c-axis direction. Kondo *et al.* [23] reported that a block crystal more than 150 mm size was produced by the RAF growth method. The quality of the 150 mm 4H-SiC wafer was evaluated by etch pits density (EPD) using molten KOH+ Na_2O_2 etching, which was estimated at approximately 3,000 cm^{-2}. In particular, both the densities of TSDs and BPDs were estimated around 300 cm^{-2}.

2. Characterization Techniques

Multiple techniques and equipment have been employed in our study on characterizing semiconductor crystalline materials, including Synchrotron X-ray Topography (SXRT), Transmission Electron Microscopy (TEM), Scanning Electron Microscopy (SEM) and Nomarski Microscopy. Each of these will be introduced in detail.

2.1 Synchrotron X-ray Topography

2.1.1 Introduction

X-ray Topography (XRT) is a nondestructive characterization technique for imaging crystalline material with low dislocation density ($<10^6$ cm^{-3}) by recording the intensity profile of X-ray diffraction. It is a very powerful tool for monitoring crystal quality and visualizing defects in many different crystalline materials, especially for semiconductor materials such as Silicon (Si), Silicon Carbide (SiC), Gallium Nitride (GaN) and Sapphire (Al_2O_3). When developing a new method to grow crystals or optimize the growth condition for crystalline materials, XRT is the best way to 'see' the interior of a single crystal or look at its surface by producing images to monitor and reveal the growth results and point out the right direction for the crystal grower.

Table 5. Milestones of the development of X-ray Topography [24]

1895	Wilhelm Röntgen	The discovery of X-rays
1931	Berg [25]	First Monochromatic x-ray diffraction pattern recorded on rock salt using laboratory source
1945	Barrett [26]	Report results from single crystals of silicon ferrite with improved contrast
1945	Wooster [27]	The establishment of 'topography' in literature
1949	Guinnier and Tennevin [28]	Using polychromatic x-ray in transmission from lab x-ray sources on aluminum samples
1957	Lang [29]	Section topography
1974	Tuomi *et al.*[27]	First synchrotron radiation topography on Silicon samples
1975	Hart [30]	'Synchrotron' White beam x-ray topography (SWBXT)
1977	Tanner [31]	'Synchrotron' Monochromatic X-ray Topography (SMBXT)

The development of synchrotron radiation sources and the construction of synchrotron light sources worldwide has enable significant improvements to high-resolution X-ray Topography development [32]. The synchrotron sources can provide high resolution, broad wavelength range (0.2-2 *Å* for white beam), and large X-ray areas up to be 5×0.7 cm^2 at X-19C (NSLS), $10 \times 1 cm^2$ at 1-BM (APS). The topographic resolution is depending on the source size in the incidence plane (S_x), source-specimen distance (D) and the specimen-film distance (d).

$$R_x = d\, S_x / D \qquad (1)$$

Small source (300×100 μm^2) combined with large source-specimen distance (25 m) imparts high spatial resolution (< 1 μm).

2.1.2 Principles of XRT Method

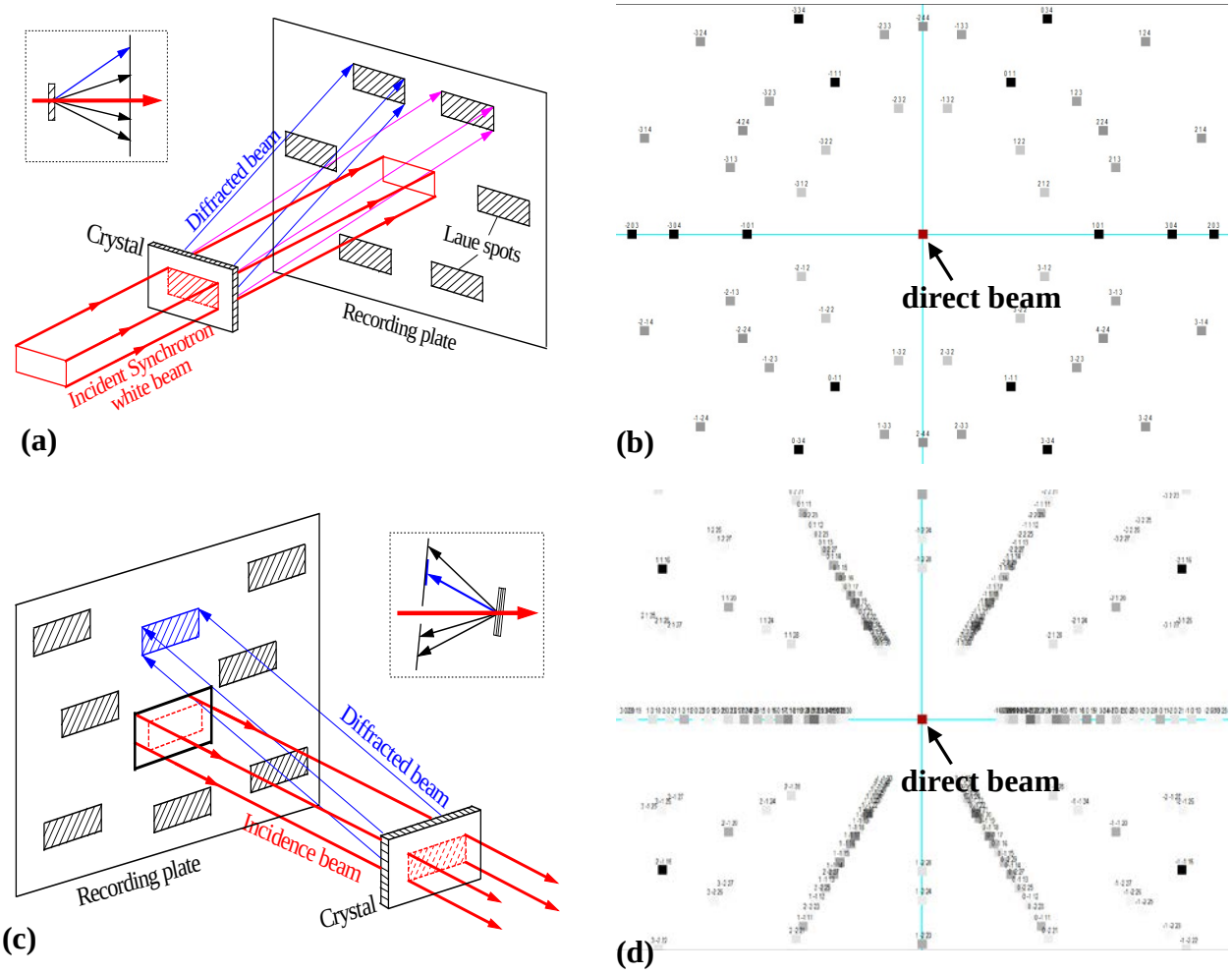

Figure 5. (a) Schematic shows diffraction patterns from sample in transmission geometry (Laue case). (b)Laue pattern map in transmission geometry when surface plane (0001), side plane (11-20) and the red dot is direct beam. (c)Schematic shows diffraction patterns from sample in reflection geometry (Bragg case). (d) Laue pattern map in back-reflection geometry with surface plane (0001), side plane (11-20)

When a white beam which is composed of a mixture of wavelengths from approximately 2 $\dot{A}$ to 0.25 $\dot{A}$ (energy from 6keV to 50 keV) impinges on a single crystal, diffraction can take place either in reflection geometry (Bragg case) shown in Fig. 5(c) or transmission geometry (Laue case) as shown in Fig. 5(a). The beam will be diffracted in many directions, creating many Laue spots comprising a Laue pattern. When the sample is placed with surface plane (0001) and side plane (11-20), the Laue pattern for Laue and Bragg cases are shown in Fig. 5(b) and Fig. 5(d), respectively. The position of each Laue spot should satisfy the Bragg Law:

$$\boldsymbol{E = \frac{hc}{2dsin\,\theta_B}},\ or\ \boldsymbol{\lambda = 2dsin\theta_B} \qquad (2)$$

where E is the incident X-ray energy , λ is the incident wavelength, d is the plane spacing of the diffracted plane, h is Planck's constant, c is the speed of light, and θ_B is the Bragg angle. Each

spot is a high-resolution X-ray topography, and the size of the Laue spots in transmission geometry is the same as the incident beam as x-ray beam is highly collimated. Each spot is labeled by a diffraction vector $\boldsymbol{g}$ in [hkl] form indicating that this single x-ray topography arises due to diffraction from a certain set of atomic planes (hkl). If the white synchrotron beam passes through a monochromator (two cooled parallel Si (111) crystals in APS), only a single wavelength or energy is available and thus only a single diffraction spot can be obtained at a time when the crystal is rotated to the right θ angle for a specific set of atomic planes. In our experiments, we mainly conducted white beam X-ray topography in Beamline station X-19C at National Synchrotron Light Source (NSLS) although some were also carried out at ANKA, while monochromatic X-ray topography was carried out at Beamline station 1-BM at Advanced Photon Source (APS) and also in CHESS (Cornell High Energy Synchrotron Source). The theoretical resolution is ~ 0.4 μm for X-19C and ~0.06 μm for 1-BM if the specimen-film distance is selected as 10 cm. X-ray topographs can be recorded either on high-resolution cameras or on photographic film. In our case, the diffracted images are recorded on Agfa Structurix D3-SC films and Slavich VRP-M high-resolution film. Exposure time depends on the intensity of diffracted beams and film sensitivity. Then the recorded film will be developed in Kodak D-19 developer and fixed in Kodak D19 Rapid Fixer solutions to process the emulsions.

2.1.3 Sample Geometry for Diffraction Imaging

There are mainly four geometries employed in study of 4H-SiC single crystals: transmission geometry (Laue case), back-reflection geometry (Bragg case), grazing geometry, section geometry, all of which will be explained in detail, respectively.

I. Section topography

Section topography is the most fundamental among the XRT techniques. The incident beam has to pass through a very narrow slit (~10 μm) before it hits the crystal as shown in Fig.6 (d). Only the transmitted image recorded from the crystal volume in which diffracted beams interact (a triangle section in Fig. 6(d)) is recorded. The same geometry is used for projection topography where the sample and the film are translated synchronously as created by Lang [33]. The resulting projection image is a superposition of multiple section images. The perfect crystal shows fringes in x-ray section topography. Even small strain caused by defects can distort the fringes and can be observed in section topographs, which can also provide us the depth information of defects [33]. It is also can be used to distinguish stacking faults [34].

II. Transmission geometry.

The incident beam enters the crystal from one side, while diffraction patterns are recorded on the other side of the sample. Because the X-ray passes through the whole bulk crystal, as a result it is a very good way to reveal the overall defect distribution especially basal plane dislocations (BPDs) in 4H-SiC crystals. Fig. 6(a) is transmission-geometry monochromatic x-ray topography recorded on a 4H-SiC wafer with 4 degree offcut along [11-20] direction carried out in CHESS. The sample is rotated 10 degree away from [-1100] direction, and the Bragg angle is set to be 31.3^{o} on the plane (11-20) for the 15 keV X-ray beam. Although the Laue spot size is limited by the size of incident beam, a wafer with larger diameter (such as 4” and 6” wafers) can be recorded by moving the sample and film synchronously controlled by motors in order to scan the whole wafer. In the x-ray topographs, the curved-black-contrast lines are basal plane dislocations.

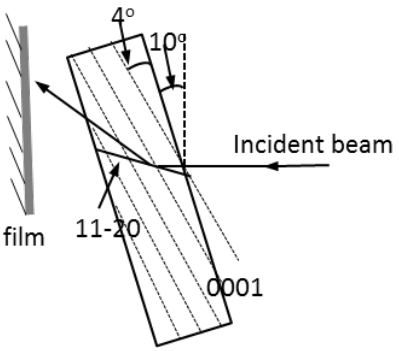

(a) Transmission g=11-20 $\boldsymbol{\theta_B}$=**31.3°**

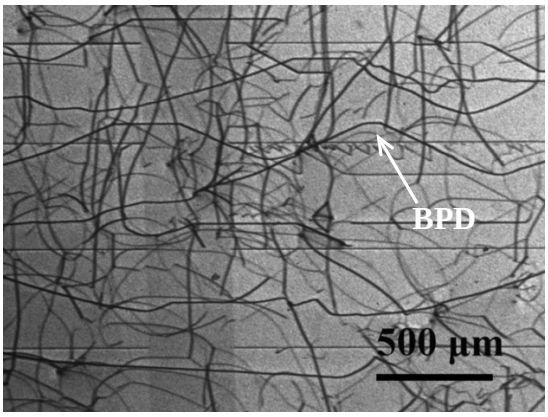

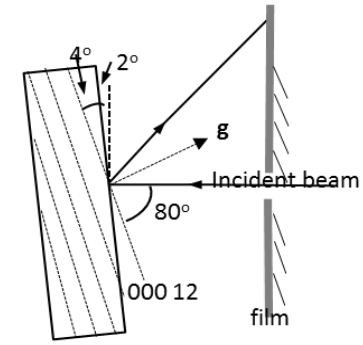

(b) Back-reflection g=00012 $\boldsymbol{\theta_B}$=**80°**

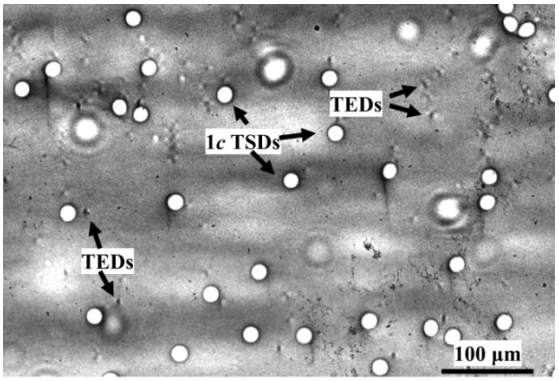

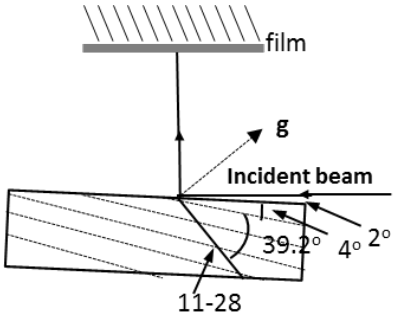

(c)Grazing-reflection g=11-28 $\boldsymbol{\theta_B}$=**45.2°**

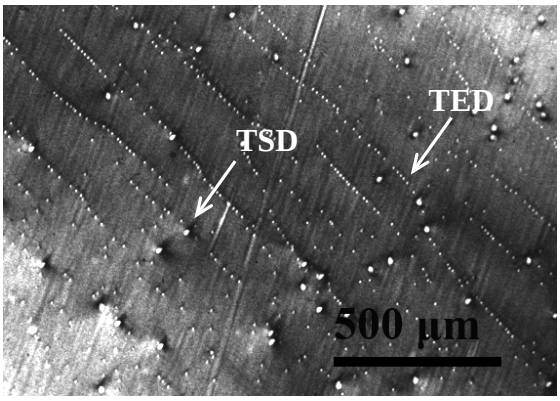

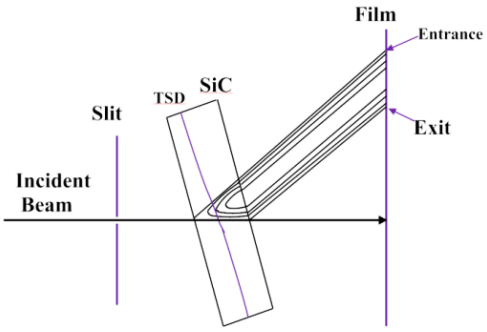

(d) Section Topography

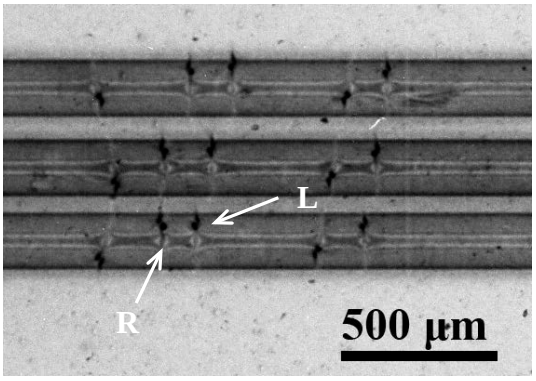

Figure 6. (a)-(d) schematic of transmission, back reflection, grazing and section geometry and X –ray topographs.

11-20 diffraction topographs are very useful to get the average BPD density of 4H-SiC wafers, while 1-100 and -1101 are used to check the existence of stacking faults and determine their types.

III. Back-reflection geometry

When the beam enters and leaves through the same surface, in other words, the incident beam and the recorded diffracted pattern is on the same side of the sample, and then this is called the Bragg geometry. When the incidence angle is large, it is called back-reflection x-ray topography as shown in Fig. 6(b). In both grazing and back-reflection geometry, only the defects within the penetration depth from the incident face can be recorded, which is a better way to characterize epilayers or the surfaces of very thick bulk crystals. Back-reflection geometry has a larger Bragg angle compared with grazing geometry which will be explained below, which is 80^o for reflection (00012), and the wavelength is set to be 1.65 *Å* (7.52 kev). In back-reflection geometry, TSDs and MPs appear as white circles surrounded by narrow dark rings with the radius proportional to the Burgers vector of the threading defects, which is effective to measure the magnitude of Burgers vector for TSDs (1~2**c**) and MPs (*n***c**, *n* is an integer larger than 2).

IV. Grazing geometry

In this geometry, the incident beam touches the crystal at grazing incidence (~2^0), where it is diffracted by planes at large angle to the sample surface, resulting in highly asymmetric diffraction conditions as shown in Fig. 6(c). Grazing-geometry X-ray topography has smaller Bragg angle (45.2^o for g=11-28, 4H-SiC) compared with back-reflection. The low grazing angle means that the penetration depth (~30 μm) is much lower than back-reflection. In Fig. 6(c), the incident angle (the angle between the incident beam and the surface) is usually 2^0, and the off-cut angle of the 4H-SiC is 4^0 along [11-20] direction. The images of TSDs & TMDs appear as white features with roughly oval shape with various orientations and dimensions, while the configuration of TEDs is similar except their size is much smaller compared with TSDs.

Usually the penetration depth can be measured directly from X-ray topographs, which is very helpful for interpreting the topographic images. It gives information about the crystal volume imaged and thus helps in the understanding of the defect configurations, especially in epilayers. It also can be theoretically calculated which may be different from the measured value. For the dislocated regions of crystal, the penetration depth *t* is governed by photoelectric absorption and is given by

$$t = \frac{1}{\mu\left(\frac{1}{\sin\phi_0} + \frac{1}{\sin\phi_h}\right)} \qquad (3)$$

where μ is the absorption coefficient (cm^{-1}), Φ_0 is the incident angle and Φ_h is the exit angle. In 11-28 reflection of *4H*-SiC [λ=1.48 Å, see Fig. 6(a)], the penetration depth based on photoelectric absorption is calculated to be 2.69 μm, while for (000.12) reflection [λ=1.65Å, see Fig. 6(b)], the penetration depth is 20.9 μm.

2.1.4 Image Contrast in X-Ray Topography

The X-ray topography of a perfect crystal is homogenous, while the contrast of defects in an imperfect crystal are mainly caused by two mechanisms: orientation contrast and extinction contrast [35].

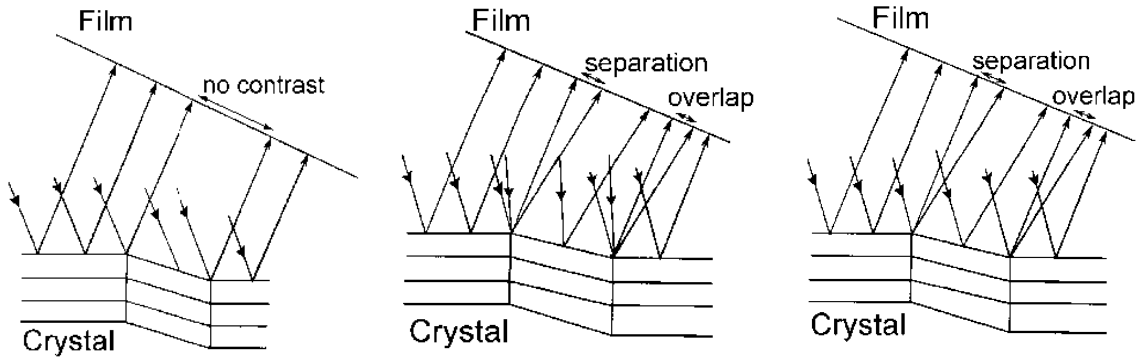

(a) misorientn. < beam div. (b)misorientn. > beam div (c)white beam

Figure 7 Orientation contrast (a) For the case of monochromatic incident beam, the diffracted beams are still parallel to each other when the misorientation of adjacent area is smaller than the beam divergence. (b) The diffracted beams are getting overlapped or separated from each other when the misorientation of adjacent area is bigger than the beam divergence. (c) When the incident beam is continuous, the diffracted beams can also give rise to the contrast of boundaries between misorientated adjacent regions.

Orientation Contrast can be explained by the simple application of Bragg's law. Contrast may also arise from some part of a crystal that is oriented to satisfy the Bragg relation, thereby diffracting x-rays, whereas an adjoining region tilted with respect to the first may not satisfy the condition. This misorientation of the lattice provides a boundary between regions of different contrast and is appropriately called orientation contrast. The choice of either an extended characteristic source or localized white beam in a topography experiment, clearly would compromise the sensitivity that is possible to achieve using this mechanism to assess the perfection of the crystal. In Fig.7 (a), when the misorientation between adjacent regions is smaller than the divergence of incident monochromatic beam, then the misorientation will not be detected. Conversely, the diffracted beams diffracted from different regions can get overlapped or separated from each other, resulting the defect contrast as shown in Fig. 7(b). When the continuous incident white beam impinges on misoriented areas, different wavelength λ is diffracted in different area where the Bragg's law is satisfied. As a result the diffracted beam gets separated or overlapped with each other, which can also give rise to the defect contrast as schematically shown in Fig. 7(c). It can also learned that monochromatic beam is very sensitive to the orientation contrast which would provide a very useful tool for detecting the surface curvature and strain mapping of wafers which is illuminated in Fig.8.

Contour mapping is used for samples with inhomogeneous strain, where a single diffraction image will cover only a small part of the sample. Multiple exposures, taken at successive angular positions, display the contours of the strain field [32]. Examples of such a multiple exposure topographs, called zebra-stripe images, are shown in Fig. 8. The wavelength required for recording grazing-geometry 01-19 is 0.86 $\dot{A}$ (14.4 keV) and the Bragg angle is 16.8^o, while the wavelength required for recording grazing-geometry 11-28 is 1.38 $\dot{A}$ (8.99 keV) and the Bragg angle is 25.2^o.

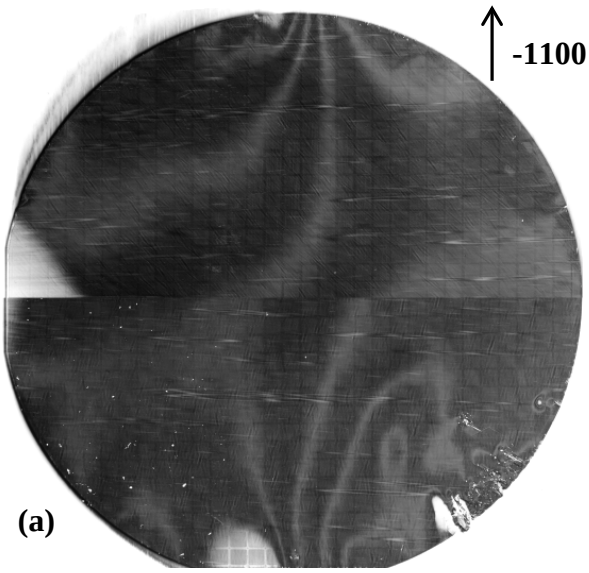

Figure 8 (a) Diffraction contour mapping of a four inch 4H-SiC crystal recorded in grazing-geometry (g=11-28) by monochromatic X-ray beam. Bragg angle was rotated in 0.01° step each time. At each angular position, an image was recorded to produce a multiple-exposure composite image of the strain in the sample. The strain is mainly positioned in the top and bottom of the wafer along [-1100] direction.

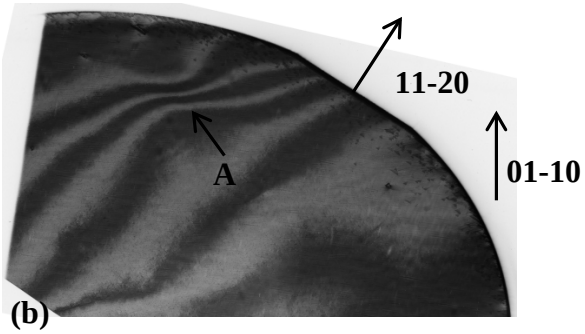

(b)Monochromatic X-ray topography recorded in grazing-geometry (g=01-19). At position 'A', several strips getting closer to each other, this indicates the existence of high strain over there.

Contrast of defects in X-ray topography that can be explained by orientation contrast includes (1) micropipes contrast in all geometry XRT; (2) threading screw contrast in grazing-incidence and back-reflection XRT; (3) TED contrast in grazing-incidence XRT; (4) BPD contrast in grazing-incidence and back-reflection XRT. One example of BPD contrast is reported by Huang *et al.* [36] where the black or white contrast of edge-type BPDs is related to the position of extra half-plane position. In back-reflection topography, the white stripe or dark line contrast of BPDs is due to the defocusing or focusing of x-ray caused by the convex or concave shaped basal planes associated with the edge component of the dislocations.

Extinction contrast is described by means of kinematic [37] and the dynamical [37-39] theories of X-ray diffraction. The fundamental difference between kinematical and dynamical theories of X-ray diffractions is that for kinematical diffraction, the scattering at each atomic site is independent which accounts for diffraction contrast in images from thin crystals and very distorted crystals, while for the case of dynamical diffraction, the incident and the diffracted waves within the crystal interact which is usually seen in thick and low dislocation density crystals. Usually the dynamical theory accounts for most of dislocation contrast in X-ray topography. But the extinction contrast is due to the strain field associated with the dislocation or other defects where the dynamical diffraction condition breaks down. The crystal lattice surrounding the dislocation core diffracts kinematically and contributes higher intensity compared with the dynamically diffracting regions away from the dislocation core.

The diffracted intensity for extinction contrast is related to μt (μ is the linear absorption coefficient and t is the thickness of the crystal). Under low absorption case, for instance, μt<1, the kinematical diffraction is operative. The diffracted intensity from the dislocation core is higher than that from the matrix, resulting in dark dislocation lines in a grey background. This is usually what we observe BPDs in transmission topographs of SiC and it is called direct image. Under intermediate absorption condition 1 <μt<10, the dynamic conditions may not be dominant, and then the image can be either dynamic image or intermediate image. Under high absorption condition (μt>10), the dynamic diffraction is operative. The dislocations appear as white lines due to anomalous absorption (Bormann effect). In the Laue geometry, the diffracted beam is extremely weak if μt is more than 10 ($I=I_0e^{-\mu t}=4.68\times10^{-5}I_0$). As for the case of SiC, the typical wavelength used in Laue geometry is ~0.8 Å and the corresponding μt is ~0.85 for a wafer of normally 400 μm thick and therefore direct images of defects are predominant.

The width of dislocations depends on the size of distorted volume, as the dislocation contrast is associated with the distorted region around the dislocation. For a screw dislocation perpendicular to the diffraction planes, the distortion can be described as

$$\Delta\omega = \boldsymbol{b}/2\pi R \qquad (4)$$

where $\boldsymbol{b}$ is the Burgers vector and R is the distance from the dislocation core. When the distortion exceeds the diffraction rocking curve width, the intensity distribution is described by kinematical theory. And the rocking curve width for symmetrical Bragg diffraction in the absence of absorption is

$$\Delta\theta = 2/\boldsymbol{g}\xi \qquad (5)$$

where **g** is diffraction vector and ξ is the extinction length. The critical condition is when the angular width of dislocation distortion is comparable with the rocking curve:

$$\frac{\boldsymbol{b}}{2\pi R} = 2/\boldsymbol{g}\xi \qquad (6)$$

Then the dislocation width for any arbitrary dislocation line direction is as below [40]. We can also conclude that the width of the dislocation is related to the rocking curve width. Broader the rocking curve, narrower the dislocation width. The width of dislocations limit the defect density that can be resolved by X-ray topography, as the width of dislocations is expected to be around several microns, and therefore, the dislocation density should not exceed 10^6 cm^{-2} in order to resolve individual dislocations.

$$W \approx \boldsymbol{b}\cdot\boldsymbol{g}\xi/2\pi \qquad \text{for screw dislocations} \qquad (7)$$

$$W \approx 0.88\boldsymbol{b}\cdot\boldsymbol{g}\xi/2\pi \qquad \text{for edge dislocations} \qquad (8)$$

The dislocation visibility is depending on the scalar product $\boldsymbol{g}\cdot\boldsymbol{b}$, where $\boldsymbol{g}$ is the diffraction vector and $\boldsymbol{b}$ is the Burgers vector of the dislocations. Screw dislocations are out of contrast when $\boldsymbol{g}\cdot\boldsymbol{b}=0$, while edge and mixed dislocations will exhibit weak contrast when $\boldsymbol{g}\cdot\boldsymbol{b}=0$, and are out of contrast when both $\boldsymbol{g}\cdot\boldsymbol{b}=0\&\boldsymbol{g}\cdot\boldsymbol{b}\times\boldsymbol{l}=0$.

The FWHM of the rocking curve width (FWHM) for perfect crystals is given by [40]:

$$2\delta_{hs} = \frac{2r_e\lambda^2}{\pi V \sin 2\theta_B}\frac{1}{\sqrt{|\gamma|}}|C|\sqrt{F_{hkl}F_{\bar{h}\bar{k}\bar{l}}} \quad \text{(Bragg case)} \qquad (9)$$

$$2\delta_{os} = \frac{2r_e\lambda^2}{\pi V \sin 2\theta_B}\sqrt{|\gamma|}|C|\sqrt{F_{hkl}F_{\bar{h}\bar{k}\bar{l}}} \quad \text{(Laue case)} \qquad (10)$$

where r_e is the classical electron radius, λ is the x-ray wavelength, V is the volume of the unit cell, θ_B is the Bragg angle, γ is the asymmetric ratio, C is the polarization factor (C=1 for σ polarization and C=cos2θ_B for π polarization) and F_{hkl} is the structure factor.

The rocking curve is a very important factor to reveal the crystalline quality. The narrower the rocking curve, the higher the crystallinity. From the above equation, it can be seen that rocking curve width is also intimately related to the magnitude of the structure factor. The larger the structure factor, the wider the rocking curve and the narrower the dislocation image. The structure factor F_{hkl} is defined as [41]:

$$F_{hkl} = \sum_i f_i \exp\{-2\pi \mathrm{i}(\mathrm{hu}+\mathrm{kv}+\mathrm{lw})\} \qquad (11)$$

where *fi* is the atomic scattering factor, (hkl) are the Miller indices of the reflection plane and (uvw) are the fractional coordinates of the atoms in the unit cell. For example, the structure factor is calculated to be 21.38 for grazing reflection 11-28 and 17.24 for back reflection 00012.

2.1.5 Sample Preparation

Sample preparation is very important for getting high-resolution X-ray topographic images.

(1) Flat, smooth and damage-free surface; X-ray diffraction, especially the asymmetric surface diffraction, is very sensitive to surface damage, such as scratches or surface etch pits. In order to avoid the contrast of this surface damage overshadowing the contrast of dislocations, the surface of 4H-SiC substrate in our experiments should go through multiple fine mechanical polishing, and then chemical-mechanical polishing (CMP) to get rid of damage layers caused by mechanical polish to reach ‘epi-ready’ standard.

(2) Put the wafer surface with damages or scratches on the x-ray beam entrance side, as minor damage on the entrance surface in transmission geometry can cause minimal obscuring of data. When doing transmission X-ray topography, epilayer are best set as the X-ray beam exit surface in order to get better contrast of dislocations in epilayer.

(3) A strain-free yet rigid mounting method should be used and the mounting regions should be as small as possible. Samples should be kept very stationary when recording X-ray topographs, therefore the mount must be very stable but with strain as small as possible. The strain introduced by mounting can either create sample curvature or big strain field near the mounting region, resulting in ‘Bragg contours’ [42] or the distortion of XRT image contrast.

(4) The camera or high-resolution film should be placed as close as possible to the sample to maximize spatial resolution. The beam size should be as small as possible while still covering the desired image area

(5) When searching for the right Bragg angle, one must rotate the crystal to get stronger intensity and smaller incident wavelength (<1.0$\dot{A}$). When selecting the appropriate diffraction spot for imaging, the larger the structure factor, the wider the rocking curve and the narrower the dislocation image.

2.2 Transmission Electron Microscopy (TEM) (JEOL-2100)

Transmission electron microscopy is one of the most powerful techniques to study the microstructure of materials, in which a beam of electrons with short wavelength is transmitted through and interact with the specimen at the same time, and then the image is formed, magnified and focused onto the detector, e.g. high-resolution CCD camera. The contrast of the image is attributed to the absorption of electrons in the material, which is related to the thickness and composition (absorption coefficient) of the materials. During the electrons interacting with the specimen, a wide range of secondary signals are created which will give us chemical composition information of the sample.

Imaging technique in TEM modes includes bright field (BF) and dark field (DF). A bright field image is the intensity distribution of the primary beam when the objective aperture is put onto the back focal plane and admits the primary beam to pass through the aperture, while a dark field image is the intensity distribution of the diffracted beam when the objective aperture is put onto a diffracted spot which only admit the diffracted beam through the aperture. The schematic of ray pass is shown in Fig. 9.

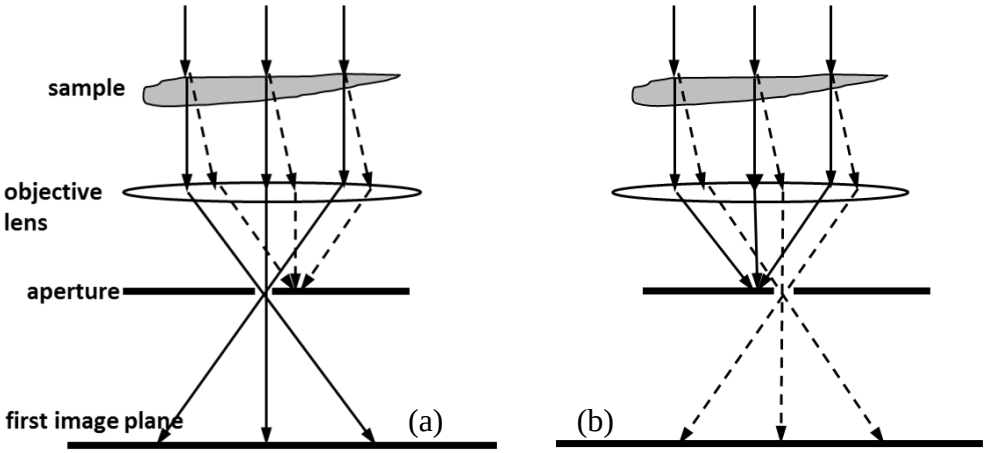

Figure 9. Schematic of ray pass for bright field image(a) and dark field image(b)

Outside of the imaging operation, the selected area diffraction (SAD) pattern can be generated by the following steps: (1) Illuminate a large area of the specimen with a parallel beam (2) Insert an aperture in the back focal plane to select an area of the image (3) Focus the imaging lens on the back focal plane. For thin crystalline samples, the diffraction patterns consists of a display of multiple diffraction spots which is unique for each material. For the case of polycrystalline or amorphous solid material, the diffraction pattern is a series of concentric rings. The equation for the TEM resolution can be:

$$R = 0.66(C_s\lambda^3)^{1/4} \qquad (12)$$

where λ is the electrons wavelength (0.027 $\dot{A}$ for 200 keV electrons), and the resolution limit can reach 0.25 nm. High resolution TEM (HRTEM) can achieve a resolution of ~ 1 $\dot{A}$, which is especially used to imaging the atomic structure and stacking sequence of stacking faults in our study. The interference between the direct beam and the reflected beam can form lattice images by including multiple reflections into the objective aperture. Zone axis alignment as shown in Fig. 10 is very important and a low index zone axis should be selected as well in order to get better resolution of atomic layers.

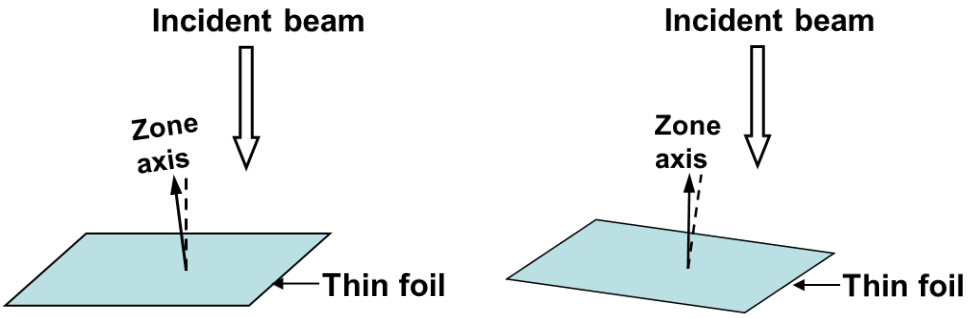

Figure 10 Schematic of zone-axis alignment for HRTEM

TEM is good for characterizing materials with high dislocation density (>10^6 cm^{-3}). It is very difficult to locate a dislocation if the materials have relatively low dislocation densities. 4H-SiC crystals has improved quality and the dislocation density is <10^6 cm^{-3}, which is not practical to employ TEM for the estimation of dislocation density, meanwhile the TEM specimen is so small which cannot represent the overall dislocation density as well. In our study, HRTEM is applied to check the lattice structure near the seed/substrate inference and thick epilayer/substrate interface. It is also used to get the stacking sequence of the stacking faults.

2.2.1 T-tool Wedging Polishing (TechCut 4, MultiPrep System)

During polishing, diamond lapping films with decreasing grain size is used with the reduction of the rotation rate of the polisher wheel speed during the process of thinning the sample. Check the polishing scratches first using optical microscopy to measure the remaining sample thickness before move to the smaller grain-size diamond polishing film. The criterion for the change to smaller size of lapping film is (1) the polishing scratches created during last step should be totally removed and the polishing scratches created by current step should be uniformly along one direction. (2) The sample thickness should not be less than the twice of the diamond grain size of the lapping film,

a. The samples are cut to the desired size (2~3 mm × 1mm × 400 μm) and immersed into acetone and alcohol successively to clean the contamination on the surface.
b. T-tool should be polished first using diamond lapping films before mounting the sample on it by wax (using heat).
c. Both faces are polished using the diamond lapping films changing gradually with the grain size from 30 μm to 0.1μm until the sample is thinned to 30 μm.

d. The T-tool is then titled to a 2 degree angle to make the front closer to the lapping film, and then further thin the sample until the front edge shows well-defined fringes in microscopy.
e. After the sample finished polishing, immerse the sample into acetone to remove the sample off the T-tool, and then mount the sample onto TEM grid by M-bond 610 adhesive.
f. Samples will be processed by iron milling to remove the contamination on the surface and further thin the wedge region before doing TEM experiments. Finally the thinnest regions have thickness of less than 30 nm and are highly electron transparent to be ideally used for HRTEM imaging.

2.2.2 Focused Ion beam (FIB) Dual SEM/FIB system

Focused ion beam has become more and more popular for the preparation of TEM specimens which allows for rapid production of site specific TEM specimens. Imaging at magnifications up to ~100 000 times is available using a FIB with a good depth of field. The FIB can also be incorporated in a dual SEM/FIB system with both electron and ion beam columns, allowing the same feature to be investigated using either of the beams, as both instruments rely on a focused beam to create a specimen image. For SEM imaging, the resolution is up to 1nm resolution, and for FIB imaging, the resolution is 5 nm. In our study, we use the FIB lift-out technique which allows little or no initial specimen preparation (as long as the sample can fit into the chamber) to obtain a site specific cross-section of SiC TEM sample. The stage is rotated 52 degree to make the ion beam perpendicular to the sample surface. (1)The first step is the deposition of several microns Pt on SiC (0001) surface to protect the top surface of interest. (2) A large stair-step FIB trench is cut on one side of the area of interest and a rectangular FIB trench is cut on the other side of the area of interest. (3) Then the isolated area is milled and thinned gradually to electron transparency. If the specimen is to be used for high-resolution electron microscopy, a final FIB cut is performed ~1-2^{o} with respect to the plane of the specimen surface. (4) A tungsten needle with a shape tip is inserted into the view and attached with the Pt deposited layer. Using the micromanipulator, the electron transparent membrane is “lifted out” of the bulk sample and is then positioned onto a Cu TEM mesh grid. Then the specimen is ready for TEM analysis. Usually the tradition T-tool wedging polishing cost 8 hours to finish, while FIB lift-out technique only take 3 hours for a skilled person.

2.3 Scanning Electronic Microscopy (SEM) (FEG LEO1550)

SEM is an electron microscope that can scan the sample surface with a focused beam of electrons. It is generally used to image the surface morphology with the resolution up to 1 nm and analysis the composition in the surface. The types of signals produced by a SEM include secondary electrons, back-scattered electrons, characteristic X-rays, light (cathodoluminescence (CL), specimen current and transmitted electrons. For imaging the sample surface, the common mode of SEM detection is by secondary electrons emitted by atoms excited by the electron beam. For element analysis, back-scattered electrons (BSE) that are reflected from the sample by elastic scattering are often used in analytical SEM along with the spectra made from the characteristic X-rays, because the intensity of the BSE signal is strongly related to the atomic number (Z) of the specimen. BSE images can provide information about the distribution of different elements in the sample. When planning to use SEM, the samples or at least the surface should be electrically

conductive and electrically grounded to prevent the accumulation of electrostatic charge at the surface. If the sample is nonconductive, then the surface needs to be coated with an ultrathin layer of electrically conducting materials, such as gold, platinum or graphite. SEM is used to image the sample surface steps and surface defects with high magnification in our study.

2.4 Nomarski Optical Microscopy (Nikon Polarizing Microscope Eclipse E600W POL)

Nomarski optical microscopy is a very convenient imaging method to magnify the topological features larger than ~0.1 μm on unstained and transparent samples by offering differential interference contrast. There are two working modes: transmission and reflection mode. The defect information at different depths can be revealed by focusing the sample at different depths. This microscopy is also equipped with polarized lighting function. Polarized light is a contrast-enhancing technique that improves the quality of the image obtained with birefringent materials when compared to other techniques such as darkfield and brightfield illumination. The microscope is equipped with both a polarizer, positioned in the light path somewhere before the specimen, and an analyzer, placed in the optical pathway between the objective rear aperture and the observation tubes or camera port. Nomarski optical microscopy is used to measure the sample thickness and observe the as-grown surface, the samples' surface morphology, defect feature and the etch pits pattern of etched 4H-SiC wafers. The resolution of the microscope can be determined by

$$d = \frac{\lambda}{2A_N} \qquad (13)$$

where λ is the wavelengths of light used, A_N is the refractive index, 0.95 with air and up to 1.5 with oil, and the resolution limit is ~200 nm for the best optical microscopy.

2.5 Selective Chemical Etching (melted KOH)

KOH etching techniques are extensively used for defect evaluation in SiC industry due to its merits of low cost, simple experimental procedure and no requirement of sample geometry. Etching only works on certain faces and a scratched or damaged surface is not useful. However, it is destructive to the wafer surface compared with non-destructive technique X-ray topography. The mechanism of chemical etching is that the reactive molecules from the etchant (melted KOH) break the bonds at the semiconductor surface and form oxides that are subsequently dissolved in the etchant. Because of the inhomogeneous nature of defects (either in composite, physical structure or both) compared with the crystal matrix, the local etch rate at a defect is different than the defect-free regions, so the defects are revealed. The etching of SiC is also dependent on the crystal surface polarity. For all SiC polytypes, the carbon face etches much faster than the silicon face at the same temperature and is not defect selective, which is attributed to the difference of surface free energies of the two faces. Pearson *et al*. [43] calculated that the surface free energy was 300 erg/cm^2 for C face and 2220 erg/cm^2 for Si face. The much smaller surface free energy of C face results in an etch pit free surface while Si face with a higher surface free energies enhances the anisotropic etching to form etch pits at a defect [44].

Fig. 11 shows a selected area on etched Si-face of a commercial PVT grown 8^o offcut 4H-SiC wafer. It is observed that TSD etch pits exhibit a large hexagonal shape; TED etch pits also show hexagonal shape with smaller size, while BPD etch pits have shell-like shape. The time of etching is very important for characterizing the defects in SiC. If the etching time is not

long enough, the etch pits such as (TSDs and MPs) will not form well-defined hexagonal shape, which can cause confusion with BPDs. If the etching time is too long, then the over-etched wafer will cause a merge of neighboring defects, and sometimes it will be hard to distinguish TEDs and TSDs etch pits as they have similar etch pit shape. Nitrogen is a common dopant in SiC and it has been found that the doping concentration also can change the etch rate. For nitrogen doped 4H-SiC, the higher nitrogen doping, the slower the etch rate. For the etching temperature used in our experiments, the etching time for 4H-SiC with nitrogen doping concentration 5×10^{18} is around 10-12 minutes, while the etching time for 4H-SiC homoepitaxial layer with nitrogen doping concentration 4×10^{15} is around 5-6 minutes. The study is consistent with the earlier observation by Gao *et al.* [4]. He reported that KOH etching is isotropic on highly n-type dope samples, while it is more preferential on lightly n-type, p-type and p+ samples.

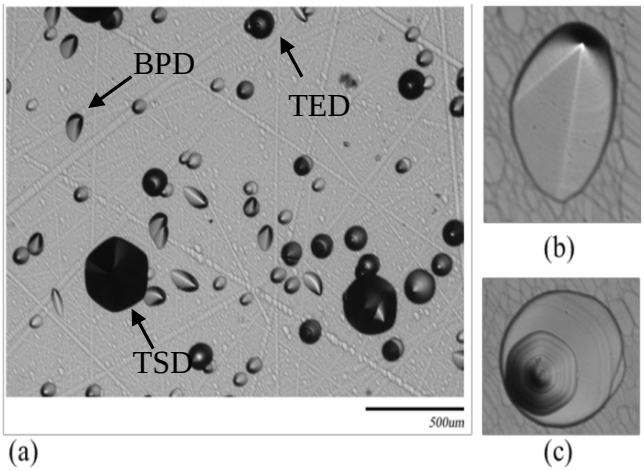

Figure 11 A Nomarski Interference Contrast (NIC) optical image showing a selected area on etched Si-face of a commercial PVT-grown 8° offcut 4H-SiC wafer (a). Three types of etch pits are observed—scallop-shell-like shaped etch pits corresponding to BPDs (b), large hexagonal etch pits to TSDs, small hexagonal etch pits to TEDs (c)

Defect-selective etching of SiC can reveal the defects that intersect with the surface, e.g. BPDs, TSDs, MPs, TSDs, stacking faults, carrot defects, polytypes and so on. One can measure the defect density in single crystalline materials by counting the etch pit density. However, because only if the defects intersect with the silicon surface that will be revealed by KOH etching, the ratio of the true BPD density calculated from topographic images to that from etch pits is estimated to be larger than $1/\sin\theta$, where θ is the offcut angle of the wafer which is discussed in Chapter 4 [45].

3. Combined Application of Section and Projection Topography for Defect Analysis in PVT-Grown 4H-SiC substrate

3.1 Outline

The combined application of section and projection topography carried out using synchrotron white beam radiation can be a powerful tool for the determination of the three-dimensional configurations of defects in single crystals. In this paper, we present examples of the application of this combination of techniques to the analysis of defect configurations in PVT-grown 4H-SiC wafers cut perpendicular and parallel to the growth axis. Detailed correlation between section and projection topography of threading screw dislocations (TSDs) is presented with particular emphasis on the determination of the signs of the dislocations. Further, information regarding the position of the dislocations as a function of the crystal depth can be obtained. In addition, similar correlation is presented for threading edge dislocations (TEDs) and basal plane dislocations (BPDs). The section topography images of dislocations can comprise direct, intermediary and dynamical contrast and all three types are observed. The application to the study of stacking faults will be also discussed in detail.

3.2 Introduction

4H-Silicon Carbide (SiC) is a widely used semiconductor for high power devices due to its outstanding properties such as higher thermal conductivity, higher breakdown voltage and high saturated electron drift velocity [46]. However, the detrimental effects of defects, e.g., dislocations and stacking faults, inside these crystals requires crystal growth scientists to gain knowledge of the formation mechanisms and behavior of the defects to develop strategies in order to lower the densities of these defects [11,15]. X-ray projection topography is a widely used non-destructive technique to characterize defects in the crystals but provides limited depth sensitivity and sensitivity to orientation contrast. In this paper, in order to address these limitations, projection and section topography are combined together to reveal the three-dimensional configuration of defects. Section topography of dislocations includes three types of image comprising direct, dynamic and intermediary contrast. Under low absorption conditions ($\mu t<1$, where μ is the linear absorption coefficient and t is the crystal thickness), direct images dominate [40]. The direct image is formed when the angular or wavelength band width of the incident beam is larger than the angular or wavelength acceptance of the perfect crystal. X-rays will diffract in the deformed region around dislocations and the diffracted beam suffers no primary extinction, and thus is called the "direct image"[47]. Most importantly such diffracted rays will run in directions determined by the local orientation within the distortion field---the phenomenon of orientation contrast. This enables determination of dislocation sign. Depth information can also be provided by the direct image. For 4H-SiC, μt is equal to 0.62 for g= [1-100] from c-plane wafers and 1.11 for g= [0004] from axial slices (for the images presented here), which belongs to low absorption case, where direct image will dominate in the section topography. Depending on the depth information of dislocations, we will discuss the section topography of dislocations in three cases, dislocations being parallel to the entrance surface, dislocations making an angle with the entrance surface and dislocations being perpendicular to entrance surface.

3.3 Results and Discussion

3.3.1 Dislocations Parallel to the Entrance Surface

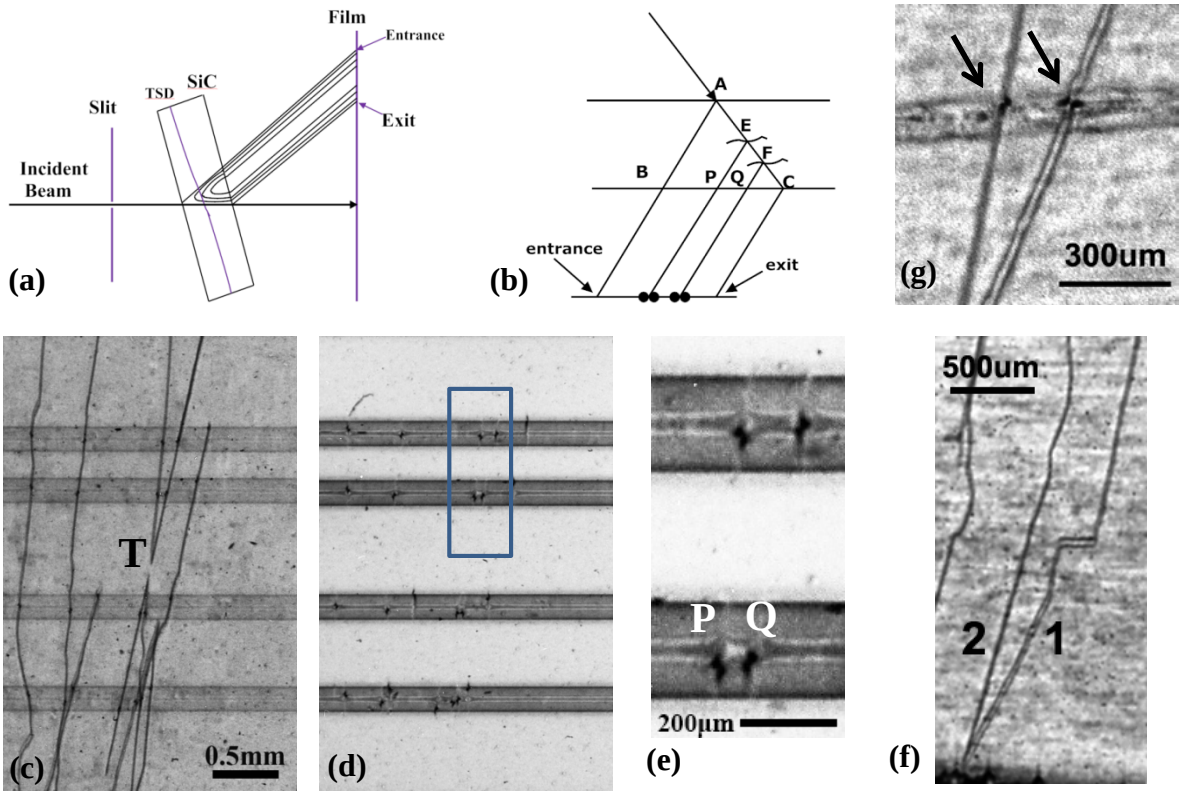

Figure 12 Side view of configuration for setting up X-ray section topography to record g= [0004] reflection of SiC axial slices. (b) The schematic diagram indicating the depth dependence of the direct image inside Bormann Fan. (c) Combined x-ray topography where transmission topography (g=0004) and several section topographs were recorded on the same film. (d) Section topographs were taken at the same position as (c). (e) The enlarged section topography of the rectangle part in (d) presents one pair of threading screw dislocations with opposite sign. (f) X-ray transmission topography showing dislocation 1 and 2 nucleate from one impurity. (g) Section topography of these two dislocations. The direct images are pointed out by black arrows.

Synchrotron white beam X-ray topography (SWBXT) was conducted at the Stony Brook Synchrotron Topography Facility, Beamline X19C at the NSLS. Figure1a shows a side view of the configuration for setting up X-ray section topography to record g=[0004] reflection from a 4H-SiC axial slice, at which case threading screw dislocations (TSDs) are approximately parallel to the entrance surface . First we recorded one transmission image on the film (only TSDs are visible at reflection vector g=0004), and then a narrow slit with 10 μm average width was placed in front of the sample. A series of section topographs were recorded on the same film (superimposed on the projection image). In such a way, we can gain a good knowledge of the position of the section topography with respect to the dislocation position, as presented in Fig. 12(c). In order to get higher resolution image, in Fig. 12(d), only the section topographs at the same position of the crystal were recorded on the film. The position of the dark direct images in section topography indicates at which depth it intersects with the direct beam, which can be schematically drawn in Fig. 12(b). Therefore the intersection of a dislocation with the incident

beam direction within the Bormann Fan provides valuable depth information. It is also observed that the distortion field associated with the dislocations disrupts the planes of constant phase for the Pendellösung fringe effects.

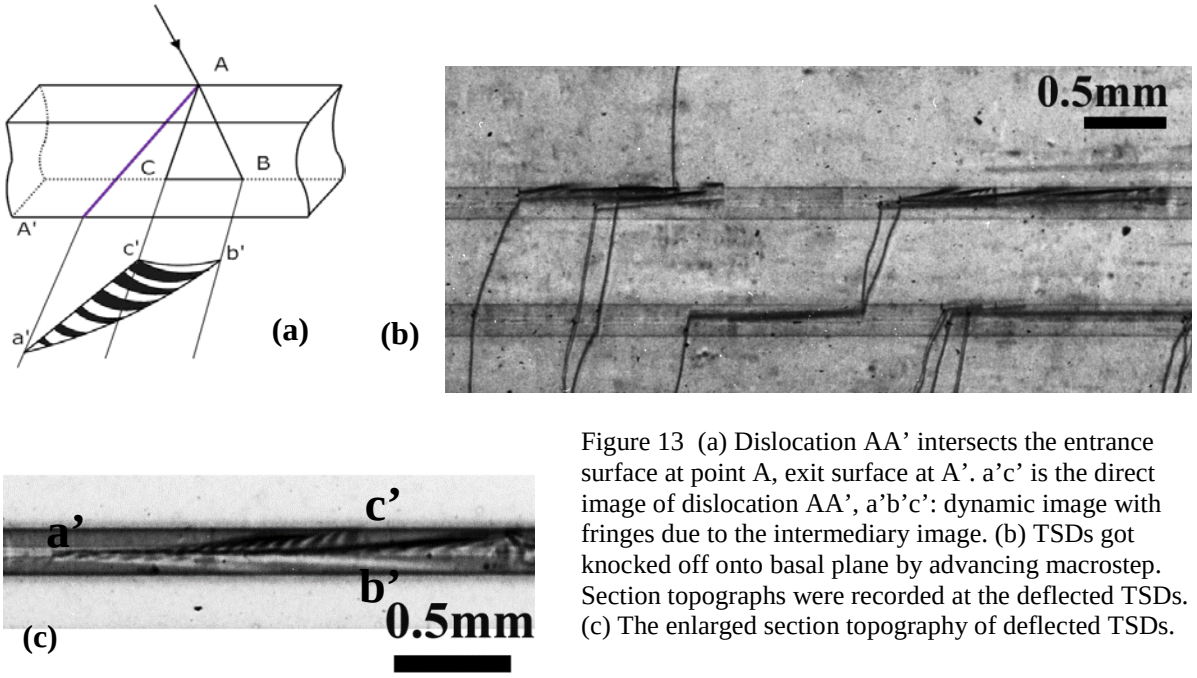

Figure 13 (a) Dislocation AA' intersects the entrance surface at point A, exit surface at A'. a'c' is the direct image of dislocation AA', a'b'c': dynamic image with fringes due to the intermediary image. (b) TSDs got knocked off onto basal plane by advancing macrostep. Section topographs were recorded at the deflected TSDs. (c) The enlarged section topography of deflected TSDs.

The crystal planes around such threading screw dislocations are adopt spiral configurations with displacement along screw axis. Around the core of such screw dislocations, the misorientation of the lattice is such that the tilt is opposite on either side of the core, and as a result the direct image comprises two components or lobes shifted in the opposite sense. The relative position of these two lobes shows opposite sense for right-handed and left-handed screw dislocations [48,49], thus enabling determination of sense. Therefore we can conclude that dislocations P and Q have opposite sign from the information provided from section topography in Figure1e, which has a good agreement with what is shown in Fig. 12(c), where dislocations mutually annihilate at point T when they get close to each other. Another example of this application is shown in Fig. 12(f) and (g). Threading screw dislocations 1 and 2 nucleate at an inclusion and then section topography was recorded at the position of these two dislocations. Their direct images indicated that they had opposite **c** component, which matches with the requirement of Burgers vector conservation during nucleation.

3.3.2 Dislocations Making an Angle with Entrance Surface

In a 4H-SiC axial slice study, we observe that threading screw dislocations can be deflected onto the basal plane via a process of macrostep overgrowth as shown in Fig. 13(b). Section topographs are recorded at the deflected TSDs; the triangular shaped fringes comprising direct, dynamic and intermediary contrast are displayed in Fig. 13(c). Through dynamic theory analysis, this kind of pattern is formed in the case that dislocations intersect the entrance surface at an angle of around 60 degrees. Take the dislocation **AA'** for example, which is schematically drawn in Fig. 13(a). At point "**A**" the dislocation intersects the top of the Bormann Fan, then the

incident beam with angular deviation from the exact Bragg angle (along AB direction) will diffract at the deformed region around " **A**"; the diffracted beam (along AC direction) appears as a dark spot on the film point "**c'**". At the same time, intensity is removed from the original direction and the dislocation will cast a shadow at point **b'**, called the "dynamic image". On the other hand, dislocation **AA'** intersects the exit surface at point "**A'**", its dynamic and direct images are overlap at point "**a'**". Thus a'c' is the direct image of dislocation AA', while a'b' is the dynamic image. The newly created wavefields due to decoupling of the wavefields inside the Bormann Fan would interfere with the original ones and show an oscillatory contrast in between.

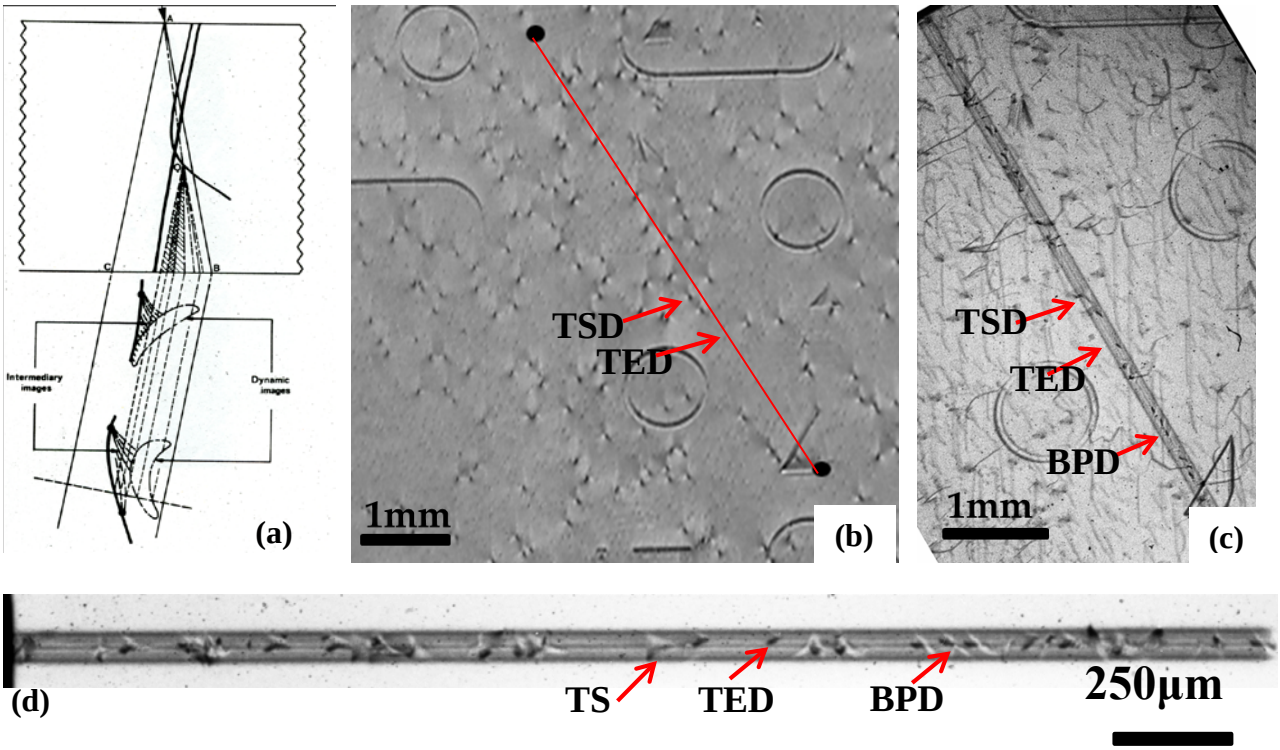

Figure 14 (a) Schematic representations of the formation of mixed direct, intermediary and dynamic image from dislocations perpendicular to entrance surface [50]. (b) Grazing topography of 4H-SiC c-plane giving information of TSDs and TEDs distribution. The red line marks the position where section topography will be recorded. (c)Combined transmission and section topography. (d) The enlarged section topography where TSDs, TEDs and BPDs having distinguishable patterns.

3.3.3 Dislocations being Perpendicular to the Entrance Surface

As the angle between dislocations and crystal surface gets bigger until 90 degree, in other word dislocations being perpendicular to crystal surface, the dynamic patterns will be formed as shown in Fig. 14(a). For this case, TEDs and TSDs in a c-plane sample are taken as an example. We pick up each TSD, TED and BPD from the same position in Figure 14(b), 14(c), and 14(d). The section topography of TSD and TED matched well with the results shown schematically in Fig. 14(a). It is also observed that the magnitude of TSD image is much bigger than that of TED which, as expected, is proportional to their Burgers vectors. Thus section topography is a good way to identify the different types of dislocations.

3.3.4 Application of Section Topography of Stacking Faults

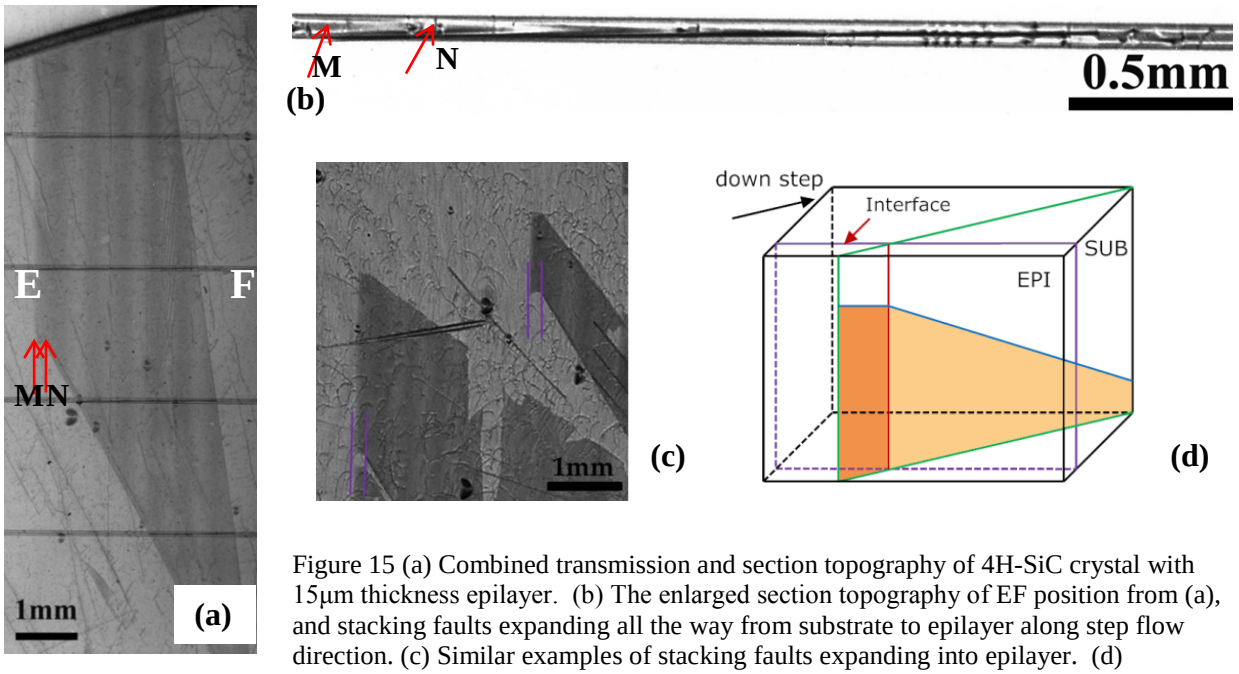

Figure 15 (a) Combined transmission and section topography of 4H-SiC crystal with 15μm thickness epilayer. (b) The enlarged section topography of EF position from (a), and stacking faults expanding all the way from substrate to epilayer along step flow direction. (c) Similar examples of stacking faults expanding into epilayer. (d) Schematically diagram showing the mechanism of stacking faults growing into epilayer as a "growth defect".

The section topography image of stacking faults appear as straight lines making an angle which is equal to off-cut angle (4 degree) to the surface, while being parallel to the basal plane, as shown in Fig. 15(a) and (b). Transmission topography was recorded on crystal with 15μm thickness of epilayer; it was observed that the right edge of stacking faults was blurred and with no sign of partial dislocations. And also the expanding trend of stacking faults had an obvious direction change (as shown in Fig. 15(a) and (c)). The epilayer thickness of 4H-SiC in our study can be estimated as $t \approx H \tan \emptyset$ where t is the epilayer thickness, H is basal plane width in the epilayer, and $\emptyset$ is the off-axis angle of the substrate. The calculated width of basal plane in the epilayer H=214.5 um, and the measured stacking faults width in epilayer H'=236.2um. Two values are approximately equal to each other with consideration of errors due to distortion of the image during image recording. It is thus assumed that the stacking fault intersects with the epilayer surface. This is subsequently confirmed by section topography in Fig. 15(b), where it is clear that the stacking fault expands all the way from the substrate into the epilayer and finally intersects the epilayer surface. MN is the part of the stacking fault inside the epilayer. This growth mechanism of stacking faults is not due to the separation of partial dislocations after growth process. Instead, stacking faults intersect the surface of the substrate and then during the epilayer growth process they are replicated into the epilayer. This is thus a "growth defect".

3.4 Conclusion

Studies are presented of combined application of projection and section topography to dislocations and stacking faults analysis in PVT-grown 4H-SiC wafers. The intersection of a dislocation with the incident beam inside Bormann Fan provides valuable sign, depth and line direction information of the dislocations. Section topography of threading screw dislocations inside axial slices shows dark contrast associated with the direct image and light contrast

associated with the dynamic image. The sense of displacement of the two components of the direct image reveals the sign information of screw dislocations due to orientation contrast. When the dislocation intersects the entrance surface at an angle, its dynamic image is accompanied by oscillatory contrast due to the intermediary image; for threading screw and threading edge dislocations in the c-plane wafer, fringes are clearly observed in section topography. Section topography of stacking faults can give us their depth information, and this technique could help to confirm that stacking faults behave as growth defects during epilayer growth when their edges intersect the substrate surface.

4. Quantitative Comparison between Dislocation Densities in Offcut 4H-SiC Wafers Measured Using Synchrotron X-ray Topography and Molten KOH Etching

4.1 Outline

Molten KOH etching and X-ray Topography have been well established as two of the major characterization techniques used for observing as well as analyzing the various crystallographic defects in both substrates and homo-epitaxial layers of silicon carbide. Regarding assessment of dislocation density in commercial wafers, though the two techniques show good consistency in threading dislocation density analysis, significant discrepancy is found in the case of basal plane dislocations (BPDs). In this paper we compare measurements of BPD densities in 4-inch 4H-SiC commercial wafers assessed using both etching and topography methods. The ratio of the BPD density calculated from topographic images to that from etch pits is estimated to be larger than $1/\sin\theta$, where θ is the offcut angle of the wafer. Based on the orientations of the defects in the wafers, a theoretical model is put forward to explain this disparity and two main sources of errors in assessing the BPD density using chemical etching are discussed.

4.2 Introduction

As one of the most important wide-bandgap semiconductor materials, silicon carbide (SiC) has shown promising application for a wide range of electronic devices operated under extreme conditions such as high temperature, high frequency, and high power, due to its outstanding intrinsic properties including high breakdown field, large bandgap, and high thermal conductivity [51]. Though great development has been made in both the crystal growth and the device fabrication of SiC, the widespread commercialization of this material is still hindered by relatively high densities of structural defects that exert negative influence on device performance as well as lifetime. Therefore it is of great importance to develop precise visualization techniques for those defects in order to understand their growth and propagation mechanisms, and to eventually reduce or even eliminate the densities of these defects.

Four types of defects are mostly observed and studied in SiC substrates—micropipes (MP), threading screw dislocations (TSD), threading edge dislocations (TED), and basal plane dislocations (BPD) [52]. While significant progress has been made in decreasing the density of MPs [53], the latter three are attracting increasing attention since they are reported to result in detrimental influence on various SiC-based device[52,54,55]. A wide range of techniques have been used to study the distribution, arrangement, and density of dislocations. Regarding the assessment of dislocation density, two major techniques—molten KOH etching and X-ray topography are preferred.

Though by nature destructive, molten KOH etching is popular in dislocation density assessment due to its low cost, ease of accessibility, and easy operation. However, it suffers the drawback of only being able to reveal the structural property near the etched surface. Additionally, problems arise when attempts are made to relate etch pits densities (number of etch pits per unit area, $/cm^2$) to the true dislocation density (total length of dislocation lines per unit volume, cm/cm^3) when the dislocations in question are far from being perpendicular to the etched surface. Detailed discussion of this will be given later. Fig.16 (a) shows a Nomarksi

Interference Contrast (NIC) optical image of a selected area on an etched commercial PVT-grown 4^o offcut 4H-SiC wafer. Three different kinds of etch pits pattern are observed. The large and small hexagonal etch pits correspond to TSDs and TEDs, respectively, while the scallop-shell-shaped pits correspond to BPDs. Both TSDs and TEDs have line directions roughly perpendicular to the (0001) plane while BPDs have the line directions contained in the basal plane, as their name would indicate. The difference in size between the TSD and TED pits, while maintaining the same symmetrical shape can be explained by their different Burgers vector magnitudes and similar line directions [56]. Occasionally, TED etch pits may deviate slightly from the symmetrical hexagonal shape due to the offcut angle [57].

Synchrotron X-ray topography (SXRT), on the other hand, as a non-destructive characterization technique, provides a true three dimensional view of the overall defect distribution in the volume imaged. Among the three major experimental arrangements involved in SXRT—transmission, back-reflection and grazing, the first one is most frequently applied for BPD characterization. In transmission topography images, BPDs usually appear as a dark single line or double lines (Fig. 17(a)).As is well known from the work of A. Authier, the direct image width *w* of a dislocation in SXRT images can be estimated as [58]:

$$w \approx \mathbf{g} \cdot \mathbf{b}\xi_g/2\pi \qquad (14)$$

where **g** and **b** represent the diffraction vector perpendicular to the diffraction plane and the Burgers vector of the dislocation imaged, respectively. ξ_g refers to the extinction distance.

Equation (14) provides the critical invisibility criterion for direct images of dislocations in SXRT—**g.b**, indicating that in the case of **g.b**=0, dislocations are out of contrast, meaning that they cannot be observed on SXRT images. For BPDs whose Burgers vector is 1/3<11-20>, when taken in transmission topography with **g=**<11-20>, **g.b** yields non-zero results and thus all the BPDs are in contrast on the (11-20) transmission SXRT images.

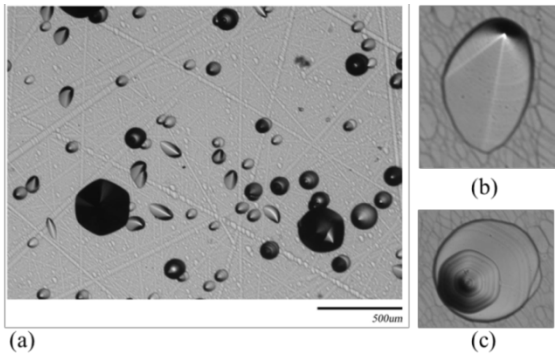

Figure 16 A Nomarski Interference Contrast optical image showing a selected area on an etched Si-face of a commercial PVT-grown 4o offcut 4H-SiC wafer (a). Three types of etch pits are observed—scallop-shell-like shaped etch pits corresponding to BPDs (b), large hexagonal etch pits to TSDs, small hexagonal etch pits to TEDs (c)

4.3 Experimental Procedure

Two commercially available 4H-SiC wafers from Dow Corning grown by the physical vapor transport (PVT) technique with an 4^o offcut angle toward the [11-20] direction were etched on Si-face in molten potassium Hydroxide (KOH) before synchrotron white beam X-ray transmission topographs using on (11-20) reflection were recorded. For each wafer, eight 1.8mm×2.3mm areas were randomly chosen from the topography images while corresponding optical images showing the etch pits were recorded from the same areas using Nomarksi

microscopy (Nikon ECLIPSE E600 POL) (Fig.17(a)-(b)). BPD densities are calculated and quantitatively compared by etch pit counting and by line length measurement from the topography images.

4.4 Results and Analysis

It is not surprising to find that significant discrepancies exist between the BPD densities obtained from the two different techniques introduced previously. Fig. 18(a)-(b) are histograms showing the discrepancy for the two tested wafers. Wafer 1, with a thickness of 380μm, bears a BPD density calculated from etch pit counting varying from 193/cm^2 to 483/cm^2, while the value calculated from topography images varying from 4051cm/cm^3 to 8092cm/cm^3. The average ratio between the BPD density obtained from topography and etch pit analysis is around 18. For Wafer 2, with the thickness of 435μm, this ratio turns out to be 20. In order to reveal the underlying reason for these disparities in value, a close inspection of how BPD density is calculated in each technique is required.

By calculating dislocation density by etch pit counting, it is assumed that Equation (15) is justified.

$$\rho = \frac{L}{V} = \frac{N_d \times l}{A \times t} = \frac{N_e}{A} \qquad (15)$$

where L represents the total length of dislocation lines in selected volume V, while l is the average length of dislocation lines. N_d stands for the total number of dislocation lines in volume V and the total number of etch pits on the etched surface of area A is denoted as N_e. t is the thickness of the wafer. Obviously the original definition of dislocation density—total length of dislocation line per unit volume, is not strictly followed during this calculation process. Equation (2) is only justified when a) N_d equals N_e and meanwhile b) the average length of dislocation line is almost the same as the wafer thickness. While these assumptions are justified for threading dislocations whose line directions are nearly parallel to the c-axis like TSDs and TEDs, the assumptions are most definitely not valid for the case of BPDs.

Fig. 17 shows an SXRT image ((a)) and NIC image of etch pits ((b)) taken in the same area of an etched 4H-SiC wafer. Though BPD1 and BPD2 can be observed in both ((a)) and ((b)), BPD3, going through the sample body without intersecting the top surface can only be seen in SXRT image. No corresponding etch pit is found in the optical image.

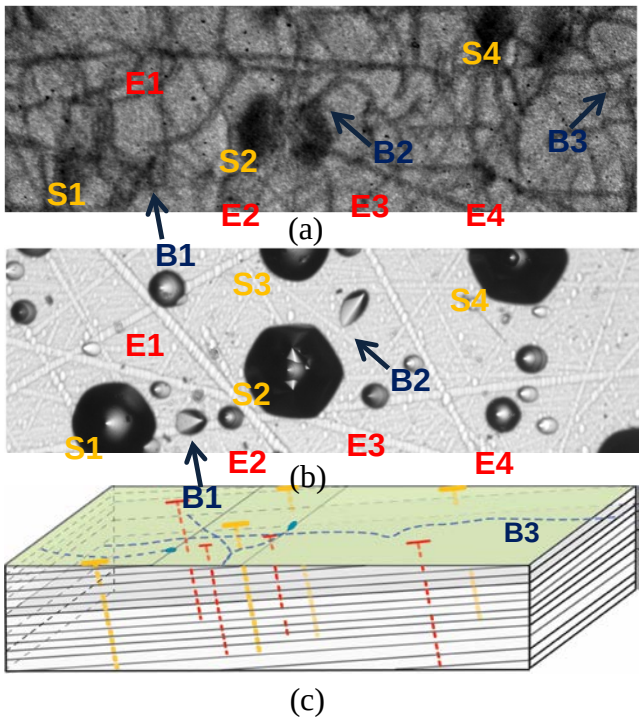

Figure 17 SXRT image (a) and NIC image of etch pits (b) taken in the same area of a pre-etched 4H-SiC wafer. The illustration (c) demonstrates how threading dislocations (S1-S4: TSDs; E1-E4: TEDs.) and BPDs (B1-B3) are oriented in the sample

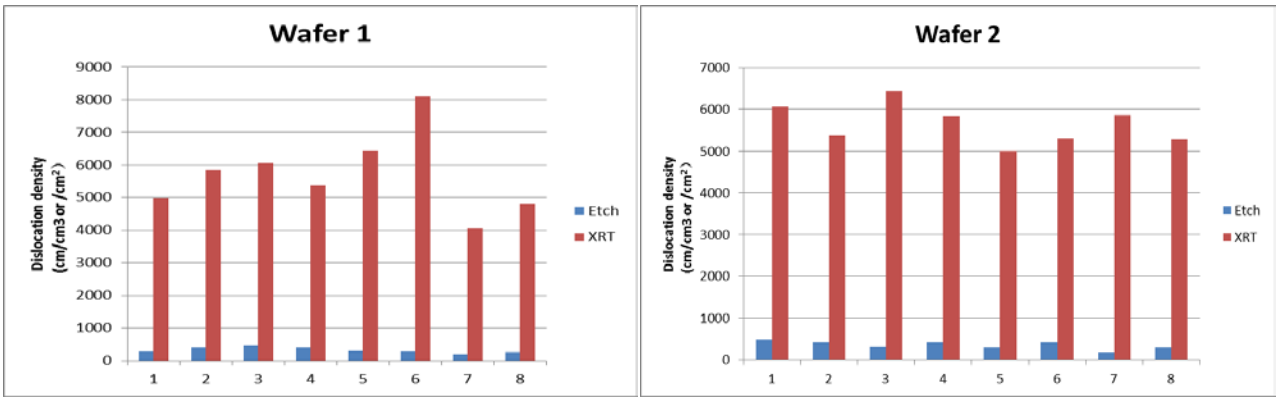

Figure 18 Histograms showing the discrepancy of BPD densities obtained from etch pit counting and SXRT image line length measurement for eight 1.8 mm×2.3mm areas on each of the two commercial 4H-SiC wafers with different thickness

As illustrated in Fig. 19(b), only those BPDs that lie within the wedge ABCDEF might have a chance to intersect the top surface, like BPD1 and BPD2. On the other hand, BPD4 and BPD5 do not emerge on the top surface and therefore corresponding etch pits cannot be observed. Even for those BPDs that lie within the wedge, not all of them will intersect the top surface. For example, BPD3 does not emerge on the top surface.

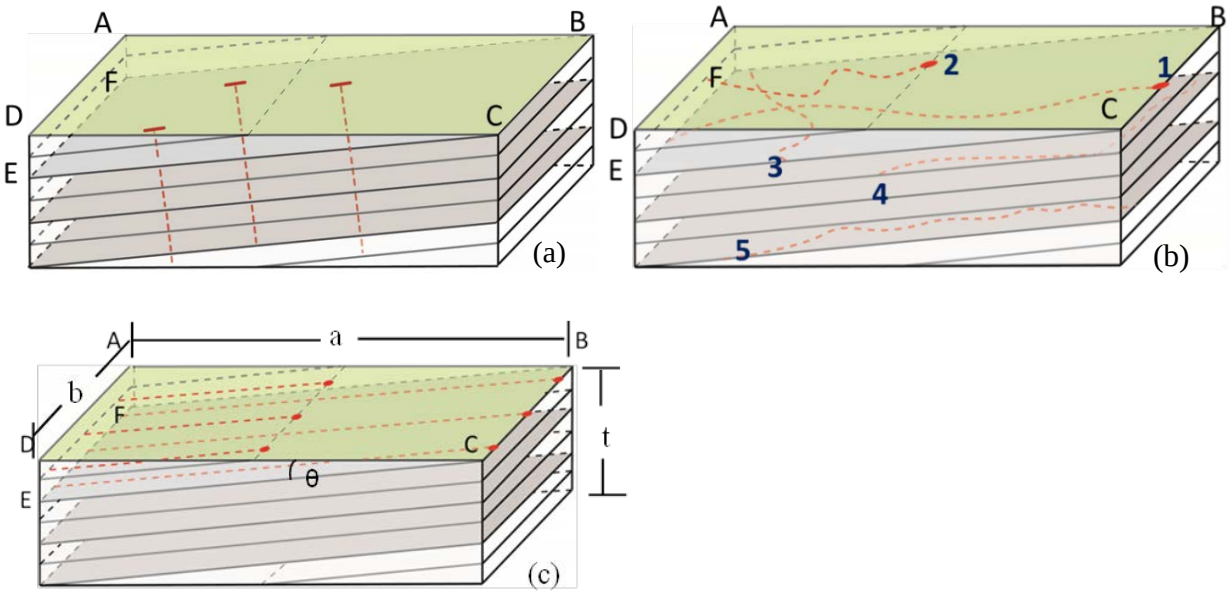

Figure 19 Schematic diagrams giving a rough view showing the morphologies of (a) threading dislocations and (b) BPDs inside a wafer. The grey-shaded planes are (0001) basal planes that have an offcut angle of θ inclining towards the top surface. (c) Illustrates a simplified model where BPDs are considered as straight lines distributed uniformly in the selected volume. a and b refer to the dimensions of the selected etched area and t stands for the sample thickness

To further reveal the magnitude of this value disparity, an analytical model is proposed based on a rough assumption that all the BPDs are distributed uniformly as straight lines within the selected sample bulk (Fig. 19(c)). This is reasonable if the selected sample volume is much smaller than the whole wafer. Considering such a uniform BPD distribution, the ratio of the number of all BPDs in the selected volume to the number of etch pits should be less than or equal to (assuming the ideal condition that all the BPDs within the wedge intersect the etched surface) the ratio of the volume of the whole selected rectangular bulk to that of the wedge, namely:

$$\frac{N}{N_e} \geq \frac{a \times b \times t}{\frac{1}{2} a \times b \times \frac{a}{ctg\theta}} = \frac{2t \times ctg\theta}{a} \qquad (16)$$

As illustrated in Fig. 16(c), a and b refer to the dimensions of the selected etched area and θ is the offcut angle. And thus the ratio of the true BPD density in volume a×b×t, denoted as ρ, to the density obtained from etch pit counting in the area a×b, denoted as ρ_e, is given in Equation (17) as below:

$$\frac{\rho}{\rho_e} = \frac{N \times L}{N_e \times t} \geq \frac{2 \times L \times ctg\theta}{a} \qquad (17)$$

When considered as straight lines, the average length of BPD in the wedge is a/ (2cosθ). Since the BPDs are naturally curving around on the basal planes (Fig. 19(b)), making their average length larger than the value above, meaning:

$$L > \frac{1}{2} \frac{a}{\cos\theta} \qquad (18)$$

Combining Equation (17) and (18) leads to the safe conclusion that the ratio of the real BPD density of the sample to the value calculated from etch pits counting is larger than $1/\sin\theta$. For example, if the offcut angle is 4^o, which is true for both wafers used in this experiment, this ratio is expected to be larger than 14 ($1/\sin 4^o$). The experiment results demonstrated before are found to be in good agreement with this model prediction (Fig. 18).

4.4 Conclusion

Though widely used as a defect characterization tool for SiC wafers, etching exhibits large limitations when applied to BPD density analysis since it 1) only reveals the defects that intersect the sample surface and 2) it wrongly considers the average length of BPDs as almost the same as the sample thickness. Therefore the value of BPD density obtained by etch pit counting is potentially very misleading. On the other hand, X-ray topography, by nature providing a true 3-D view of the overall defect distribution reveals all dislocations not only intersecting the surface but also lying inside the wafer. It gives more precise results when used in density assessment. The ratio of BPD density calculated from SXRT image (considered as representative of real density) to that from etch pits is larger than $1/\sin\theta$, where θ is the offcut angle of the wafer.

5. Basal Plane Dislocation Multiplication in (0001) Plane via the Hopping Frank-Read Source Mechanism in 4H-SiC Substrate

5.1 Outline

Synchrotron white beam X-ray topography (SWBXT) observations are reported of single-ended Frank-Read sources in 4H-SiC. These result from inter-conversion between basal plane dislocations (BPDs) and threading edge dislocations (TEDs) brought about by step interactions on the growth interface resulting in a dislocation comprising several glissile BPD segments on parallel basal planes interconnected by relatively sessile TED segments. Under stress, the BPD segments become pinned by the TED segments producing single ended Frank-Read sources. Since the BPDs appear to "hop" between basal planes this apparently dominant multiplication mechanism for BPDs in 4H-SiC is referred to as the "Hopping" Frank-Read source mechanism.

5.2 Introduction

The detrimental effects of dislocations on the performance of Silicon Carbide (SiC) electronic devices have made the lowering of their densities a primary goal of SiC crystal growth community [59]. Such "defect engineering" requires knowledge of the detailed configurations of the various kinds of dislocations as well as an understanding of the origins of these configurations so that strategies might be formulated to enable control to be exerted over the processes involved.

Among the dislocations observed in 4H-SiC, the routine observation of complicated curved configurations of basal plane dislocations confirms the generally accepted fact that 1/3<11-20>(0001) is the preferred slip system. However, no clear understanding of the mechanism of BPD multiplication in 4H-SiC has emerged. Generally speaking, one of the primary mechanisms of dislocation multiplication in crystals, the Frank-Read (FR) mechanism [60], has been well documented in the literature. Both single-ended and double-ended FR sources have been observed in a variety of crystals including ranging from semiconducting silicon to ice [61-64]. The FR mechanism relies on the presence of irregular arrays of dislocations in crystals whereby some particular dislocations have segments which are "stranded" on their active slip planes with one or two pinning points where the dislocation enters and/or exits the slip plane. If these segments of dislocation are long enough (typically $>10^4$ b in length [65], the dislocations can glide under stress and will rotate about their pinning points enabling dislocation multiplication. Whether or not such "stranded" segments of dislocation exist in SiC, facilitating the operation of Frank-Read sources, remains an open question. Interactions between BPDs and threading dislocations cannot provide such segments [66]. For example, a pair of TEDs will initially pin a mobile BPD but once the leading segments draw out dislocation dipoles as they pass beyond the pinning points, the dipoles self-annihilate as they are on the same slip plane [66]. For the case of a pair of TSDs, the dipoles comprise dislocations on parallel basal planes separated by the Burgers vector of the TSD. These experience huge attractive forces which either lock the dipole in place or, in the case of a screw oriented dipole, cross-slip and self-annihilate allowing the dislocations to advance beyond the barrier albeit pinned by the relatively sessile jog left behind by the annihilation process [66].

In this paper we report on how repeated double deflection processes leading to inter-conversion between BPDs and TEDs, involving overgrowth of dislocation outcrops by macrosteps followed by impingement of the overgrowing macrostep on a step moving in the

opposite direction, can lead to the isolation of segments of BPD on parallel slip planes. We will show that these glissile segments of BPD are separated by distances along the c-axis large enough for them to overcome any mutual attractive forces and can thus operate as independent single-ended Frank-Read sources. This double deflection process is somewhat analogous to the stress induced double cross-slip mechanism that leads to slip band broadening [67] although the processes described here are "growth processes" that occur on the moving crystal growth interface rather than "stress induced" deformation processes occurring behind the growth interface.

5.3 Results and Discussion

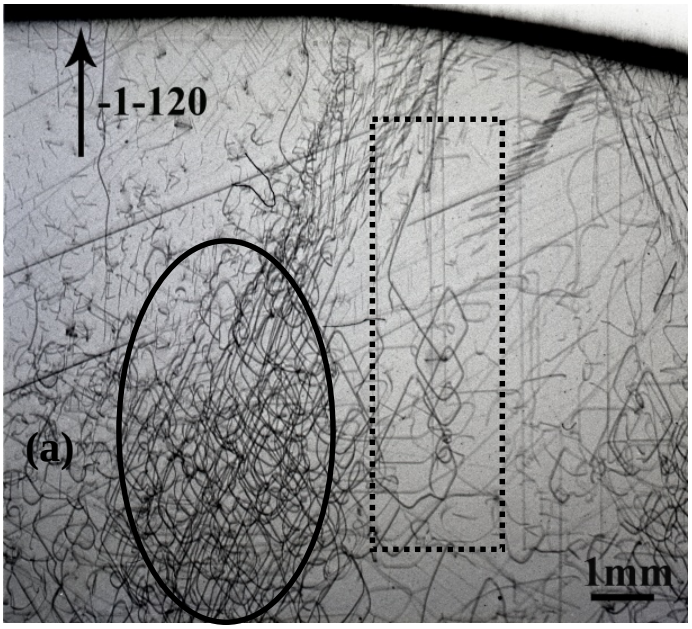

Figure 20 Synchrotron White Beam X-ray Topography (SWBXT) transmission image (g=$\bar{1}\bar{1}20$) recorded from a wafer cut with 4 degree offcut towards [$11\bar{2}0$] from a PVT-grown boule.

Fig. 20 shows a Synchrotron White Beam X-ray Topography transmission image recorded from a wafer cut with 4 degree offcut towards [$11\bar{2}0$] from a PVT-grown boule. Note the many diamond shaped basal plane dislocation spiral loops within the full ellipse. The adjacent dotted rectangular frame highlights an isolated example of a configuration of such loops that is suitable for detailed study. Enlarged images of this region recorded with different g-vectors are shown in Figs. 21(a)-(d). Close examination of this sequence of diamond shaped spiral loops displaced in the vertical direction on this and many other reflections show that it comprises a single dislocation that enters the crystal face at *starting point (SF)* and ending point (EP) exits on the opposite face at *b* on Fig. 21(a).

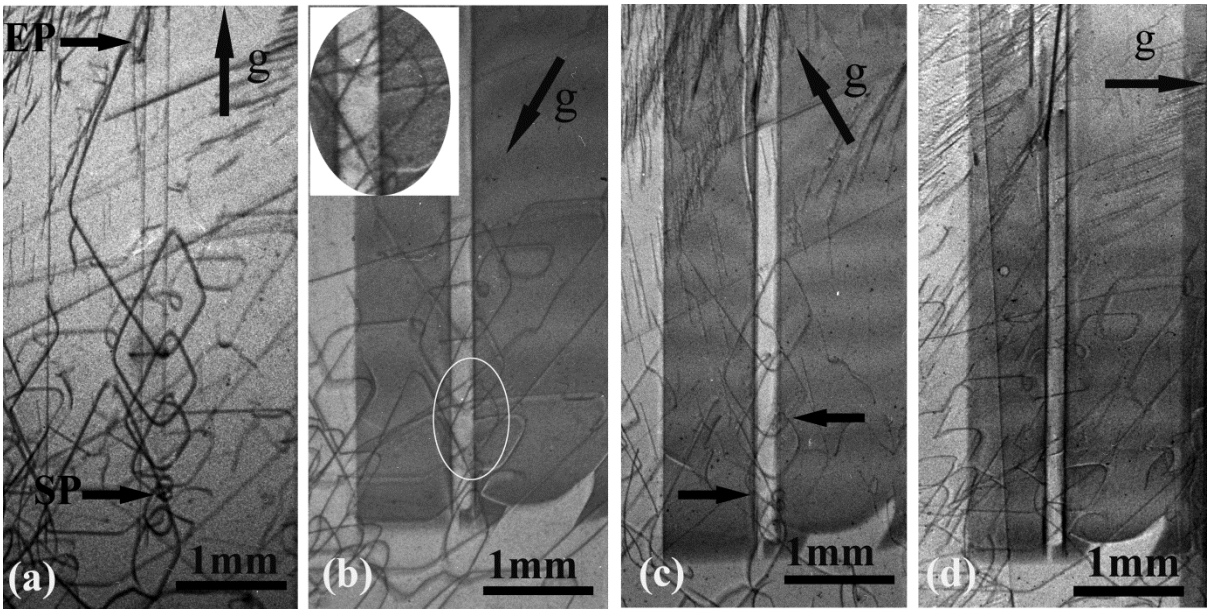

Figure 21 SWBXT images recorded from the same area of one 4H-SiC wafer show the various contrasts of the diamond shaped loops in different g vectors (a) g=-1-120, (b) g=10-10, (c) g=0-111, (d) g=-1101. The arrows in (b) and (c) indicate the location of jogs.

Fig. 21 shows a BPD which has developed into a sequence of diamond-shaped loops. The fact that parts of the loops appear to superimpose upon each other not only dictates that they are not on the same basal plane but also that they must be on basal planes sufficiently displaced from each other to reduce their mutual interaction forces. The dislocation is out of contrast on Fig. 21(d) (g=-1101), indicating that the Burgers vector is 1/3[11-20]. In addition, it can be seen that the segments comprising the loops have <1-100> line directions, i.e. they have 30 degree character indicating orientations of low Peierls energy on the basal plane.

The configurations of these loops have enabled us to postulate a mechanism for their formation. This mechanism initially involves repeated inter-conversion processes between BPDs and TEDs, which can start with either the BPD or the TED but involve the same basic steps. If one starts with a TED, the initial stage of the mechanism involves the macrostep deflection of the surface outcrop of the TED onto the basal plane to create a segment of BPD (Fig. 22a). This deflection occurs since the macrostep (created on off-axis regions of the growth interface by step bunching, as unit cell or half unit cell high steps are retarded by various obstacles they encounter on the growth surface, for example, screw dislocation outcrops, foreign particles, other steps, etc.) cannot admit the dislocation into its structure leaving the dislocation with no alternative but to be deflected into the direction of step flow. Once the TED is deflected onto the basal plane, if the BPD segment is in screw orientation, further advancement of the macrostep will replicate the basal plane dislocation in the direction of step flow (Fig.22(b)) (BPDs intersecting the growth interface in screw orientation are most likely to be replicated and not modified during growth). If the advancing macrostep encounters a step advancing in the opposite direction, for example a spiral step from a screw dislocation which emerges on an adjacent terrace located in the overall downstep direction, the dislocation will be re-deflected into the threading direction as shown in the schematic cross-sections in Fig. 22(c). At a later stage of growth, if the outcrop of the re-deflected TED encounters another advancing macrostep, the whole process can be repeated, as shown in Fig. 22(d).

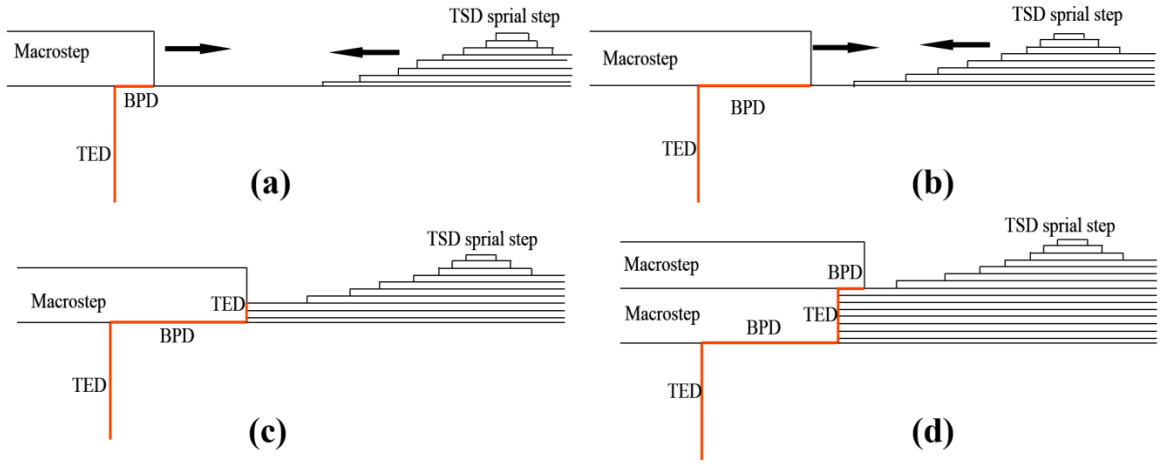

Figure 22 (a)-(d) Schematic cross-sectional view of the deflection on a TED onto the basal plane by a macrostep followed by re-deflection up into threading orientation through the encounter between macrostep and a TED spiral advancing in the opposite direction.

Since the primary slip system in 4H-SiC is 1/3<11-20>(0001), the threading edge segments interconnecting the BPD segments of the dislocation can be considered as jogs. Therefore, during this process of repeated deflection, thermal shear stress on the basal plane (experienced whilst still at high temperature in the growth chamber) can cause the relatively sessile jogs to act as pinning points for the glissile BPD segments, which are initially in screw orientation. In fact, as shown in Fig. 23(a), as soon as the TED is deflected onto the basal plane, a single-ended Frank-Read (marked as No.1 in Fig. 23(a)) source will begin to operate. Note that as the source begins to operate, the deflected BPD segments move away from screw orientation and is expected to become more susceptible to conversion into a TED segment. When the BPD is re-deflected into threading orientation, a second single-ended source (marked as No.2 in Fig. 23(b)) will initiate at that point. As this TED segment in deflected again onto the basal plane, a third single-ended source (marked as No.3 in Fig. 23(c)) will initiate. In order for these latter two sources to be able to operate independently the BPD segments on parallel basal planes must be separated by a distance large enough that their mutual repulsive forces can be overcome. Under stress the advancing BPD segments will initially draw out a dislocation dipole comprising opposite sign BPD segments. In order for these dislocations to be able to pass beyond this configuration and advance past each other the force per unit length τb on each segment of the BPD due to the applied stress τ need exceed the maximum value of their mutual attraction force,

$$\tau b > \frac{0.25Gb^2}{2\pi(1-\nu)y} \qquad (19)$$

where y is the length of the TED component. This can be translated into a minimum length for the TED component,

$$y > \frac{0.25Gb}{2\pi(1-\nu)\tau} \qquad (20)$$

If y is too small, the gliding BPDs will simply continue to draw out the dislocation dipole which will remain locked in place as shown in Fig 24(a). On the other hand, if y is large enough, the two BPD arms can effectively behave independently of each other as single-ended sources, as shown in Fig. 24(b).

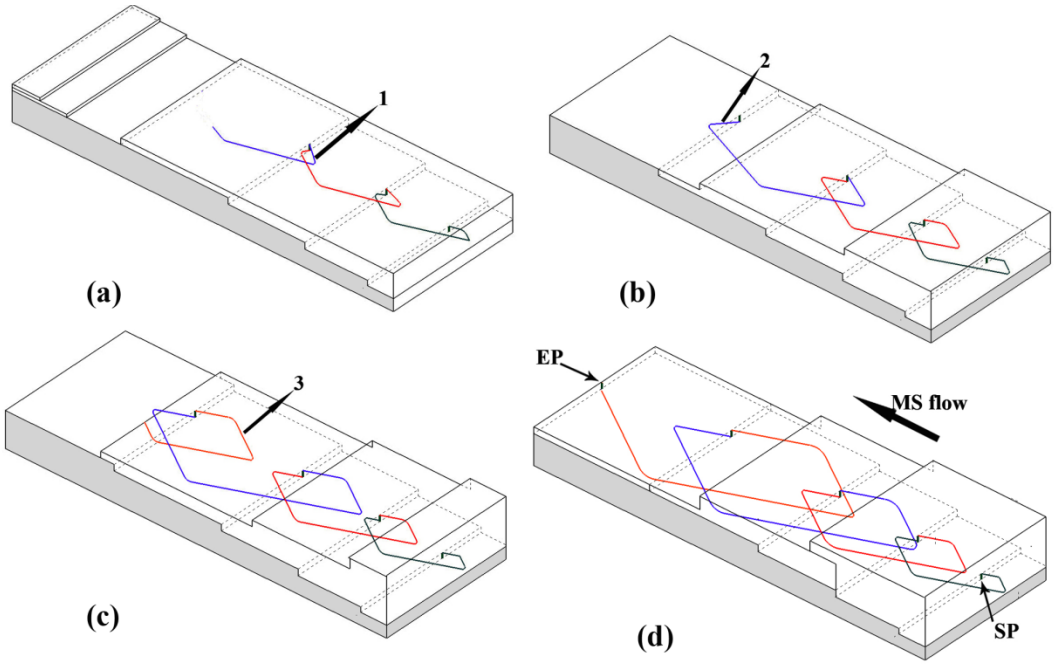

Figure 23 (a)-(c) Schematic of the formation of a single-ended Frank-Read Source through the deflection of a TED into a BPD and back again. The TED segments act as pinning points for the BPD glide; (d) the final configuration of the loops produced by the Hopping Frank-Read Source. "SP" indicates the starting point, and "EP" end point.

The existence of such jogs comprising TED segments has been confirmed by close examination of Fig. 21(b) (see the inset). Further confirmation of the existence of such double deflection processes is provided by examination of axial wafers cut parallel to the growth axis. This enables observation of the "hopping" mechanism in cross section, as shown in the SWBXT image presented in Fig. 25(a).

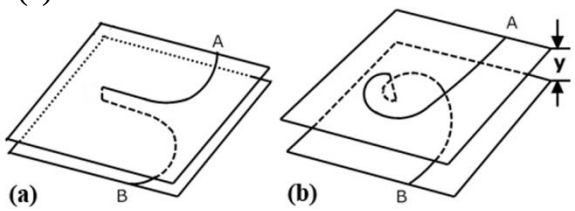

Figure 24 Schematic of two BPD arms on parallel basal planes separated by a jog comprising a segment of TED with the length of "y" (a) When y is small, the BPDs are locked as a dislocation dipole; (b) when y is sufficiently large, the BPDs can glide independently as single-ended Frank-Read sources.

Fig. 25(b) shows a transmission image from a typical wafer with a broader field of view. Note the well-defined "Hopping" Frank-Read sources near the bottom of the image. It can also be seen that the upper, higher dislocation density region, is made up of many such sources superimposed. Such configurations are routinely observed, demonstrating that this mechanism of BPD multiplication is widespread and may well be dominant in 4H-SiC.

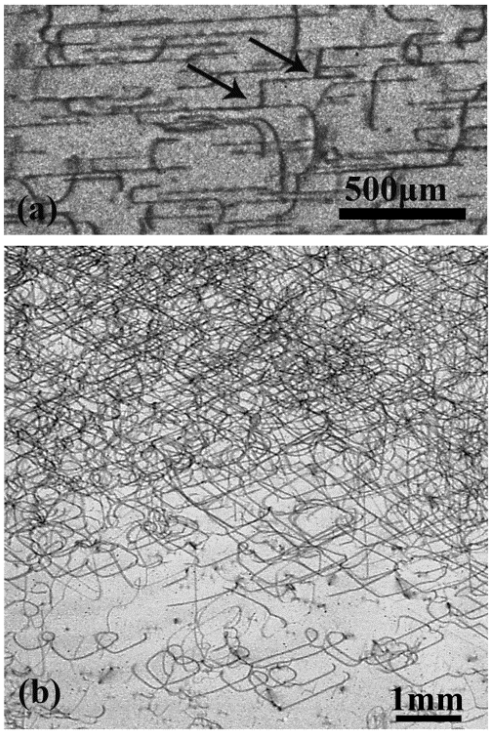

Figure 25 SWBXT of an axial wafer cut parallel to the growth axis of a 4H-SiC boule confirming the existence of the double deflection process between TED and BPD segments. (b) Transmission SWBXT image (g=-1-120) recorded from a wafer cut perpendicular to the growth axis of 4H-SiC boule. Note the isolated Hopping Frank Read sources in the lower part of the image as well as many such sources superimposing in the upper part of the image.

5.4 Conclusion

In conclusion, we have reported observations of a mechanism of basal plane dislocation (BPD) multiplication in 4H-SiC. Studies of the configurations and behavior of BPDs in wafers cut from Physical Vapor Transport (PVT) grown SiC boules have enabled us to identify the operation of single-ended Frank-Read sources which are interconnected on different basal planes. These configurations result from a sequence of processes involving inter-conversion between non-screw oriented glissile BPDs, which intersect the slightly off-axis growth interface, and TEDs. These inter-conversion processes are brought about by step interactions on the growth interface. These processes repeat resulting in a dislocation comprising several glissile BPD segments on parallel basal planes interconnected by relatively sessile TED segments. Should such interconnected BPD and TED segments experience thermal stress whilst in the growth chamber, the glissile BPD segments would readily glide but would be pinned at their connection points to the relatively sessile TED segments leading to the operation of single ended Frank Read sources. Through such processes, BPDs appear to “hop” from one basal plane to another through what is termed here as a Hopping Frank-Read source mechanism. Moreover, the glissile BPD segments adopt <1-100> line directions demonstrating that such 30 degree orientations correspond to the Peierls valleys on the basal plane. This mechanism of BPD multiplication in 4H-SiC appears to be dominant.

6. Stacking Faults Created by the Combined Deflection of Threading Dislocations of Burgers Vector c and c+a during the PVT Growth of 4H-SiC

6.1 Outline

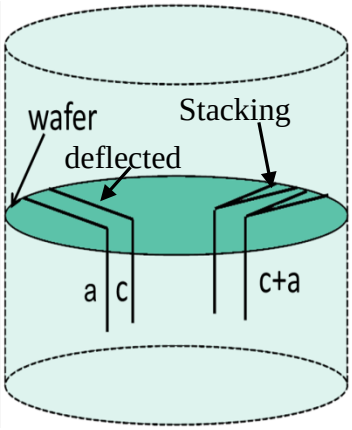

Figure 26 Schematic of the deflections of threading edge dislocations with burgers vector **c** and **c+a** onto the basal plane form stacking fault.

A review is presented of Synchrotron White Beam X-ray Topography (SWBXT) studies of stacking faults observed in PVT-Grown 4H-SiC crystals. The strength of the contrast observed on different reflections and comparison with calculated phase shifts ($\delta=-2\pi\, \boldsymbol{g}\cdot\boldsymbol{R}$) for postulated fault vectors enables determination of the faults [68,69] and analysis of these observed fault morphologies has enabled us to develop models for their formation mechanisms. These models involve the macrostep overgrowth of the surface outcrops of threading dislocations with Burgers vector **c** and **c+a**, which causes them to be deflected onto the basal plane, shown in Fig 26. Three types of faults were observed and analyzed in this way: (a) Shockley Faults; (b) Frank Faults; (c) Combined Shockley + Frank Faults with fault vectors **S**+**c**/2; Complex combinations of fault vectors arise as all of the dislocations are deflected onto the same basal plane resulting in the observed fault vectors

.

6.2 Introduction

Three types of stacking fault have been observed to date in SiC: Shockley faults, Frank faults and those which comprise some kind of combination of these two. The presence of Shockley faults is explained by the low Shockley stacking fault energy [70] so that dislocations are dissociated on the basal plane into Si-core and C-core partial dislocations separated by a Shockley stacking fault. Above the brittle to ductile transition temperature (BDTT), the partial pairs move in tandem with partial separations on the order of 30-70 nm [70] whereas below the BDTT C-core partials are sessile so that glide of mobile Si-core partials leads to Shockley fault expansion [71]. Similar stacking fault expansion occurs during the forward bias of *pin* junction diodes where again C-core partials are sessile and Si-core partials glide (driven by electron-hole recombination) leading to Shockley fault expansion [72]. Frank faults are considered to be "in-grown" stacking faults and are thought to result from the overgrowth of *c*-axis screw dislocations whose surface growth spiral steps were separated into *c*/4, *c*/2, and 3*c*/4 step heights [73]. "So called" 8H faults have been observed by many groups [74-76] and are also considered to be "in-grown" in nature although no model has been postulated for their formation mechanism. Benamara *et al* [77], Chen *et al* [78] and Tsuchida *et al* [73] have made observations of stacking faults associated with "Carrot" defects which have fault vectors of $1/12\langle 44\bar{0}3\rangle$ which comprises the sum of a *c*/4 Frank fault with a $1/3\langle 1\bar{1}00\rangle$ Shockley fault. Chen *et al* [78] postulated that such faults arise from the overgrowth of *c*-axis screw dislocations which have dissociated basal plane dislocations pinned at their cores. Dudley et al [79] recently reported that such faults can

arise from the deflection of *c*-axis threading dislocations of Burgers vector **c**+**a** onto the basal plane. If the spiral step risers of such dislocations divide into *c*/4 and 3*c*/4 increments, overgrowth can be facilitated by the simultaneous dragging of one of the Shockley partials associated with the core structure of the original dislocation by the overgrowing macrostep. This acts like an interfacial Shockley partial and adds the Shockley component to the *c*/4 Frank component of fault vector. In the paper three types of stacking faults will be explained in details.

The contrast from stacking faults in X-ray topography arises from the phase shift experienced by the X-ray wavefields as they cross the fault plane [68]. This phase shift has been computed to be equal to $\delta=(-2\pi \boldsymbol{g}.\boldsymbol{R})$, where $\boldsymbol{g}$ is the active reciprocal lattice vector for the reflection and $\boldsymbol{R}$ is the fault vector. Contrast is expected to disappear when $\delta=0$ (corresponding to $g.R$=integer) and is expected to be very weak when $\delta=\pm\pi/6$ (corresponding to $g.R=\pm1/12$, $\pm11/12$) and weak but visible for $\delta=\pm\pi/3$ (corresponding to $g.R=\pm1/6$, $\pm5/6$). Contrast should be very well marked for $\delta=\pm\pi$ and $\pm2\pi/3$ (corresponding to $g.R=\pm1/2$, $\pm1/3$ and $\pm2/3$).

6.3 Results and Discussion

6.3.1 Deflection of Threading Screw Dislocations

Regarding the growth dislocations, the most prominent of these, c-axis screw dislocations have attracted most attention. These dislocations are found to exist with Burgers vectors of *nc*, where *n* is an integer. For 6H-SiC, those with n> 2 have hollow cores while in 4H the same is true for those with n>3 [80]. Such hollow core screw dislocations are referred to as “micropipes.” Detailed studies of the correlation between Burgers vector and hollow core diameter confirmed satisfactory compliance with Frank’s theory of hollow core dislocations [81]. In the meantime, detailed transmission electron microscopy work carried out by Heindl *et al.*[82] suggested that threading, hollow-core dislocations possessing an **a**-component to their Burgers vectors also exist in SiC. Indeed, the lack of extinction of Synchrotron White Beam X-ray Topography images of micropipes recorded from axial slices (cut parallel to the [0001] growth axis) using reflection vectors perpendicular to the **c**-axis could have been interpreted as being consistent with the presence of a Burgers vector component not parallel to c. However, at the time such behavior was interpreted as a residual contrast effect resulting from “interbranch scattering” effects occurring at the open core of the micropipe, as first suggested by Krishna *et al.* [83]. Detailed and unambiguous extinction analysis of smaller Burgers vector **c**-axis dislocations carried out on studies of axial slices was made difficult at that time due to the relatively high densities of these defects. Vetter *et al* [84] showed that such **a**-components are also difficult to discern from White Beam Synchrotron Topographs recorded in Back Reflection geometry from c-plane wafers and from their simulations (based on Ray Tracing) and so such imaging could not be used to detect their presence. It was also suggested in Vetter *et al* [84] that topographs recorded in Grazing Incidence geometry were, in principle, capable of discerning these **a**-components although no detailed observations were presented at that time. More recently, Chaussende *et al* [7] have presented optical birefringence studies of threading defects in c-plane 4H-SiC wafers that clearly show the presence of this a-component.

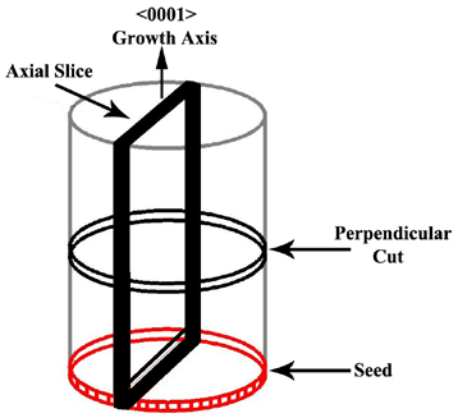

Figure 27 Two ways of cutting crystals: (1) Perpendicular-cut, which is cut perpendicular to [0001] direction, with surface plane (0001). (2) Axial slice, which is cut parallel to [0001] direction.

Usually the commercial c-plane wafer is cut perpendicular to [0001] direction, while the axial slice cut from SiC ingot parallel to [0001] direction which is the best way to study the behavior of the growth dislocation. The axial slice studies in Fig.28 is cut parallel to (-12-10) with thickness 300 μm.

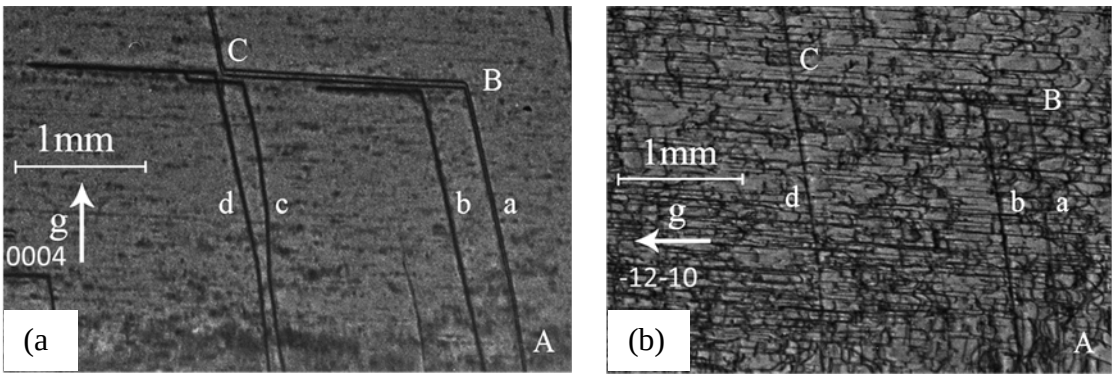

Figure 28 SWBXT images of axial slices (a) g=0004; (b) g= $1\bar{2}1\bar{0}$.Threading screw dislocation a, b, d are visible on both g vectors, and c is only visible on (0004), out of contrast on ($1\bar{2}1\bar{0}$).

There are four TSDs marked as ‘a’, ‘b’, ‘c’ and ‘d’ observed at 1 cm from the edge of axial slices in transmission-geometry X-ray topography at g=0004 in Fig. 28. It is obvious that dislocations get deflected onto the same basal plane. According to **g** · **R** analysis, Burgers vector of dislocation ‘c’ only contains **c** component ([0001]) as it is appears on 0004 but disappears on -12-10. On the other hand, dislocations a, b, and d exhibit strong contrast on both 0004 and -12-10 suggesting that their Burgers vector have both **a** component (1/3<11-20>) and **c** component ([0001]) (i.e. they are not TEDs/BPDs nor TSD’s). Their presence in SiC has been suggested previously [66,84-86], which are mixed dislocations.

For the phenomenon of deflected TSDs, it is observed that the deflection of threading screw dislocations were towards the same direction, i.e. the edge of the axial slices. It is seemed that all the four threading dislocation are deflected onto the same basal plane as the same macrostep advancing from the center of the wafer towards the edge. Sometimes, the deflected TSDs will reconvert into threading direction, like dislocation **‘a’** in Fig. 28 (a), In order to study the macrosteps behavior during PVT growth, microscopic images are recorded at the facet of the as-grown ingot surface, which shows large macrosteps in Fig. 29 (a) and TSD spiral steps in Fig. 29 (b). The growth of SiC requires the existence of step risers which contains the information of

stacking sequences on the surface, atoms will deposit onto the surface and get attached with these step risers at the supersaturating condition. Based on the sources of the steps, there are two growth mechanisms happening at the same time (1) step flow mechanism (dominant); (2) TSD spiral step growth (accelerate the growth rate). During step-flow growth, macrosteps (1-100 μm height) are created by step bunching as unit cell (or half unit cell) high steps retarded by various obstacles they encounter on the growth surface (for example, screw dislocation outcrops, foreign particles, other steps, etc.).For the spiral steps, <10-10> are preferred directions which is corresponding to lowest Peierls valleys on the (0001) slip plane. At certain positions (e.g. position 'A' in Fig. 29(b)), it will experience the advancing of macrostep and threading screw dislocations from opposite directions.

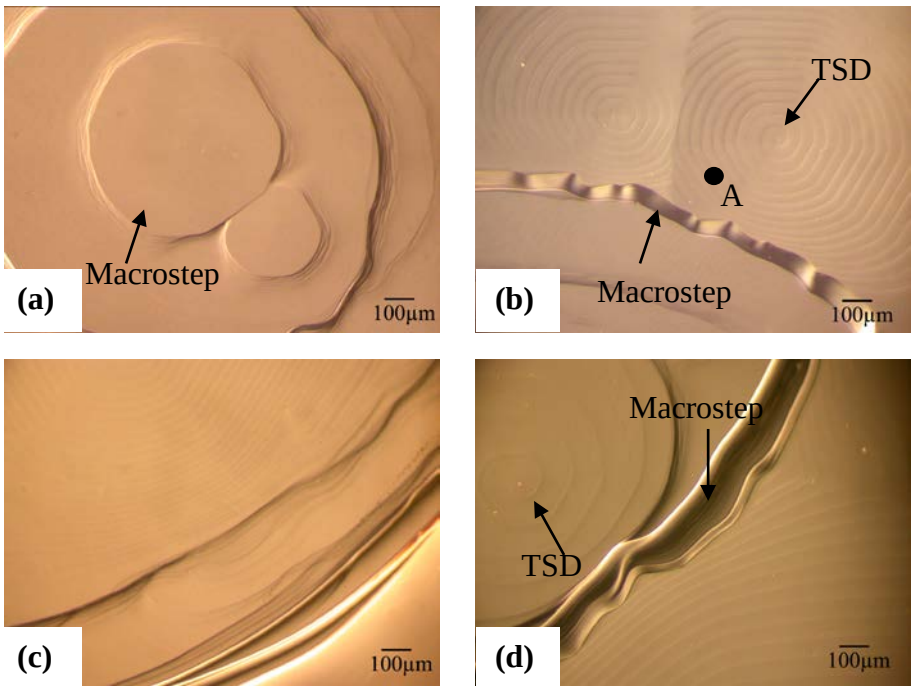

Figure 29 (a)-(d) Microscopic images of growth surface of wafer boule. The big steps called macrostep can be seen in the images. And the spiral loops shows the existence of threading screw dislocation (TSD).

After understanding the mechanism of crystal growth, the configuration of threading screw dislocations in Fig. 28 can be explained by the schematic diagram in Fig. 30.

(a) The deflection of TSDs are due to the movement the macrosteps since they cannot admit the dislocation into its structure leaving the dislocation with no alternative but to be deflected onto the direction of step flow. The flow direction of macrostep is from the center towards the outside edge of the crystal.
(b) When the same macrostep come into threading screw dislocation a, b, c and d in Fig. 28(a), they all get deflected onto basal plane. Further advancement of the macrostep will replicate the deflected threading screw dislocations in the direction of step flow.
(c) If the advancing macrostep encounters a step advancing in the opposite direction, for example, a spiral step from a screw dislocation which emerges on an adjacent terrace located in the overall downstep direction, the dislocation will be re-deflected into threading direction, for example, dislocation **a** in Fig. 28(a). For these dislocation that

doesn't re-converted into threading direction, might form stacking faults on basal plane, which will be discussed in details below.

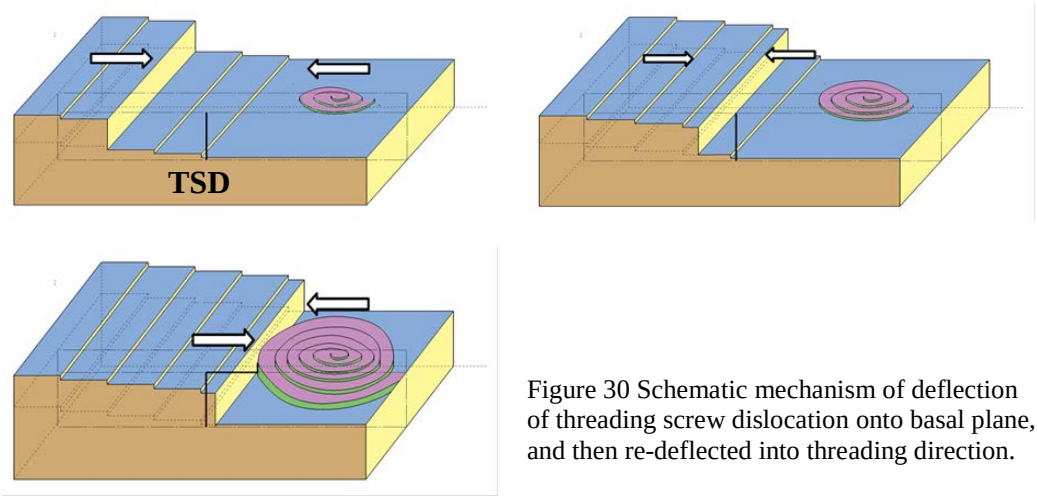

Figure 30 Schematic mechanism of deflection of threading screw dislocation onto basal plane, and then re-deflected into threading direction.

6.3.2 Shockley Faults

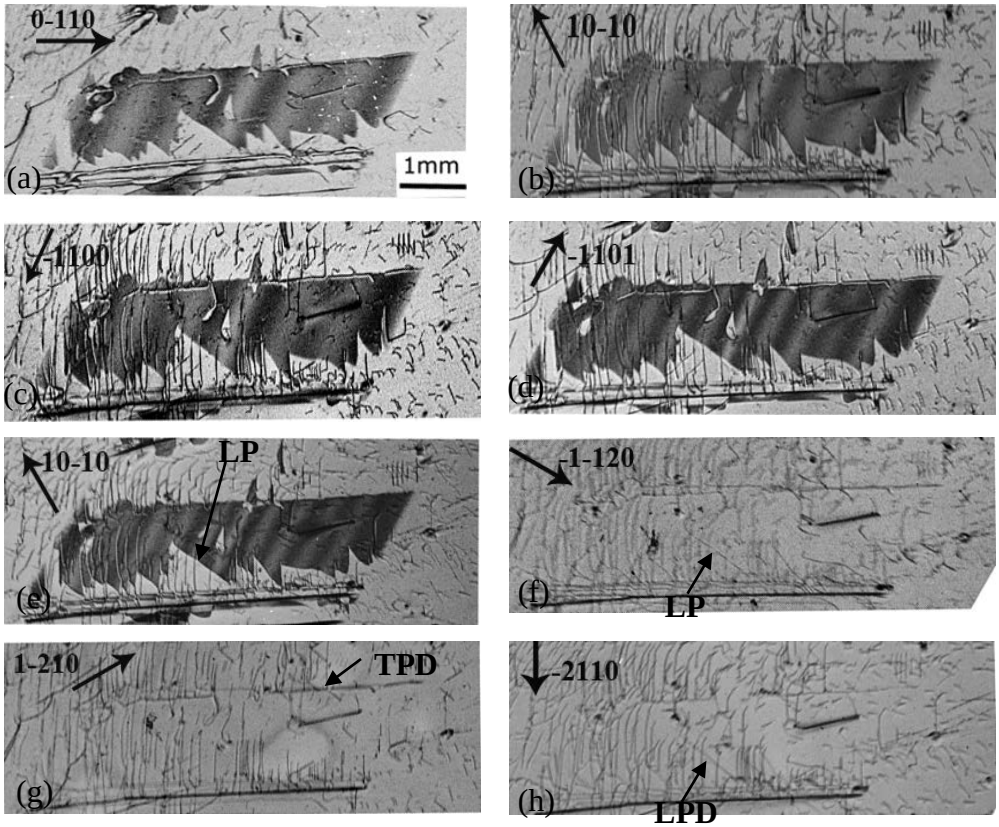

Figure 31 (a)-(h) SWBXT images with various g vectors recorded at the same area from 4H-SiC wafer with 4° offcut from the [11-20] direction.

The presence of Shockley faults is explained by the low Shockley stacking fault energy (14.7 ± 2.5 mJm^{-2} for 4H-SiC and 12.2 ± 1.1 mJm^{-2} for 6H-SiC) so that all the basal plane

dislocations were found to be dissociated into two partials bounding a ribbon of stacking faults, and the separation width is ~33 nm wide in 4H-SiC, which has been reported by Hong *et al* [70] using two-beam bright-field and weak-beam dark-field techniques of TEM. On the other hand, the dislocation width in X-ray topography is several microns, which makes it difficult to resolve two partials. As a result, BPDs are shown as single line features in XRT images. The Burgers vector of a perfect basal plane dislocations is $\vec{\boldsymbol{b}}$=1/3<$2\bar{1}\bar{1}0$>, and they are dissociated into two partials with Burgers vectors $\vec{\boldsymbol{b}}$=1/3<$1\bar{1}00$> and $\vec{\boldsymbol{b}}$=1/3<$10\bar{1}0$>. Because the partials belong to the glide plane (either Si surface or C surface), they are named as Si-core or C-core partials, whereas the activation energy for Si partial is much smaller than C partials. Above the brittle to ductile transition temperature (BDTT), the partial pairs move in tandem with partial separations on the order of 30-70 nm [70] whereas below the BDTT C-core partials are sessile so that glide of mobile Si-core partials leads to Shockley fault expansion [71]. Similar stacking fault expansion occurs during the forward bias of *pin* junction diodes where again C-core partials are sessile and Si-core partials glide (driven by recombination) leading to Shockley fault expansion [87] .

SWBXT Images showing one stacking fault recorded from a region near the edge of a 76mm wafer cut with 4 degrees offcut towards [$11\bar{2}0$] are shown on Fig. 31. The fault in the picture is bounded by a straight partial on one side and a curved partial on the other. This is consistent with the model in that the glissile Shockley partial (also called leading partial dislocation (LPD)) is expected to be curved as it glides and gets pinned at various obstacles while the sessile partial dislocation (also called trailing partial dislocations (TPD)) is expected to be trapped at the straight **c**-height step. The Burgers vector of the LPD can be determined as 1/3[10-10] as the PD is out of contrast at g=1-210, while still in contrast at g=-1-120 and -2110. From the contrast analysis shown in Table 6, it is concluded that the stacking fault is Shockley Fault, as it exhibits strong contrast on three different {$01\bar{1}0$} and three different {$0\bar{1}11$} reflections, out of contrast on three different {11-20} ones.

Table 6 Contrast Behavior of Shockley Fault with R=1/3[10-10]

R	01-10	-1100	10-10	-1011	-1101	0-111	1-210	-1-120	-2110
g·R	1/3	-1/3	2/3	-2/3	-1/3	-1/3	0	-1	-1
visibility	Y	Y	Y	Y	Y	Y	N	N	N

Usually, above the brittle to ductile transition, pairs of Shockley partials would move in tandem under shear stress (τ). Under the stress, the leading partial converts the tetrahedra protruding onto the glide plane from twinned configuration (primed) into untwinned and the trailing partial reverses this process [88]. However, if the ***c***-height step riser associated with the ***c***-component of the Burgers vector is oriented so as to bisect the two extra half planes associated with its ***a***-component. In this case, if the crystal experiences stress with a sense as indicated in Fig. 32(a), then the leading partial is on the terrace below the **c**-height step. This partial converts the tetrahedra protruding onto the glide plane from twinned configuration into untwinned, while the trailing partial is prevented from reversing this process since it encounters a terminating glide plane and so becomes sessile. Thus the glide of the leading partial dislocation will form Shockley-type stacking fault as shown in Fig. 32.

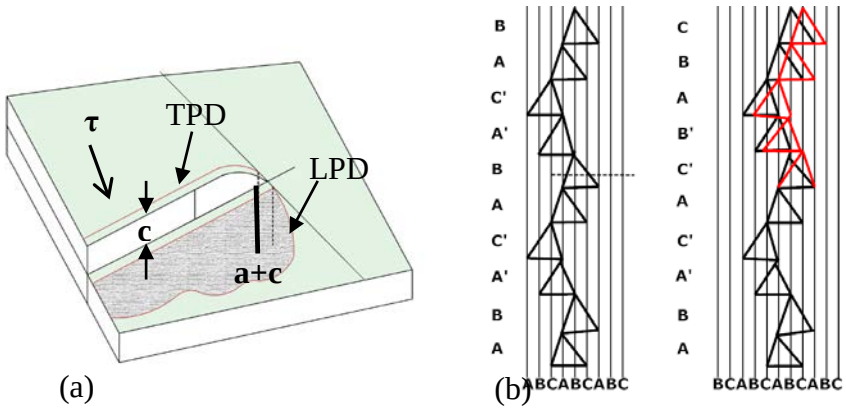

Figure 32 (a) Schematic shows the deflected of **a**+**c** threading screw dislocation. The leading partial and the trailing partial are separated by **c**-height step which is caused by deflection of threading screw dislocation with Burgers vector **c**, and the leading partial can move under stress, while the trailing partial cannot, resulting the formation of Shockley faults. (b) Schematic shows the stacking sequence change after one step glide of the leading partial dislocation.

6.3.3 Frank Faults

SWBXT Images recorded from a region near the edge of a 76mm wafer cut with 4 degrees offcut towards [11$\bar{2}$0] are shown on Fig. 33. From the figures, we can see one triangle-shaped stacking fault with two straight partial dislocations, and the fault contrast is visible when $\ell \neq 0$ (ℓ is the fourth index number of $\boldsymbol{g}$ vector ($hki\ell$)), and invisible when ℓ=0. Then the stacking faults are Frank Faults with fault vector either ½[0001] or ¼ [0001]. Additional **g** vectors *e.g.* <1-102> are required to record in order to determine the stacking fault vector. If the stacking fault is out of contrast at g=1-102, then the Frank fault is ½[0001], otherwise it is ¼ [0001].

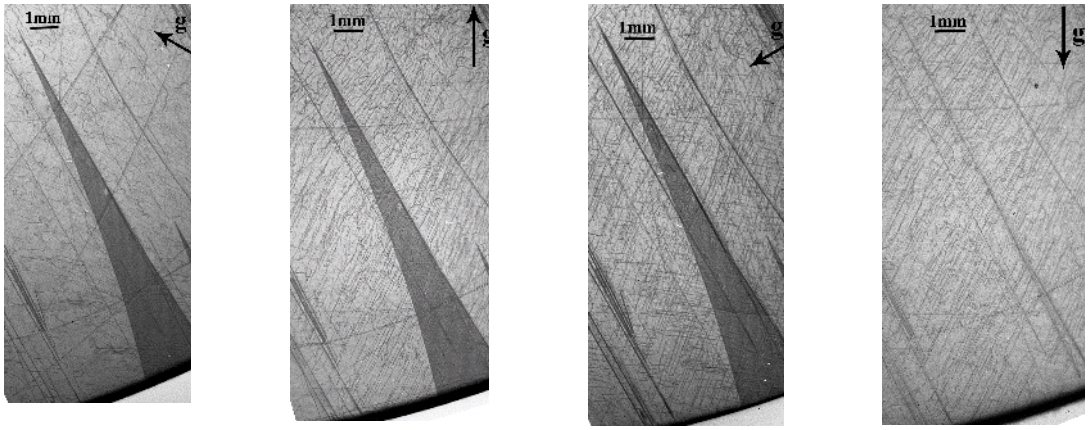

10-11 -1101 0-111 1-100

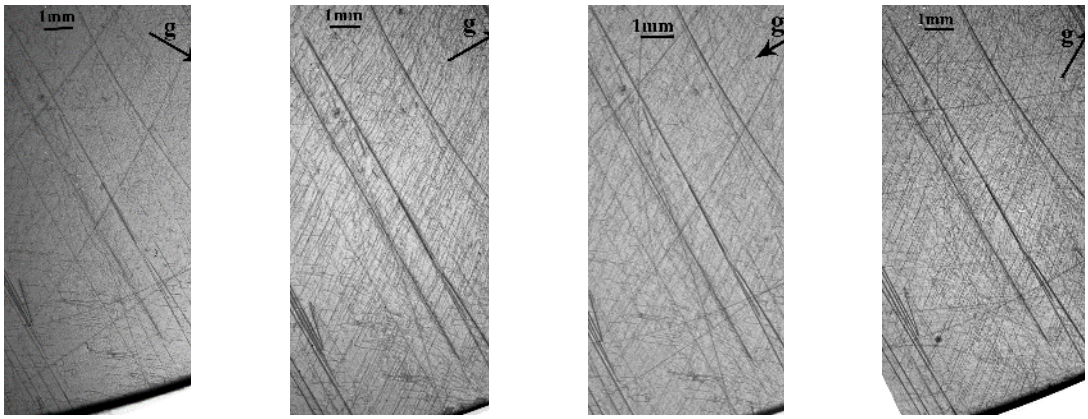

10-10 01-10 -1-120 -12-10

Figure 33 SWBXT Images recorded from a region near the edge of a 76mm wafer cut with 4 degrees offcut towards [11$\bar{2}$0]. One triangle stacking fault is visible on [10-11], [-1101] and [0-11], and out of contrast when the fourth number of the g vectors is zero.

Table 7 Contrast Behavior of Frank Fault with R=1/2[0001]

R	-1011	-1101	0-111	1-100	10-10	01-10	-1-120	-12-10	-2110
g·*R*	1/2	1/2	1/2	0	0	0	0	0	0
visibility	Y	Y	Y	N	N	N	N	N	N

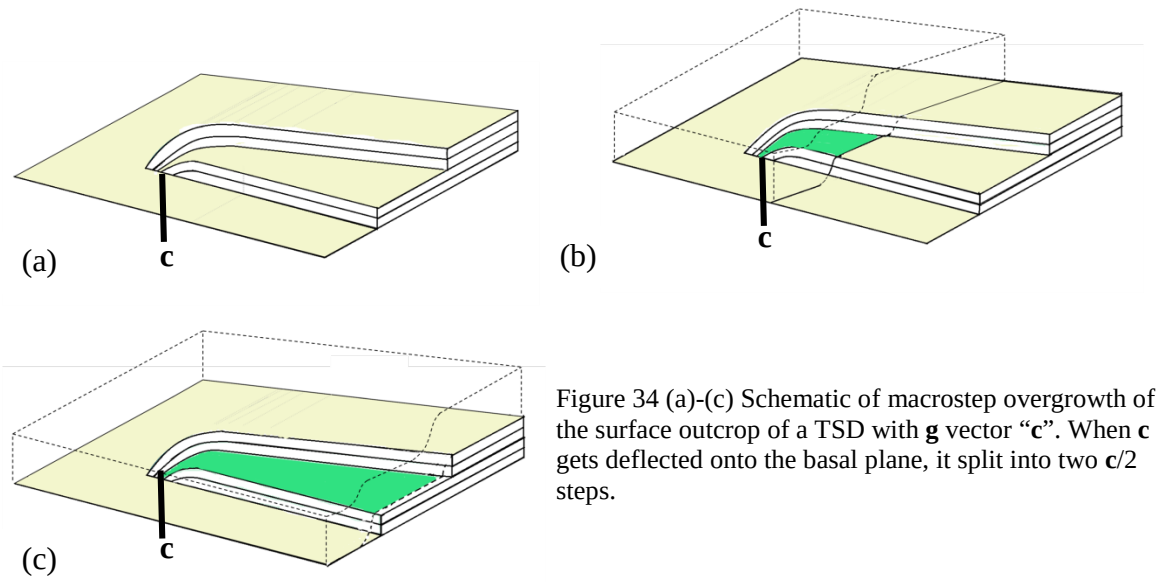

Figure 34 (a)-(c) Schematic of macrostep overgrowth of the surface outcrop of a TSD with **g** vector "**c**". When **c** gets deflected onto the basal plane, it split into two **c**/2 steps.

These Frank faults are considered to be "in-grown" stacking faults and are thought to result from the overgrowth of *c*-axis screw dislocations whose surface growth spiral steps were separated into *c*/4, *c*/2, and 3*c*/4 step heights [89]. "So called" 8H faults have been observed by many groups [74-76] and are also considered to be "in-grown" in nature although no model has been postulated for their formation mechanism. The promoted formation mechanism of Frank fault is shown in Fig. 34. The deflected TSD with Burgers vector **c** onto the basal plane, resulting

c step riser can be split into two 1/2**c** steps. After the overgrown of macrostep, Frank fault with fault vector 1/2**c** has been formed.

6.3.4 Shockley + c/4 Frank Faults

Figs. 35 (a)-(d) show SWBXT images recorded from a region near the edge of a 100mm wafer cut from a boule grown under low stress conditions showing triangular shaped stacking fault configurations fanning out towards the outer edge of the wafer. Two types of fault are present, labeled A and B. Both types are visible on (a), while type A only is visible on (b), and type B only is visible on (c). All fault contrast is extinguished on (d). The overall fault morphology is consistent with nucleation at the deflected outcrop of a threading dislocation, as described previously [90]. Dislocations *a*, *b* and *c* (see 35(d)) also appear to have been deflected onto the basal plane. The disappearance of the latter on (b) is consistent with their being Frank dislocations originating from the deflection of c-axis screw dislocations since both **g**.**b** and **g**.**b**x**l**=0.

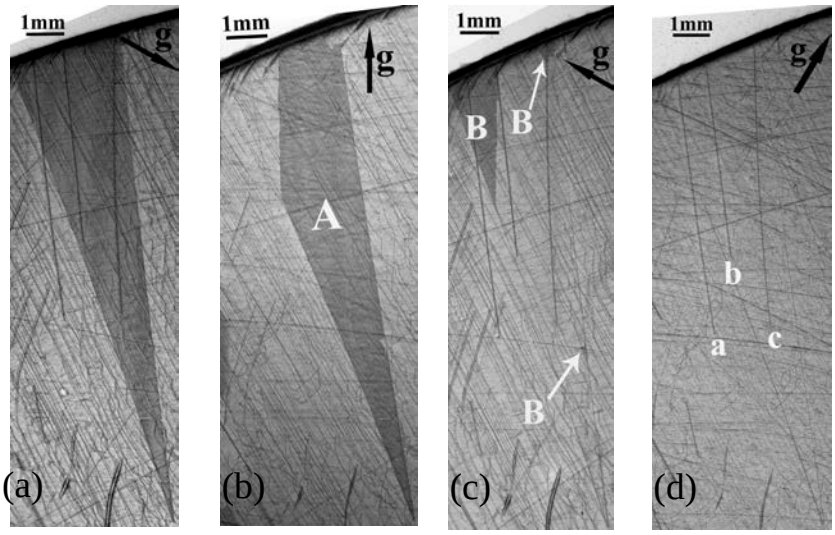

Figure 35. (a)-(d), SWBXT Images recorded from a region near the edge of a 100 mm wafer cut with 4 degrees offcut towards [11-20]: (a) 10-10 reflection showing triangular faults; (b) -1101 reflection from same area showing stacking fault contrast from fault A only; (c) -1011 reflection from same area showing contrast from faults B only; (d) -12-10 reflection showing absence of all fault contrast. Dislocations *a*, *b*, and *c* are indicated. These can also be seen on (a) and (c) but not (b)

The contrast behavior of the faults is consistent with fault vectors of 1/12[-4043] for fault A and 1/12[-4403] for faults of type B. Note the extremely low density of threading defects with **c** component of Burgers vector in this region; this is around 187 cm^{-2} and comprises densities of 38 cm^{-2} of pure screw dislocation and 149 cm^{-2} of **c**+**a** dislocation. While the presence of c-axis screw dislocations has long been accepted, those with **b**=**c**+**a** have long been a subject of discussion [12-14]. For **c**+**a** dislocations, the extra half-planes associated with the "**a**" component and the surface step associated with the "**c**" component are anchored together at the dislocation core as shown in the schematic of the surface outcrop in Fig. 36(a) showing, in this case, a unit cell high step bisecting the extra half-planes associated with the **a** component of the dislocation. If the dislocation outcrop is overgrown by a macrostep at this instant, the lines along which the

two extra half-planes terminate on the surface (which are mutually displaced by the step height associated with the **c**-component) become the line directions of the two Shockley partials, one glissile and one sessile (since its slip terminates at the step edge), associated with the **a** component of the deflected dislocation, while the overgrown step riser becomes the core of the Frank dislocation associated with the **c**-component (see Fig. 36(b) and (c)). The spiral steps can also subdivide into c/4 increments. For example, for the case of fault A, this can be created via a mechanism which involves overgrowth of a threading dislocation with **b**=**c**+**a** whose spiral surface steps have divided into one of ¼ c and another of ¾ c as shown schematically in Fig. 36(d)-(f).

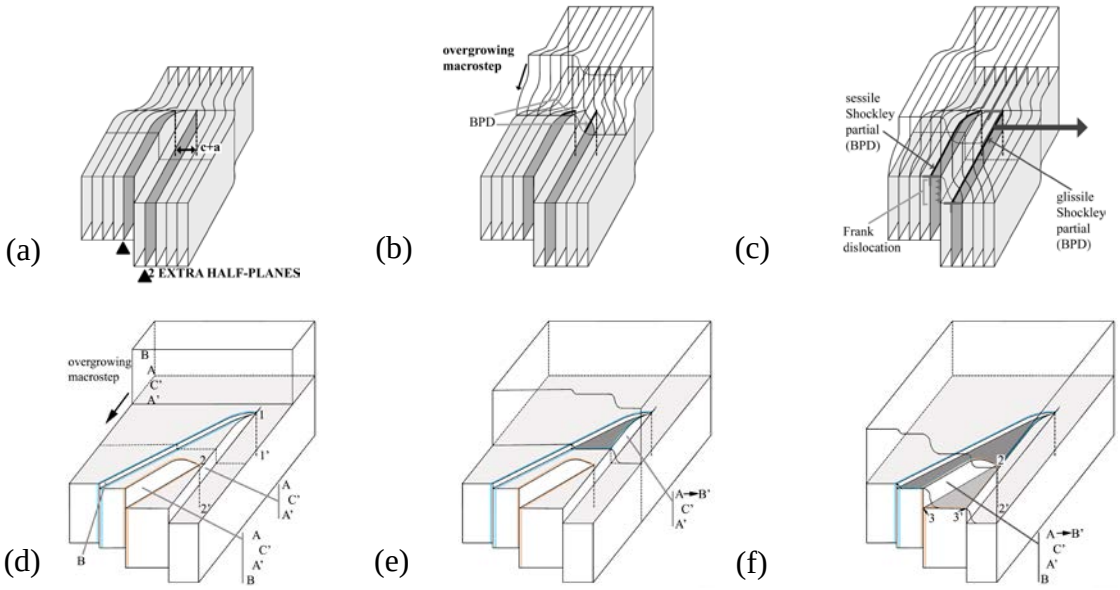

Figure 36 (a)-(c) Overgrowth of **c** + **a** dislocation with a c-height step converting it into a Frank dislocation plus two Shockley partials, one sessile (since its slip plane terminates) and one glissile; (d)-(f) Overgrowth of **c** + **a** dislocation 11' with c/4- and a 3c/4-height steps which has a second **c** + **a** dislocation, 22' with c-height spiral step protruding onto the terrace between these two step risers. Stacking sequences are indicated (normal 4H stacking sequence is ABA'C'). In (e) the "interfacial Shockley" converts the A layer into B', allowing overgrowth by the A' layer at the bottom of the macrostep. Following overgrowth in (f) the Shockley associated with the deflected 22' dislocation located at 23 glides under stress until it reaches the edge of the step 23' creating the fault of type B.

Under normal circumstances, overgrowth of such a step configuration would be disallowed by the stacking rules and would result in step bunching. However, if overgrowth occurs at the point where the **c**/4 dislocation step riser bisects the extra half-planes associated with the a component, the Shockley partial whose extra half-plane terminates on that terrace can be dragged across the terrace surface by the advancing macrostep, allowing the tetrahedra exposed on the upperside of the terrace to bond to those on the underside of the macrostep. Thus, the gliding partial acts like an interfacial dislocation between the terrace and the macrostep, only affecting the tetrahedra terminating the terrace. The net fault vector of this composite fault would then comprise **c**/4 plus the Shockley component, i.e. 1/12[4-403]. Fault B can be explained by the overgrowth of a second **c**+**a** dislocation which protrudes on the terrace in between the c/4 and 3c/4 step risers of the original dislocation (see Fig. 36(d)-(f)). If this second dislocation has a

spiral step riser of height **c** which bisects its two associated Shockley partials, one of the Shockleys can become glissile leaving behind its partner in sessile mode (trapped at the upper step edge where its slip plane terminates) plus the naturally sessile "**c**" component which is a Frank type dislocation. Once this has been overgrown in the same manner as was described earlier, the glissile Shockley would be susceptible to any local stresses present in the boule post growth. Under stress the glissile Shockley could freely expand until it reaches the 3c/4 high step edge associated with the original dislocation. All faults formed by such mechanisms are expected to have straight edges, corresponding to the locations of the original dislocation step edges. This is consistent with observations of fault morphology and contrast extinction for the partials involved.

Table 8 Contrast Behavior of two (S+C/4) Faults together

*** Fault A: R_A=1/12[-4043] Fault B: R_B=1/12[-4403]**

R	01-10	10-10	1-100	0-111	-1011	-1101	-1-120	-12-10	-2110
$g \cdot R_A$	-1/3	-2/3	-1/3	7/12	11/12	7/12	1	0	1
visibility	Y	Y	Y	Y	N	Y	N	N	N
$g \cdot R_B$	1/3	-1/3	-2/3	-1/12	7/12	11/12	0	1	1
visibility	Y	Y	Y	N	Y	N	N	N	N

6.3.5 Influence of Stacking Faults on Device Performance.

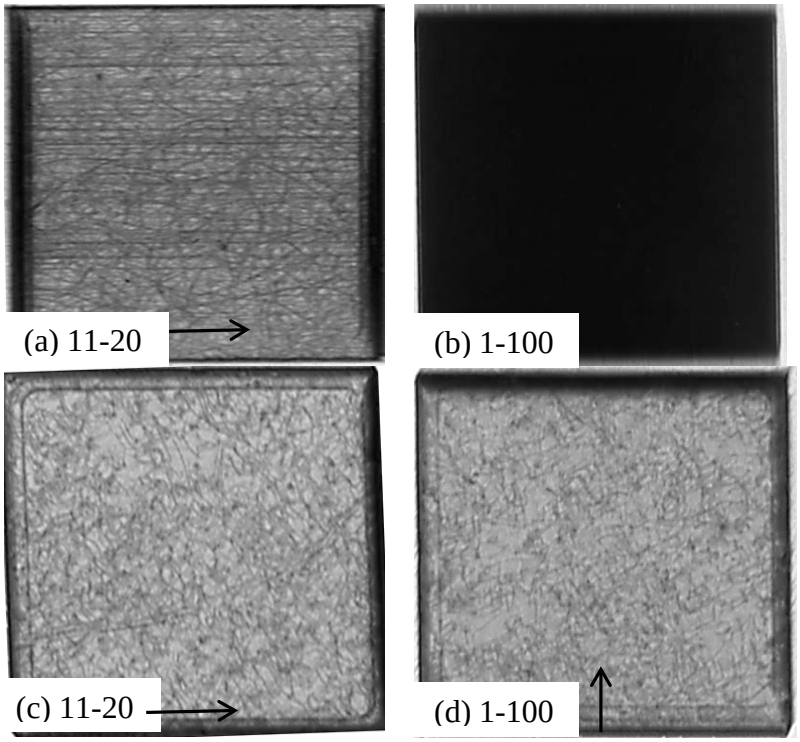

Fig. 37 (a) and (b) SWBXT images recorded on one 'bad' performance *pin* diode. (c) and (d) SEBXT images recorded on one 'good' performance *pin* diode.

In order to investigate the influence of stacking faults on device performance, SWBXT images were recorded from.~2×2 mm^2 pin-diode chips which exhibit difference device performance during forward-biased operation. The degradation of SiC PiN diode takes place in the chip 'A' during forward-biased operation whose SWBXT images are shown in Fig. 37(a) and (b), while chip 'B' has much better performance and its SWBXT images are shown in Fig. 37(c) and (d). Compared their SWBXT images, the big difference between these two chips are the existence of stacking faults. Chip 'A' is occupied by 100% stacking faults after test as shown in Fig. 37(b) while no stacking faults are found in Chip 'B' as shown in Fig. 37(d). It can be concluded that the degradation of SiC diode is associated with the existence of the stacking faults in the active region of the device [91]. The activation energy for dislocation glide in SiC is about 2.5 eV and the brittle-to-ductile transition temperature in SiC is about 1000℃, while the stacking faults formation in the diode take place at near room temperature during forward-biased operation, which indicates that an extra energy provided by an extra amount of energy ΔE provided by forward biasing that promote the glide of Shockley partial dislocations called 'electron-hole recombination-enhanced defect reaction".

6.4 Conclusion

The deflection of **c** and **c**+**a** threading dislocations onto basal plane (0001) can lower the density of threading dislocations in the boules, however it also leads to the formation of stacking faults; three types are discussed in this paper. (1) Simple Shockley Fault: Overgrowth of a **c** + **a** dislocation with a **c**-height step such that the Shockley partials associated with the **a** component of the deflected dislocation are located on slip planes displaced by the **c** component such that one becomes sessile and other glissile. (2) Simple Frank Fault: Overgrowth of demi-steps associated with **c** dislocation. (3) Combination of 1 and 2, with additional **c** + **a** dislocations protruding onto the terrace between the two c/2 steps followed by postgrowth glide.

7. Studies of the Operation of Double-Ended Frank-Read Partial Dislocation Sources in 4H-SiC with Heavily Nitrogen Doping

7.1 Outline

Synchrotron White Beam X-ray Topography (SWBXT) has been used to image and analyze a distinctive stacking fault pattern observed in 4H-SiC wafers. The pattern often consists of a six-pointed star comprised of multiple layers of rhombus-shaped stacking faults with three different fault vectors of the Shockley type bounded by 30° Shockley partial dislocations. Formation of this stacking fault pattern is associated with a micropipe at its center which can act as nucleation sites for dislocation half-loops belonging to the primary basal (1/3<11-20> (0001)) slip system and occasionally the secondary prismatic (1/3<11-20>{1-100}) slip systems. In this case, the rhombus-shaped Shockley type stacking faults are nucleated on the basal plane by dissociation of 1/3<11-20> pure screw dislocations cross-slipped from the prismatic plane and subsequent expansion caused by glide of the leading partial and locking of the trailing partial by interaction with 60° 1/3<-2110> dislocations on the basal plane. Based on these observations, a formation mechanism involving the operation of a double-ended Frank-Read partial dislocation source has been proposed. In the limit, this glide and cross-slip mechanism leads to 4H to 3C polytype transformation in the vicinity of the micropipe by a mechanism similar to that proposed by Pirouz (1993).

7.2 Introduction

The excellent properties of silicon carbide (SiC), a wide bandgap semiconductor, make it highly suited for electronic and optoelectronic devices operating under high temperature, high power, high frequency and/or strong radiation conditions [92]. However, physical vapor transport (PVT) grown commercial SiC wafers contain crystalline imperfections such as micropipes, deformation induced basal plane dislocations (BPDs), planar defects (stacking faults, small angle boundaries), etc. that affect device performance and limits widespread application. Especially, Synchrotron white beam X-ray topography (SWBXT) [93] has played a key role in revealing the detailed configurations of these defects and shed much light on the mechanisms of formation thereby enabling the development of strategies for eliminating or lowering their densities [94,95]. In the case of stacking faults, three types of stacking faults according to their fault vectors have been reported: Shockley fault with fault vector of (a/3)<1-100> type [69,71,87], Frank fault with fault vector of (c/2)[0001] or (c/4)[0001] [89], and those comprising some kind of combination of the first two [73,77-79,96]. Expansion of Shockley faults into rhombus shapes in the SiC epilayer has been shown to be associated with degradation of power devices [87]. The fault expands though a mechanism whereby the Si-core partials are electrically active, while the C-core partials are not, and the Si-core partials can couple with electron-hole recombination and move. Similarly Shockley faults can expand in response to applied stresses below the brittle-to-ductile transition temperature when C-core becomes sessile and mobile Si-core partial glides [71]. In this study, SWBXT observations of such rhombus-shaped Shockley type stacking faults on the basal plane emanating from micropipes in PVT-grown 4H-SiC wafers have been analyzed and a detailed model proposed to explain their nucleation. This model derives from the previously reported interaction between dislocation loops emanating from the micropipes which belong to the prismatic and basal slip systems [97].

7.3 Experimental

SWBXT images were recorded from PVT-grown 100mm diameter 4H-SiC wafers with high nitrogen doping (>10^{19} cm^{-3}) in the transmission (1-100, -1101 and 11-20 type reflections) and grazing incidence (11-28 type reflections) geometries. Grazing-incidence images were recorded from Si-faces of the samples at an X-ray incident angle of 2°. All images were recorded on Agfa Structurix D3-SC film. The imaging was carried out at the Stony Brook Synchrotron Topography Station, Beamline X-19C, at the National Synchrotron Light Source at Brookhaven National Laboratory. High resolution transmission electron microscopy (HRTEM) was carried out on the JEOL 2100F at the Center for Functional Nanomaterials (CFN) at Brookhaven National Laboratory.

7.4 Result and Discussion

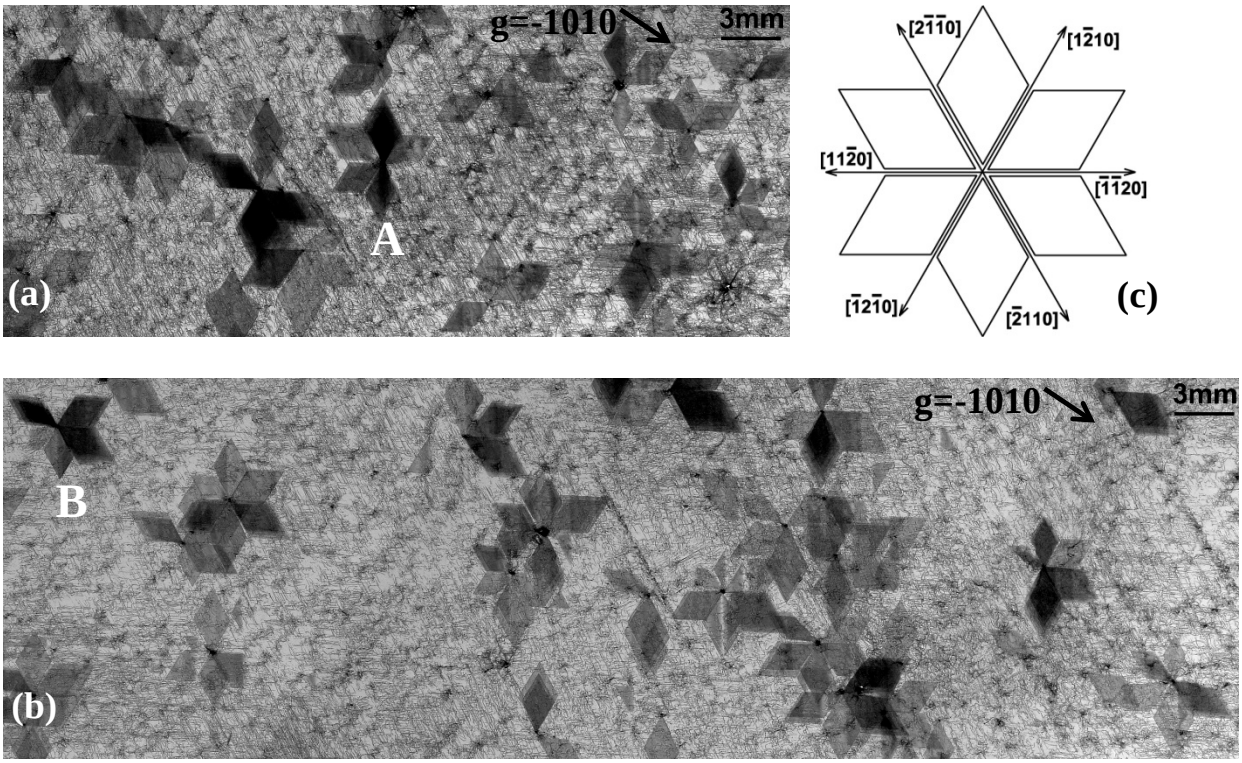

Figure 38. (a) and (b) X-ray transmission topographs from a 4H-SiC substrate showing various configurations of rhombus-shaped stacking faults anchored to micropipes in groups forming rosette-like configurations; (c) Schematic showing <11-20> traces of the intersecting {1-100} type planes around a micropipe.

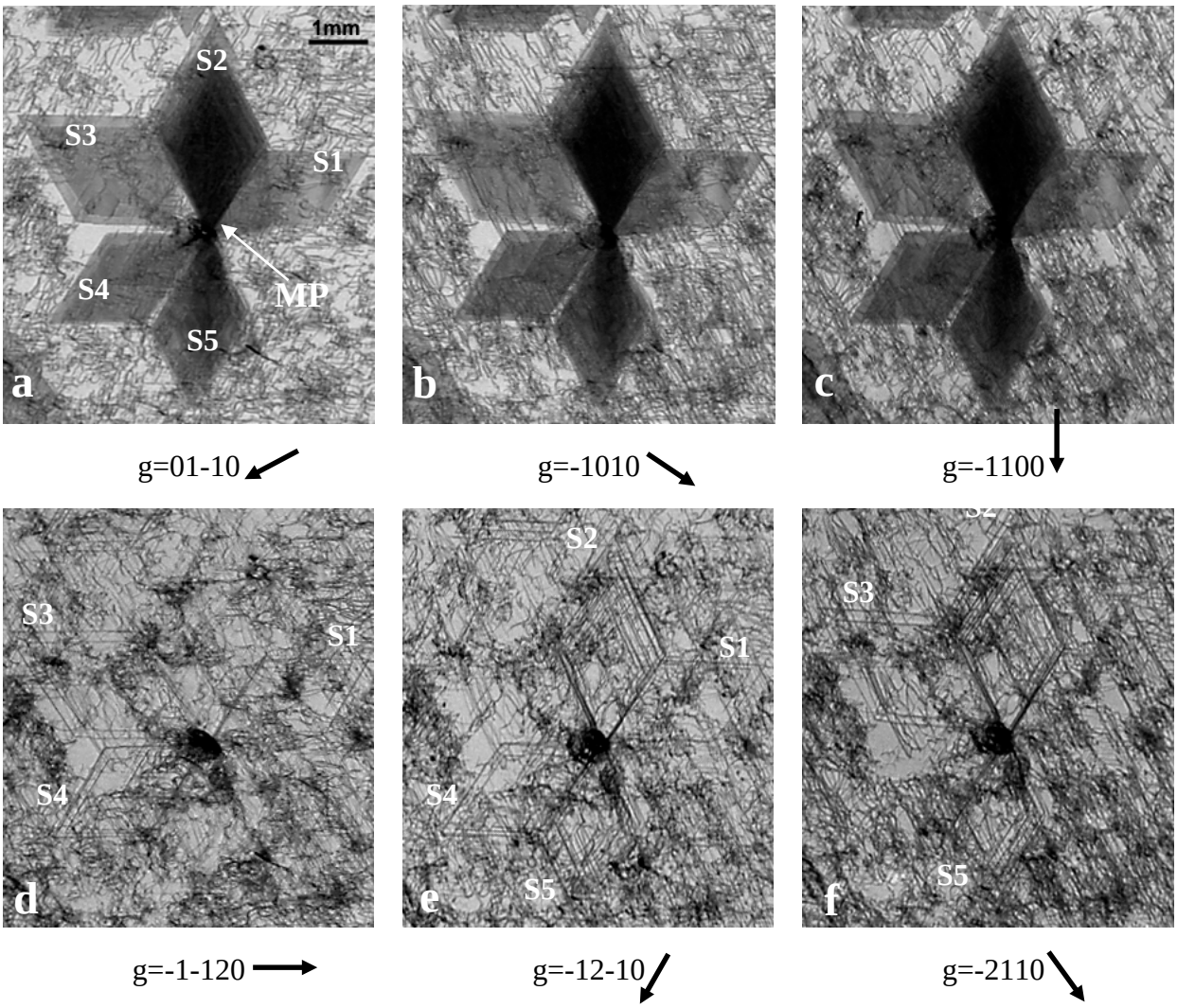

Figure 39 (a)-(c) Enlarged X-ray transmission topographs recorded from region A in Fig. 1(a). (a)-(c) {1-100} type reflections showing a rosette comprising five rhombus-shaped stacking faults (marked S1-S5) surrounding a micropipe (MP); (d)-(f) {11-20} type reflections where the stacking faults are not visible but dislocation lines bordering the faults are selectively visible. Dislocations bordering faults S1, S3 and S4 are visible on (d), those outlining S1, S2, S4 and S5 are visible on (e) while those outlining S2, S3 and S5 are visible on (f).

Selected areas of a transmission X-ray topographs recorded from a 4H-SiC substrate are shown in Figs. 38(a) and (b). Various configurations of rhombus-shaped stacking faults can be observed distributed throughout the images. Close examination reveals that the faults are anchored to micropipes in groups forming rosette-like configurations. Each rhombus-shaped fault appears to be confined to one of six sectors defined by the intersections of two {1-100} type planes (with a dihedral angle of 60°) with the micropipe, as shown schematically in Fig. 38 (c) where the <11-20> traces of these planes on the sample surface are shown. In some cases only one or two of these sectors contain faults, in others up to five of the six are occupied. Figures 39(a) - (c) show a series of enlarged {1-100} white beam x-ray transmission topographs recorded from region A in Fig. 38(a), show a rosette comprising five rhombus-shaped faults (marked S1-S5) surrounding a micropipe, denoted by MP in Fig. 39(a). It can be clearly seen that the edges of each rhombus are along the <11-20> directions. The faults are not visible on the

{11-20} type reflections shown in Figs. 39(d) - (f) although dislocation lines apparently forming the outlines of the faults are selectively visible. For example, the dislocations forming the outlines of faults S1, S3 and S4 are visible on Fig. 39(d), those outlining S1, S2, S4 and S5 are visible on Fig. 39(e) while those outlining S2, S3 and S5 are visible on Fig. 39(f). Application of the **g**·**R** criterion (where **g** is the reflection vector, **R** the stacking fault vector) to Figs. 39(a) - (f) demonstrates that all five stacking faults are Shockley type with fault vectors of type 1/3<1-100> bounded by 1/3<1-100> Shockley partials where both the fault and partial Burgers vectors point along the long diagonals of the rhombuses so that each of the partial loop segments is of 30° character. The variations in the density of fault contrast observed in Figs. 39(a) - (c) suggest that faults S1-S5 comprise several faults superimposed. Clearer evidence for such multiple fault configurations can be found in Figs. 40(a) - (f) which show enlargements of the {1-100} and {11-20} images of one of the faults from region B indicated on Fig. 38(b) located in a area with a lower background dislocation density. The superimposition of a number of Shockley faults on different basal planes is discerned from the fact that the outer perimeters of the faults do not precisely superimpose, with fault sizes decreasing towards the micropipe, with the smaller faults closer to the micropipe appearing darker due to contrast overlap. Further evidence for this can be found in the enlargements shown in Figs. 40(d) and (f) (**g**={11-20}) where the Shockley partials delineating the perimeters of the faults are in contrast and have the appearance of approximately concentric loops of size increasing away from the vicinity of the micropipe which have been sequentially emitted from there. The fact that these partials are absent on Fig. 40(e) confirms through the application of the **g**.**b** criterion that the Burgers vector of the loops is 1/3[10-10], i.e., they are Shockley partial loops which bound Shockley faults with the same fault vector. In addition, in the same region various sets of approximately concentric basal plane half-loops can be seen emanating from the micropipe, for example as indicated by B1 and B2 on Figs. 40(d) - (f).

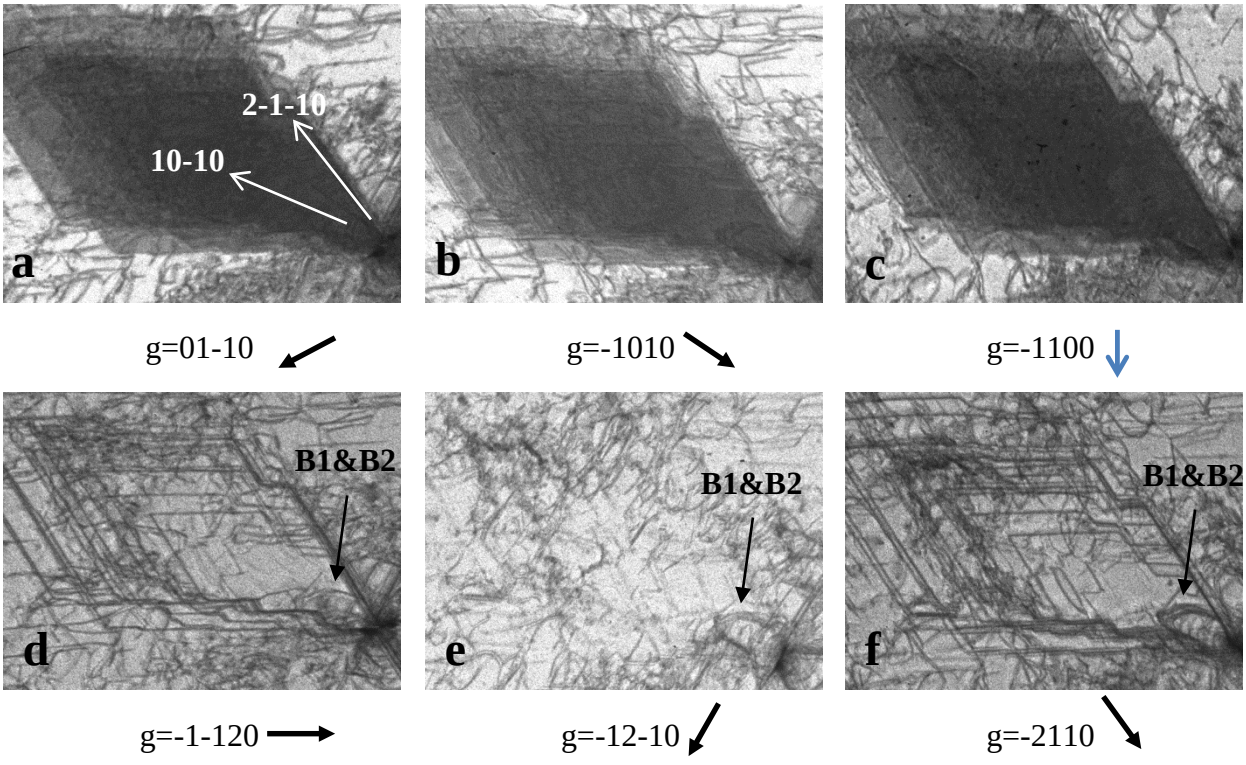

Figure 40 (a)-(c) Enlarged X-ray transmission topographs recorded from region B in Fig. 38(b). (a)-(c) {1-100} type reflections; (d)-(f) {11-20} type reflections where the stacking faults are not visible but dislocation lines bordering the faults are selectively visible. For this fault, the dislocations are out of contrast for g = -12-10 indicating that the Burgers vectors of the dislocations is 1/3[-1010].

Single rhombus-shaped Shockley faults have been previously observed to form during the forward bias of p-i-n diodes wherein the dissociation of basal plane dislocations (BPDs) is driven by electron-hole recombination which preferentially activates the motion of Si-core Shockley partials while leaving the C-core partials sessile [72]. However, the current observation is in a substrate crystal where no such driving force for BPD dissociation exists. Other observations of Shockley faults in SiC substrates result from macrostep overgrowth of threading dislocations with Burgers vectors of $c + a$ [69,97]. However, the morphology of such faults is quite different from those observed here. These unique Shockley fault configurations are only observed around micropipes when there is evidence for slip on both the primary basal and secondary prismatic slip systems originating from there. The X-ray topograph in Fig. 41(a) clearly reveals dislocation half loops belonging to both basal (indicated by B) and prismatic slip systems (indicated by P) emanating from the micropipe similar to those previously reported [98]. Such nucleation and expansion of slip bands takes place in the crystal boule whilst still in the growth chamber. When the boule is subsequently sliced into wafers, prismatic slip bands in a particular wafer can appear as a linear trail of threading edge dislocations (TEDs) or may comprise long screw or mixed component dislocations. Whatever their appearance, each prismatic slip band will exhibit weak contrast on one of the {1-100} reflections according to the **g**.**b** criterion for dislocations belonging to the 1/3<11-20>{1-100} slip system. On the other hand, as expected, the basal plane half-loops anchored to the micropipe are much more clearly identifiable as half-loops since the basal plane is only slightly inclined to the wafer surface (see Fig. 41(c)). In a similar way, the basal plane half-loops exhibit weak contrast on one of the {1-100} reflections according to the **g**.**b** criterion for dislocations belonging to the 1/3<11-20>{0001} slip system. In the background of Fig. 41(a) one can also observe the same kind of rhombus-shaped dislocation loops (indicated by D) in the vicinity of the micropipe as were shown in Figs. 40(d) and (f).

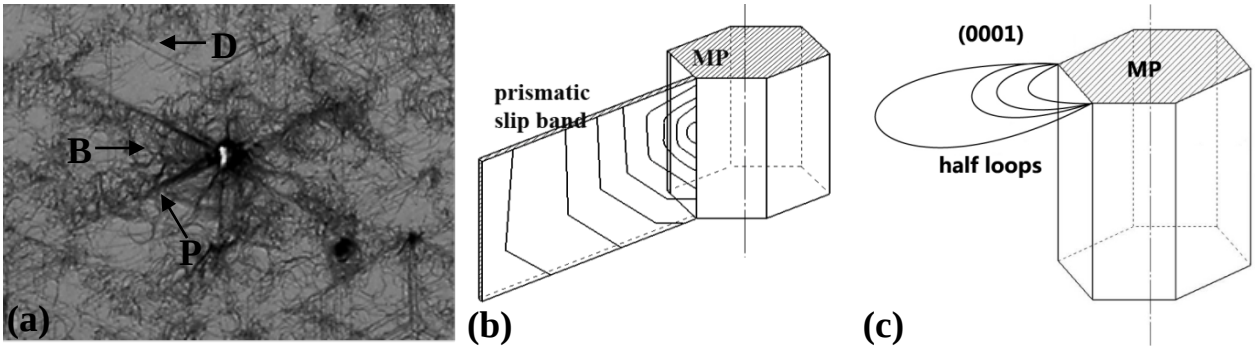

Figure 41 X-ray transmission topograph showing dislocation half loops are belonging to both basal (B) and prismatic slip systems (P) emanating from a micropipe. Prismatic slip appears as narrow bands aligned along the six {11-20} directions, corresponding to the traces of the 6 prismatic {1-100} planes on the wafer surface; Schematic representation of the nucleation of prismatic (b) and basal (c) dislocation half-loops from a micropipe showing pile up of prismatic dislocations.

While basal plane slip at micropipes has been fairly routinely observed [99,100], prismatic slip is relatively rarely observed [101,102]. Slip on both systems simultaneously would

seem to require rather special stress conditions. Micropipes also act as a stress concentrator raising locally the level of thermal shear stress to that required to activate both slip systems. However, even if both systems are activated, the strong preference for basal slip over prismatic slip means that dislocations from the prismatic system will have a tendency to cross-slip onto the basal plane whenever possible. This of course requires that a segment of dislocation on the prismatic plane adopt screw orientation such that its line direction lies along the intersection between the prismatic and basal plane allowing it to cross-slip onto the basal plane where it will dissociate into two 30° Shockley partials.

Now close to the micropipe core, the densities of both types of dislocations can be quite high and interactive forces can become quite large. Under such conditions, the interaction forces between Shockley partials associated with a cross-slipped segment of prismatic dislocation and those associated with a BPD on an adjacent basal plane can lead to pinning of one of the former partials [72]. Thus, under appropriate thermal shear stress, glide of the unpinned partial can lead to Shockley fault expansion. Further, the configuration of the Shockley partials on Fig. 40(d) and (f) resembles the kind of loop configuration generated by a double-ended Frank-Read source. Since the Shockley partials bounding Shockley faults are involved this would constitute a double-ended partial Frank-Read source as considered by Pirouz and Yang [88]. In their case, it was assumed that under the temperature conditions considered, the leading partial was more mobile than the trailing partial.

The First Possible Model

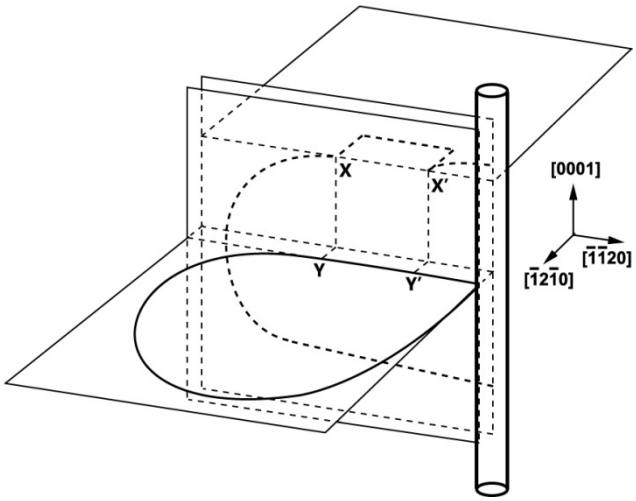

Figure 42 Schematic representation of cross slip of a prismatic screw dislocation segment XX' on to the basal plane which is then pinned by the Shockley partial, YY', associated with a BPD in an adjacent basal plane.

In our case we propose again that it is the interaction between a cross slipped segment of prismatic dislocation and a segment of basal plane dislocation that causes one of the partials associated with the cross-slipped segment of prismatic dislocation to become locked allowing the other partial to glide leaving a Shockley fault in its wake. Figure 42 shows a schematic representation of the situation hypothetically corresponding to the case shown in Fig 40. We assume that only a short segment of the prismatic dislocation was in screw orientation and was able to cross-slip and dissociate into two Shockley partials. The remainder of the prismatic dislocation lies on the prismatic plane so that the two ends of the screw segment are effectively pinned by their connections to the non-screw segments at X and X' (assuming that mobility of the prismatic dislocation segments are much lower than the cross-slipped basal segment). Based on the **g**.**R** and **g**.**b** analysis in Fig. 40, we know that the leading Shockley partial Burgers vector is 1/3 [10-10]. If the original screw

oriented prismatic dislocation was aligned along [11-20] then the Burgers vector of the trailing partial is 1/3[01-10]. If we assume that the trailing partial is pinned by a short segment of an opposite sign Shockley partial, YY', associated with the basal plane dislocation on an adjacent basal plane, then under thermal shear stress the leading partial will glide leaving a Shockley fault in its wake. This would require the Burgers vector of the basal loop to be 1/3[1-210] so that its Shockley components are 1/3[1-100] and 1/3[0-110] with the latter being opposite in sign to the trailing partial from the cross slipped dislocation.

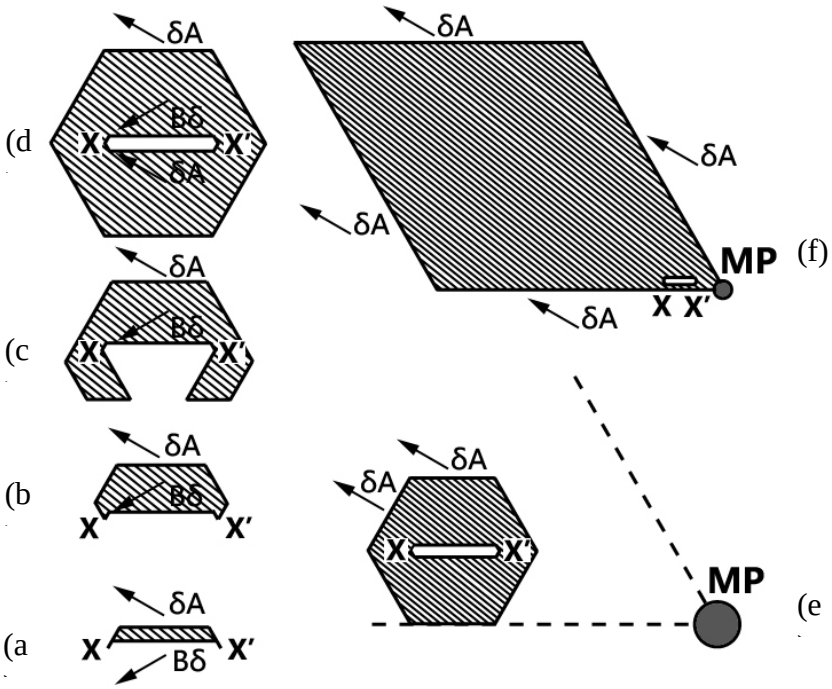

Figure 43 Schematic representation of the operation of a double-ended partial Frank-Read source: (a) Screw dislocation segment XX' with Burgers vector AB is dissociated into two 30º partials: AB → Aσ+σB; (b)-(e) Leading partial Aσ advances and rotates around pinning points XX' to form stacking fault loop. (f) The stacking fault expands form the rhombus shape observed.

Under this condition, the operation of the partial Frank-Read source can be described in the following way:

(i) Expansion of stacking fault: Using the bipyramid notation for HCP-type structures, the screw dislocation with Burgers vector AB is dissociated into two 30º partials: AB → Aσ+σB AB =½[11-20], Aσ=1/3[10-10]; σB=1/3[01-10]. The leading partial, Aσ, will begin to advance similar to the case for a regular Frank-Read source. The partial will rotate around its pinning points as shown in Fig. 43(a)-(c) until two opposite sign segments meet and annihilate leading to the situation shown in Fig. 43(d).

(ii) Cross-slip onto prism plane: At this point, the leading partial Aσ approaches the trailing partial, σB, from behind and cannot advance any further. This leads to an unsustainable stress build up, as described by Pirouz and Yang [88], and treated in detail by Escaig [103], which is relieved by cross-slip onto a prismatic plane. This requires a constriction of the original

dissociated dislocation. For compound semiconductors such as SiC, the order of the partials is reversed while on the {1-100} type cross-slip plane due to symmetry considerations [104] .

(iii) Double cross-slip back onto basal plane: Reversal of partials on the prism plane gives rise to a compressive stress between the partials that again provides a driving force for the dissociated screw dislocation to double-cross slip back onto the primary basal glide plane when the opportunity arises whereupon it will dissociate again into its Shockley components in their original order. This can only happen if the plane onto which the double-cross slip occurs can accommodate the glide of a Shockley partial without violating the stacking rules of the structure.

This is illustrated in Figure 44 which is a representation of how the stacking sequence of the 4H structure is modified by glide, cross slip, and double cross slip of a Shockley partial. The 4H-SiC structure comprises corner shared tetrahedra, and the stacking position of the tetrahedra can be represented by the letters A, B, C (where each letter indicates a double plane of the type Aα, Bβ, or Cγ) while their relative orientation is indicated by the absence or presence of a prime (a primed letter represents a tetrahedron in twinned orientation, rotated by 180° about the c-axis with respect to an untwinned one). Thus the furthest left column represents the stacking sequence of the 4H structure ABA'C'. If the plane upon which the pinned Shockley partial lies is just below row 1, then the leading 1/3[10-10] partial forms a faulted loop wherein the stacking position of layer 1 is converted from A to B' where the untwinned sheet of tetrahedra in stacking position A are sheared to a twinned sheet in position B, i.e., B'. Meanwhile the stacking position of all those layers above is also sheared (without affecting the orientation of those tetrahedra) so that the original ABA'C' stacking sequence of column 1 is transformed to B'CB'A'B. The horizontal arrow between columns 1 and 2 indicates the motion of the leading Shockley partial on the (0001) primary glide plane. Following this, cross slip of the leading partial occurs to the next available (0001) plane as indicated by the vertical arrow in column 2. The dislocation now dissociates again on the primary glide plane and forms a faulted loop in a similar way to before so that the stacking sequence is changed from B'CB'A'B to B'A'C'B'C.

The process then repeats so that the leading partial cross slips to the next (0001) plane as indicated by the vertical arrow in column 3. However, the next (0001) plane already comprises a layer of twinned tetrahedra, C'. This plane cannot admit the Shockley partial since not only is it already twinned (further shearing would produce an unacceptably high energy bonding configuration) but also it would be sheared to position A leading to a further violation of the stacking sequence (A / A type stacking). The cross slip process therefore continues until the Shockley encounters a basal plane onto which it can double-cross slip, i.e., a layer of untwinned tetrahedra. In Figure 44 this is plane number 5. In this way, it can be seen that the faulted loops are produced on two successive basal planes after which two planes are skipped since faulting on those planes would violate the stacking rules required for tetrahedral bonding. This faulting on three successive planes followed by cross-slip by two layers changes the structure from 4H to 3C.

(iv) Repetition of steps (i)-(iii): The whole process will continue until the attractive force exerted by the original basal plane dislocation diminishes to the point where the trailing partial is able to unlock itself at some point during one of the cycles of the source, or until the local driving force for any dislocation motion diminishes (perhaps through crystal cooling). At this point, the local phase transformation process effectively terminates.

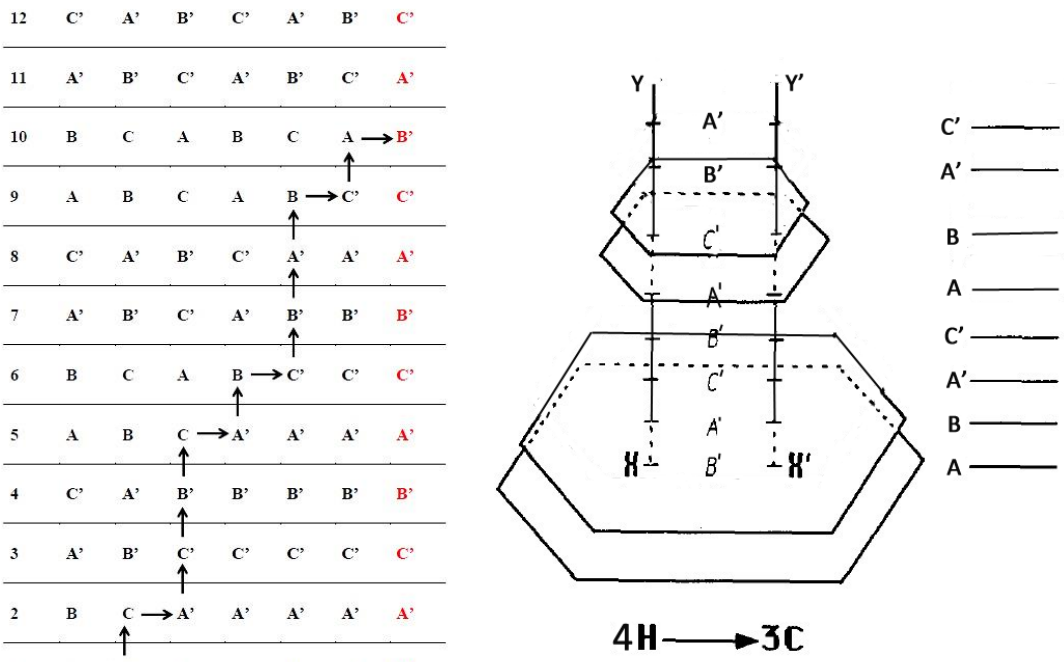

(a) (b)

Figure 44 (a) Modification of the stacking sequence of the 4H structure by glide, cross slip, and double cross slip of a Shockley partial as shown in Fig. 6 to form a 3C stacking sequence; (b) Illustration of the mechanism of transformation from 4H polytype to 3C polytype through the sequential formation of faulted loops followed by double-cross slip to the next plane.

As mentioned earlier, each of the sets of rhombus-shaped faults appears to be confined to the sectors defined by the intersections between two {1-100} type planes (with a dihedral angle of 60°) and the micropipe. There may be several contributory factors leading to this confinement. First, one might expect that the presence of prismatic slip bands along the six <11-20> directions would provide an effective barrier to the motion of the partial dislocations on the basal plane. As portrayed schematically in Fig. 43(f), it is assumed that the original cross-slipped prismatic dislocation segment is located close to the micropipe core. Such proximity to the micropipe, in addition to the barrier provided by the prismatic slip bands, is expected to make the expansion of the faulted loops appear somewhat asymmetric in that they are expected to pile up both at the micropipe core and up against the prismatic slip band, expanding more freely on the side remote from both the micropipe and the slip band. Second, the partial loops expand until their edges lie parallel to the <11-20> direction which appears to represent a low energy Peierls valley direction on the basal plane. Once the partials reach these low energy directions, further glide may be prohibitive.

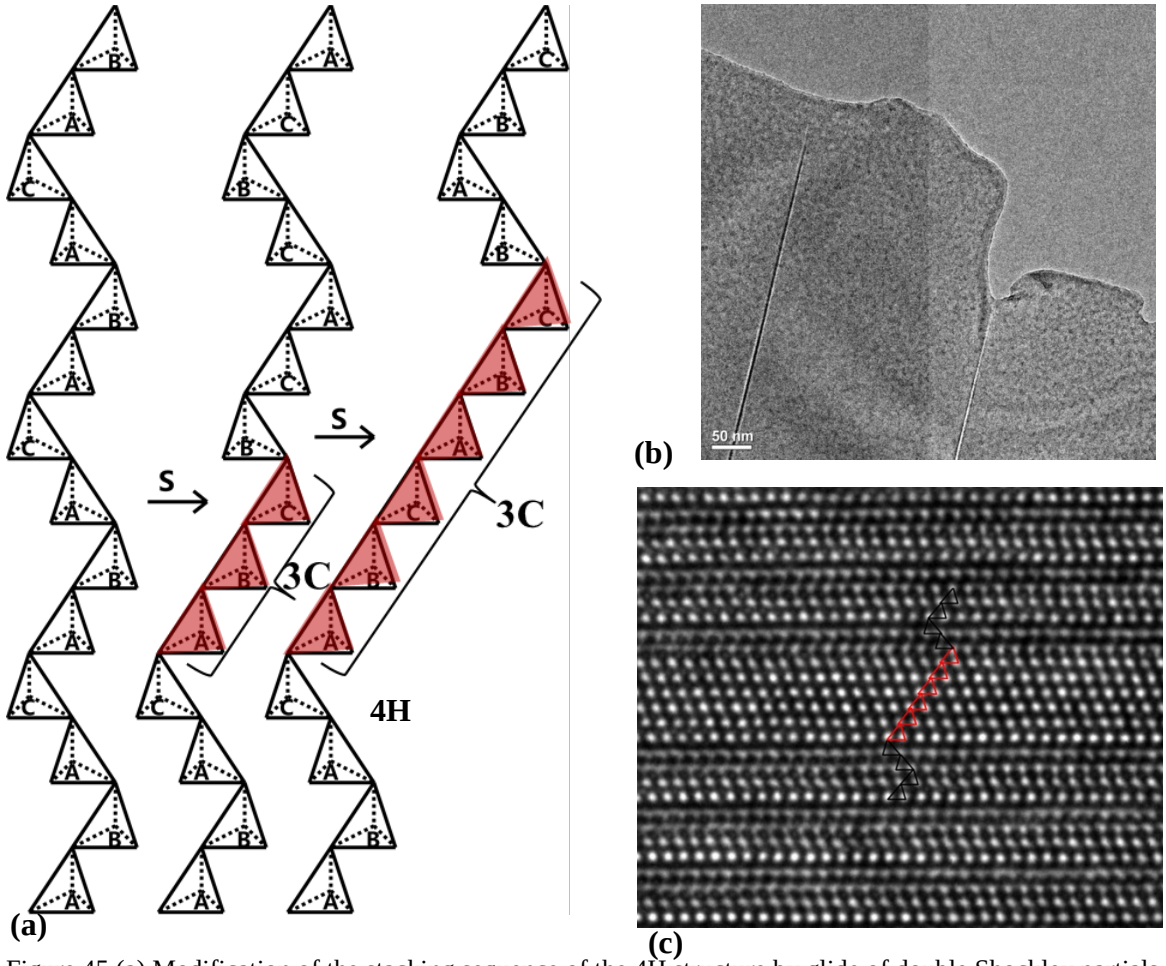

Figure 45 (a) Modification of the stacking sequence of the 4H structure by glide of double Shockley partials to form a six layer 3C stacking sequence; (b) TEM micrograph showing two double Shockley faults in low resolution. (c) HRTEM micrograph showing the predicted 3C stacking

High resolution transmission electron microscopy (HRTEM) micrographs recorded from the stacking faults show that the Shockley faults are actually double Shockley faults formed by the glide of double Shockley partials (see Fig. 45). The stacking sequence of the faults is effectively 3C indicating the early stage of 4H to 3C transformation. If a large number of such faults are closely placed in a small region, this region would effectively diffract as a 3C inclusion embedded in a 4H lattice. Such inclusions are in fact observed in regions of the wafer where this type of fault expansion occurs. Two examples of microscopic 3C inclusions anchored to micropipe cores are shown in Fig. 46. Fig. 46(a) and (d) are transmission images (g=10-11) recorded from regions showing a 3C inclusion while Figs. 46(b) and (c) and (e) and (f) are corresponding grazing incidence images (g=11-28) recorded from the two sides of the wafer. In both cases, part of the image is found to be missing on the images presented with those regions of crystal diffracting to a different position on the film. Selected area diffraction patterns recorded from these regions confirm the presence of 3C polytype. The fact that the inclusion can be observed on the grazing images from both sides of the crystal indicates that the inclusions run through the crystal thickness. In each case, the 3C inclusion is anchored to at least one micropipe (indicated by MP on Figs. 46 (b) and (c)), and rhombic-shaped faults can be observed in the same regions. It would appear therefore that in this case, the phase transformation process

initiated by the double-ended Frank-Read partial dislocation source has continued until the 3C inclusion becomes large enough to produce its own diffraction pattern.

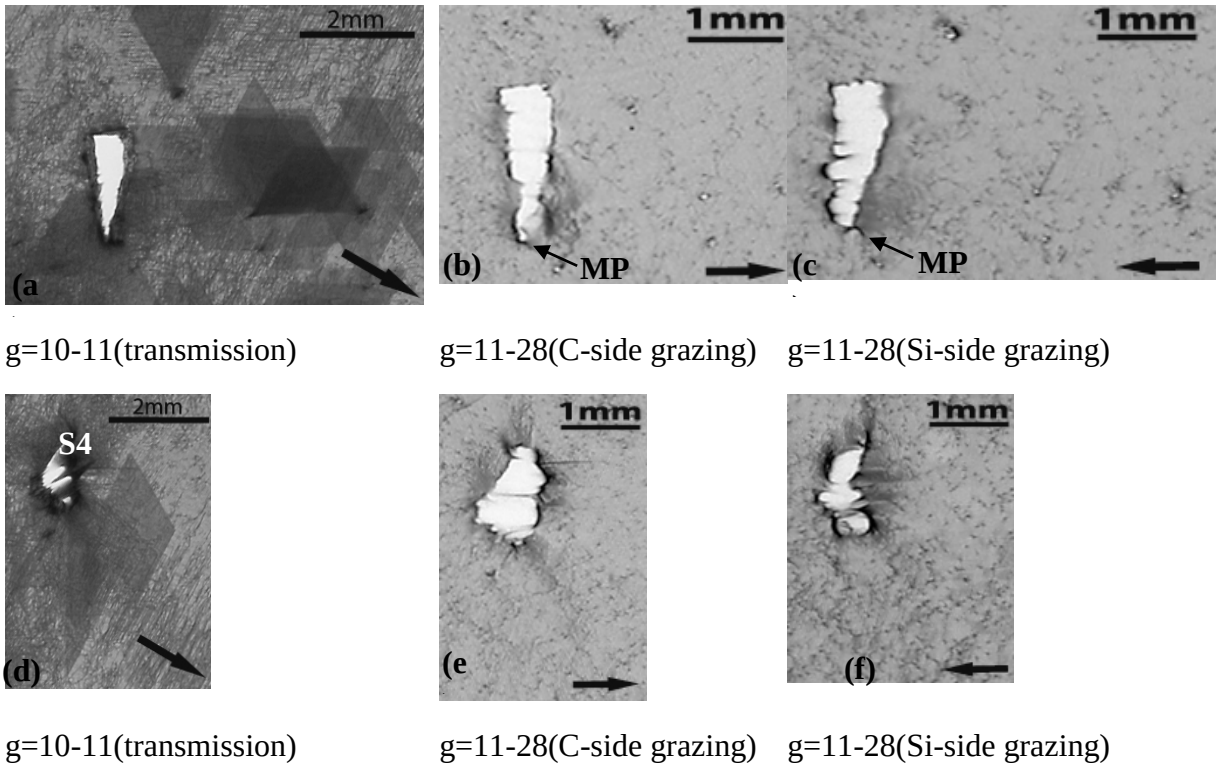

Figure 46 X-ray topographs from regions showing 3C inclusions. (a), (d) are transmission images (g=10-11); (b), (c) and (e), (f) are corresponding grazing incidence images (g=11-28) recorded from the two sides of the wafer. White contrast is the location of the 3C inclusion that diffracts to a different position on the X-ray film.

The Second Possible Model

High resolution transmission electron microscopy (HRTEM) image recorded from the rhombic-shape stacking faults shows that the Shockley faults are actually double Shockley faults (DSF) formed by the glide of two leading Shockley partials on adjacent (0001) planes (see Fig. 41) The observed stacking sequence is '22622'in Fig. 45(b), which can be formed due to the glide of double Shockley partial as schematically shown in Fig. 45(a). Pirouz *et al*. [105] has observed that in wafers used for Schottky Diodes (10^{16} cm^{-3} nitrogen doping in epilayer and $1.0 – 2.7 \times 10^{19}$ cm^{-3} in substrate), double Shockley Faults (DSFs) appeared only in those areas with the higher substrate doping concentration after normal device processing. Similar observation made previously by Skowronski *et al* [106] and Skromme *et al* [107]. It is claimed that the DSFs form due to the conduction band offset (0.7 eV) such that the stacking faults (quantum wells) to narrow energy bands in the bandgap [108] . These wells can accommodate electrons from the conduction band thus rendering its free energy lower. Thus when the donor doping in the crystal is high enough to raise the Fermi level to above the DSF level, a faulted 4H-SiC crystal can actually be more stable than a perfect unfaulted crystal, implying that there will be a built-in driving force for the formation of DSFs. DSFs also formed in highly doped specimens that were: (1) scratched and then annealed; (2) scratched, bent plastically at room

temperature and then annealed (550 ˚C for 30 minutes) – faults extend further in the bent sample [105]. However in our case, no obvious scratches are on the surface of the wafer and these unique DSF configurations are only observed around micropipes. The similarity between scratches and micropipes is that they both can act as a stress concentrator raising locally the level of thermal shear stress to that required for the nucleation of BPD loops. The BPD loop nucleation and expansion at micropipes has been fairly routinely observed [99,100]. The X-ray topography in Fig. 41(a) recorded from a normal wafer with regular nitrogen doping (5×10^{18} cm^{-3}) reveals dislocation half loops gliding on the basal plane emanating from the micropipe similar to those previously reported [98], and no staking faults are observed to associated with this micropipe . Such nucleation and expansion of slip bands takes place in the crystal boule whilst still in the growth chamber. Close look of Fig. 40(f), the perfect BPD loops are observed marked as "B1&B2".

In the second model, it is assumed that the partials are provided by the BPD half loops (composed by two partials with narrow faults band between them) nucleated from micropipes in the primary slip system <11-20>{0001}. Because the wafer with observation of star faults is heavily doped ($>10^{19}cm^{-3}$), the Fermi level is higher than DSF level, which will promote the glide of leading partial, while the sessile partial is immobile. Now close to the micropipe core, the densities of basal plane dislocations can be quite large distributing at different layers. Therefore, leading partials are available at different layers along the micropipe, and their glide would cause multiple rhombic-shape stacking faults overlapping with each other in one direction as shown in Fig. 40. The nucleation of BPD loops from micropipe are three-axis symmetrical expanding towards <1-100> directions, which will result six star faults pattern as shown in Fig. 39 and Fig. 40.

7.5 Conclusion

A possible model for the expansion of rhombic-shaped Shockley type stacking faults bounded by Shockley partial dislocations has been presented which involves the operation of a double-ended Frank-Read partial dislocation source. The Shockley partials are postulated to dissociate from a segment of a prismatic dislocation which has cross-slipped onto the basal plane. The trailing partial of this cross-slipped segment is locked in position by the force exerted by an opposite sign Shockley present in a nearby segment of BPD. This enables the leading partial to expand leaving a double Shockley fault in its wake. Subsequently, the glide and cross-slip of the leading partial leads to a local transformation from 4H to 3C polytype via the mechanism postulated by Pirouz and Yang [69]. In the limit, this process leads to the formation of microscopic 3C inclusions which are large enough to diffract independently. The second possible model for the formation of rhombic-shape double Shockley faults is by the leading partials provided by the dissociation of basal plane half-loops nucleated from micropipes. More studies are required to analysis the origins of double-Shockley partials.

8. Prismatic Slip and Cross-Slip Behavior of Threading Edge Dislocations

8.1 Outline

X-ray Topography and KOH etching were employed to study of prismatic slip and cross-slip of threading edge dislocations. In X-ray topography, it is observed that dislocation slip emanates from the micropipes in the form of slipbands along <11-20> directions. These bands mainly comprise screw type dislocations of the 1/3<11-20> type. After KOH etching, rows of etch pits corresponding to dislocation arrays were also observed in vicinity of micropipes. In the early stages, the arrays consist of threading edge dislocations and later on, more and more BPD etch pits are observed mixing with the TED etch pits. The dislocation configurations in the slip bands are interpreted as initial prismatic slip of TEDs on <11-20> {-1100} of the hexagonal SiC structure during the growth process and when certain segments of TED loop adopt screw-orientation they cross-slip onto primary slip system. <11-20>{0001}.

8.2 Introduction

Glide of many dislocations result in slip when plastic deformation of crystals occurs. In close-packed hexagonal crystals, the basal plane is the most widely spaced and close packed, and the shortest lattice directions are 1/3<11-20>; therefore slip often occurs on the (0001) basal plane in directions of <1-210>, which is the most favorable and commonly observed one called the Primary Slip system. Some hexagonal materials with low c/a lattice parameter ratios exhibit glide on other planes: the Prismatic Slip system <1-210> {1-100} or < 1-210> {11-20} and the Pyramidal Slip system <1-210> {10-11} or <1-210> {11-22}. When the lattice parameter ratios c/a of hexagonal materials are high, then the basal slip preferred [109]; when c/a ratios are low, dislocation gliding on other slip systems (prismatic or pyramidal) are observed for 4H-SiC, c/a=10.05/3.08=3.26, which is relative higher, thus the primary slip system 1/3<11-20>{0001} is the most commonly observed when hexagonal SiC is subjected to mechanical deformation [70,110,111] **.** This chapter will talk about identification of the Prismatic Slip of threading edge dislocations in PVT-grown 4H-SiC substrate. Understanding the different slip system in SiC crystals is very important to interpret the plastic behavior of 4H-SiC crystals under the action of stress.

8.3 Result and Discussion

The primary slip system <11-20> (0001) is the most common one observed in 4H-SiC, which is caused by the resolved shear stress in the (0001) glide plane provided by ‘excess thermoplastic stresses during growth’ which can reach 55 MPa at some points in a PVT boule [112], while the critical shear stress for the glide of basal plane dislocation at PVT growth temperature is estimated around 1MP [14]. In that way, basal plane dislocations will be multiplied and its density gets larger. The activation energy for the second slip is more difficult, but it has been experimentally observed by Ha *et al.* using TEM and KOH etching [101]. He observed rows of TED etch pits extending along <11-20> directions, which was interpreted as slip bands formed by TED glide in the prismatic slip system <11-20> {-1100} of 4H-SiC during post-growth cooling. However, there was no direct observation of TED loops gliding on prismatic plane from cross-section sample.

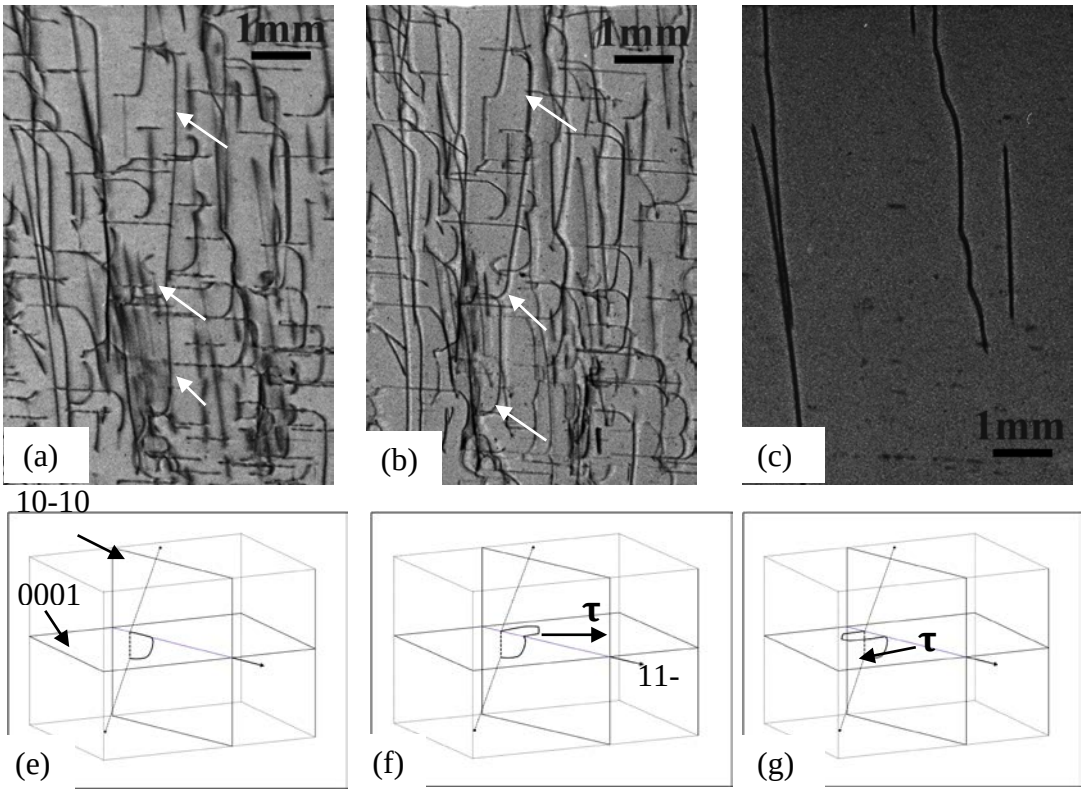

Figure 47 (a)-(c) SWBXT transmission images of axial slices recorded at various diffraction vector (a) g=01-10 (b) -12-10 (c) 0004. (e)- (f) Schematic mechanism of cross slip of threading edge dislocation. (f) and (g) threading edge dislocation cross glide in opposite directions due to the direction of shear stress

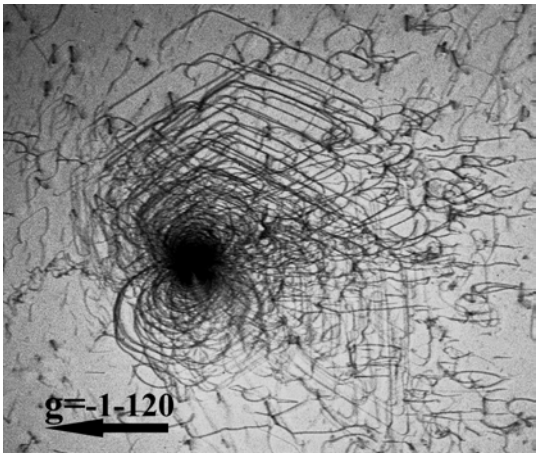

Fig. 48 Analysis of basal plane dislocations: Dislocation morphology consists of concentric loops and pile-ups, indicating that they were clearly generated through deformation processes. This occurs at crystal edge and at micropipes under the action of thermal stress.

In our experiments, 4H-SiC axial slices were cut along [0001] growth direction from the boule. The side plane of the axial slice is <11-20> direction and thickness is around 300 μm. Then the axial slices were recorded in transmission-geometry of X-ray topographs with different diffraction g vectors as shown in Fig. 47. It is observed that TEDs are not straight linear feature as it expected to be, all of them are curved and bowing towards one direction, which indicates the gliding of TEDs. According to $\boldsymbol{g} \cdot \boldsymbol{b}$ analysis, TEDs with Burgers vector <1-100> should be invisible at g=0004. In Fig. 46(c), only four linear features visible at g=0004 are TSDs, while all TEDs are invisible. From above it is known that threading edge dislocations can glide on prismatic plane {10-10}. However, slip on the prismatic plane is less energy favorable compared with the primary slip system <11-20> (0001). So when some segment of TEDs attain screw orientation, this segment will cross slip

onto the basal plane and start the primary slip as schematic shown in Fig. 47(e)-(g). Depending on the direction of shear stress, the cross slip will glide in different direction.

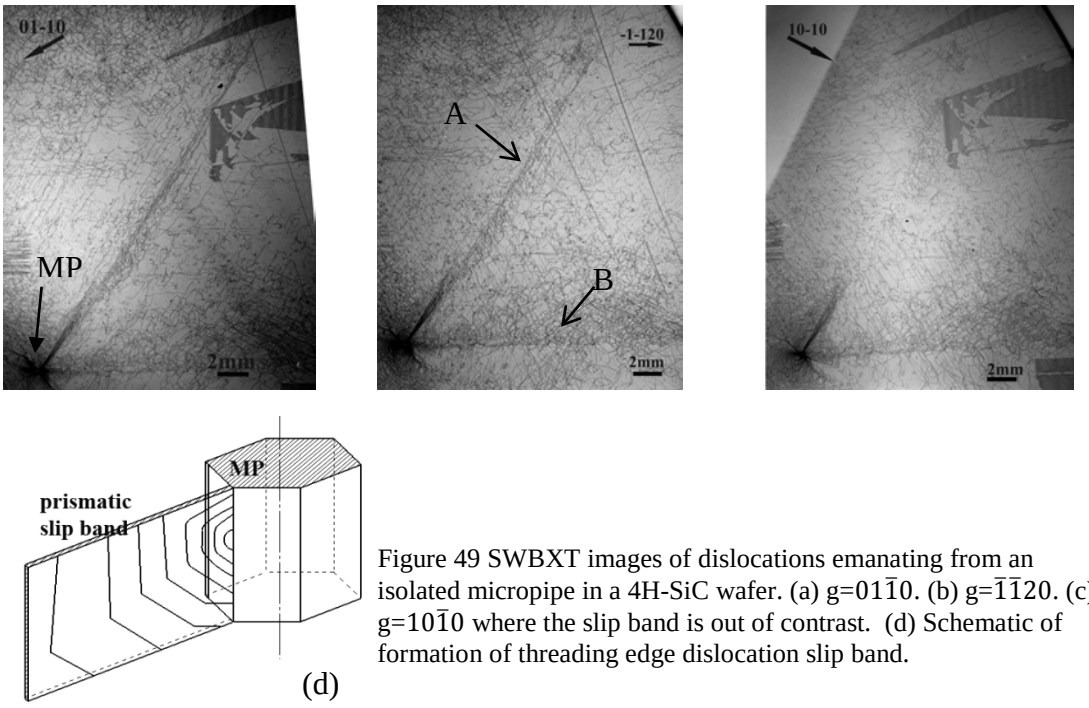

Figure 49 SWBXT images of dislocations emanating from an isolated micropipe in a 4H-SiC wafer. (a) g=$01\bar{1}0$. (b) g=$\bar{1}\bar{1}20$. (c) g=$10\bar{1}0$ where the slip band is out of contrast. (d) Schematic of formation of threading edge dislocation slip band.

Vetter *et al.* [113] has observed complex aggregation of concentric BPD loops and pile-ups looping outwards from the micropipes in plane-view geometry, as that is where their lines are often seen to terminate, indicating that micropipes was involved in the generation of BPD loops, acting as stress concentrators for basal plane slip during crystal growth. Most time, the generation of BPDs loops from micropipes is observed in 4H-SiC wafers as shown in Fig. 48. However, it is also observed that two dislocation long slip bands 'A' and 'B' emitted from the micropipe in Fig. 49 expanding along [-12-10] and [11-20] directions. Slip Band 'A' is out of contrast at g=10-10, when g vector direction is perpendicular to the slip band direction. According to $\mathbf{g} \cdot \mathbf{b}$ analysis, the Burgers vector of these dislocations composing into slip bands is 1/3[1-210], and these dislocations are screw-type. In order to interpret the slip band, two adjacent wafers sliced from the same SiC ingot are etched by melted KOH in Fig. 50. The largest pits (20~30 μm) in hexagonal shape in the bottom-right corner are corresponding to micropipes. Medium (10~20 μm) hexagonal-shape etch pits represent threading screw dislocations, while the smallest hexagonal-shape etch pits are threading edge dislocations. The BPD etch pits are shell-like shape, having similar size to that of threading edge dislocations. At the same position on the two wafers, rows of etch pits corresponding to dislocation arrays are observed in the vicinity of the same micropipe. The wafer in Fig. 50(a) is closer to the seed, where the slip band is composed by many TEDs along <11-20> direction (see the enlargement in Fig. 50(a)), while the slip band is composed by the mixture of TEDs and BPDs etch pits (see the enlargement in Fig. 50 (b)). Also the width of the arrays gets narrower as it is away from the micropipe. It can be concluded that at the earlier stage, TED loops emanate from the micropipe as schematic shown in Fig. 48 (d). Although the activation of prismatic slip system is difficult, micropipes act as a

stress concentrator raising locally the level of thermal shear stress to that required to activate both slip systems. As a result, TED loops nucleate from the micropipe starts to glide along <11-20> direction in prismatic plane {0001}. As the growth continues, TED loops will glide further away from the micropipes. When some segments of TED loops adopt screw orientation, they will cross-slip onto primary slip plane (0001) which requires less thermal stress for dislocation gliding. As a result, more BPD etch pits are observed in the later-growth wafer.

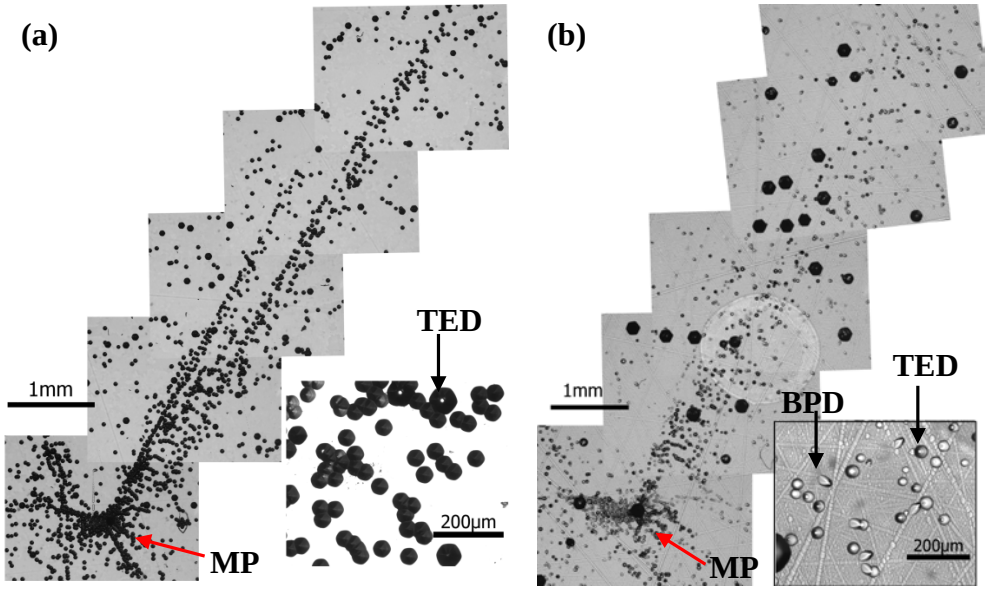

Figure 50 (a)-(b) etch pit patterns recorded at different wafers sliced from the same SiC ingot. The micropipes in (a) and (b) can be called the same one, as they locate at the same position on these two parallel wafer. Wafer (a) is closer to the seed than wafer (b).

8.4 Conclusion

Prismatic slip of threading edge dislocations directly observed in axial slices, as most of the threading dislocations are not straight along [0001] direction, but curved towards the same direction. In the plane-view wafers, prismatic slip of threading edge dislocations are observed in the vicinity of micropipes. Slip bands formed by glide of threading edge dislocation in the prismatic slip system <11-20> {-1100} during growth is observed. Some segments of TED loops adopt screw-orientation and then they will be able to cross-slip back to basal plane in the later growth stage.

9. SiC Homoepitaxy on Off-cut (0001) Substrates

9.1 SiC Epitaxial Growth Processes

Although the quality of 4H-SiC substrate has been improved dramatically in the last 20 years, there are still a considerable number of dislocations (such as TSDs, BPDs, and TEDs) still jeopardizing the operation of devices. Especially, BPDs composed of pairs of Shockley partials will generate stacking faults caused by electron-hole recombination [72]. Usually, most SiC devices are not fabricated on PVT-grown substrate directly, but are instead fabricated on SiC epitaxial layers which have much lower BPD densities and superior electrical properties. Researchers have worked on different substrates for SiC epitaxial growth based on the availability, lattice mismatch and device requirement, such as Si [114] , sapphire [115] and TiC [116]. As larger size of (0001)-oriented SiC substrate becomes commercially available and cheaper price, SiC substrate has been chose to grow SiC homoepitaxy. Typically, Si face of SiC substrate is employed to grown SiC epilayer, since epilayer surface morphology is better compared with C face growth. In 4H-SiC homoepitaxial growth, the nitrogen doping in substrate is around 10^{19}~10^{18} cm^{-3}, while the epilayer has much lower nitrogen doping which is around 10^{14}~10^{15} cm^{-3} which varies based on the requirements of customers.

There are numerous growth methods studied for SiC epitaxial growth, which include atmospheric pressure chemical vapor deposition (APCVD), molecular-beam epitaxy, metalorganic CVD and liquid-phrase epitaxy. Among those growth methodologies, CVD growth technique is generally accepted as the most promising method for growing high quality, more controllable and mass production of SiC epitaxy. Conventional SiC CVD epitaxial growth processes employ Silane (SiH_4) and Propane (C_3H_8) as precursors which provide Si and C sources separately with a large amount of H_2 carrier gas carried out at temperature up to between 1200 to 1800 ℃, pressure varying from several tens of Torr to atmosphere [117-119].

Table 9 The comparison of different SiC epitaxy growth

Growth method	Description	Advantage	Disadvantage
Liquid-phase Epitaxy (LPE)	Substrate fixed on a graphite holder and heated up to between 1000 and 2000 ℃ , dip into Si-based melt, C source provide by crucible [120,121]	Micropipe closing efficiency up to 80% ; higher growth rate (ranging from several μm/h to mm/h) [122]	Accurate control of thermal equilibrium condition required; difficult to control the doping concentration; rough surface morphology
Molecular-beam Epitaxy (MBE)	Two electron guns for evaporating Si and C separately from high-purity poly-crystalline silicon and graphite; gaseous elements then condense on the seed [123,124];	Low growth temperature (<1000); used for growing SiC on Si; the clean growth ambient;	Low growth rate (several nm/h); thin epitaxial layer deposition; not good for thick epilayers required by high-voltage power devices
Chemical Vapor	Heating SiC substrates in a chamber ‘reactor’ with flowing silicon- and carbon- containing gases	Precise control of epilayer thickness and impurity	Carefully control of C/Si ratio; use of high-purity

Deposition (CVD)	that decompose and deposit Si and C onto the wafer allowing an epilayer to grow in a well-ordered single-crystal fashion under well-controlled condition	doping; reasonable growth rate (a few μm/h); good surface morphology	chemicals such as silane and propane required

For SiC CVD epitaxial growth, a variety of reactor configurations have been developed for the last 30 years. For example, reactors can be divided into horizontal [125,126] and vertical [127,128] configurations based on the flow direction of reactant gases; they can also be divided into 'hot-wall' or 'warm wall' [125,126] and 'cold-wall' [129] configurations due to the surrounding heating design difference. Most reactors need to rotate the susceptor and attached samples at up to 100 rpm to ensure high uniformity of epilayer parameters across the wafer. There are reports of growing high quality 4H-SiC homoepitaxial layer at growth rate 2-5 μm/h employing horizontal cold wall [130], horizontal hot-wall [131] and planetary CVD reactors [132,133]. Vertical hot-wall reactor has been used for the purpose of growing thick epitaxial layers for high-power application.

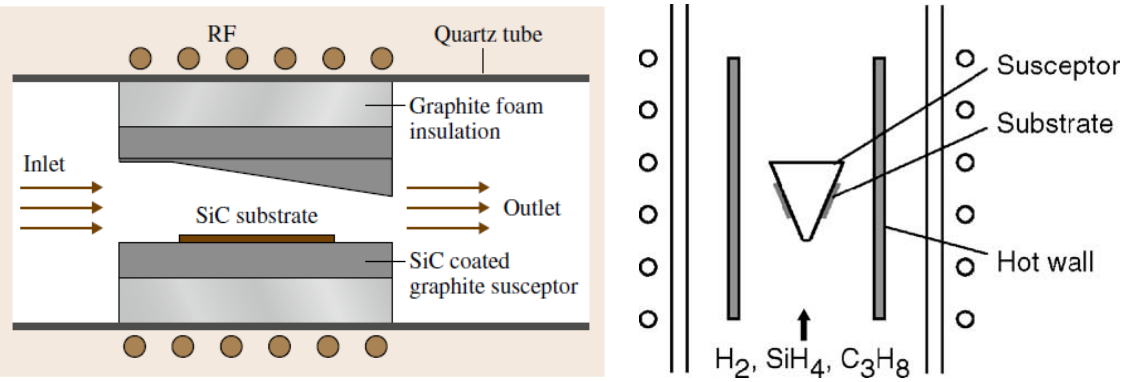

Figure 51 Schematic of typical horizontal hotwall SiC CVD reactor ; (b) typical vertical hotwall SiC CVD reactor [134].

Fig. 51(a) shows the schematic of typical horizontal hotwall SiC CVD reactor. H_2 gas carry the precursors in a fixed C/Si ratio and transport them from left side of the reactor, depositing the C and Si atoms onto the substrate, and the excess precursors coming out of the right side. Fig. 51(b) is the schematic of typical vertical hotwall SiC CVD reactor. The growth temperature can be around 1500~1700℃, SiH_4 (10~24 sccm) and C_3H_8 (3~11 sccm) were used as a precursor gases with a C/Si ratio of 0.6~1.3 and Pd-cell purified H_2 (3~10 slm) as a carrier gas at a reactor pressure of 100~165 Torr [135].

Things to consider when growing epitaxial layer:

(1) Growth rate. Depend strongly on reactor pressure and growth temperature. Growth rate is found to be the highest under reduced pressure as low as 50-70 mbar [134]. In order to reduce the production cost, fast CVD epitaxial growth techniques have been demonstrated by reducing system pressure using an $H_2 + SiH_4 + C_3H_8$ [136,137] or adding HCl to the gas system [138] or using Cl-containing source gas [139]. SiC homoepitaxial growth rate up to 90

μm/h has been reported by Lu *et al* [140] by using methyltrichlorosilane (MTS) as the precursor in chemical vapor deposition. Meanwhile, the incorporation of HCl or Cl-containing source gas has no significant difference in terms of defects, doping and thickness uniformity compared with the standard process without adding them in.

(2) Crystal structure and defect density. Low BPD density, good control of polytypes and misfit dislocations are strongly relying on growth temperature and the flow rate of propane for a given rate.

(3) Surface roughness. C/Si ratio is too small, resulting in a wavy surface; too higher resulting in macro step bunching.

(4) Epilayer thickness uniformity especially for large thickness growth.

(5) Doping uniformity. Nitrogen doping can be controlled by the flow rate of N_2.

9.1.1 Step- Control Epitaxy and Substrate Surface Preparation

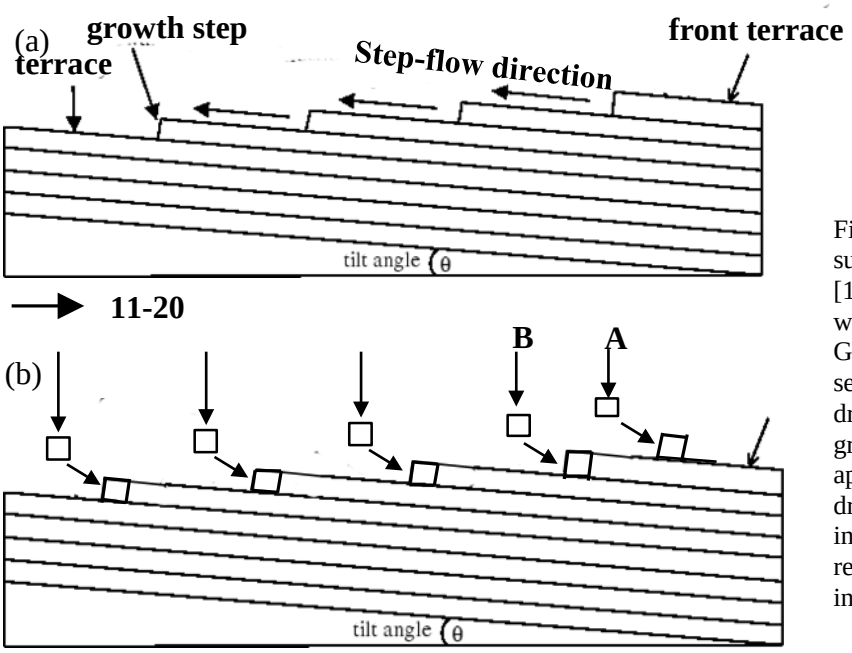

Figure 52 Schematic show a substrate surface with 4 degree off cut along [11-20] direction, resulting a surface with terraces and growth steps. Growth steps contain the stacking sequence information. (b) Atom 'A' drop onto front terrace which has no growth step ahead resulting the appearance of 3C polytype. Atom 'B' drop onto other terraces and is incorporated into step risers replicating the stacking sequence information of 4H-SiC.

As mentioned above, the best way to grow high-quality SiC film is homoepitaxial growth which can avoid the large lattice mismatch between the epilayer and substrate. One of the biggest problems when grow on-axis 4H/6H-SiC epitaxy is 2D nucleation of big triangle defects, which are identified as 3C polytypes. The reason is because 3C is the most stable polytype for SiC when the temperature below 1800 ℃ [141] while the reaction temperature for 4H/6H-SiC homoepitaxy growth is between 1400-1600 ℃. In order to keep the epilayer having the same stacking sequence as the substrate, a technique called 'step-controlled' epitaxy has been developed since 1987 [142], in which case a substrate are polished at a certain angle 4 or 8 degree off (0001) plane[130,143], resulting a surface with numerous terraces and atomic steps, and those steps can reflect the stacking sequence of substrate as shown in Fig. 52. When there is a sufficient short distance between steps (terraces smaller enough), carbon and silicon atoms will migrate on the surface and get to the atomic steps which have lower surface potentials, and then

bond with the adjacent atoms, as a result atoms are incorporated into the step riser. Since the steps contain the information of the stacking sequence, the stacking sequence is transferred to the growing layer. But when the supersaturation is very high, spontaneous 2D nucleation can also happen on the bigger terraces. Recently, great efforts have been put to reduce the off-cut angle, since it can reduce the crystal waste while slicing wafers from the ingot and reduce the density of basal plane dislocations replicated from substrate into epilayer [144]. It is also reported that the off-cut angle can influence the anisotropy of the MOS channel characteristics in the case of a trench MOSFET [145]. At present, 4 degree off-axis substrates are generally used in commercially. However, as the diameter of 4H-SiC wafers has reached 150 mm, even more wafer waste resulting from the slicing (0001) plane wafers in off-cut angle from an ingot will be produced. Meanwhile, step bunching becomes a serious problem when decreasing the off-cut angle. Therefore, the growth of 2^o off-cut 4H-SiC homoepitaxial layers has been studied by several groups [144,146-149] and the surface morphology has been significantly improved [149].

The surface quality is also very important for SiC homoepitaxial growth. Prior to Epitaxial growth, SiC substrates are prepared by chemical-mechanical polishing (CMP), which can achieve mirror-like surface and excellent surface roughness [150]. In a typical CMP process, a chemical modified surface is formed when the chemical interacts with the materials surface, and then, the abrasives will mechanically interact and removal the chemically modified surface. However, the residual surface damage caused from polishing is still exiting. Then in-situ etching by the hydrogen carrier gas or mix of hydrogen with hydrogen chloride (HCl) has been investigated for many year [151,152]. This in-situ etching is usually carried out at the growth temperature inside the growth chamber before the epilayer growth to further eliminate surface contamination and thin layers damaged during polishing. In situ H_2 etching was performed at 1400℃, 40 mbar for 30-45 min in typical. Sometimes, a short amount of hydrogen Chloride (HCl) added into the hydrogen carrier during the in-situ etching can further improve the surface quality. Meanwhile, the etched threading screw dislocation can provide a continual spiral steps which provide more sites for atomic vicinal growth.

9.2 Dislocation Replication during Off-axis Homoepitaxial Growth

When the defects, such as low angle grain boundaries composed by close packed TEDs, threading screw dislocations, threading edge dislocations and screw-oriented basal plane dislocations pierce through the Si face of 4H-SiC substrate, they will be kept their own characters, threading into epilayer during epitaxial growth. Compared with on-axis growth, basal plane dislocations are parallel to the interface, thus they cannot propagate into epilayer. Each type of extended defects has different influence on the device performance, and BPD is one of them researchers having paid most attention on. The dissociate of BPS partials resulting the formation of Shockley faults can lead to lifetime limiting forward voltage drops [153], while TEDs are less-harmful during device operation. Various strategies have been developed to convert BPDs into TEDs during device operation and the details will be explained below.

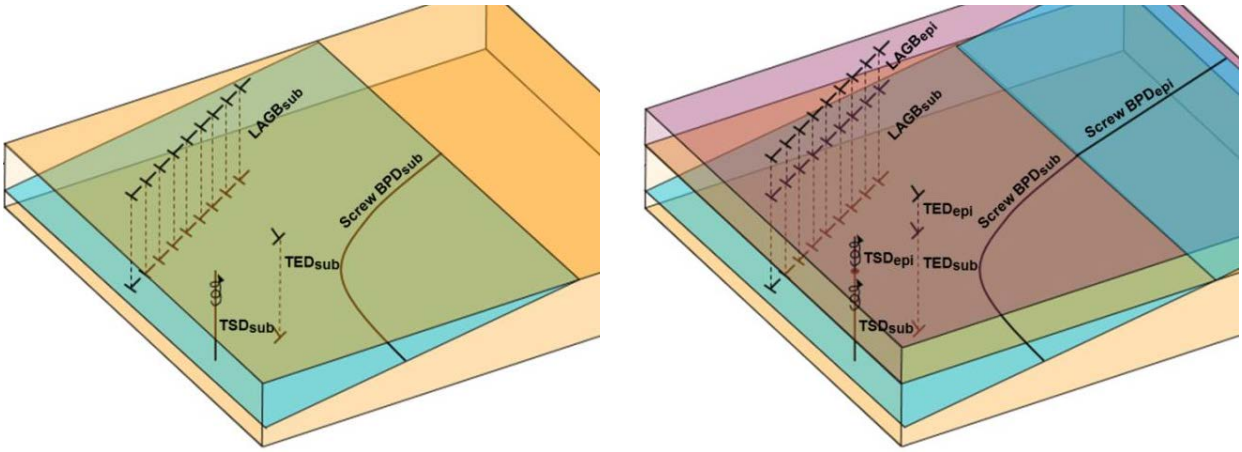

Figure 53 Schematic shows how defects (low angle grain boundaries, threading screw dislocations, threading edge dislocations, screw-oriented basal plane dislocation) are replicated from substrate into epilayer.

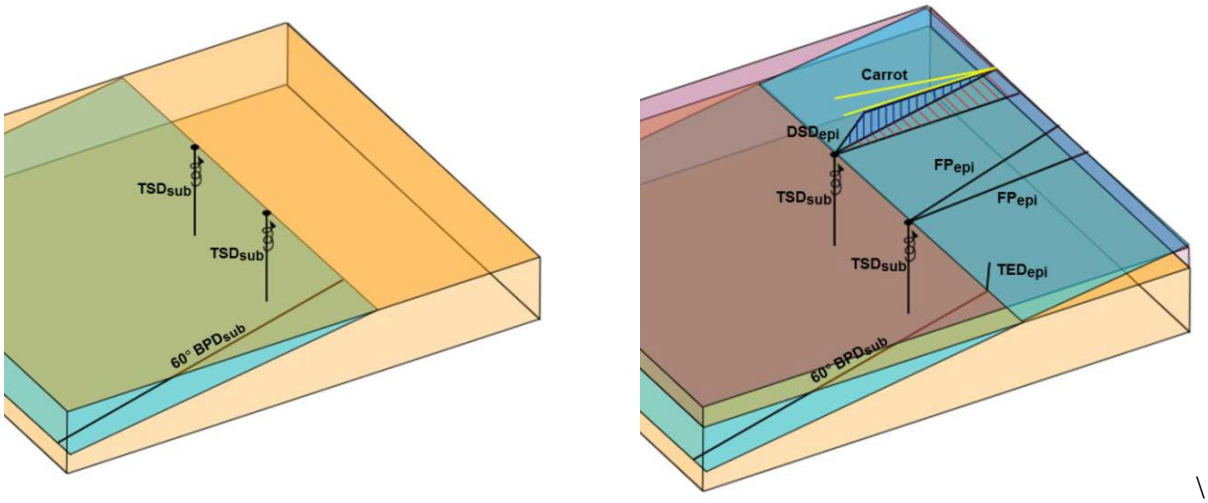

Figure 54 Schematic shows threading screw dislocations and non-screw oriented basal plane dislocations can be converted into other defects during epitaxial growth.

One way to reduce the threading dislocations is to convert them into basal plane defects, while the conversion phenomenon of TSDs to Frank partial dislocations has been reported [154,155]. It was also reported that the deflection of TSD in epilayer could produce carrots

defects which were associated with a Frank-type fault on the basal plane connected to a prismatic fault[156]. The carrot defects can degrade device performance by increasing the reverse leakage current of 4H-SiC Schottky and *p-i-n* junction diodes[54,157]. Both the Frank stacking faults and carrots defects have even worse influence on device. Thus the only way to eliminate TSDs is to optimize the PVT growth of substrate to get lower TSD density in substrate.

9.2.1 Conversion of BPDs into TEDs

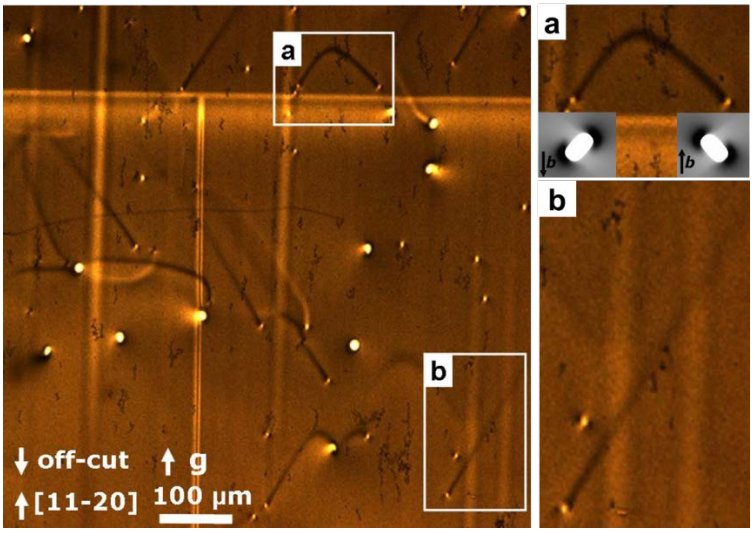

Figure 55 SMBXT image showing the conversion of BPDs into TEDs after 4H-SiC homoepitaxial growth.(a) BPD half-loop have two surface intersections with the interface which convert into two opposite-sign TEDs as shown in the magnified picture (b) straight BPD convert into TED in its downstep direction.

It is well known that basal plane dislocations (BPDs) that are replicated from Physical Vapor Transport (PVT) grown 4H-SiC substrates into Chemical Vapor Deposition (CVD) grown homoepitaxial layers can have a detrimental effect on device performance [158-160] by inducing the expansion of Shockley faults in the epilayer which can cause forward voltage drop. As a result, significant advances have also been made in engineering the processes by which BPDs are replicated into the epilayer. For example, the conversion of BPDs into less harmful threading edge dislocations (TEDs) at the substrate/epi interface can be enhanced by direct KOH etching of the substrate surface intersections of the BPDs [161,162] or by growth interrupts which induce etching [163]. Conversion rates of up to 99% have been reported [164,165]. Fig. 55 is monochromatic x-ray beam topography with grazing geometry g=11-28 recorded on 4H-SiC homoepitaxial layer.. Since the penetration depth of grazing image is larger than the epilayer thickness, the information of dislocation behavior at the interface has been revealed. The dark (sometimes white) linear features are basal plane dislocation, all being converted into TED based on the evidence that TEDs are attached at their ends along the downstep direction. In enlarged area ‘a’, both ends of the curved BPD half-loop get converted into TEDs at the interface. Since these two ends have opposite line direction, but the same Burgers vector, the converted TEDs are of opposite signs, which match well with the simulation result.

Zhang *et al* [161] studied the mechanism why the creation of BPD etches pits before epitaxial growth could enhance the conversion of BPDs into TEDs in epilayer. He used AFM to study the BPD etch pits and found out that the growth steps got curved when they tried to cover up the BPD etch pits during CVD growth. There was not only the usual step-flow growth in the down-step direction, the lateral growth from curved sides of the steps perpendicular to the step-

flow direction also happened. If the lateral growth was dominant, the two sides of the curved step will come closer and merge, forming a perfect crystal in front of BPD which is corresponding to Fig. 56. As a result, the path for the BPDs to propagate into epilayer was blocked and BPDs got converted into TEDs in order to keep Burgers vector conservation. In conclusion, BPDs will be converted into TEDs if lateral growth dominates. On the other hand, they will be propagated into epilayer if step-flow growth dominates.

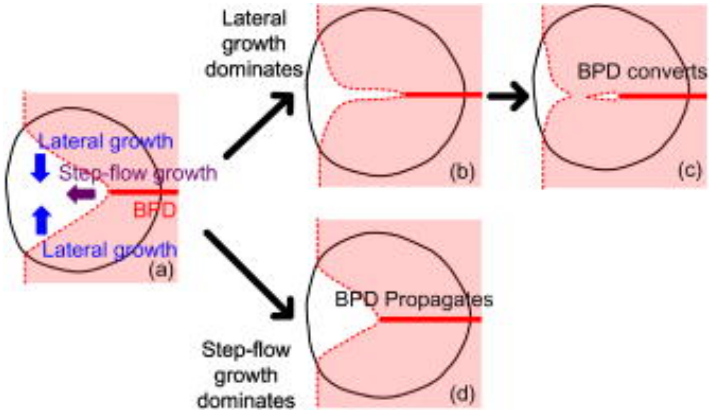

Figure 56 schematics of (a) after KOH etch on Si face, BPD line attached with one etch pit on the surface. Two growth directions (lateral and step-flow directions) can happen to fill the etch pit; (b) and (c) evolution of the basal plane during epitaxy if lateral growth dominates, and (d) evolution of the basal plane during epitaxy if step-flow growth dominates[161].

9.3 Introduction of Interfacial Dislocation

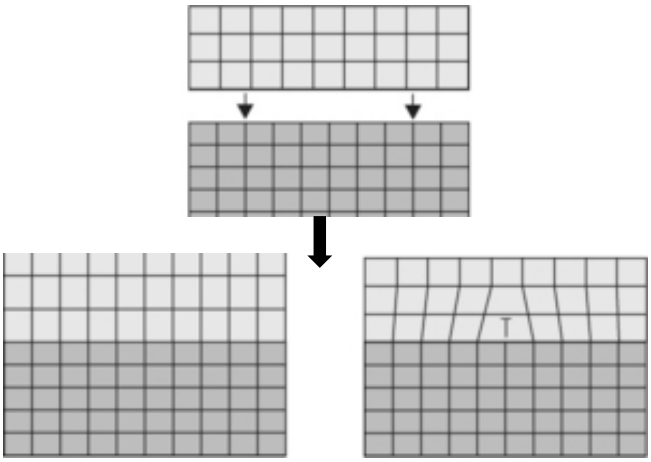

Figure 57 Schematic shows the different lattice parameters due to the nitrogen doping difference in substrate and epilayer, which leads to the formation of misfit dislocation with extra half plane in the bottom.

Although it is homoepitaxial growth for SiC epilayer, there is still misfit strain existing between substrate and epilayer due to the nitrogen doping difference between them. The nitrogen doing concentration for substrates that are commercially available is between 10^{19} ~10^{18} cm^{-3}, while for epilayer is 10^{14}~10^{16} cm^{-3}. The nitrogen atom is smaller than the replaced carbon atom, therefore N doping leads to lattice contraction. Because the pilayer is more lightly doped than substrate, thus the lattice parameter in the epilayer is smaller than that in substrate (i.e reduced by a lesser amount). The formation of edge type misfit dislocation can relax the mismatch stress between epilayer and substrate. And the extra half-plane of the misfit dislocation should be pointing downwards, i.e. inside the substrate.

Jacobson *et al.* [166]observed straight BPDs segments which are interpreted as misfit dislocations formed by the misfit strain between 4H-SiC substrate and the epilayer induced by

different nitrogen doping concentration. With the aid of X –ray topography, the Burgers vector of these misfit dislocations are 1/3[11-20], and they belong to edge-type according to the image conditions $\boldsymbol{g} \cdot \boldsymbol{b} = 0$ and $\boldsymbol{g} \cdot \boldsymbol{b} \times \boldsymbol{l} = 0$. The misfit dislocations observed in SiC are usually straight linear feature lying on the interface between substrate and epilayer, thus it is called interfacial dislocation later on. Zhang *et al.* [167,168] also studied the morphology of interfacial dislocations which were connected to a BPD segment in the substrate at one end and another BPD segment in the epilayer intersecting with the epilayer surface. And these interfacial dislocations were suggested to be generated by sideway glide of BPDs replicated from substrate in the epitaxial layers which matched well with the Matthews-Blakeslee model [169,170].

9.3.1 Matthews-Blakeslee (M-B) Model for Interfacial Dislocation Formation

According to M-B model [169,170], a substrate dislocation piercing the growth interface is initially replicated into the epilayer, for example a dislocation 'AB' meets a growth surface as shown in Fig. 58. As the epilayer is growing thicker, the line tension of the dislocation will prevent it from gliding in the epilayer. At the critical thickness h_c, the line tension of the dislocation F_L is exactly balanced by the force exerted upon it by the mismatch stress F_H, and further growth will enable the dislocation to side-glide along the interface, thereby depositing an interfacial dislocation 'BC' at the interface, and leading to the simultaneous generation of half-loop arrays. At the end of epilayer growth, the gliding segment 'CD' is fully contained inside the epilayer.

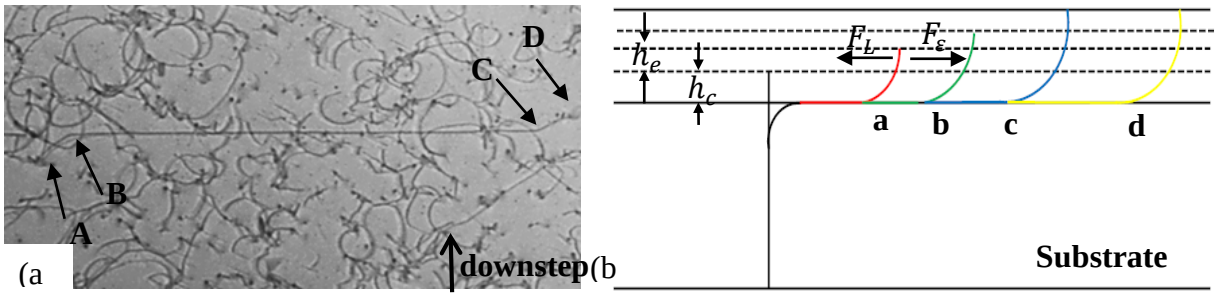

Figure 58 (a) White Beam x-ray topography with transmission-geometry g=11-20 recorded form 4H-SiC homoepitaxial wafer shows screw-oriented dislocation 'AB' gets replicated into epilayer and form interfacial dislocation 'BC'. (b)Schematic shows the formation process of the interfacial dislocations according to Matthews-Blakeslee model, where $h_c$the critical thickness for interfacial dislocation formation is; $h_e$is the epilayer thickness; F_L is the line tension exerted on threading BPD; F_ε is the stress caused by misfit between substrate and epilayer.

Matthews-Blakeslee model is based on mechanical force balance that exerted on threading dislocations.

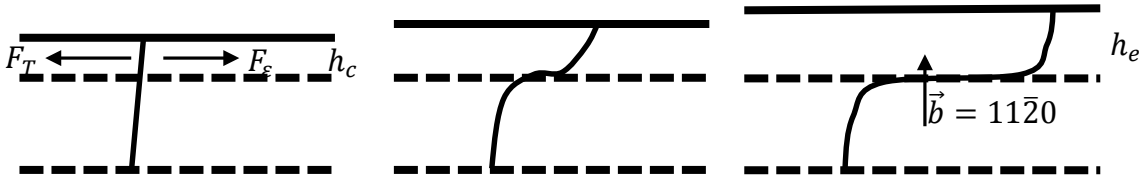

(a) Screw-oriented threading dislocation $\vec{b} = 11\bar{2}0$ begins to grow into epilayer.	(b) Elastic strains in film causes dislocation to bow out when it exceeds the critical thickness.	(c) edge-type interfacial dislocation forms and the threading part in epilayer is fully contained inside epilayer

The main forces that exerted on the dislocation are misfit stress and line tension which are being considered in our study. The gliding force acting on the dislocation is due to the misfit strain, while dislocation line tension disfavors glide.

Plane stress due to geometry, assuming stress is equal to the two in-plane directions (0001).

$$\sigma_3 = 0, \sigma_1 = \sigma_2 = \frac{E\sigma}{1-v} \qquad (21)$$

We can also write this in terms of the shear modulus sine $E = 2\mu(1+v)$

$$\sigma_1 = \sigma_2 = \frac{2\mu\,(1+v)}{1-v}\varepsilon \qquad (22)$$

The maximum resolved shear stress which results from this misfit stress

$$\tau_{res} = \frac{2\mu(1+v)}{1-v}\varepsilon\, cos\varphi\, cos\lambda \qquad (23)$$

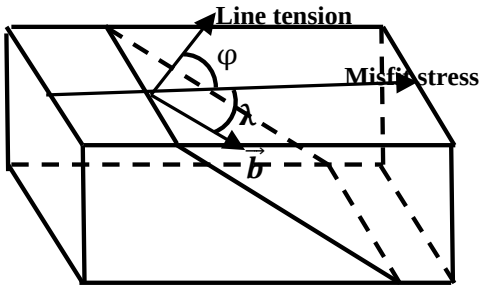

The gliding force acing on the dislocation due to τ_{res} is $\tau_{res} b \frac{h}{cos\varphi}$

So the gliding force is

$$F_\varepsilon = \frac{2\mu\varepsilon(1+v)}{1-v} bhcos\lambda \qquad (24)$$

The line tension on the dislocation can be written

$$F_T = \frac{\mu b^2}{4\pi(1-v)}(1 - v\, cos^2\theta)\ln(\frac{h}{r_o}) \qquad (25)$$

Critical thickness is reached when $F_\varepsilon = F_T$

$$h_c = \frac{b(1-v\, cos^2\theta)}{8\pi\varepsilon\, cos\lambda\,(1+v)}\ln(\frac{h_c}{r_o}) \qquad (26)$$

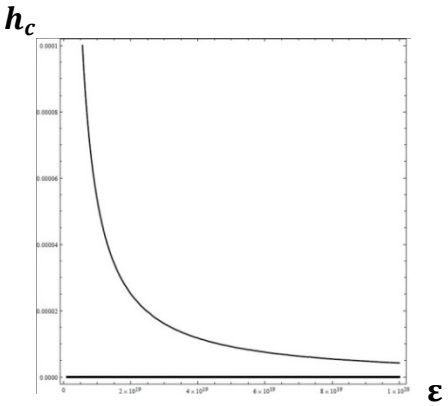

Diagram.1 Schematic of the relationship between critical thickness h_c and misfit strain ε.

9.3.2 People and Bean Model

People and Bean also proposed a model to calculate the critical thickness for interfacial dislocation formation [171,172]. Differently from Matthews-Blakeslee model, it is assumed that the growing film is initially free of threading dislocations in People-Bean model, and that the first half-loop will be generated on the epilayer surface when the areal strain energy density exceeds the self-energy of an isolated screw dislocation. Thus People and Bean model is more suitable for surface sources that nucleated at the epilayer steps and then caused the formation of interfacial dislocation, while Matthews-Blakeslee model is used for the formation of interfacial dislocations from preexisting BPDs replicated from substrate. As a result, The Mathews-Blakeslee approach is based on mechanical force balance while People and Bean method is based on energy balance between strain and dislocation network formation. Based on P-B model, the areal energy density associated with isolated screw dislocation at a distance *h* from a free surface is approximately

$$\varepsilon = \sqrt{\frac{b^2(1-v)}{h_c 16\pi\sqrt{2}a_o(1+v)} \ln\frac{h_c}{r_o}} \qquad (27)$$

where *a* is the bulk lattice constant of the film, v is Poisson's ratio, r_o is the dislocation core radius and h_c denotes the film thickness.

10. Studies of Relaxation Processes and Basal Plane Dislocations in CVD Grown Homoepitaxial Layers of 4H-SiC

10.1 Outline

Dislocation behavior during homo-epitaxy of 4H-SiC on offcut substrates by Chemical Vapor Deposition (CVD) has been studied using Synchrotron X-ray Topography and KOH etching. Studies carried out before and after epilayer growth have revealed that, in some cases, short, edge oriented segments of basal plane dislocation (BPD) inside the substrate can be drawn towards the interface producing screw oriented segments intersecting the growth surface. In other cases, BPD half-loops attached to the substrate surface are forced to glide into the epilayer producing similar screw oriented surface intersections. These screw segments subsequently produce interfacial dislocations (IDs) and half-loop arrays (HLAs). In addition, we show that IDs and HLAs can be formed from BPD loops generated in the epilayer surface, 3C inclusions, micropipes, and surface scratched. The HLAs are known to result in Shockley fault expansion within the epilayer which results in forward voltage drop and device failure.

10.2 Introduction

It is well known that basal plane dislocations (BPDs) present in CVD grown homo-epitaxial layers of 4H-SiC can have a detrimental effect on device performance [158-160] by inducing the expansion of Shockley faults in the epilayer which cause forward voltage drop. Previously it was thought that these BPDs are produced in the epilayers via replication processes occurring at the surface intersections of BPDs in the Physical Vapor Transport (PVT) grown 4H-SiC substrates. Consequently, one of the approaches adopted to mitigate this problem was to engineer the processes by which BPDs are replicated into the epilayer at their substrate surface intersections. For example, the conversion of BPDs into less harmful threading edge dislocations (TEDs) at the substrate/epi interface can be enhanced by direct etching of the substrate surface intersections of the BPDs [161,162] or by growth interrupts which induce etching [163]. Conversion rates of up to 99% have been reported [164,165] with only the remaining 1% which are usually in screw orientation, with Burgers vector along the offcut direction, being available for replication. While such screw oriented BPD segments present in the drift layer of devices can themselves lead to Shockley fault expansion, they can become even more harmful if strain relaxation occurs whereby they are forced to glide in the epilayer leading to the simultaneous production of interfacial dislocations (IDs) [158,166,167] and arrays of dislocation half loops known as Half Loop Arrays (HLAs) [159,167,173,174]. Sasaki *et al.* recently demonstrated that the mismatch stress at the CVD growth temperature, in similarly doped systems as those studied here, is large enough to lead to such relaxation [175]. Within the HLAs, each half loop comprises of a short BPD segment connected to the surface by two TED segments. The short BPD segments provide multiple sites for the expansion of the Shockley faults that cause forward voltage drop thus further exacerbating the problem [173].

In this paper we report Synchrotron White Beam X-ray Topography (SWBXT), Synchrotron Monochromatic Beam X-ray Topography (SMBXT) and KOH etching studies of HLA and ID generation carried out before and after homo-epitaxial growth of 4H-SiC. We will show that, in some cases, the BPDs which produce the IDs and HLAs in the epilayers do not initially intersect the growth surface but rather are drawn towards it from deeper in the substrate during epilayer growth under the action of mismatch stress. In other cases, the substrate surface

intersections of half loops of BPD which are initially converted to TEDs at the onset of growth are shown to act as pinning points about which the BPD half loop pivots as it glides into the epilayer under the action of mismatch stress. Both of these cases result in opposite sign pairs of screw oriented BPDs which pierce the moving growth front which can then glide forming IDs and HLAs. In addition, we show that IDs and HLAs can be formed from new BPDs generated in the epilayer from 3C inclusions, micropipes, substrate surface scratches and surface dislocation sources.

10.3 IDs and HLAs Resulting from BPDs Inherited from Substrate

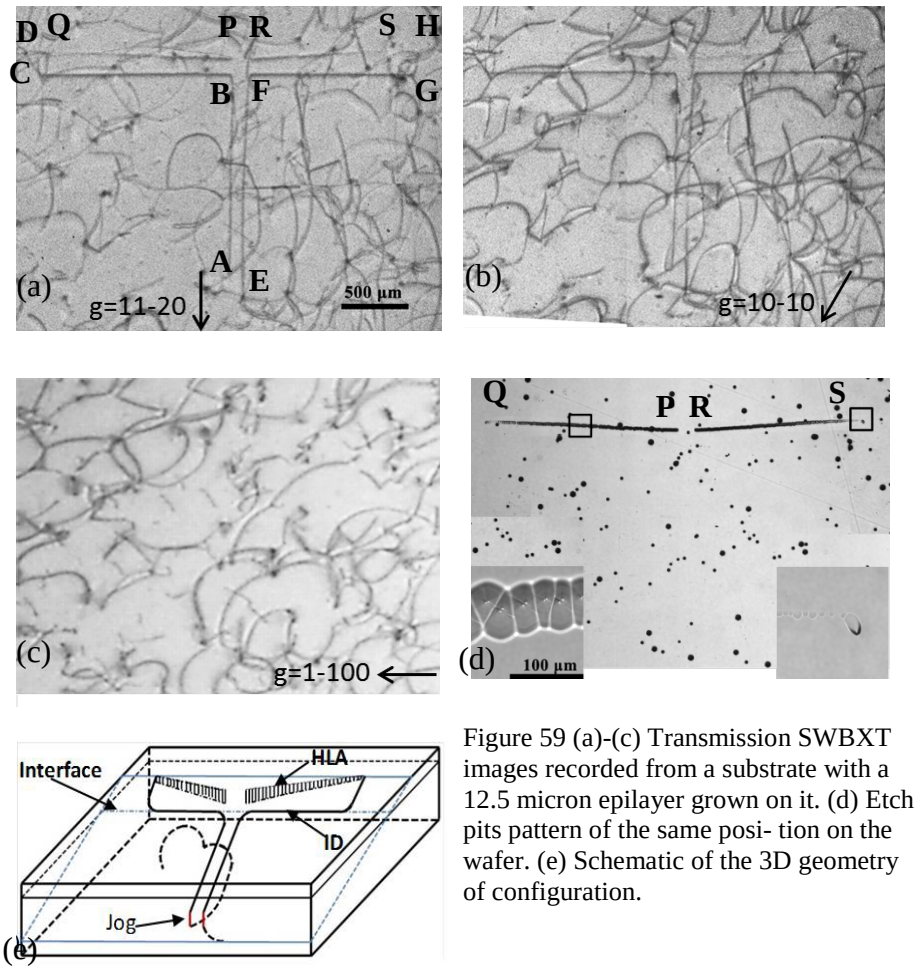

Figure 59 (a)-(c) Transmission SWBXT images recorded from a substrate with a 12.5 micron epilayer grown on it. (d) Etch pits pattern of the same posi- tion on the wafer. (e) Schematic of the 3D geometry of configuration.

Fig. 59 show transmission SWBXT images recorded from a region of a 100 mm low dislocation density PVT-grown substrate (4 degrees off-axis towards <11-20>) with a 12.5 µm epilayer by CVD technique grown on its Si face. The nitrogen doping concentration is around 5×10^{18} cm^{-3} in substrate and 4.8×10^{15} cm^{-3} in epilayer. In Fig. 59(a), note the segments of dislocation ABCD and EFGH. These segments are also visible on Fig. 59(b) while invisible on Fig. 59(c) indicating that they have a Burgers vector of 1/3 [11-20] (oriented along the offcut direction). The lengths of segments CD and GH, which are approximately screw oriented, indicate that they are contained within the epilayer. D and H are the epilayer surface intersections of these segments. Segments CD and GH are connected to segments BC and FG, which are therefore located at the interface and which are edge oriented. These segments are therefore

interfacial dislocation segments. These latter segments are connected to segments AB and EF, which are screw oriented BPD segments extending down into the substrate. The end points of these straight segments, A and E appear to be connected to the curved segments ending at M and N, respectively. These configurations are apparently consistent with the operation of a Matthews-Blakeslee type of mechanism [170] wherein two opposite sign screw oriented substrate BPD segments from the substrate appear to have been initially replicated into the epilayer in screw orientation but which are forced to glide sideways under mismatch induced stress once critical thickness has been reached. The fact that they glide in opposite directions indicates that they are of opposite sign.

Table 10 various characters of different segments of misfit dislocations in 4H-SiC

BPD segments	Position	Line direction	Burgers vector	Type
AB (threading dislocation)	Substrate	11-20	1/3[11-20]	screw
BC (interfacial dislocation)	Interface	-1100	1/3[11-20]	edge
CD (mobile segment)	Epilayer	11-20	1/3[11-20]	screw
PQ (half-loop arrays)	Epilayer	Slightly off -1100	1/3[-1-120]	nearly edge

Close examination of Figs. 59(a) and (b) reveals the presence of two additional linear features, PQ and RS which are slightly inclined to the interfacial dislocation. These features are also invisible on Fig. 59(c) indicating the same Burgers vector. Fig. 59(d) shows an optical micrograph recorded from the same region as the transmission topographs following KOH etching showing features corresponding to PQ and RS (labeled as P'Q' and R'S'). There is another type extended defects nucleated accompanying the side-gliding of interfacial dislocations along the interface which are called half-loop arrays [159,168]. The half-loop are composed of threading edge dislocations connected by a short BPD segment at the bottom. The enlargement (inset) shows that these linear features are made up of the overlap of sets of surface intersections of pairs of closely spaced TEDs that comprise part of the HLAs (these connect to short BPD segments). In addition, the pits associated with the surface intersections of the two opposite sign gliding BPD segments in the epilayer are located at the ends of the two HLAs, consistent with the previously reported HLA formation mechanism [173]. These features are shown schematically in Fig. 59(e).

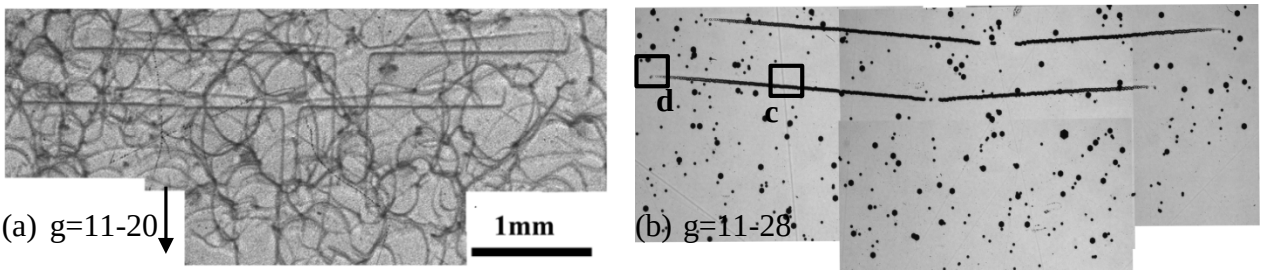

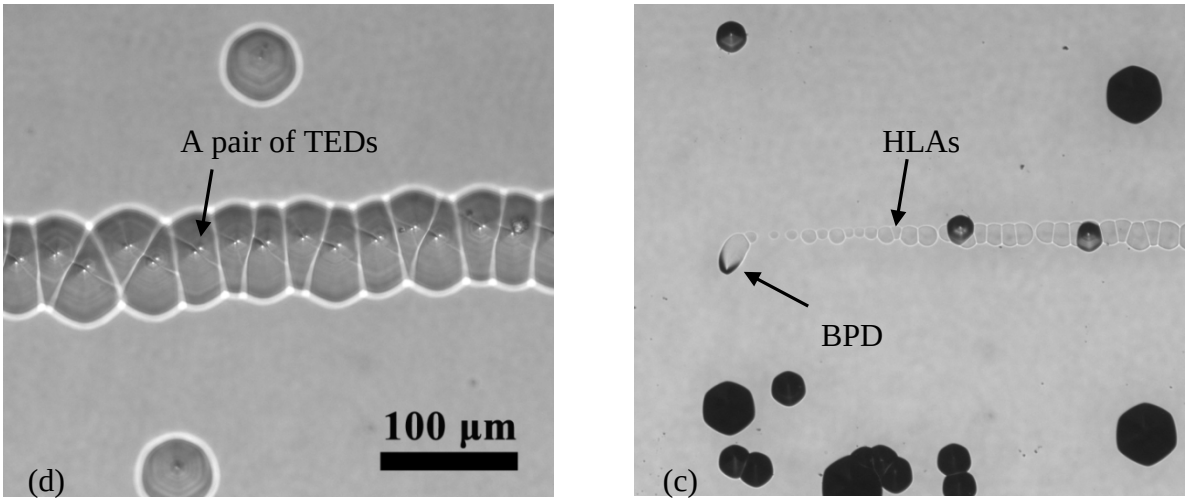

Figure 60 SWBXT showing two pairs of interfacial dislocations. (b) NOM image showing two pairs of half-loop arrays corresponding to the interfacial dislocation in (a). (c) The enlarged picture of half-loop arrays. (d) One BPD etch pit connected with the end of half-loop arrays.

Fig. 60(a) shows more examples of interfacial dislocations and half- loop arrays. Interfacial dislocations are the straight linear features perpendicular to the off-cut direction [11-20], while half-loop arrays are several degrees slightly off that direction. And the number of half-loop arrays is the same as the interfacial dislocations, which can be concluded that the side-gliding of the mobile segment of interfacial dislocations leads to the formation of half-loop arrays. In Fig. 60(c), it is clearly observed each hexagonal shape etch pit has two apexes, which suggests two TEDs sit very close to each other. At the outage of each half-loop array, there is always a BPD etch pit inclined to upstep direction as shown in Fig. 60(d), which is corresponding to the surface intersection of the mobile segment of interfacial dislocation. And the sizes of TED etch pits at the end of half-loop array in Fig. 60(d) are much shallower than the other ones in Fig. 60(c). Based on the position of these etch pits marked in Fig. 60(b), it is suggested that the depth of half-loop arrays are gradually decreasing from one end to the outage end, which also indicates the chronological formation of half-loop arrays.

10.3.1 Formation Mechanism of Half-loop Arrays

Regarding the HLA formation mechanism, Fig. 61(a) shows a screw-type BPD with Burgers vector 1/3[11-20] intersecting the surface of the substrate which is expected to be replicated during epitaxy in contrast to those with significant edge components which are likely to be converted into TEDs [73]. As soon as the epilayer exceeds critical thickness, as per the predictions of Matthews and Blakeslee [169,170], the threading segment of the screw oriented BPD will be forced to glide sideways leaving a trailing interfacial segment in its wake at or near the substrate/epilayer interface (see Fig. 61(b)-(c)). During this glide process, the mobile threading segment adopts more edge character near the growth surface (see Fig. 61(d)) rendering it susceptible to conversion to a TED during continued growth. Slip in SiC is confined to the basal plane, so that the sessile TED segment pins the surface intersection of the mobile BPD segment. During further growth, the TED segment is replicated while the mobile basal segment of dislocation pivots about the pinning point as shown in Fig. 61(d). At this juncture, part of the mobile BPD segment can escape through the epilayer surface (creating a surface step of magnitude equal to the Burgers vector), as shown in Fig. 61(e) leaving two further BPD surface

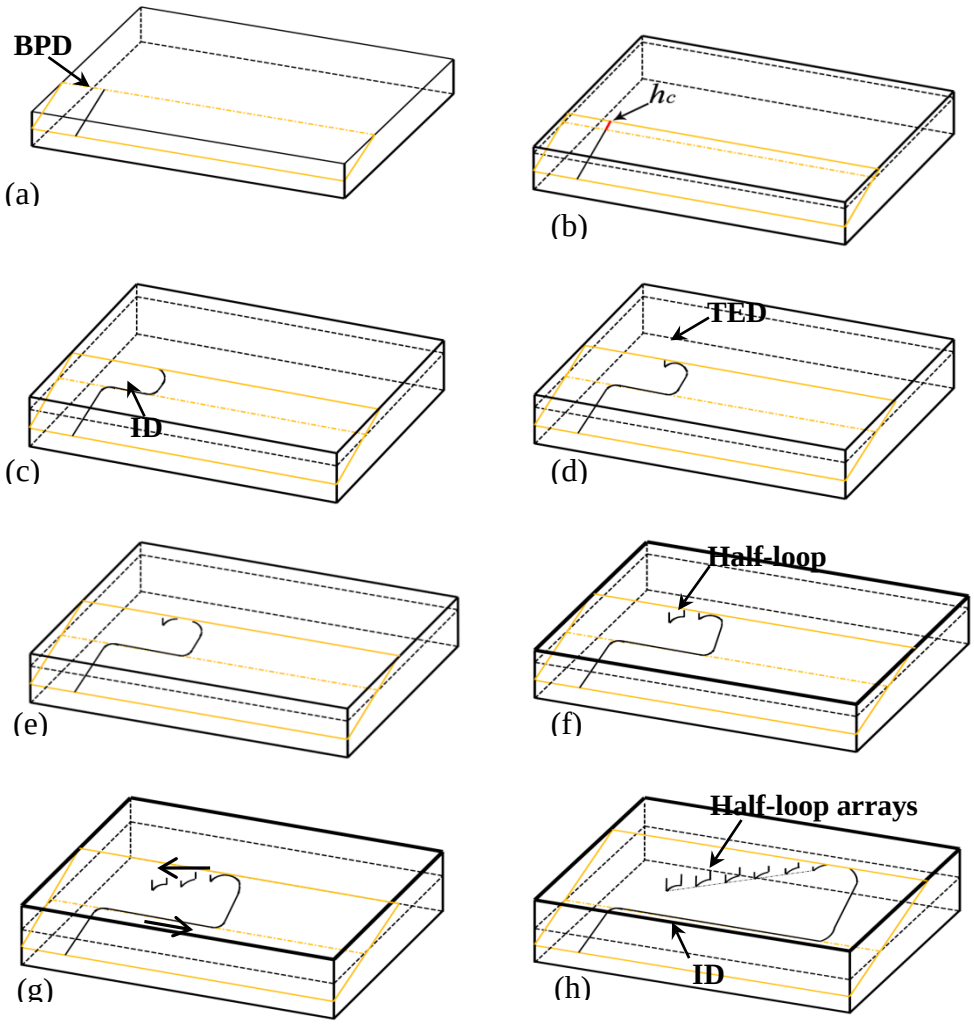

Figure 61 Schematic showing the formation mechanism of a HLA. (a) – (g) sequential stages in the process; (h) Summary of process.

intersections which, since they are not in screw orientation, are susceptible to conversion to TEDs in Fig. 61(f). Upon conversion, one of these TEDs is connected via a short BPD segment to the TED segment created in Fig. 61(f), thus creating a half loop comprising two TEDs and a connecting BPD. The other TED again acts as a pinning point for the still mobile segment of threading BPD, as the process repeats during continued growth as the TED segments further replicate and the threading BPD segment continues to glide. The net result of this process is an array of half loops with short, large edge component BPD segments, all deposited on the exact same basal plane. The direction of the array is nearly perpendicular to the off-cut direction as summarized in Fig. 61(h) and shown in Fig. 59 and Fig. 60. The value of this angle depends on the competition between the growth rate and the rate of sideways glide of the threading BPD segment. Note that the short BPD segments are not expected to glide under the mismatch stress since the force required for such a short segment pinned at both ends is much larger than for the longer threading segment [176]. This configuration is consistent with the observed expansion of

the HLA BPD segments in opposite directions and the annihilation of opposite sign partials which merge from adjacent HLA elements.

10.3.2 IDs and HLAs Generated by Half-loops from Substrate

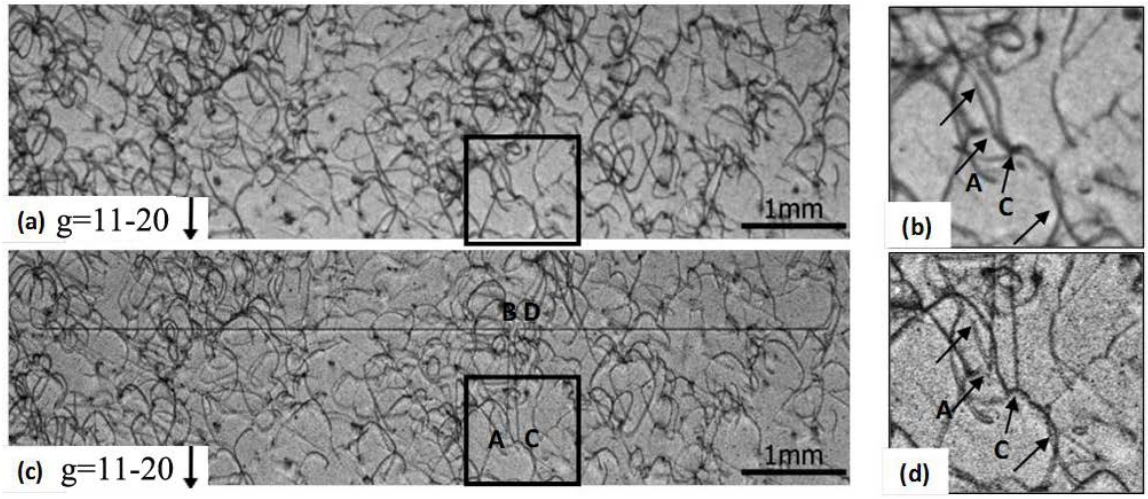

Figure 62 (a) and (c) transmission x-ray topographs with g=11-20 recorded at the same area before and after epitaxy growth. (b) and (d) are the enlarged pictures of the black frames in (a) and (c).

In order to study the origins of the opposite sign pairs of BPDs that are apparently responsible for the formation of the IDs and HLAs, X-ray topographs were recorded from a similar substrate with nitrogen doping around 5×10^{18} cm^{-3} prior to epitaxy and subsequently compared to those recorded following growth of a 30 μm thick epilayer with nitrogen doping around 2×10^{15} cm^{-3} using growth conditions similar to those used for the case shown in Figure 59. Fig. 62 shows transmission SWBXT images recorded from the center region of one 4-inch 4H-SiC wafer before and after epilayer growth which provide some insight into this.

Fig. 62(c) shows a similar configuration to that observed in Fig. 59. Fig. 62(a) clearly shows that the parallel, screw oriented segments AB and CD shown in Fig. 62(c) were not present prior to epitaxy and detailed comparison indicates that they originate from a short segment of approximately edge oriented BPD that is apparently pinned at A and C (see enlargement shown Fig. 62(b)). Close examination of this and other topographs reveals that there are images of several different dislocations, some with the same and others with different Burgers vectors, that are superimposed in that region of crystal that come together at A and C to form complex nodes. It is possible that the pinning may originate in part from large jogs created by cross-slip of opposite sign screw segments in the dislocations that come together at A and C. The segment between the two pinning points that glides towards the surface apparently appears to be more weakly bound along its length than the other dislocations that appear to mimic its shape enabling it to move under the thermal stress. As the short edge segment glides, it leaves a pair of nearly parallel segments of screw oriented BPD in its wake. In this case, the depth below the substrate surface from which the short edge oriented segments are dragged is less than 75 μm. Ideally, the edge segment would stop at the interface and contribute to the relaxation of the mismatch stress. However, if it overshoots the interface and escapes through the epilayer surface this creates two parallel, screw oriented BPDs with opposite sign piercing the growth interface. Since they are close to screw orientation they will continue to be replicated in the same

orientation as the epilayer grows. Once critical thickness is reached, they glide in opposite directions under the action of the mismatch stress depositing the edge oriented IDs in their wake as well as the HLAs.

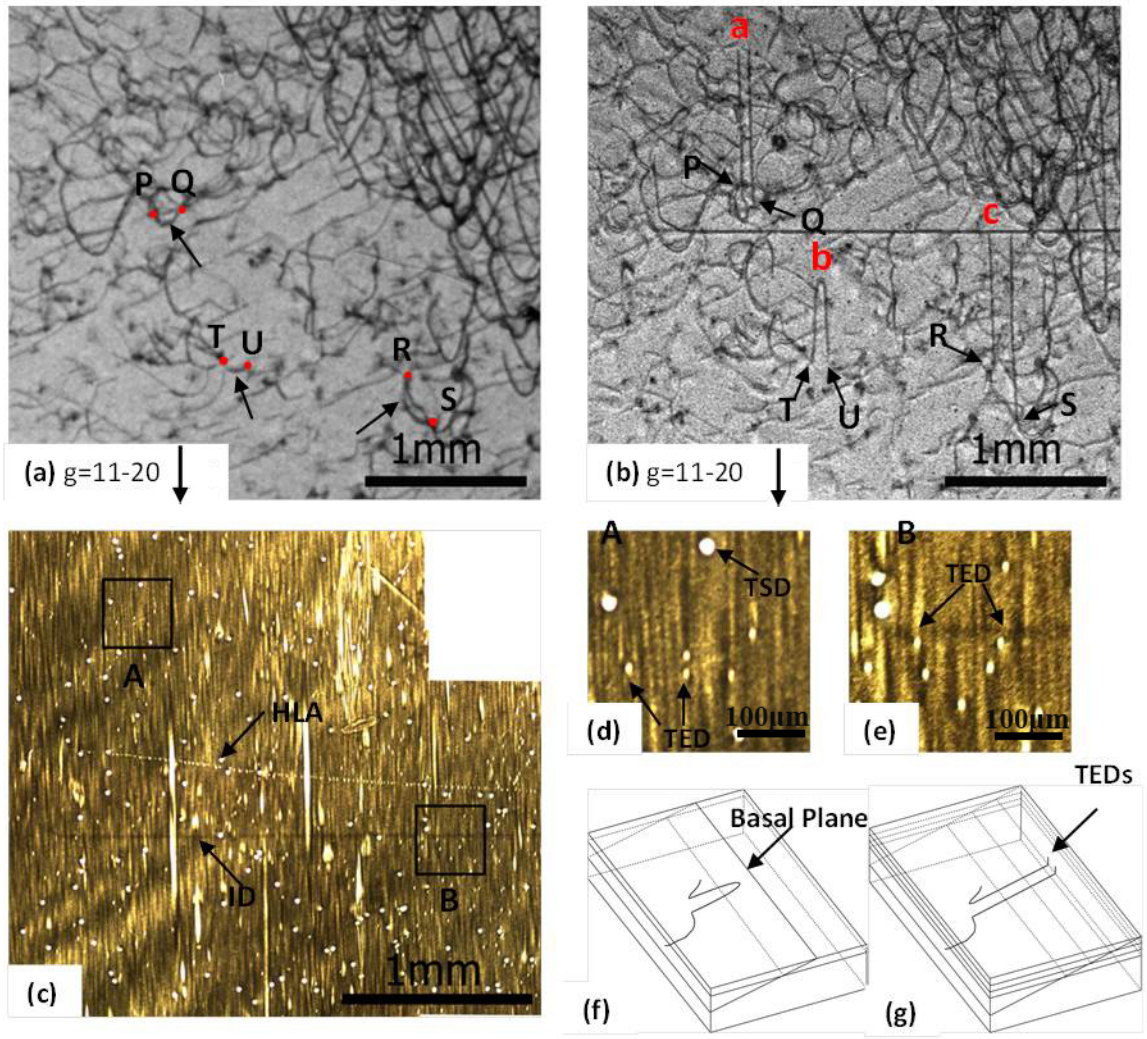

Figure 63 (a) and (b) transmission white-beam x-ray topographs with g=11-20 were recorded on the same area of 4H-SiC wafer before and after epilayer growth. (c) Grazing geometry mono-chromatic x-ray topography with g=11-28 recorded at the same area. (d) and (e) are the enlargement of area 'A' and 'B' in (c).

Further evidence for the pulling of edge oriented BPD segments from the substrate to participate in strain relaxation can be observed in the topographs recorded before and after epilayer growth shown in Fig. 63. Note how the short, curved segments of approximately edge oriented BPD labeled PQ, RS and TU on Fig. 63(a) are the apparent origin of the straight parallel pairs of approximately screw oriented BPDs shown at 'a' and 'c' and the elongated half-loop of BPD at 'b'. The short segments of BPD are apparently pinned at PQ, RS and TU. Close examination of this and other images again reveals that there are several dislocations which superimpose at those locations. It is again thought to be likely that the pinning may originate in part from large jogs created by cross-slip of opposite sign screw segments in the original dislocations. In some cases, a threading screw dislocation can be observed in the vicinity (e.g. at

'R' and 'S') which may act as a strong pinning point which originally brings some of the BPD's on parallel basal planes into close proximity. None of cases 'a', 'b' and 'c' lead to the formation of IDs and HLAs. In case 'b', the mobile segment of BPD never reaches the surface, its progress being stopped by a TSD. For cases 'a' and 'c', their surface intersections have been converted to TEDs as indicated by the monochromatic images shown in Fig. 63 (d) and (e) which are enlargement of 'A' and 'B' area in Fig. 63(c) . This conversion may happen if the overshot edge oriented segments lead to surface intersections which deviate slightly from screw orientation.

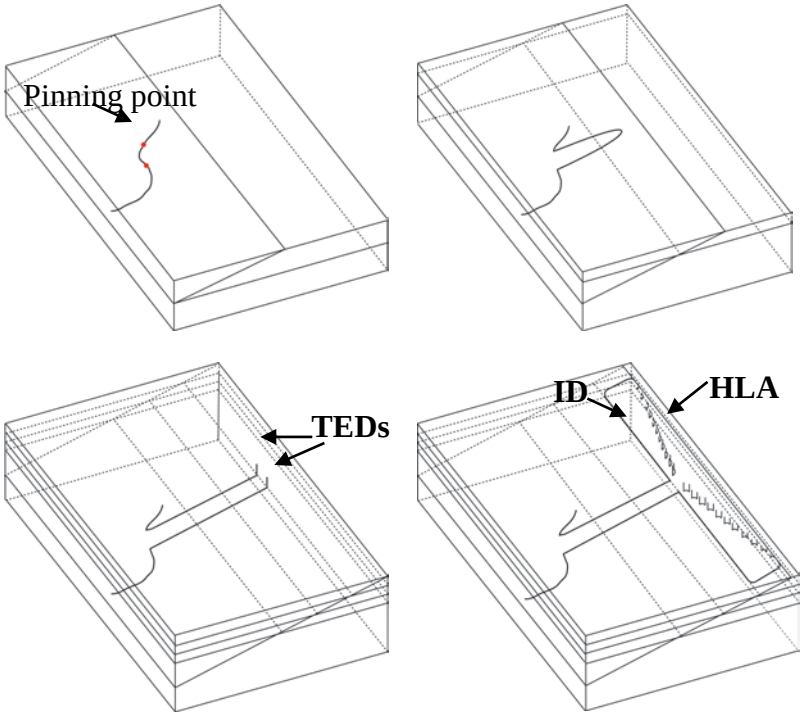

Figure 64 (a) A curved basal plane dislocation in substrate has two pinning points (red dots). (b) The short BPD component pinned by two ends is dragged towards interface under the combination of line tension, and thermal stress. (c) If the BPDs piecing into epilayer are slightly off screw-orientation, then BPDs will be converted into opposite sign TEDs. (d) If the BPDs piecing into epilayer are still in screw-orientation, then BPDs will convert into interfacial dislocations and half-loop arrays once critical thickness is exceeded.

The Summarized schematic is shown in Fig. 64 based on the analysis from Fig. 62 and Fig. 63. In Fig. 64(a), a short curved basal plane dislocation deep inside the substrate (can be up to 100 μm) has two pinning points which might originate from threading screw dislocations, threading edge dislocations or big jogs formed by interaction with nearby basal plane dislocation. It is worth to mention that interfacial dislocations and half-loop arrays are always observed in high BPD density areas (like grain boundaries). Zhang *et al* [177] reported that the presence of radial temperature gradients during epitaxial growth could play an important role in the formation of interfacial dislocations and half-loop arrays. In their studies, if the temperature at the center of the wafer is lower than that at the periphery, this produces compressive stress which leads to resolved shear stress on the basal plane which reaches a maximum value at the center and drops to zero at the periphery. They observed that interfacial dislocations and half-loop arrays were observed at the center region. In our case, interfacial dislocations are always observed in an elliptically shaped region near the wafer center. It is therefore thought to be possible that, at the beginning of epitaxial growth, the resolved shear stress resulting from compressive thermal stress can exceed the critical value for dislocation glide and draw suitably pinned segments of BPD from below the surface of the substrate up towards the epilayer surface. In addition, line tension also plays a part to help the short curved BPD segments to move towards interface. Under the combination of thermal stress, and line tension, the short curved BPD segment start to glide towards the interface. Sometimes the mobile BPD segment does not glide

fast enough to reach the surface or delayed by some barriers, such as TSDs or other basal plane dislocations. Then it will never reach the surface as shown in Fig. 64(b). If the mobile BPD segment moves fast enough, then the gliding front overshot the surface (the 'surface' indicates the surface during growth, not exactly the final epitaxial surface), leaving two paralleling screw-orientated BPDs with opposite sign. If their surface intersections are slightly off screw-orientation, BPDs will be converted into a pair of TEDs with opposite signs as shown in Fig. 64(c). If their surface intersections are still in screw-orientation, then BPDs will be replicated into epilayer and form interfacial dislocations under mismatch stress once critical thickness is exceeded as shown in Fig. 64(d).

It is also observed several pairs of interfacial dislocations without two parallel screw segments attached with them as shown in Fig. 65 which shows a similar set of transmission images recorded from a different region of the same crystal before and after epitaxy. Fig. 65 (b) shows a pair of interfacial dislocations which have apparently been produced as the result of glide in opposite direction of two mobile BPD segments, CD and EF similar to the cases in Fig. 62 and 63 except that there are no parallel screw segments of BPD in the substrate attached to them. Fig. 65 (a) reveals the existence of a half-loop of BPD intersecting the substrate surface at positions A and B that correspond to the points A and B on Fig. 65(b). Since a dislocation cannot terminate inside the crystal, the points A and B in Figure 65(b) must be connected to another dislocation that intersects the surface. The monochromatic image, recorded from the region of enclosed by the black frame in Fig. 65 (b), shown in Fig. 65 (c) clearly reveals a pair of opposite sign TEDs at those locations. This leads us to a model for the formation of the configurations shown in Fig. 65(b). The schematic diagram in Fig. 65 (d) shows the BPD half-loop piercing the substrate surface prior to epilayer growth. Since the surface intersections of this half-loop, A and B, are not in pure screw orientation they are prone during epilayer growth to conversion into TEDs as shown in Fig. 65(e). Following this, thermal stress drags the half-loop towards the interface as shown in Fig. 65(f) and (g) whereupon it is thought to overshoot and exit through the epilayer surface as shown in Fig. 65(h). This would leave two approximately screw oriented BPD segments with opposite sign, threading the epilayer surface. These BPD segments will initially continue to replicate until critical thickness is reached and will then glide sideways in opposite directions under misfit stress according to the Matthews-Blakeslee mechanism, creating interfacial dislocations and half-loop arrays simultaneously in the process, as shown in Fig. 65(j).

Looking back at Fig. 59(a), the curved segment of dislocation 'MAEN' may have been the original dislocation present in the substrate which was pinned at points A and E. Again it seems possible that the pinning may originate in part from large jogs (the red short segments indicated in Fig. 59(e)) created by cross-slip of opposite sign screw segments in the dislocations that come together at A and E. The mobile segment would then glide towards the interface, overshoot the interface and produce two screw oriented BPDs intersecting the surface, eventually gliding sideways to form IDs and HLAs.

It is worth highlighting that the observations here differ from the predictions of the Matthews-Blakeslee model. According to the original model, a substrate dislocation piercing the growth interface is initially replicated into the epilayer, as is required when a dislocation meets a growth surface. As the crystal grows, the line tension of the dislocation will prevent it from gliding in the epilayer. At critical thickness, the line tension of the dislocation is exactly balanced by the force exerted upon it by the mismatch stress, and further growth will enable the dislocation to glide, thereby depositing an ID at the interface, and leading to the simultaneous

generation of HLAs. Our observations here have shown that, in some cases, short edge segments of BPD can be drawn from below the substrate surface towards the interface under the action of the thermal stress. Then these dislocations appear to overshoot the interface, and exit through the epilayer surface. The surface intersections of these dislocations are in screw orientation making them prone to replication into the epilayer. From this point on, the usual Matthews-Blakeslee mechanism takes over with glide occurring at critical thickness.

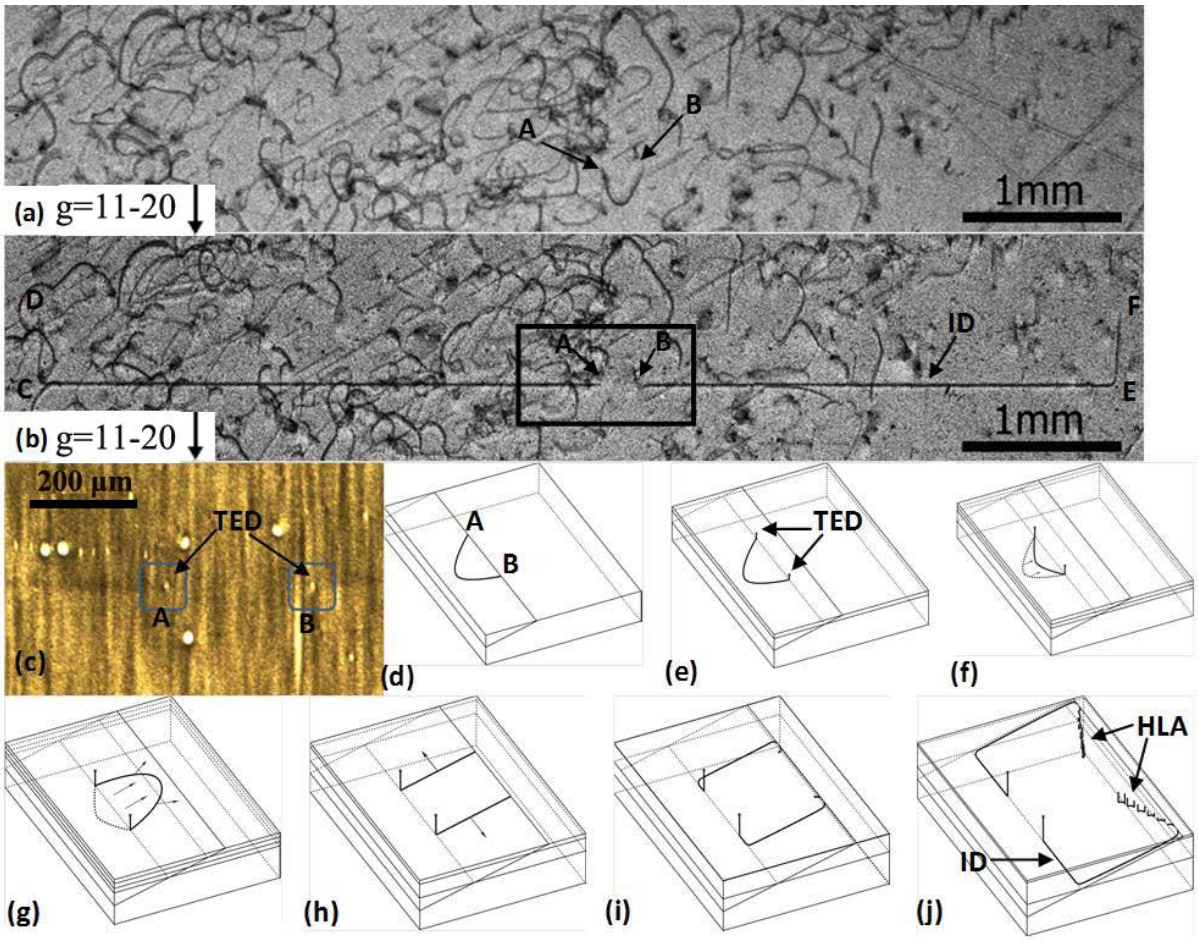

Figure 65 (a) and (b) transmission white-beam x-ray topographs with g=11-20 were recorded on the same area of 4H-SiC wafer before and after epilayer growth. (c) Grazing geometry mono-chromatic x-ray topography with g=11-28 recorded at the area enclosed in the black frame in (b). (d)-(j) Schematic diagrams show the formation mechanism of pairs of interfacial dislocations and half-loop arrays.

Similarly, in the other case reported, the dislocations piercing the growth interface are again provided by a glide process. This occurs when the non-screw oriented substrate surface intersections of a BPD half loop are initially converted to threading edge orientation, as is expected. As growth ensues, the BPD half loop, which is now pinned by the two TED segments, initially glides towards the interface under the action of thermal force. The BPD again overshoots the interface and exits through the epilayer surface leaving two screw oriented surface intersections which are then replicated.

10.3.3 Conclusions

Observations indicate that a Matthews-Blakeslee type mechanism of relaxation occurs during homo-epitaxial growth of 4H-SiC. However, the mechanism appears to differ in some cases in that the source for the IDs does not initially intersect the substrate surface and simply get replicated into the epilayer. Short edge-oriented BPD segments located up to 100 microns below the substrate surface are forced to glide on the basal plane towards the interface under compression thermal stress. Having overshot the interface, they produce, opposite sign pairs of screw oriented BPDs which initially replicate into the epilayer, but once critical thickness is reached glide sideways creating IDs and HLAs. In another type of case, the surface intersections of a BPD half loop are initially converted to TEDs as the half-loop is drawn towards the interface by thermal stress. It again overshoots the interface, eventually inverting its shape and crossing into the epilayer, where it escapes through the surface producing two opposite sign, screw oriented BPD segments. These again initially replicate and then glide sideways in opposite directions once critical thickness has been reached forming IDs and HLAs.

Further statistical analysis carried out on other epiwafers, grown by a similar growth technique, indicates that the densities of interfacial dislocations and half-loop arrays produced are proportional to the basal plane dislocation density in substrate. In high BPD density areas, there is an increased probability of finding short BPD segments pinned by two points below the substrate surface. Such short segments can then be dragged towards interface by thermal stress to form IDs and HLAs once critical thickness has been reached. Similarly, the probability of finding a BPD half loop, with Burgers vector along the offcut direction, attached to the surface is proportional to the local BPD density.

The significance of these findings is threefold. First, it demonstrates that it is not necessary for a BPD to intersect the substrate surface for it to become involved in strain relaxation during epilayer growth. Second, for the case of the half loop attached to the surface, conversion of its surface intersections to TED orientation does not render it benign with respect to its possible deleterious effects on device performance. The implications are that while BPD to TED conversion helps in eliminating most of the BPD transfer into the epilayer, further mitigation may only be possible by continued efforts to reduce the BPD densities in the substrates by careful control of temperature gradient induced stresses during their PVT growth [69]. Third, it is important to avoid generation of new BPDs in the epilayer from inclusions, micropipes and surface sources.

10.4 Studies of Relaxation Processes

10.4.1 Critical Thickness Measurement

In this paper we report on measurements of critical thickness made using synchrotron white beam X-ray topography. We discuss these in light of calculations of critical thickness based on the Matthews-Blakeslee model [169,170].

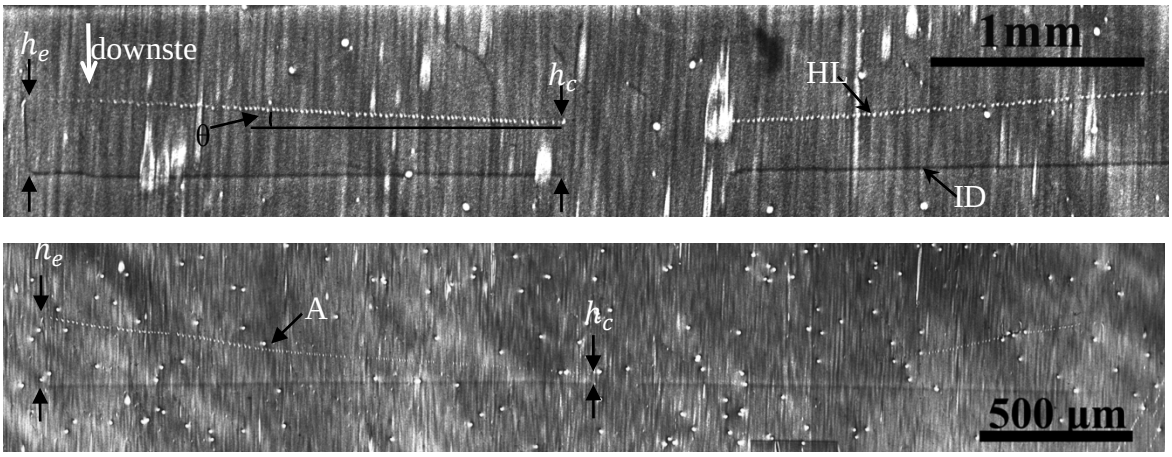

Figure 66 (a) SMBXT image recorded in grazing geometry (g=11-28) on the homoepitaxy wafer with 12.5 µm; the nitrogen doping concentrate of the substrate and epilayer is 5 x 10^{18} cm^{-3} and 4.8 x 10^{15} cm^{-3} respectively. (b) SWBXT image recorded on the other wafer with the epilayer thickness around 30 µm; the nitrogen doping concentrate of the substrate and epilayer is 5 x 10^{18} cm^{-3} and 2 x 10^{15} cm^{-3} respectively

Fig 66(a) shows IDs and HLAs generated during the homo-epitaxial growth of n-doped 4H-SiC. The epitaxial structure contained 0.5 µm nitrogen doped buffer layer and 12.5 µm *n* doped epilayer; nitrogen concentrations in the substrate and epilayer were 5 x 10^{18} cm^{-3} and 4.8 x 10^{15} cm^{-3} respectively. According to the formation mechanism of ID and HLA [173], the inclination angle θ between the HLA and the $[1\bar{1}00]$ surface intersection direction of the basal plane is determined by the epitaxy growth rate v_e and the ratio of the dislocation velocity v_g:

$$\tan\theta = \frac{v_e}{v_g} \qquad (28)$$

If the HLA is approximately straight this means that this ratio is approximately constant as shown in Fig. 66(a). Furthermore, this means that the HLA direction can be extrapolated back towards the original surface intersection position of the screw-oriented BPD at the point where mismatch induced glide began. Therefore this enables the critical thickness to be measured directly from the topographs. The epithread is fully contained in the epilayer after epitaxy growth. In Fig. 66(a), h_e is corresponding to the depth of epilayer and h_c is corresponding to the critical thickness when the interfacial dislocation starts to glide. In Fig. 66(a), the calculated h_c is 8µm when h_e is 12.5 µm, while the calculated h_c is 4.4 µm when h_e is 30µm of the wafer with the nitrogen doping concentrate of the substrate and epilayer 5 x 10^{18} cm^{-3} and 2 x 10^{15} cm^{-3}, respectively. According to the Matthews-Blakeslee model, the calculated misfit stain needed for producing the misfit at the critical thickness 4.4 µm in Fig. 65(b) is 2 x 10^{-5}. Chidambarrao *et al* [178] have extended Matthew-Blakeslee mechanism for determining the critical thickness in semiconducting heteroepitaxial films by including the effect of the Peierls barrier. He claimed

that Peierls barrier at the higher temperature is lower, which will allow the motion of epithreads and hence the formation of misfit dislocations. MB theory does not assure any Peierls barrier for the motion of dislocations. Thus M-B theory would work well for semiconductor materials at higher temperatures, where the Peierls barrier effects can be neglected.

The mismatch strain which is defined as:

$$\varepsilon = \frac{a_e - a_s}{a_s} \qquad (29)$$

where a_e and a_s are the lattice parameters of the epilayer and substrate, respectively. According to Matthews and Blakeslee[169,170], this can be written as:

$$\varepsilon = \frac{b(1-\upsilon cos^2\theta)}{8\pi h_c cos\lambda\,(1+\upsilon)} ln\frac{h_c}{r_o} \qquad (30)$$

Where $\boldsymbol{b}$ is the Burgers vector of the dislocation (1/3[11-20]), υ is Poisson's ratio, θ is angle between the stress and the gliding direction, λ is the angle between the stress and the plane normal, r_0 is the core radius of the dislocation (assumed to be 1~4 times the Burgers vector) and h_c is the critical thickness. The critical thickness will decrease dramatically when the misfit strain is bigger than 10^{-5}.

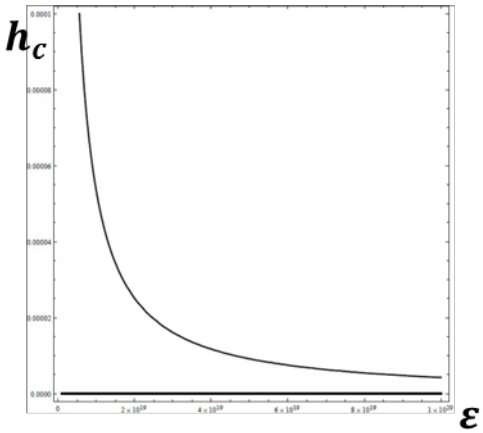

Diagram 2. The simulated relationship between the critical thickness and the misfit strain.

Nitrogen substitutes for carbon in the SiC lattice and, since its atomic radius is smaller, cause a lattice contraction. With the doping level of the epilayer being lower than that of the substrate, a lesser degree of lattice contraction means that the lattice parameter of the epilayer will be larger than that of the substrate. Jacobsen *et al* [166] have proposed a model to calculate the magnitude of the lattice contraction associated with doping. And the isotropic lattices stain due to incorporation of dopants is as following.

$$f_e = \frac{a_s - a_e}{a_s} 4\pi N(r_s^3 - r_h^3)\left(\frac{3K+4G}{27K}\right) \qquad (31)$$

where N is the density of substitutional dopants (in cm^{-3}); r_s is the radii of substitutional (N) atoms (nitrogen); r_h is the radii of host atoms (carbon); K (225 GN/m^2) and G (167 GN/m^2) are

the bulk and shear moduli. The estimate misfit strain for the epilayer structures studied here is around 9 x 10^{-7}. Based on the Matthews-Blakeslee formula this would lead to a critical thickness value of some 116 µm. This is far in excess of the measured value suggesting that the doping difference between epilayer and substrate is not large enough to account for the misfit strain. Application of this model to the epilayers studied here shows that the calculated mismatch strains would be too small to measure because this calculation is based on the room temperature.

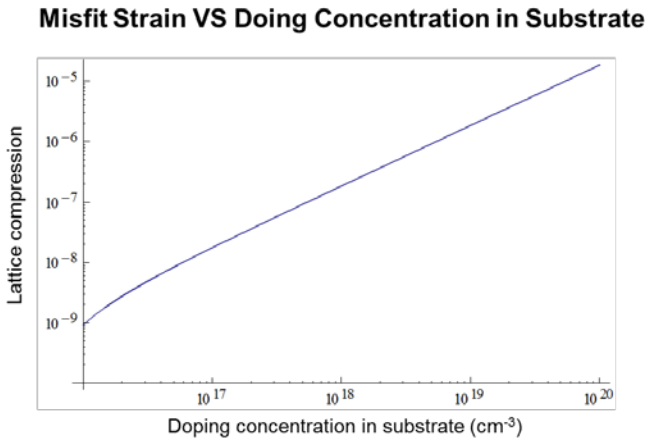

Diagram 3. Simulated compression at different substrate doping levels of N, while the doping level of epilayer is fixed at 5 x 10^{18} cm^{-3}

Sasaki *et al* [175] recently made measurements of mismatch strain in similar systems. This work showed that at room temperature the mismatch strain is negligible in agreement with the predictions of Jacobsen's model. However, measurements made at elevated temperatures revealed measureable mismatch strains along both the ***c*** and ***a*** directions indicating that the thermal expansion coefficient of SiC is a function of nitrogen doping concentration. The *c*/*a* ratio remained constant as a function of temperature. Measurements made at 1100 ℃ on a sample comprising a substrate with doping concentration of 2 x 10^{19} cm^{-3} and an epilayer with 6 x 10^{14} cm^{-3} revealed a mismatch strain of 1.6 x 10^{-4}. The extrapolated value at 1600℃ is around 2-3 x 10^{-4}. The substrate doping in our case is 5 x 10^{18} cm^{-3} four times smaller than 2 x 10^{19}, which leads us to expect that the value of misfit strain expected for our samples can be estimated to be about four times smaller than the quoted in the Sasaki's paper, i.e. 5-8 x 10^{-5}. The calculated misfit strain required for the creation of ID at the critical thickness 4.4 µm is around 2x 10^{-5}, which is comparable to the value extrapolated from Sasaki's work. Thus the misfit strain due to the doping difference between substrate and epilayer is large enough to produce ID when the condition is suitable.

Misfit Stress

According to M-B model, interfacial dislocations are produced due to the existing misfit strain between epilayer and substrate. In the above diagram 3, the misfit strain is 5-8 x 10^{-5} extrapolated from the work of Sasaki *et al*, the resolved shear stress on basal plane is around 1.66-2.65 MPa based on the following equation.

$$\tau_{res} = \frac{2\mu(1+\nu)}{(1-\nu)} \varepsilon \cos\emptyset \cos\lambda \qquad (32)$$

where μ is shear modulus, v is Poisson's ratio, $\emptyset$ is the angle between stress and the normal to the slip plane and λ is stress and the slip direction.

Line Tension

In addition to the force due to an externally applied stress, a dislocation has a line tension which is analogous to the surface tension of a soap bubble or a liquid. It is known that strain energy of dislocation is proportional to its length and a decrease in length results in the decrease in energy. The line tension will produce forces tending to straighten the line and so reduce the total energy.

$$\tau_0 = \frac{\alpha G b}{R} \qquad (33)$$

In this case, the radius of the curved dislocation is around 46 μm, thus the line tension is estimated to be around 0.5~1.09 MPa.

Thermal Stress

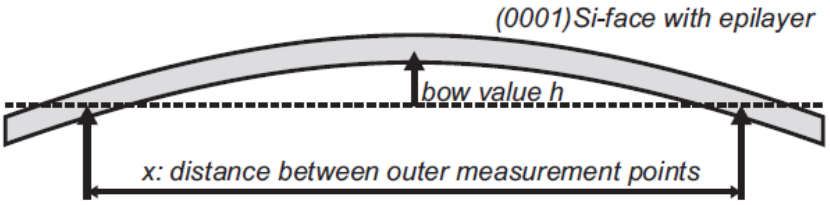

Figure 67 the bow shape of epilayer during epitaxial growth [179].

Kallinger *et al* [179] reported that all epilayers exhibit a convex curvature as shown in Fig. 67. In case of low N-doped epilayer with C_N <5 × 10^{17} cm^{-3}, and the doping level of the substrate constant at 2 × 10^{19} cm^{-3}, the curvature is constant at a value of $\kappa \approx 0.02$ m^{-1}. It has to be pointed out that the measurement is carried out at room temperature, which ignores temperature's influence on doping induced wafer curvature. Actually, at growth temperature around 1600 ℃ to 1700℃, the curvature is expected to be much larger than 0.02 m^{-1}. The curvature of the wafer will cause the inhomogeneous of heating as the wafer is usually heated by the graphite attached with them, resulting the lower temperature distribution in the center compared with the edge. Meanwhile, the wafer is also heated radially from the furnace wall, which can also cause the lower temperature in the center, where thermal compressive stress is created.

Fig.68 (a) schematically shows the creation of IDs and half loop arrays from a dislocation segment "a", pinned at both ends, lying deep inside the substrate. This dislocation segment glides towards the epilayer surface passing through configurations "b" and "c" and eventually escaping through the advancing epilayer surface, leaving two opposite sign screw segments piercing the epilayer surface. These will initially replicate until critical thickness is reached whereupon their epilayer segments glide creating the IDs "d". The sense of the dislocations is indicated by the arrows on the lines. It is clear from this that segment "a" is of opposite sign to the resulting ID "d". The dark contrast exhibited by the ID on the monochromatic topography image shown in

Fig. 66 (a) and (b) indicate that the extra half-plane of the ID lies on the substrate side of the interface [36]. This is expected from the doping differences between the epilayer and substrate.

The nitrogen atom is smaller than the carbon atom it replaces so doped crystals should have an associated lattice contraction. Since the doping concentration in the epilayer is smaller than that in the substrate, the epilayer lattice constant should be larger than the substrate so that the epilayer should experience compressive mismatch stress. Relaxation of this mismatch stress can be provided by edge oriented IDs with their extra half-plane on the substrate side of the interface. Since segment "a" has opposite sign to this, its extra half-plane should be pointing up towards the epilayer surface. Simple geometric analysis concludes that segments such as "a" with the extra half-plane pointing up should be pulled up towards the surface under in-plane compressive stress as shown schematically in Figs. 68 (b) and (c). This can be interpreted as evidence for in-plane compressive stress, which is consistent with the observations of Zhang *et al* [177] who attributed such stress to radial temperature gradients. It is also worth noting that since segment "a" is of opposite sign to the ID, it can play no role in strain relaxation and as such has no incentive to stop at the interface as it passes through.

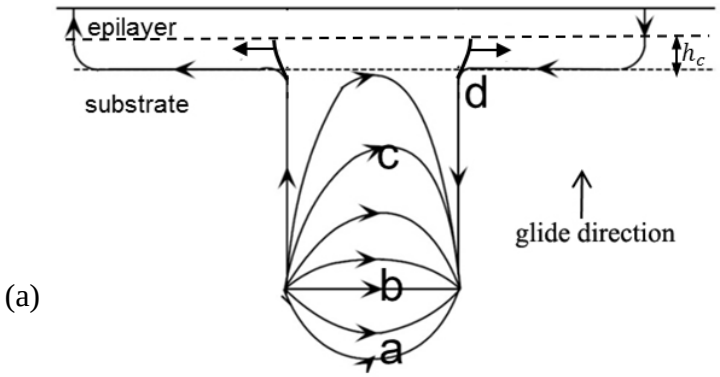

(a)

Figure 68 (a) schematic shows gliding process of dislocation half-loop from 'a'→ 'b' → 'c' → 'd'. The line direction of dislocation 'a' is opposite to that of interfacial dislocation 'd'.

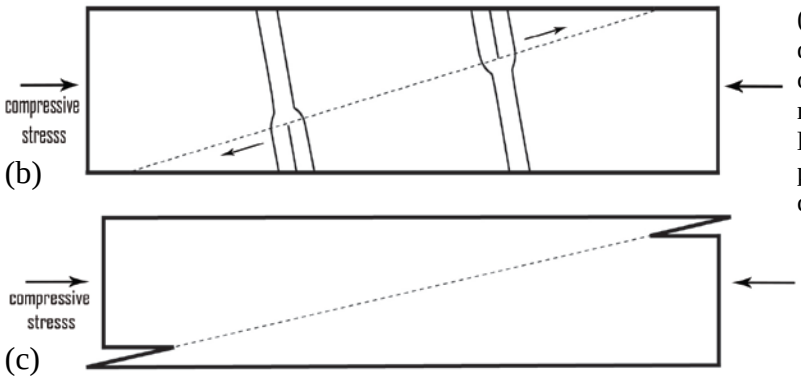

(b)

(c)

(b)-(c) Schematic showing how the deformation created by in-plane compressive stress can be effected by the motion edge dislocation segments of a loop. The dislocation with the extra half-plane pointing up in the upper region of crystal is drawn towards the surface.

Zhang *et al* [177] has also reported that the presence of radial temperature gradients during epitaxial growth could play an important role in the formation of interfacial dislocations and half-loop arrays. In their studies, if the temperature at the center of the wafer is lower than that at the periphery, this produces compressive stress which leads to resolved shear stress on the basal plane which reaches a maximum value at the center and drops to zero at the periphery. They observed that interfacial dislocations and half-loop arrays at the center region. In our case,

interfacial dislocations are always observed in an elliptically shaped region near the wafer center. It is therefore thought to be possible that, at the beginning of epitaxial growth, the resolved shear stress resulting from compressive thermal stress can exceed the critical value for dislocation glide and draw suitably pinned segments of BPD from below the surface of the substrate up towards the epilayer surface. Once these mobile BPD segments have been provided in the epilayer, misfit stress can take over leading to the formation of interfacial dislocations and half-loop arrays once critical thickness is reached.

` The stress components due to a centro-symmetric radial temperature gradient are:

$$\sigma_{rr} = \alpha E[\frac{1}{R^2}\int_0^R Trdr - \frac{1}{r^2}\int_0^r Trdr] \quad (34)$$

$$\sigma_{rr} = \alpha E[\frac{1}{R^2}\int_0^R Trdr + \frac{1}{r^2}\int_0^r Trdr - T] \quad (35)$$

Resolved shear on screw BPDs along the step flow direction [11-20]

$$\tau = (\sigma_{rr}cos^2\theta + \sigma_{\theta\theta}sin^2\theta)sin8^o \cos 8^o \quad (36)$$

As a result,

$$\frac{dT}{dr} > 0,\ \tau < 0 \text{ Compressive stress in the center} \quad (37)$$

$$\frac{dT}{dr} < 0, \tau > 0 \text{ Tensile stress in the center} \quad (38)$$

Note that the sign of the ID segments is opposite to that of the original edge oriented segment drawn up from the substrate. This means that the original edge-oriented segment could play no role in relaxing the mismatch between epilayer and substrate so that the mismatch stress as such cannot account for its motion. This means that the thermal stress associated with the radial temperature gradient is responsible for this motion. Therefore the resolved shear stress on basal plane from thermal stress and line tension should exceed the critical resolved shear stress (CRSS) required for dislocation glide in order to be able to drag the dislocation from deep inside the substrate up towards the epilayer. Samant *et al* [14] reported that there was a linear relationship between CRSS and temperature as following:

$$\ln \tau_c = \frac{Q}{nkT} + \frac{1}{n}[\ln \dot{\gamma} - \ln A] \quad (39)$$

where τ_c is critical resolved shear stress, *A* is a constant, *n* is the stress exponent, *Q* is the stress-independent activation enthalpy, and $\dot{\gamma}$ is the temperature dependence of the plastic strain rate. The second term on the right hand side of equation is clearly a constant. Thus, a plot of $\ln \tau_c$ vs 1/T should be linear with a slope of Q/nk. The critical resolved shear stress at T=1600 ℃ is extrapolated to be around 4.8 MPa at the strain rate of 6.3×10^{-5} sec^{-1}. It is known that the lower the stain rate, the smaller the observed critical resolved shear stress. The strain rate on the wafer during CVD growth is several orders smaller than 6.3×10^{-5} sec^{-1}. On the other hand, the experimental data was based on engineering stress (s) vs engineering strain (e) curves of SiC samples, and the critical resolved shear stress (τ_c) was assumed to be the stress value at the onset of non-linearity after the elastic region of the engineering stress-strain curve, multiplied by the Schmid factor (S=0.5), assuming that slip occurred on the <2-1-10> (0001) primary slip system

of SiC samples. As a result, the measured CRSS is the stress causing multiple dislocation gliding. The critical resolved shear stress for initiating a single short, curved half-loop dislocation to glide is required in our case only. Therefore it can be expected that τ_c should be much smaller than 4.8 MPa.

Once the resolved thermal stress on slip plane (0001) is larger than the critical shear stress for dislocation gliding, the short, curved dislocation pinned at two ends will be dragged towards the interface. If the dislocation glides fast enough, the edge segment has escaped through the surface, leaving two opposite-sign, screw oriented segments that intersect the surface. Those two segments are also in a position to glide under the compressive mismatch stress, and when they do generate IDs which are of the correct sign to help with mismatch stress relaxation. Therefore the glide of the original edge oriented segments plays a critical role in that it provides the mobile basal plane dislocation segments (in screw orientation) which enable the relaxation to occur.

10.4.2 Conclusion

a. Jacobson model is not suitable for calculating the misfit strain at the CVD growth temperature at around 1600~1700 ℃, while the misfit stain extrapolated from the previous work carried out by Sasaki *et. al.* [175] has very good agreement with the critical thickness measured using X-ray Topography.
b. Therefore the resolved shear stress on basal plane from compressive thermal stress and line tension should exceed the critical resolved shear stress (CRSS) required for dislocation glide in order to be able to drag the dislocation from deep inside the substrate up towards the epilayer.
c. Once these mobile BPD segments have been provided in the epilayer, misfit stress can take over leading to the formation of interfacial dislocations and half-loop arrays once critical thickness is reached.

10.5 Different Nucleation Sources for Interfacial Dislocations and Half-loop Arrays.

10.5.1 Surface Sources

Interfacial dislocations generated from surface nucleated half-loops have been previously observed during growth of InGaAs epilayers on GaAs substrates [180]. The same phenomenon I also observed during 4H-SiC homoepitaxial growth. For example, Fig. 69(a) shows an SMBXT image recorded from a different sample. A series of half-loops are observed to have nucleated at the epilayer surface and to have subsequently glided towards the substrate/epilayer interface. The surface intersections of the first of these to nucleate appear to give rise to the generation of another extended defect in epilayer i.e. half-loop arrays observed on Fig. 69(a). Fig. 69(b) shows stages in the formation of a misfit dislocation by the nucleation and expansion of a half-loop. Under the misfit strain, dislocation half-loop starts to bow out and touches the interface, its threading arms move further apart and deposit a misfit dislocation at the interface. At this case, there is initially free of threading dislocations in the epilayer, half-loops will be generated at the epilayer surface (which is different from final surface) when the stain energy density of the epilayer film exceeds the self-nucleation energy of half-loop dislocation.

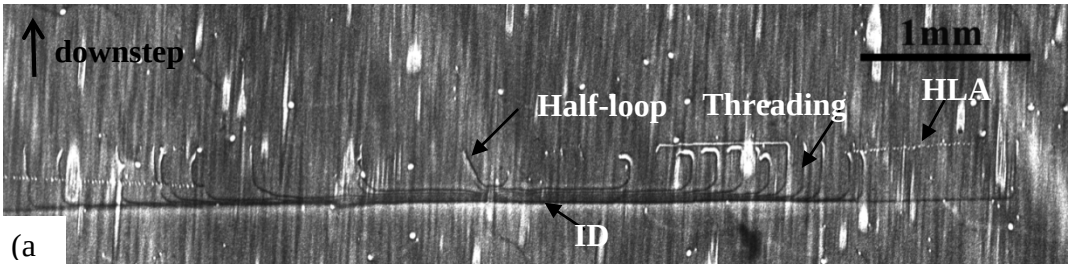

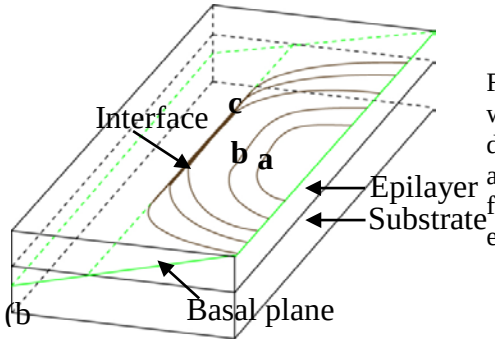

Figure 69 Monochromatic Beam X-ray topography with grazing-geometry g=11-28 shows expansion of a dislocation half-loop to form interfacial dislocations and half-loop arrays. (b) Schematic shows stages in the formation of a misfit dislocation by the nucleation and expansion of a half-loop on the surface.

10.5.2 3C polytypes

As we mention above, SiC is a polytypic material crystallizing into some 200 different polytypes, and cubic 3C-SiC is the most stable phase at all temperatures up to 1800 ℃ [141], which makes it the most common polytypes during 4H/6H-SiC homoepitaxial growth. In order to control the polytypes, the CVD-growth of 4H-SiC epilayer is using off-axis growth; the surface cut 4 degree off basal plane along [11-20] direction. The growth on off-axis is realized by the exact replication of the steps on the seed surface when the step density is high and the terrace width is narrow enough for absorbed species to reach steps, which is called “step-controlled growth” or “step-flow growth” as schematically shown in Fig. 70(b). However, if the

step terraces are too big, 2D island nucleation of 3C polytypes will happen at high supersaturation condition, followed by the expansion of the islands as shown in Fig. 70(a). This growth mode called “2D nucleation mode” causes a large amount of polytype inclusions because the islands may not copy the exact stacking sequence of the substrate and cubic SiC is the stable phase at the commonly used temperatures. Islands expand followed by coalescence and misorientation between separate islands provides sites for dislocation nucleation, such as BPD half-loops. Half-loops in epilayer can expand and multiplicate under the thermal stress and misfit strain, forming interfacial dislocations and half-loop arrays once critical thickness is exceeded.

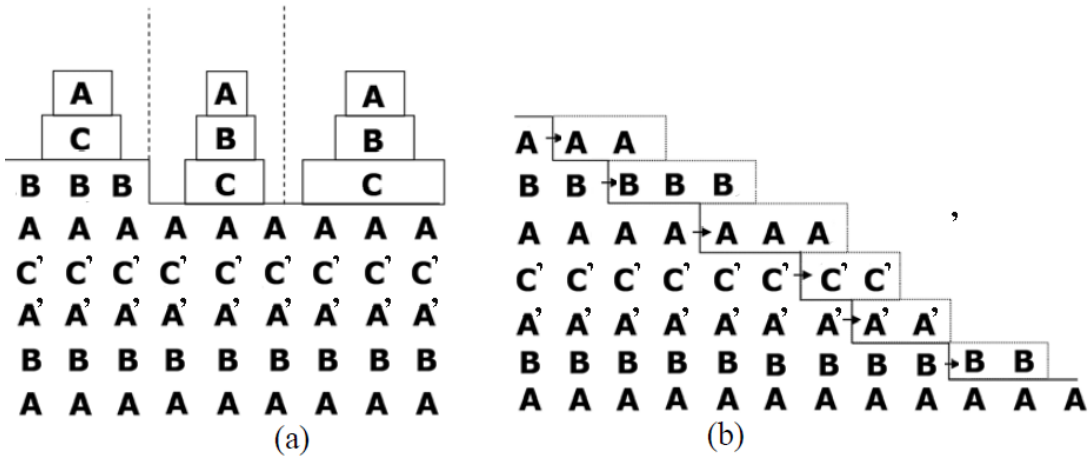

Figure 70 Two different growth modes of CVD epitaxy on 4H-SiC. (a) 2D nucleation mode; (b) step-controlled growth mode.

Fig. 71(f) is a grazing incidence SMBXT image recorded from certain region showing BPD half-loops emanating from a 3C inclusion in the epilayer. Successive half-loops are observed to have expanded, each one depositing an interfacial dislocation and generating half-loop arrays exhibit white contrast. From the topography, the interfacial dislocation doses not overlap with the apex of the 3C triangle at position ‘A’ because the Laue pattern of the 3C polytype gets shifted. In order to study more details on the formation of IDs and HLAs from 3C-polytypes, another area is selected and recorded under different diffraction g vectors as shown in Fig. 71(a)-(e). There are two types interfacial dislocations based on the line direction of threading arms. Interfacial dislocation ‘BC’ has the threading arm ‘AB’ along off-cut direction [11-20], which is out of contrast when diffraction vector (g=1-100) is perpendicular to the line direction. Thus the Burgers vector of ID ‘AB’ is 1/3[11-20]. On the other hand, the line direction of threading arm ‘DE’ of interfacial dislocation ‘CD’ is along [-2110], and they are invisible when g=01-10. Thus the Burgers vector of ID ‘CD’ is 1/3[-2110]. Compared with etch pits pattern in Fig. 71(b), Interfacial dislocation ‘BC’ with $\vec{b} = 1/3[11\bar{2}0]$ has the corresponding half-loop arrays ‘MN’, while interfacial dislocation ‘CD’ with $\vec{b} = 1/3[\bar{2}110]$ does not.

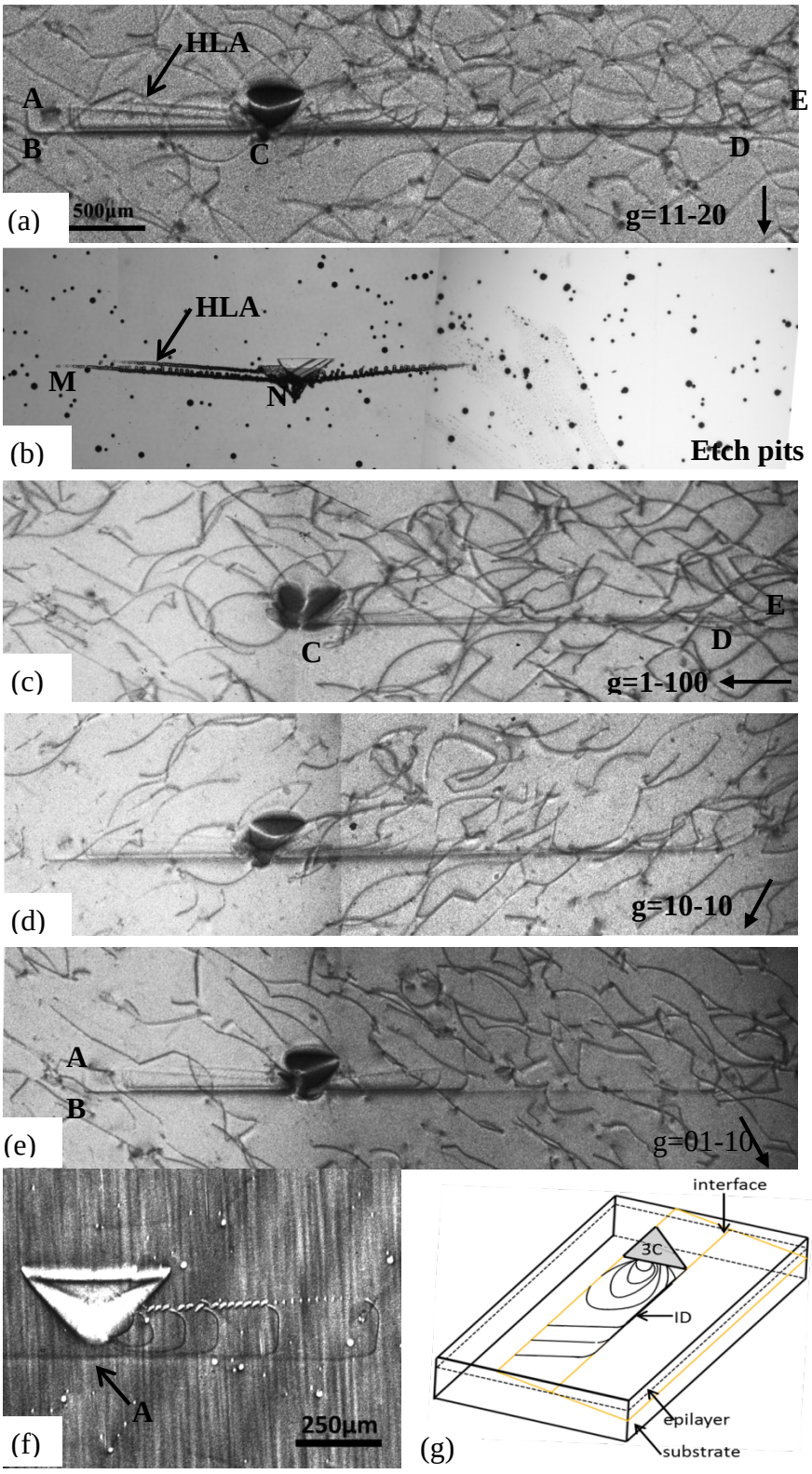

Figure 71 (a), (c)-(e) white beam X-ray topographs with transmission geometries with different diffraction g vectos recorded at the same area on 4H-SiC wafer with 12.5 µm homo-epitaxial layer. (b) A Nomarski Interference Contrast optical image showing the etch pit pattern of the same area. (f)Monochromatic beam X-ray topography with grazing geometry g=11-28 recorded on a different area. (g) Schematic shows the formation stages of interfacial dislocations from 3C polytype.

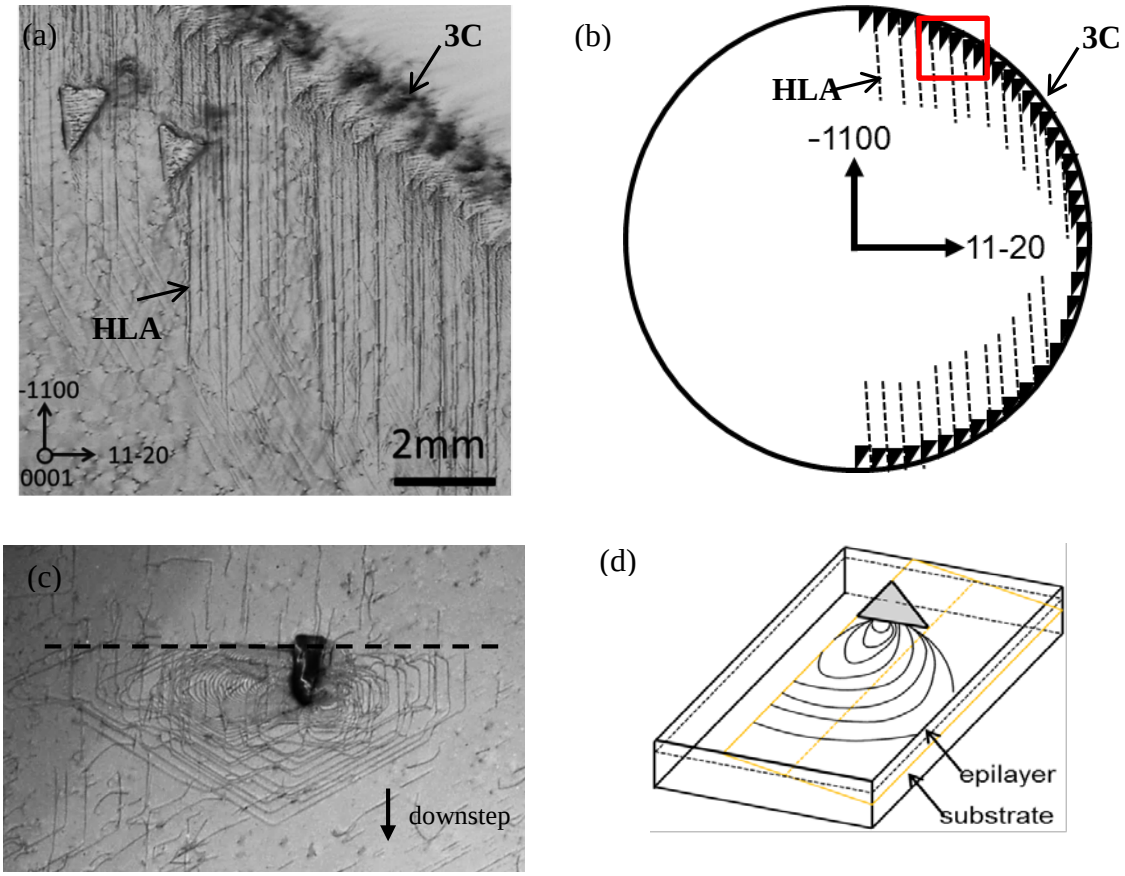

Figure 72 (a) SWBXT grazing image g=11-28 shows the 3C polytypes and half-loop arrays emanating from the edge of the wafer. (b) the schematic shows how 3C polytypes and HLAs distributing at the upstep edge of the wafer.

It is also observed a high density of 3C polytypes and HLAs distributing along the upstep edge of 4H-SiC homoepitaxial wafer as schematically shown in Fig. 72(b). In Fig. 72(a) the topography of the edge of the wafer is distorted due to the big strain field caused by close packed 3C polytypes. The straight linear feature identified as HLAs with the line direction slightly off [-1100] direction are emanating out of 3C polytypes and will grow further into the center of the wafer as the epilayer thickness gets larger. The following schematic is going to explain the reason why 3C inclusions mainly distribute at the upstep side of epilayer. It is worth to mention that no existence of interfacial dislocation where HLAs are observed in the edge of wafers. Therefore it is not necessary to have IDs to produce HLAs, and the HLAs will be produced as long as BPD segments glide in the epilayer. Further evidence can be found in Fig. 72(c). BPD half-loops emanated from one 3C-polytype expand in the epilayer, cross the interface and then continue gliding inside the substrate under thermal stress. As a result, HLAs are produced at the dash line while no interfacial dislocations are formed. Therefore the gliding of basal plane dislocations in the epilayer will create half-loop arrays.

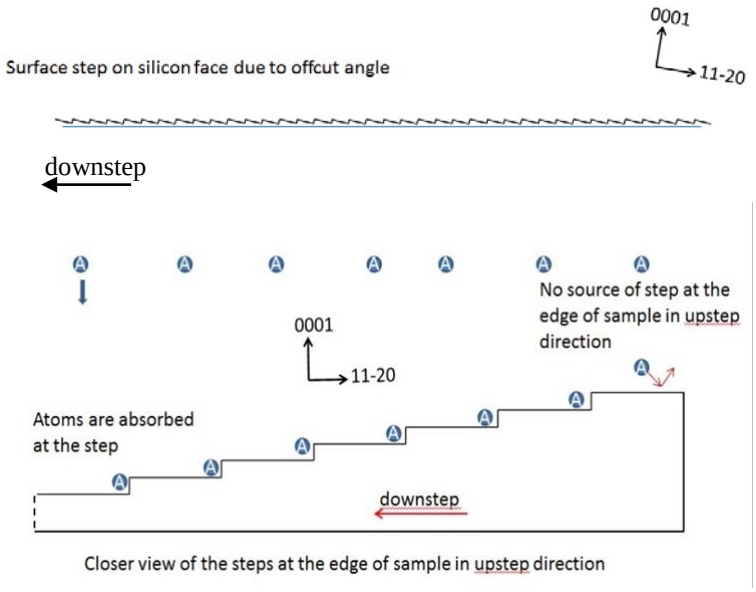

1. It is known that epilayer is grown on the substrate surface with 4 degree offcut along [11-20] direction.

2. The surface is composed by small terraces and atomic steps. If the terraces are small enough, then the atoms will be absorbed at the atomic step risers, as a result the correct stacking sequence will be replicated. While at the upstep-most terrace, there are no step risers at the edge of the wafer for the atoms to drop on.

3. As the growth continues, more atoms will be accumulating on the upstep terrace and they can diffuse freely.

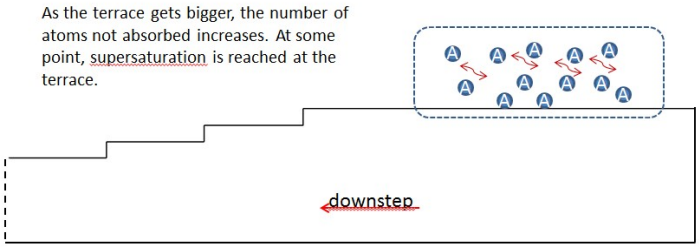

4. As the upstep-most terrace gets bigger, the number of diffusing atoms will increase. At certain point, supersaturation will be reached over there.

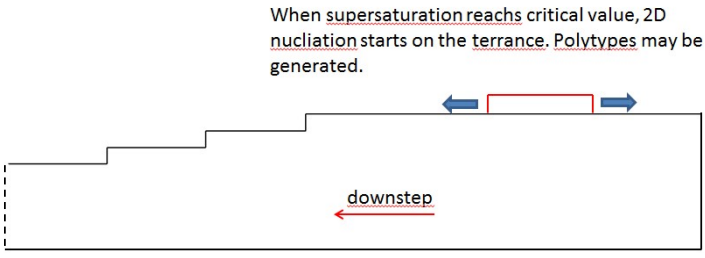

5. 2D nucleation starts to happen on the terrace when the supersaturation reaches critical value. Si and C atoms will form more stable polytype---3C polytype under no constriction.

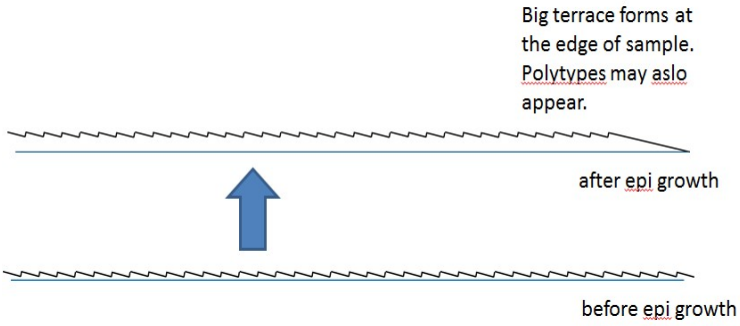

6. 3C polytype will grow bigger as the epilayer gets thicker.

10.5.3 Micropipes

Vetter *et al.* reported that BPD half-loops emanating around micropipes under the action of thermal stress [113]. The morphology of those loops consists of concentric loops and pile-ups, indicating that they were clearly generated through deformation processes. Certain parts of loops might intersect with the substrate/epilayer interface, which will be replicated into substrate if they are in screw-orientation and form interfacial dislocations and half-loop arrays. The other case is that BPD loops nucleated from micropipes can further expand under thermal stress during homoepitaxial growth until some segments touch the substrate/epilayer interface. Because the doping difference between substrate and epilayer, dislocation loops cannot across the interface and glide further into substrate, starting to side-glide along interface and creating interfacial dislocations and half-loop arrays as shown schematically in Fig. 73(e). Fig. 73(a)-(d) show examples of the formation of interfacial dislocations and half-loop arrays due to the existence of micropipes and BPD half-loops.

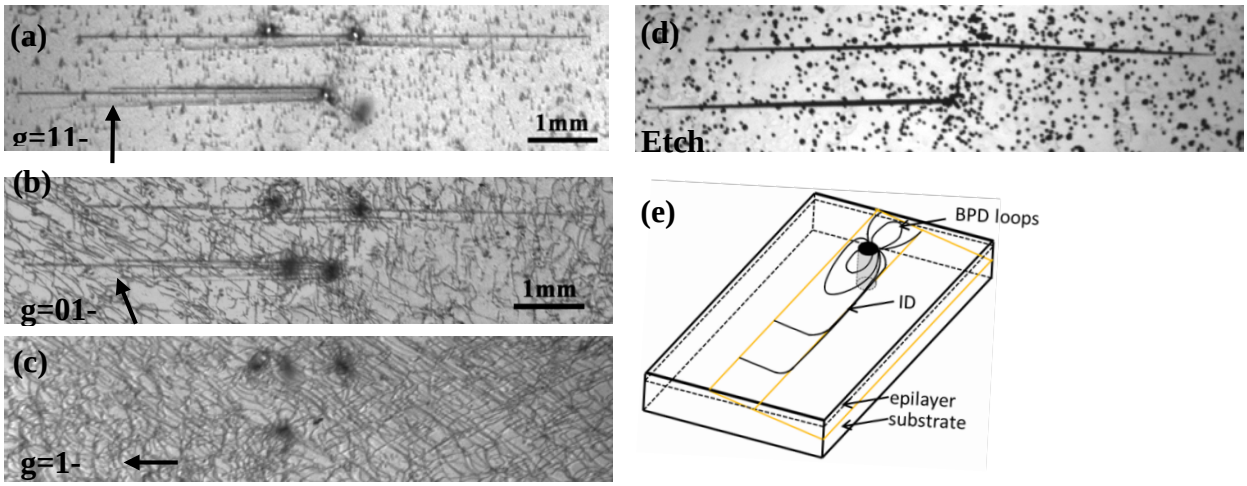

Figure 73 (a)-(c) SWBXT images recorded at different g vectors on the same area of 4H-SiC epiwafer. (d) Microscopic images of HLA etch pit patterns coming out micropipes recorded on the same area as (a)-(c). (e) Schematic shows the formation of interfacial dislocations from a micropipes during epitaxy growth.

10.5.4 Scratches

The observation of dislocation nucleation occurring at substrate surface scratches during 4H-SiC CVD homoepitaxial growth was reported by M. Dudley *et al* [1]. Sub-surface residual damage associated with the scratches is observed to act as nucleation sites for BPD half loops. And the surface intersections of these BPD half-loops on the substrate surface can create both TED and BPD arrays in the epilayer.

The Surface scratches on the Si face of 4H-SiC substrate wafer, residual from polishing, are generally accepted as dislocation nucleation sites during the epitaxial growth. In order to study how dislocations loops nucleated from scratches are replicated into the epilayer, X-ray monochromatic topographs were recorded on epilayer surface of a 4H-SiC homoepitaxial wafer with scratches at the interface. The penetration depth of grazing-geometry diffraction g=11-28 was larger than the epilayer thickness. Followed by, the wafer was etched by molten KOH at 600 ºC for 10 minutes. Then, the etch-pit patterns and monochromatic x-ray topographs recorded on the same areas were compared.

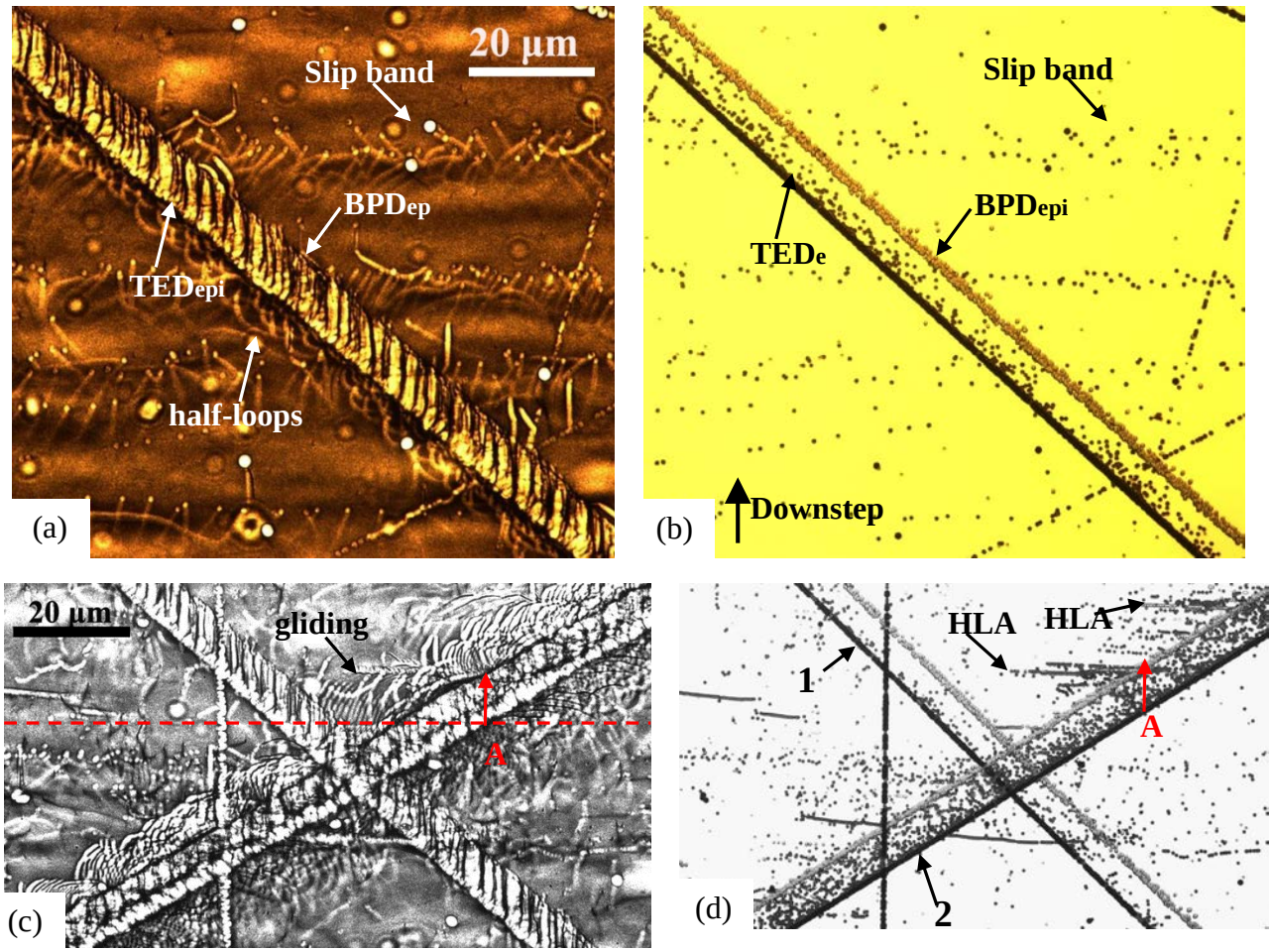

Figure 74 (a) and (c) A Nomarski Interference Contrast optical image showing two selected areas from Si face of KOH etched 4H-SiC homoepitaxial wafer. (b) and (d) Monochromatic x-ray topography with grazing geometry g=11-28 recorded on the same two areas. (a) and (b) are belonging to the same area, while (c) and (d) belongs to another area.

Fig.74 (a) is a synchrotron topography image recorded from an epilayer where the X-ray penetration depth is just down beyond the substrate-epilayer interface. There is one scratch visible on the image, positioning from top left to the low right. The scratch exhibits a broad band of contrast comprising rows of white dots at their lower ends which correspond to small hexagonal-shape TED etch pits in Fig.74 (b). There are also straight linear features emerging from the lower end and emanating parallel to the offcut direction (vertical) on the image. Compared with the etch pit pattern, shell-like-shape BPD etch pits are positioned at the end of these linear features. In addition, the length of linear features is all the same, which is corresponding to the projection length of epilayer thickness along the downstep direction. At the opposite side of the scratch, dislocation half-loops are identifiable to expand towards the substrate. Four horizontal slip bands composed of curved BPDs with TEDs attached at the downstep direction are also visible on this X-ray topography image, which exhibits the conversion of BPDs into TEDs at the interface during epitaxial growth.

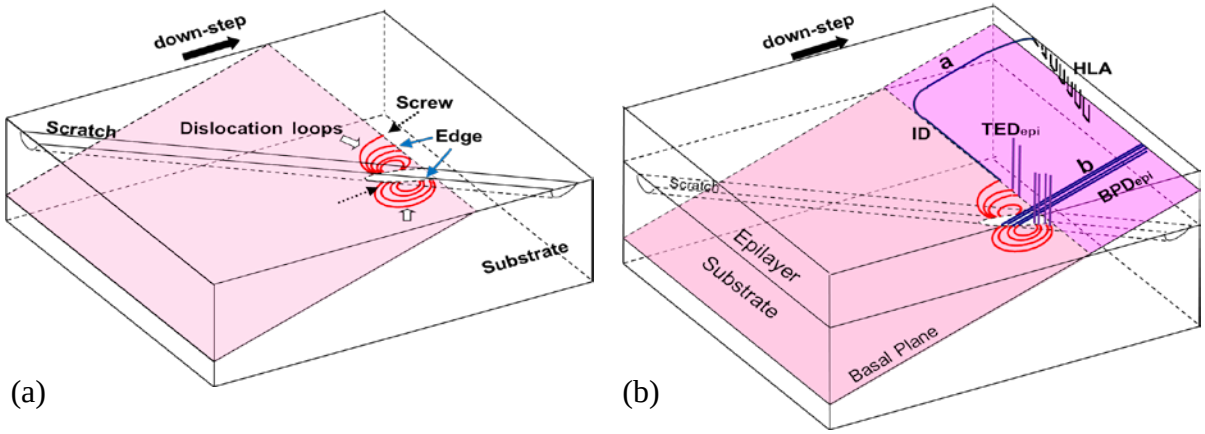

Figure 75 Schematic diagrams show (a) generation of dislocation loops near the substrate surface due to the scratch, and (b) Two possibilities for replication of the loop surface intersections during CVD epitaxial growth.

During homoepitaxial growth, the residual BPD half-loops associated with the deeper scratches can be replicated during growth. This replication involves conversion of the original deformation induced half-loops, at their points of surface intersection, into pairs of growth dislocations. The character of the growth dislocations produced during this conversion process is determined by the nature of surface intersections of the BPD half loops. The surface intersection of BPD loops emanating from scratches can be either in screw orientation or edge orientation as shown in Fig. 75(a). It is well known that BPDs intersecting a growth surface close to screw orientation are likely to be replicated on the basal plane in contrast to edge oriented surface intersections which are likely to be converted to TEDs. Thus, each single scratch are likely to lead to the production of one BPD array and one TED array during CVD growth as schematically shown in Fig. 75(b), which explains the reason why TEDs are positioned at or very close to the scratch at the downstep direction, and the length of all BPD segments along the downstep direction are the same which is equal to the projection length of epilayer thickness onto basal plane. At the same time, the BPD half-loops can also extend deeper into substrate at the opposite side of the scratch if the thermal stress is larger than critical shear stress required for the dislocation glide.

The subsurface damage associated with another scratches from bottom-left to the top-right in Fig. 74(c) and (d) appear to be a little more severe than the one in Fig. 74(a) such that higher densities of TEDs and screw-oriented BPDs are discernible at the scratch site. Differently, the broad band of BPDs replicated into epilayer from the scratch 'a' is composed by curved BPDs, instead of straight linear features. It seems that these BPDs replicated from the substrate at position 'A' start to side-gliding along certain interface (indicated by red-dash line) once the critical thickness is exceeded. Meanwhile, half-loop arrays are also produced as pointed out in Fig. 74(d)

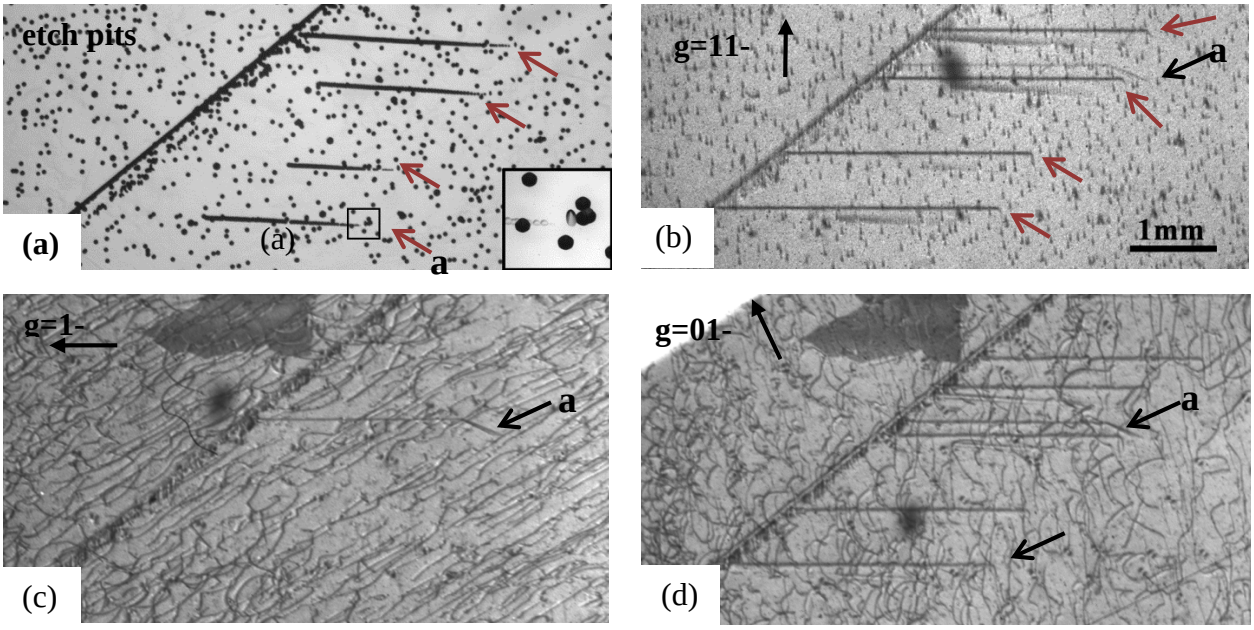

Figure 76 (a) A Nomarski Interference Contrast optical image recorded from Si face of KOH etched 4H-SiC homoepitaxial wafer. (b) – (c) SWBXT images with various diffraction g vector recorded on the same area.

Fig. 76 shows examples of a scratch which generates BPDs that can expand during epilayer growth to produce IDs and HLAs. Four interfacial dislocations which produce each HLAs are pointed out by red arrows in Fig. 76(b). According to the dislocation contrast analysis $\boldsymbol{g} \cdot \boldsymbol{b}$, their burgers vector are 1/3[-2110] as they are out of contras at g=1-100, while interfacial dislocation 'a' having no corresponding HLAs is still in contrast at g=1-100. Moreover, the line direction of its threading arm is not along off-cut direction as the other four are.

In conclusion, detailed confirmation is presented that screw-oriented threading BPDs which are forced to glide when replicated to a critical thickness (according to the Matthews-Blakeslee mechanism) in the epilayer in turn give raise to HLA's. It was also shown that HLAs can be generated from BPD half-loops nucleated in epilayer surface, BPD half-loops generated from 3C inclusions in the epilayer, BPD half-loops produced from micropipes and BPD half loops emanating from substrate/epilayer interface scratches. In addition, it was found that only those screw BPD segments with Burgers vectors parallel to the offcut direction appear to create HLAs.

10.6 Study the Sign of Interfacial Dislocations and Half-loop Arrays.

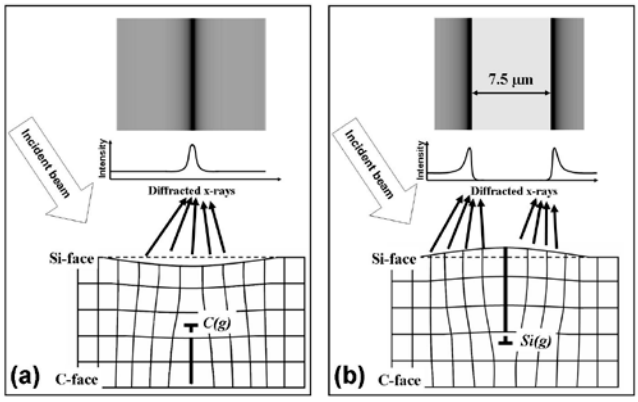

Figure 77 (a) the simulated X–ray back-reflection topography of edge dislocation with extra half plane pointing downward (b) the simulated X-ray back-reflection topography of edge dislocation with extra half plane pointing upward [36].

Huang *et al.* [36] reported that the contrast of edge-type BPD is related to its extra half-plane position. In Fig. 77, the white stripe or dark line contrast of basal plane dislocation is due to the defocusing or focusing of x-ray caused by the convex or concave shaped basal planes associated with the edge component of the partial dislocations. As it is explained in the above chapter, the extra half-plane of interfacial dislocation is pointing downward *i.e.* inside the substrate, thus the contrast of interfacial dislocation should be dark line; BPD segments of the HLA and ID are produced together by the same gliding BPD, but they have nearly opposite line directions leant from the formation mechanism of HLAs, therefore the extra half plane of BPD segments of the HLAs is pointing upward *i.e.* inside the epilayer, thus the contrast of half-loop arrays should be white.

A SiC polytype can be considered as the stacking sequence of 'tetrahedra' with Si core or C core. Each tetrahedra is composed by one carbon atom in the center and covalently bonds to four Si atoms separately (or vice versa). One of Si-C bonds is parallel to (0001) direction, which is normal to the plane determined by the other three Si atoms called 'c-plane'. If the tetrahedra rotate around c-axis by 180°, a different variant called 'twinned' tetrahedra is formed as shown on Fig. 78(a). The projection of SiC tetrahedra along $<11\bar{2}0>$ direction will appear in the form of acentric triangle as shown in Fig. 78(b), since the tetrahedron has trigonal symmetry about c-axis. The projected triangle only shows two Si atoms at the base, which suggests that two Si atoms at the base get overlap with each other. There are two kinds of Si-C bonds at the base; the longer one indicate by the arrow in Fig. 78(b) is called 'single-dangling bond', while the short one composed by two overlapped Si-C bonds is called 'double-dangling bond'.

The gliding of dislocations is realized by translating atoms on the slip plane by the magnitude of dislocation Burgers vector. In Fig. 78(b), the dislocation Burgers vector of $\frac{1}{3}[\bar{2}110]$ (equal to the magnitude of lattice parameter **a**) is required if translation of atoms *i.e.* the Si atom at the top from one tetrahedra to the adjacent one. However, basal plane dislocations are composed by two partials with narrow stacking fault band in between (~33 nm wide in 4H-SiC [70]), since SiC is known to have very small stacking faults energy (14.7 ± 2.5 mJm^{-2} for 4H-SiC and 12.2 ± 1.1 mJm^{-2}). Usually, A perfect screw dislocations, for example 1/3[11-20] is dissociated into two 30 degree partials 1/3[10-10] and 1/3[01-10].

$$\frac{1}{3} < 11\bar{2}0 > \rightarrow \frac{1}{3} < 1\bar{1}00 > + \frac{1}{3} < 01\bar{1}0 >$$

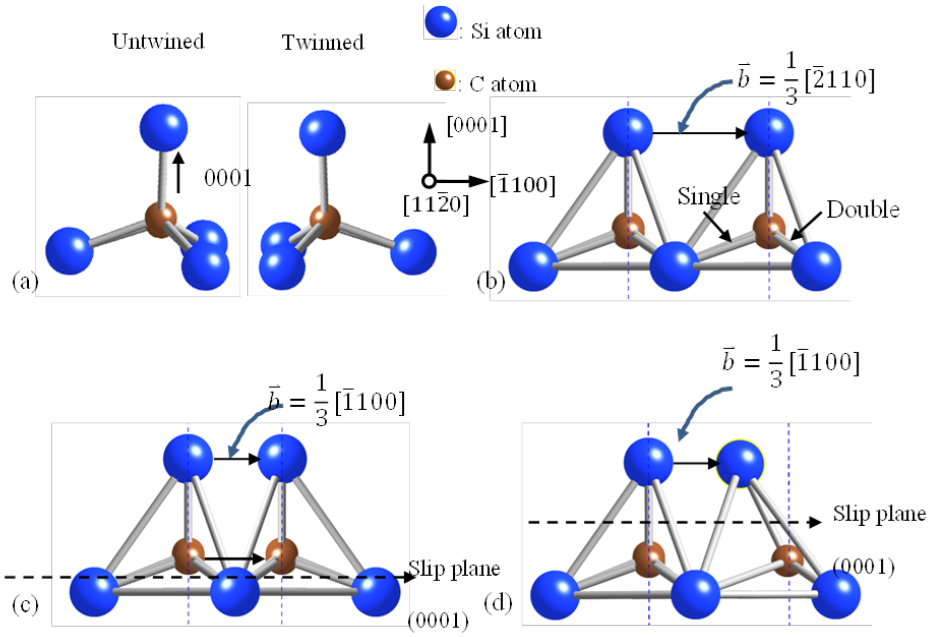

Figure 78 (a) untwinned and twinned SiC tetrahedras which are composed by one C atom at the center and bonded with four Si atoms symetricaly around it. (b) triangle variants obtained by the projection of SiC tetrahedra along <11$\bar{2}$0> direction. (c) The motion of partial dislocation belongs to 'glide' set. (d) The motion of 'shuffle' set.

The partial dislocation glide causes atomic translation in SiC. There are two possible (0001) slip planes in SiC: either between the narrowly spaced C and Si planes in Fig. 78(c) known as 'glide plane' , or alternatively, between the widely spaced C and Si planes in Fig. 78(d) known as 'shuffle plane"[181]. These two different slip planes give rise to dislocations which have different core structure, i.e. either Si core or C core, and behavior. As the partial dislocation with the Burgers vector $1/3[\bar{1}100]$ moves, all the atoms above the slip plane are sheared by the magnitude of this dislocation's Burgers vector. In the case of partials belong to glide set, both Si and C atoms above the slip plane will shear by the magnitude of $1/3[\bar{1}100]$, resulting a twinned variant in Fig. 78(c), the same bond energy as before. In the case of shuffle set, only the Si atom above the slip plane is translated by the magnitude of $1/3[\bar{1}100]$, resulting a distorted and unstable Si-C bond with high energy which can be seen in Fig. 78(d). Therefore, the motion of partial dislocation in SiC can only happen on the slip between narrowed spaced Si and C planes i. e. glide set.

For an undissociated BPD, the magnitude of the 1/3<11-20> Burgers vector is twice the *d*-spacing of the (11-20) planes so that dislocations close to edge orientation are expected to have cores comprising two extra half planes as shown in Fig 79(a) (as was originally established for HCP materials)[182]. Upon dissociation, partials of the same sign are expected, with either Si or C-core depending on the sign of the original dislocation, separated by a Shockley fault as shown in Figs. 79(b) and (c). Likewise, if dislocations with significant screw components dissociate, opposite sign partials are expected as shown in Figs. 79(d) and (e). As it is explained above interfacial dislocations and BPD segments of half-loop arrays belong to pure edge dislocation, their partials are having either two Si cores or two C cores, which is denoted by Si(g) and C(g) following the notation of Alexander *et al* [183]. Since the motion of Si(g) and C(g) involves the

breaking Si-Si or C-C bonds separately. And the energy to break Si-Si bond is around 2.3 eV while 3.7 eV for C-C bond. As a result, Si-core is more mobile compared with C core.

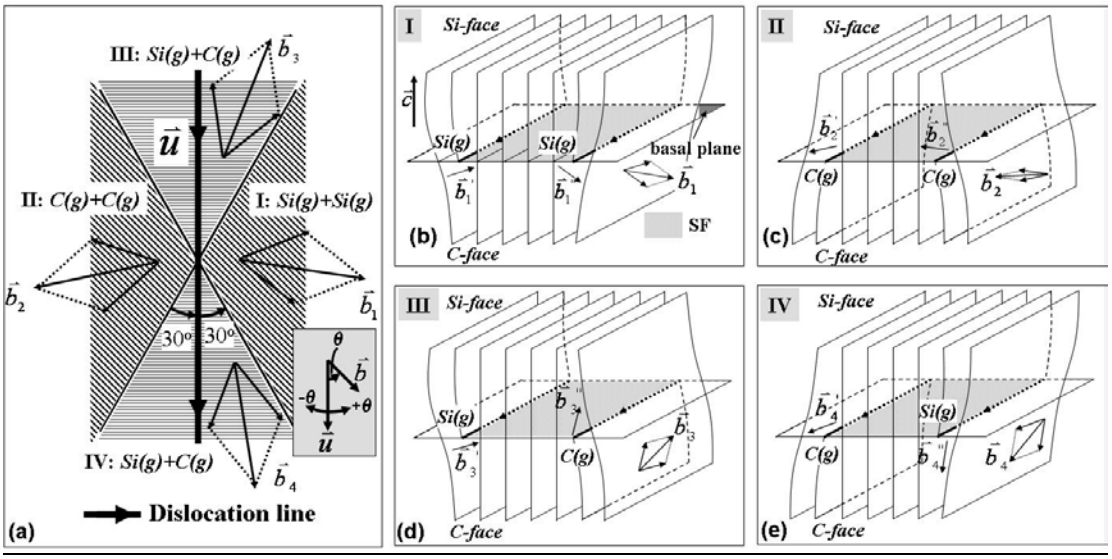

Figure 79 Schematics showing Shockley partial dislocations of different core structures dissociated from a perfect BPD. (a) Partial dislocation core structure for various angles θ between the Burgers vector, **b**, and line direction, **u**, of the perfect BPD, defining regions I-IV; (b) Region I: $30^o<\theta<150^o$, the BPD is dissociated into two Si-core partials; (c) $210^o<\theta<330^o$, the BPD is dissociated into two C-core partials; (d) $-30^o<\theta<30^o$, one Si-core and one C-core; (e) $150^o<\theta<210^o$, one Si-core and one C-core. θ is defined in the inset of (a) [173].

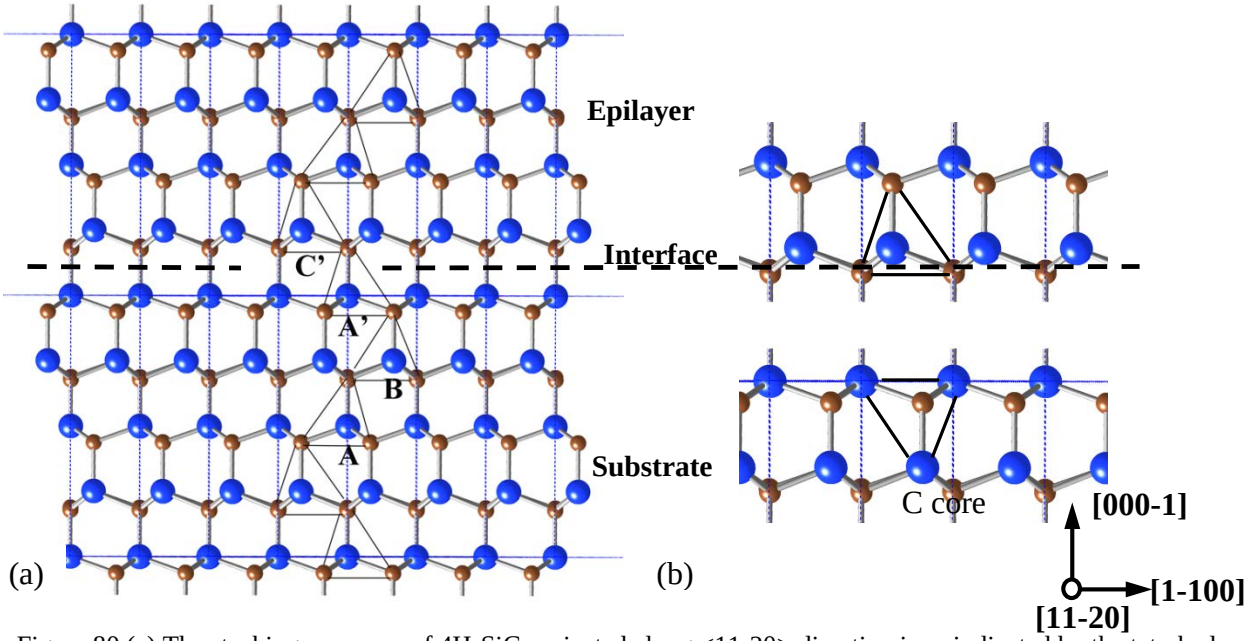

Figure 80 (a) The stacking sequence of 4H-SiC projected along <11-20> direction is as indicated by the tetrahedra ABA'B', and the interface is indicated by the dash line. (b) The magnified image of tretrahedra at the interface. The Si-core tetrahedron above the interface and C-core tetrahedron below the interface are marked out.

4H-SiC epilayer is grown on the Si-face of its substrate. The surface breakage always happen at the widely spaced C and Si planes where Si-C bonds need less energy to break. The interface between substrate and epilayer is as indicated in Fig. 80(a), substrate terminating at Si

atoms and epilayer starting at C atoms along <000$\bar{1}$> direction. As it is mentioned above, the slip plane of the partials are only between the narrowly spaced Si and C planes. Therefore the extra half plane inside the epilayer (BPD segments of half-loop arrays) has to terminate at Si atom; the extra half-plane pointing downwards (interfacial dislocations) has to terminate at C atom. The interfacial dislocation has two partials with immobile C(g), while the BPD segment of half-loop array is dissociated into two mobile Si Cores. During device operation, BPD segments of HLAs can expand into stacking faults caused by electron-hole recombination more easily compared with interfacial dislocations.

10.6.2 Formation of Shockley Faults Associated with HLAs

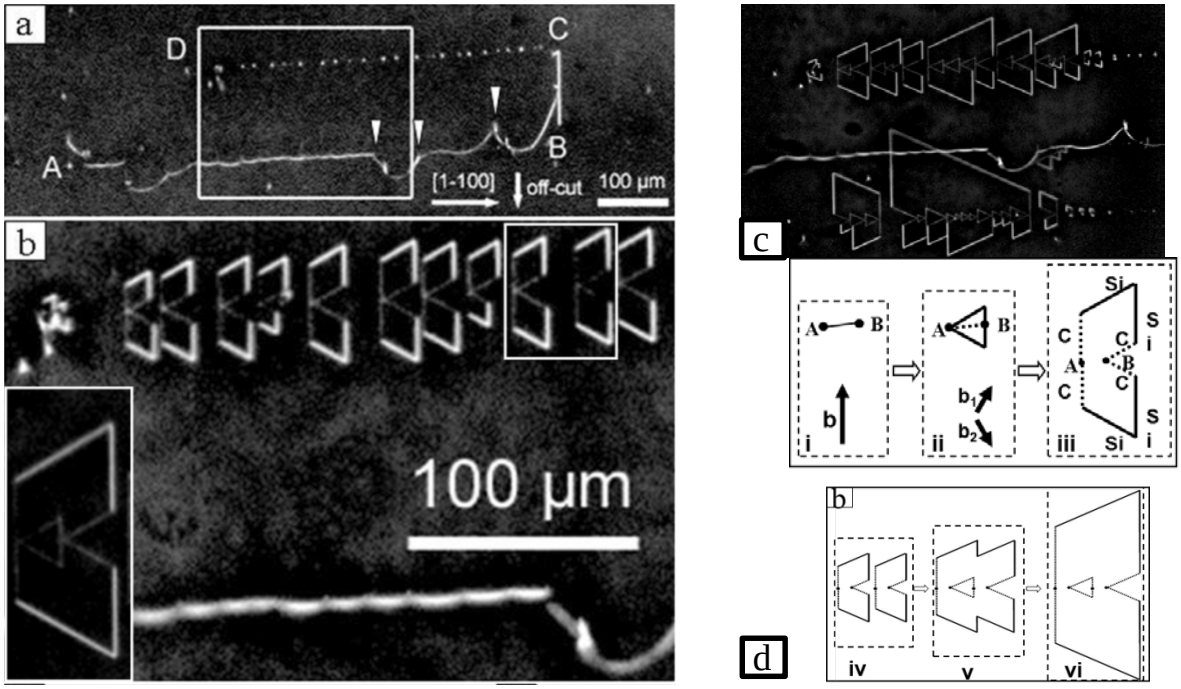

Figure 81 (a) UVPL image of a HLA (the array of dots along the line DC) before extended UV exposure. The HLA is connected to the mobile threading segment of the BPD at C. The interfacial segment of BPD is along AB. (b) Magnified view of boxed area in Fig. 1(a) after extended UV exposure. (c) HLA and ID configuration after longer UV exposure. (d) Schematic diagram showing the evolution of the rhombic shaped faults during dissociation [173].

Previous work has shown that there are pairs of closely-spaced TED surface intersections associated with each of the dots in the HLA, and based on the behavior of the HLAs in *p-i-n* diodes under forward bias these are connected by a short BPD segment to form a half loop [159,173,184]. When the as-grown sample is subsequently subjected to extended UV exposure, electron-hole recombination causes the BPD segment at each of the white dots in the HLA in Fig. 81(a) to expand in the form of rhombic shaped Shockley faults, and the two brighter segments bounding each rhombic shape, which expand in opposite directions, are mobile Si-core partials leaving the two fainter segments which are the immobile C-core partials, as shown in Figure 81(b). Both types of partials have been shown to have 30° character. As expansion continues further, the partials emanating from adjacent HLA basal segments merge and annihilate indicating that they are all on the exact same basal plane as shown in Fig. 81(c). The expansion of the faults continues until they span the epilayer. The dissociation of Si-core partials and the

evolution of the rhombic shaped faults are schematically shown in Fig. 81(d). In (i), the initial BPD segment is pinned between A-TED and B-TED. In (ii), this BPD segment dissociates in the form two inclined and two vertical segments of mobile, Si-core and 30^0 partials gliding towards opposite directions. In (iii), the further partial expansion creates two inclined and two vertical segments of immobile, C-core and 30^o partial (dashed lines). In (iv)-(vi), the annihilation process occurs as the Si-core partials from one element in the HLA meets the C-core partials from the adjacent element as they have opposite Burge's vectors. This also indicates that all of the partials are on the exact same basal plan. In another word, all the BPD segments of a HLA are lying on the same basal plane, which further confirm the formation mechanism of HLAs.

It should be noted that, during UV exposure, the ID composing of two C-core partials does not experience stacking fault expansion along most of its length as shown in Fig.82 (a) and (b) except at short segments (e.g. those indicated by arrow tips) where pinning causes its line direction to deviate sufficiently from [1-100] to endow it with a significant screw component. Learnt from Fig.79, screw-oriented BPD is composed of one mobile Si-core partial and one immobile C-core partial. The mobile segment which interfacial dislocation is attached with is screw-oriented, which is observed to expand into stacking faults as shown in Fig. 82, since the partials are gliding at different speed due to the electron-hole recombination enhanced dislocation glide.

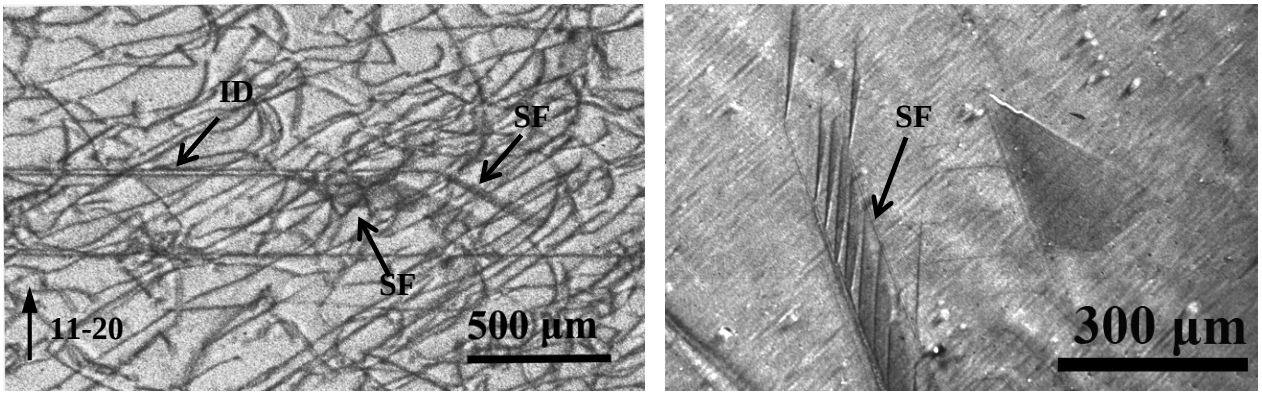

Figure 82 (a) and (c) examples of the mobile segments that interfacial dislocations are attached with can form stacking faults which are pointed out by arrows.

10.6.3 Conclusion

The interfacial dislocation is composed of two immobile C-cores, while the basal plane segments of half-loop array are composed of two mobile Si-cores. As a result, during device operation or UVPL image, BPD segments of HLAs will dissociate into two inclined and two vertical segments of mobile, Si-core, 30^o partials via electron-hole recombination enhanced dislocation glide, which will expand towards opposite direction and form Shockley faults on the basal plane, a phenomenon which leads to lifetime limiting forward voltage drop. Meanwhile, the edge component of interfacial dislocation will not form stacking faults. Sometimes, the screw-oriented gliding segments of interfacial dislocations composed by one Si-core and one C-core are observed to form stacking faults.

11. Study of V and Y shape Frank-type Stacking Faults Formation in 4H-SiC epilayer

11.1 Outline

Nomarski optical microscopy, KOH etching and Synchrotron Topographic studies are presented of faint needle-like surface morphological features in 4H-SiC homoepitaxial layers. Grazing incidence synchrotron white beam x-ray topographs show V shaped features which transmission topographs reveal to enclose ¼[0001] Frank-type stacking faults. Some of these V-shaped features have a "tail" associated with them and are referred to as Y-shaped defects. Geometric analysis of the size and shape of the V-shaped faults indicates that they are fully contained within the epilayer and appear to be nucleated at the substrate/epilayer interface. Detailed analysis shows that the Y-shaped defects match well with the substrate surface intersections of **c**-axis threading dislocations with Burgers vectors of **c** or **c**+**a** in the substrate which were deflected onto the basal plane during substrate growth, similarity, the positions of some V-shaped stacking faults in the center match with the positions of **c**-axis threading dislocations with Burgers vectors of **c** or **c**+**a** in the substrate and thus appear to result from the deflection of these dislocations onto the basal plane during epilayer growth. However, most V-shape stacking faults around the edge are not associated with any defects in the substrate and it appears that opposite sign of Frank partials generating from the interface. Based on the observed morphology of these defect configurations we propose a model for their formation mechanism.

11.2 Introduction

It is generally acknowledged that defects within the active regions of 4H-SiC devices can have a deleterious effect on their performance. Since most of the defects in homoepitaxial layers are inherited from the substrate upon which they are grown, much effort has recently been expended on minimizing the defect density in PVT-grown 4H-SiC substrates. However, for the finite density of defects that currently remains in the substrate, a key issue is understanding how they propagate into the epilayer since this can present an opportunity to engineer the defect configuration in the epilayer. For example, if basal plane dislocations (BPDs) are allowed to propagate into the epilayer and result in the formation of Shockley stacking faults they are known to cause forward voltage drop in *pin* devices [185]. Consequently, much effort has been devoted to ensuring that basal plane dislocations are converted to relatively benign threading edge dislocations (TEDs) at the substrate-epilayer interface. This is achieved through modification of surface morphology (etching) [161] or by the use of epilayer growth interruptions [163]. Currently, some 97% of basal plane dislocations are typically converted to TEDs with the remaining few per cent constituting BPDs in pure screw orientation which are notoriously difficult to convert to TEDs. Other epilayer defects such as carrots, which have been associated with screw dislocations in the substrate, also have surface morphological features associated with them [156]. Both the surface morphological defects and the underlying crystallographic defects associated with carrots can have a negative influence on device performance thus warranting significant efforts towards their elimination.

Generally speaking, all defects piercing the substrate growth surface must propagate into the epilayer either in their original form or alternatively be deflected into a different direction of propagation. In all cases, the displacement vectors associated with the defects must be conserved

across the interface. For the case of dislocations, Burgers vector must be conserved across the interface although line direction can be modified (a case in point would be the redirection of BPDs into TEDs). For stacking faults, the sum of the Burgers vectors of the bounding partial dislocations plus the fault vector must be conserved. Note that it is also possible that a perfect dislocation in the substrate can dissociate into partial dislocations separated by a stacking fault as it crosses the interface. This has been observed to happen during bulk growth of 4H-SiC but is also governed by the conservation of displacement across the growth surface.

In this paper we present observations of epilayer defects predominantly observed close to the edges of an n-buffer plus n-type drift structure. These defects appear to be faint needle-like linear surface morphological features. Synchrotron white beam topography images show that these features are associated with configurations of stacking faults in the epilayer. A formation mechanism for these defects is presented.

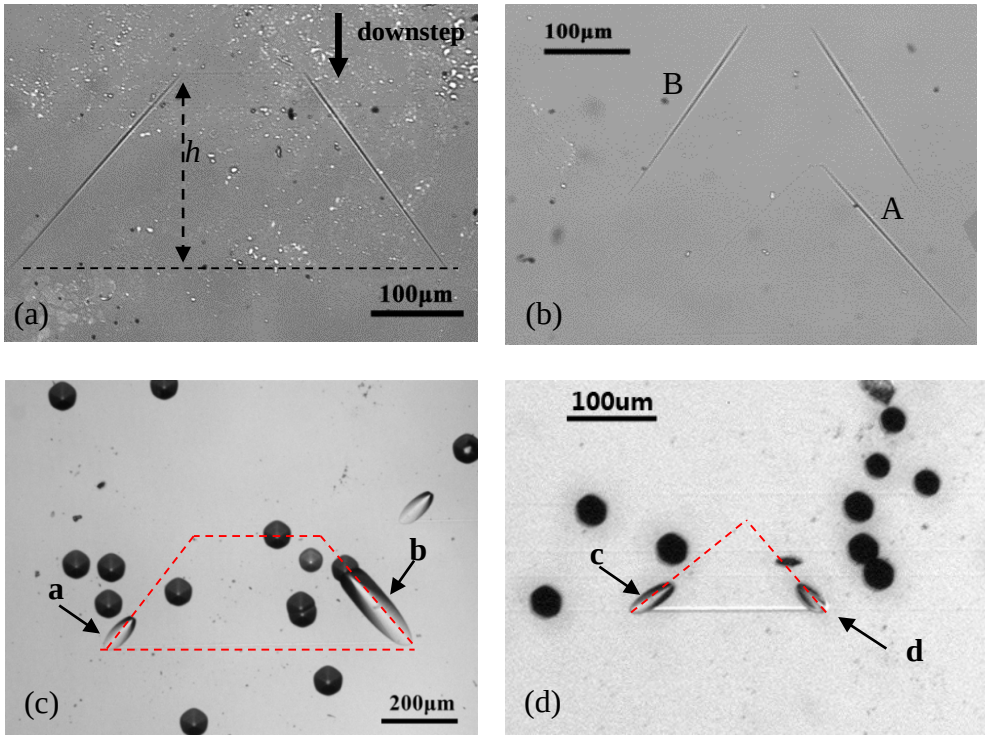

Figure 83 (a) and (b) Nomarski optical micrographs show the surface morphological features associated with the defects of interest. (c) Nomarski optical micrographs recorded on KOH etched Si face of 4H-SiC show Frank partials ‘a’, ‘b’, ‘c’ and ‘d’.

11.3 Results and Discussion

Fig. 83 shows optical micrographs showing the morphological features on the epilayer surface (Si-face) associated with the defects of interest. They comprise needle-like features which can be in pairs forming either triangular (e.g. at ‘A' on Fig. 83(b)) or trapezoidal configurations (e.g. at B on Fig. 83(b)). The projected “height” of each triangular or trapezoidal feature measured along the offcut direction (the downstep direction shown on Fig. 83(a)) corresponds to the thickness of the epilayer. There are two types of etch pits associated with

these features as shown in Fig. 83(c) and (d). Note etch pits ‘a’, ‘b’, ‘c’ and ‘d’ corresponding to the surface intersections of the two sides of the trapezoidal and triangle features, respectively.

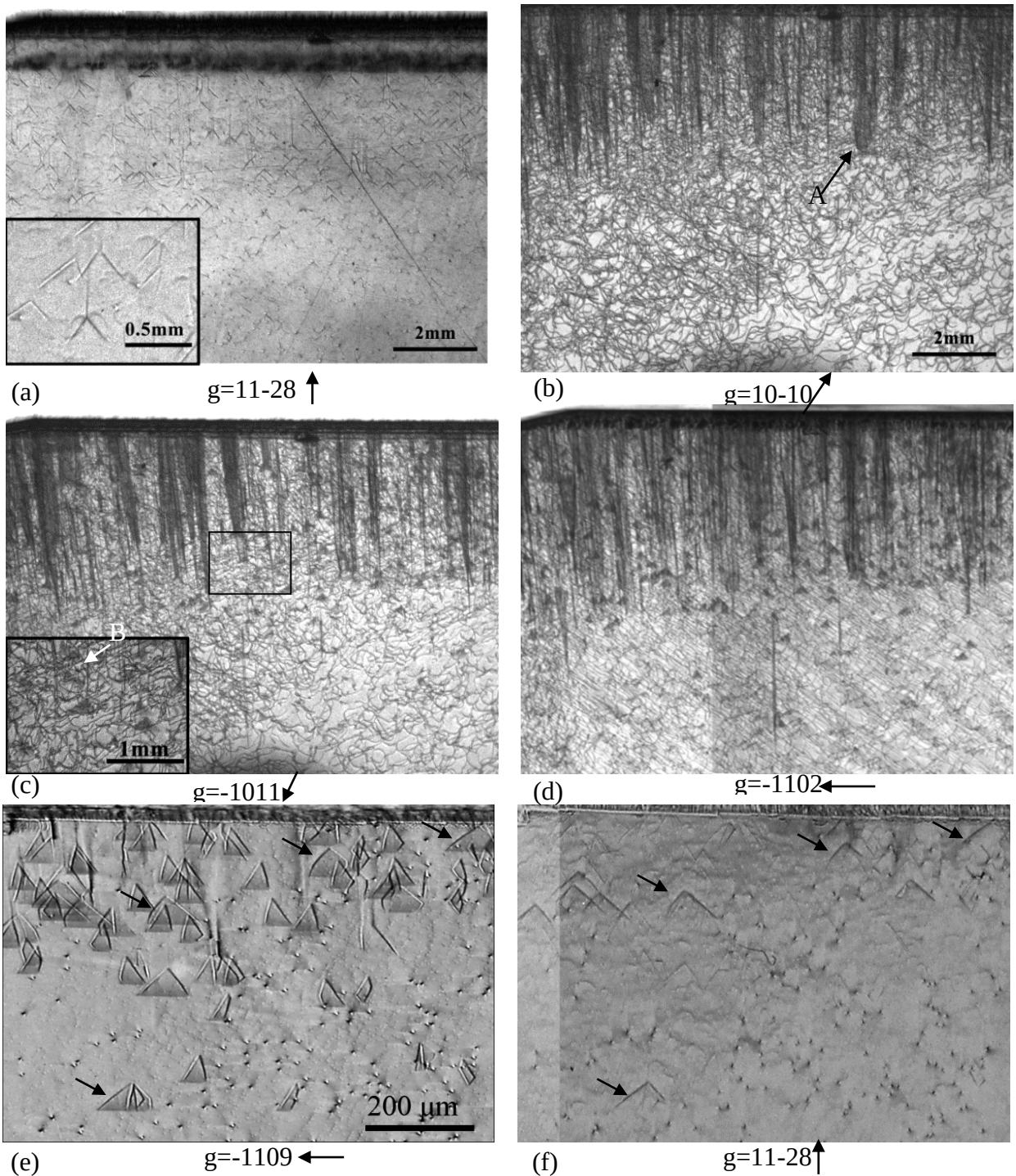

Figure 84 (a) a white beam synchrotron topography image is recorded in grazing incidence (g=11-28) on the epilayer surface (Si-face) from a region near the edge containing many such features. (b) - (d) transmission topography images with different g vectors are recorded from the same region. ‘A’ indicates the stacking faults from the substrate and ‘B’ indicates the small triangle stacking fault inside the epilayer.(e) and (f) grazing geometry topographs recorded from another wafer with epilayer thickness around 30 μm with diffraction vectors are 1-109 and 11-28, respectively.

The projected length of large etch pit ‘b’ on downstep direction is around three times bigger than the etch pit ‘a’, while ‘c’ and‘d’ are the same.

Figure 84(a) shows a white beam synchrotron topography image recorded in grazing incidence (g=11-28) from the epilayer surface (Si-face) from a region near the edge containing many such features. Figures 84(b) - (d) show topography images recorded in transmission geometry (with the Si-face epilayer on the X-ray exit surface) from the same region. Arrays of stacking faults resulting from the deflection of threading dislocations with c-component of Burgers vector inside the substrate can be observed on Figs. 84(b) - (d). (e.g. at A). In addition, Figs. 84(c) - (d) show small triangular stacking faults (as indicated by B) which correspond in size and aspect to the feature at A in Fig. 83(b). Thus it would appear that the large bases of the trapezoids or triangles (which are at the downstep end of the faults and which project perpendicular to the offcut direction) correspond to the intersections of these stacking faults with the epilayer surface. Similarly, the apexes of the triangles or the small bases of the trapezoids would appear to correspond to the intersections of the faults with the substrate-epilayer interface. The small triangular or trapezoidal stacking faults are in contrast at g=-1011 and g=-1102, while they are out of contrast at g=10-10. According to calculated phase shifts ($\delta=-2\pi\ \mathbf{g}\cdot\mathbf{R}$) which determine the stacking fault contrast behavior [68], where g is the active reciprocal lattice vector for the reflection and R is the fault vector, the fault vector for these small triangle stacking faults turns out to be ¼ (0001). Fig. 84 (e) and (f) are both grazing-geometry topographs which further confirm the Burgers vector of these V shape stacking faults, which are recorded on the same area from another 4H-SiC homoepitaxy wafer with epilayer thickness 30 μm. V shape stacking faults at g=-1109 are in-contrast while they are out of contrast at g= 11-28, confirming they are Frank-type stacking faults. It is appeared that the partial contrast is more obvious when g=-1109.

Figs. 85 shows enlargements of grazing incidence images recorded from regions A to H shown on the schematic (in the center of the figure) which shows the distribution of the features at the various positions around the wafer periphery. No matter where the location on the wafer, the triangles or trapezoids always open up towards the downstep direction of the epilayer and their projected “height” measured along the offcut direction invariably corresponds to the epilayer thickness so that they are all fully contained within the epilayer. In some cases, the individual linear features in the epilayer and the triangles are observed to have a linear “tail” attached to their apexes consisting of a dislocation projecting backwards towards the upstep direction of the epilayer. This means that this tail is penetrating down into the substrate. Similarly, trapezoids are sometimes observed to have a double tail consisting of a pair of partial dislocations bounding a stacking fault penetrating into the substrate (e.g. at ‘**a**’ on Fig. 85 (f)). The contrast from these “tails” is observed to diminish with distance from the substrate-epilayer interface in accordance with the attenuation of incident and diffracted rays in the material and their length projected along the crystal surface normal gives an indication of the depth of penetration of the X-rays into the substrate. Occasionally, the defect in the epilayer consists of a single line whose length projected along the offcut direction corresponds to the epilayer thickness. Two such features with tails attached can be observed on Fig. 85(e) at ‘**b**’ and Fig.85 (f) at ‘**c**’. No stacking fault is observed at these locations on the transmission images.

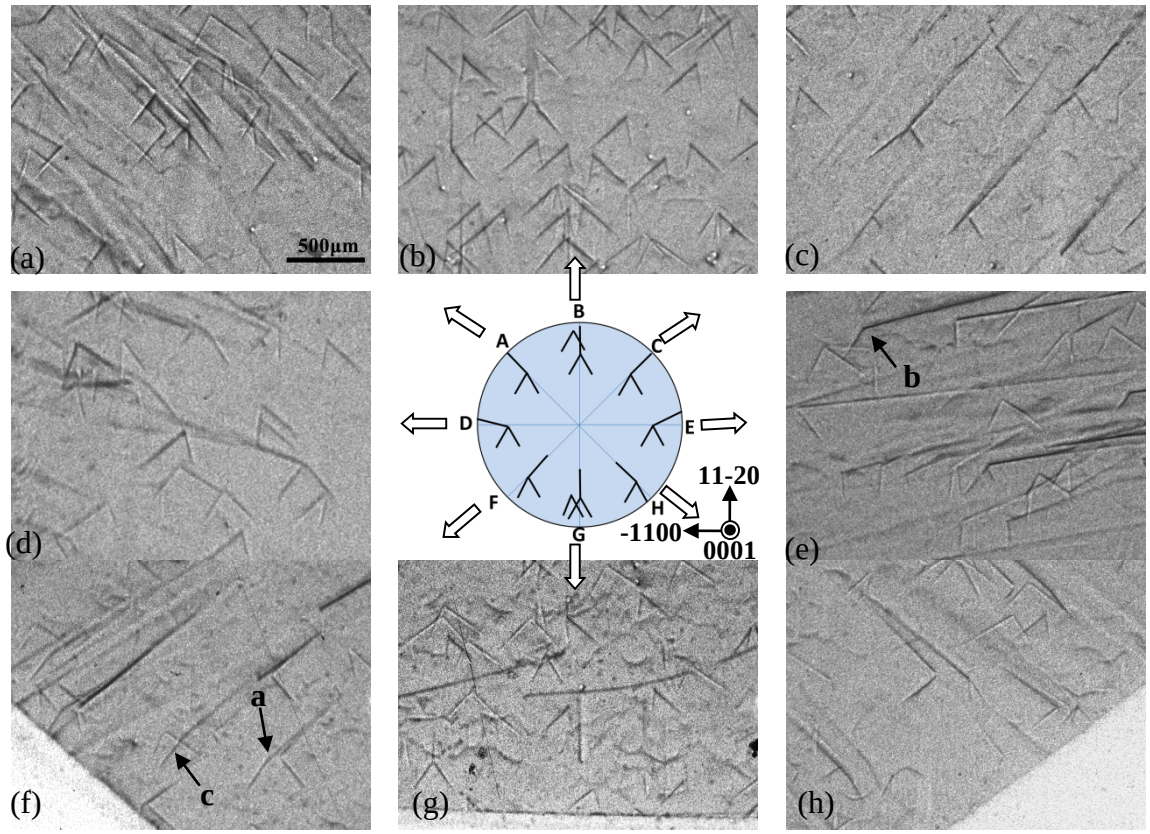

Figure 85The schematic in the middle shows how the V and Y shape defects distribute around the periphery of the wafer. (a)- (h) the grazing topographs of selected areas from point A-H on the edge of the wafer.

For those cases where the triangular fault has no tail attached (the so called "V" defects) threading dislocations with c-component of Burgers vector can be observed at the location of the apex in the epilayer (as indicated at 'A' position on grazing incidence images recorded on the epilayer surface shown in Figs.86(a1). This corresponds to the simultaneous nucleation of a stacking fault and a threading dislocation with c-component of Burgers vector at the substrate-epilayer interface. Examples of this case are shown in Figs. 86(a1) – (a2) with the schematic of the formation mechanism in (a3). Similar cases have been reported previously by Tsuchida [89]. This type of V shape stacking faults is mainly distributed in the central region of the wafer and the number is quite low. However, at the wafer periphery (<10 mm from the edge) where many V shape defects exist, threading screw dislocations (TSDs) cannot be observed at the location of the apex neither in substrate nor in the epilayer as shown at the point 'B' in the Figs.86(a2)-(b2). This is thought to be because the opposite signs ($\pm\frac{1}{4}c$) of a pair of Frank partials generate at the epilayer/substrate interface (as shown in Fig.86(f)), which is corresponding to the etch pit pattern shown in Fig. 83(d) since the magnitudes of these two partials' Burger's vector are the same. The third case shown in Fig.84 (c1)-(c2) is that the deflection of TSD with Burger's vector **c/c+a** at the substrate/epilayer interface, as the schematic shown in Fig. 84(c3). Fig. 84(d2) shows a deflected TSD intersecting with Si face before epitaxial growth at position 'D', where a Y shape Frank fault is generated as shown in Fig. 84(d3). The density of Y shape defects ae associated with the density of deflected **c/c+a** in the substrate. There is no observed direct correlation between the deflected **c/c+a** in the substrate with the Frank faults caused by pair generation of

opposite sign Frank partials, but the statistical analysis shows that these V shape SF density is also proportional to the density of deflected **c/c+a** and stacking faults in the substrate.

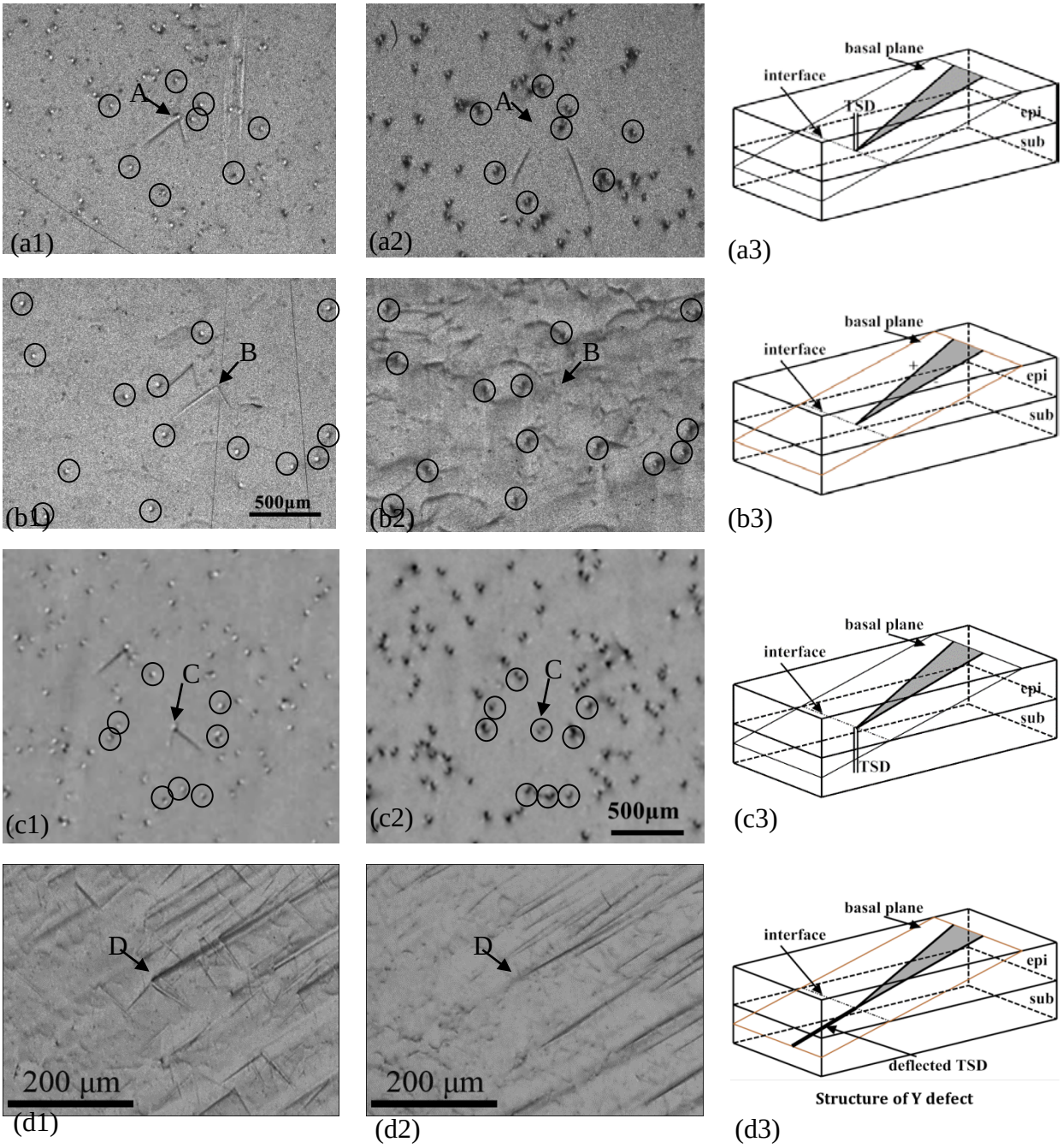

Figure 86 (a1), (b1), (c1) and (d1) are grazing topographs recorded on the epilayer surface after epilayer growth, while (a2), (b2), (c2) and (d2) are grazing topographs recorded on the substrate without epilayer. The open black dots in the images are threading screw dislocations. (a3), (b3), (c3) and (d3) are the schematic of the formation mechanism of Frank-type stacking faults.

In order to understand the morphology and formation mechanism of these defects it is instructive to first consider the defect configurations present in the substrate crystals and how

they intersect the Si-face upon which the epilayer is grown. The original PVT growth is carried out on the C-face of the seed crystal. As has been described previously, threading dislocations with c-component of Burgers vectors are prone to being deflected onto the basal plane close to the outer edges of the growing boules due to overgrowth by macrosteps which are prevalent in these regions due to the curvature of the growth interface [79,96]. This is shown most clearly on transmission topographs recorded from axial slices cut parallel to the growth direction of the boule as shown in Figs. 87(a) and (b). Threading dislocations are observed to have been deflected towards the left (a) and right (b) outer edges of the boule (occasionally they are re-deflected back into threading orientation). These deflection processes are shown schematically in Fig.87(c). The substrates used for epilayer growth are offcut by 4 degrees towards [11-20] as indicated by the red and black dotted lines on Fig. 87(c) (note the vicinal nature of the Si-face is also represented on this figure and in 87(d)). Since epilayer growth is carried out on the vicinal Si-face, any substrate dislocations which intersect that face must necessarily propagate into the epilayer in such a way that the Burgers vector is conserved. The various intersections are shown schematically in Fig. 87(d) and comprise those dislocations with **c**-component of Burgers vector in threading orientation (such as points B and C in Fig. 87 (d)) and those lying on the basal plane which intersect the seed surface at an acute angle to the offcut on both the left and right-hand sides (point A and D in Fig. 87(d)). The left-hand side of Fig. 87(a) corresponds to region G on Fig. 85 while the right-hand side corresponds to region B. Since the threading dislocations in the substrate are always deflected radially outwards, one can readily predict the configurations shown schematically in Fig. 85. During epilayer growth, A and D in Fig. 87(d) will generate Y shape defects, like those in Fig. 86(d1), while B and C in Fig.87(d) will generate V shape defects.

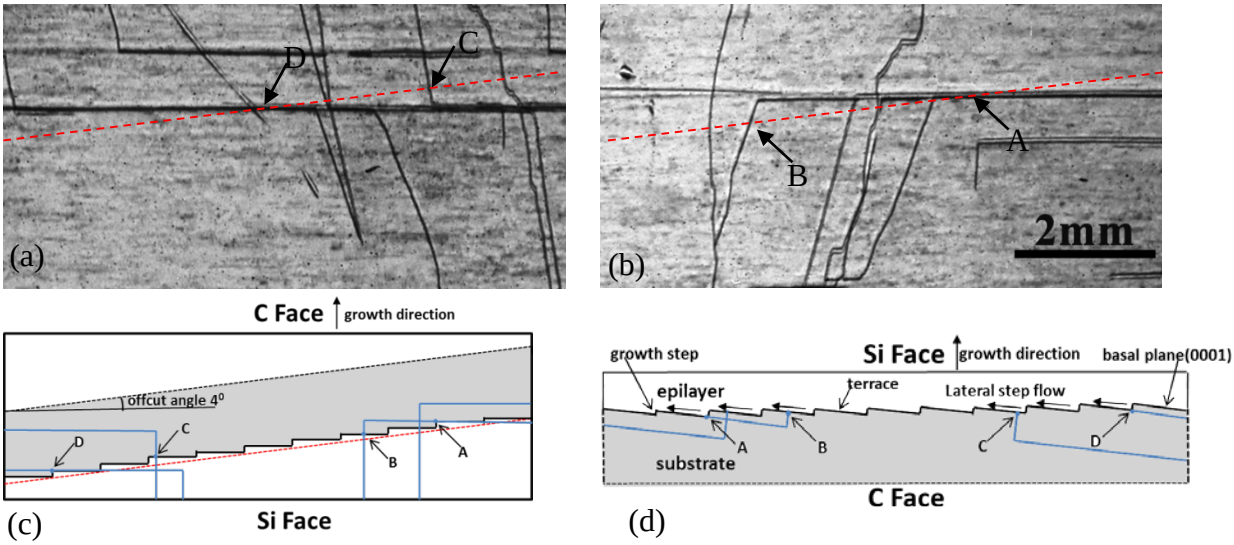

Figure 87 (a) -(b) x-ray topographs with g=0004 of axial slice show how the deflected TSD and deflected TSD at the left and right edges of the wafer intersecting with the Si surface, which is similar to those shown schematical in (c). (c) Schematic cross-section of a SiC boule (grown on the C-face) showing as-grown TSDs which have been deflected onto the basal plane. Substrate wafers are then cut from the boule with a 4 degree offcut towards 11-20 as represented by the shaded region in between the black and red dashed lines. The Si-face of such wafers (shown pointing down in (c)) is then used for epilayer growth. The upturned substrate is shown in (d). The intersection point between TSD and Si face are marked as 'A', 'B', 'C' and 'D'. (d) The intersection of TSD and deflected TSD with the interface will grow Frank-type stacking fault on basal plane towards downstep direction . The red dash lines in (a) and (b) are corresponding to the red on in (c)

In order to understand how the V and Y-shaped stacking fault configurations are created during epilayer growth it is necessary to consider the surface step configurations associated with the substrate surface intersections of these various defects and how these step configurations can be modified during the various stages of substrate surface processing prior to epilayer growth. The Si-face of the substrate is initially mechanically polished. Following this procedure, the step configuration associated with the Si-face surface intersection of a threading dislocation with c-component of Burgers vector is expected to look something like that depicted schematically in Fig. 88 (a). On the other hand, the step configuration associated with the surface intersection of a dislocation with **c**-component of Burgers vector which has been deflected onto the basal plane is expected to look something like that depicted schematically in Fig. 88 (d). Typically, following mechanical polishing, the seed is made ready for epilayer growth by an in-situ cleaning process wherein the steps often split into ¼ unit cell high increments during reverse step-flow. It is possible that some degree of step bunching can occur during this reverse-step flow leading to ¼ and ¾ unit cell height steps as shown in Fig. 88(b) & (e). Such step bunching has been previously reported during hydrogen-etching of 4H-SiC by Zhang [186]. Subsequently, when growth is initiated, vicinal steps advance over these exposed step configurations leading to the creation of V-shaped or Y-shape, **c**/4 stacking faults bounded by **c**/4 and 3**c**/4 Frank partial dislocations as shown in Fig. 88(c) for V-shape fault and (f) for Y-shape fault. In cases where the steps around the dislocation core surface intersection retain unit cell height, overgrowth would simply lead to a Frank dislocation deflected towards the epilayer step flow direction.

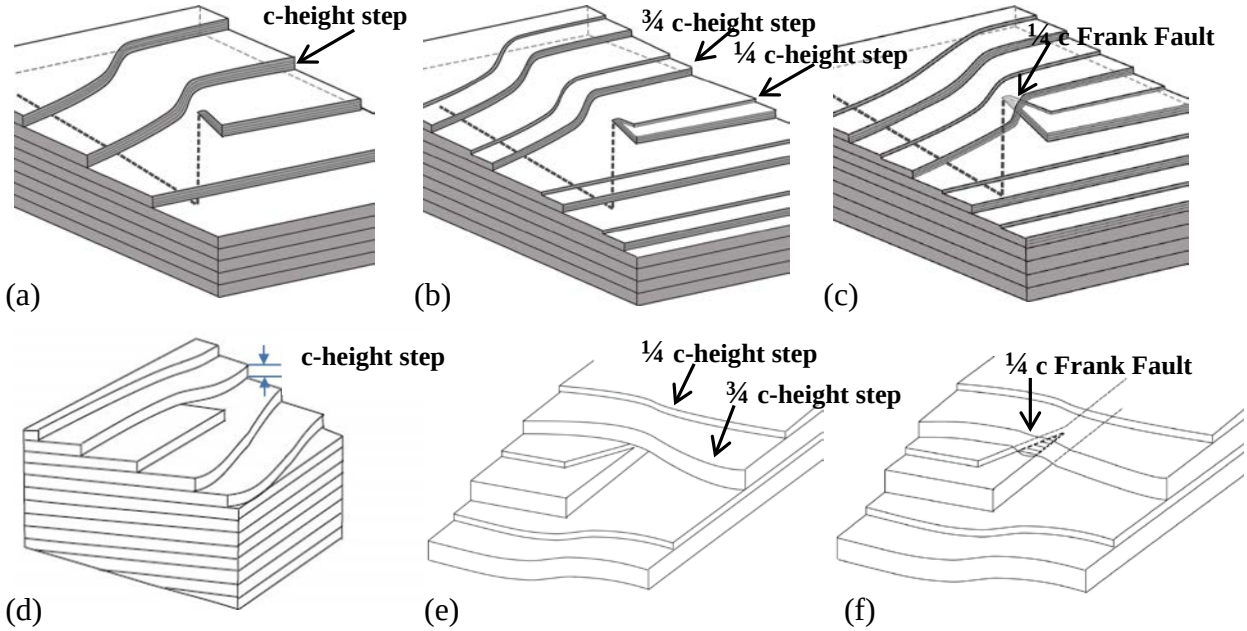

Figure 88 (a)-(c) the formation mechanism of V shape stacking fault during epitaxial growth; (d)-(f) the formation mechanism of Y shape stacking fault during epitaxial growth

11.4 Conclusion

Nomarski optical microscopic,.KOH etching and Synchrotron Topographic observations and analysis is presented of faint needle-like surface morphological features in 4H-SiC homoepitaxial layers. Grazing incidence synchrotron white beam x-ray topographs recorded from the areas containing the linear features show V and Y shaped features which transmission

topographs reveal to be ¼[0001] Frank-type stacking faults. Geometric analysis of the size and shape of these faults indicates that they are fully contained within the epilayer and appear to be nucleated at the substrate/epilayer interface. Detailed analysis shows that the positions of the V shape stacking faults around the edge of the wafer does not match with the positions of **c**-axis threading dislocations with Burgers vectors of **c** or **c+a** in the substrate, and their Frank partials are opposite sign ¼c. Therefore these V shape stacking faults are due to 2D nucleation near the edge of wafer at supersaturation condition. Similarly, the Y shaped defects match well with the substrate surface intersections of **c**-axis threading dislocations with Burgers vectors of **c** or **c+a** in the substrate which were deflected onto the basal plane during substrate growth. The observed morphology of these defect configurations allows us to propose a model for their formation mechanism. For the V shaped defects, this is based on the overgrowth of the surface spiral steps associated with the surface intersections of the threading dislocations. For the Y shaped defects this is based on overgrowth of the special configurations of steps at the surface intersections of the threading dislocations that were deflected onto the basal plane during substrate growth.

Conclusions

The relationship between growth condition and defect nucleation in 4H-SiC substrate, epilayer and devices has been investigated using synchrotron x-ray topography as well as other characterization techniques.

1) Studies are presented of combined application of projection and section topography to dislocations and stacking faults analysis in PVT-grown 4H-SiC wafers. The intersection of a dislocation with the incident beam inside Bormann Fan provides valuable sign, depth and line direction information of the dislocations. Section topography of threading screw dislocations inside axial slices shows dark contrast associated with the direct image and light contrast associated with the dynamic image. The sense of displacement of the two components of the direct image reveals the sign information of screw dislocations due to orientation contrast. When the dislocation intersects the entrance surface at an angle, its dynamic image is accompanied by oscillatory contrast due to the intermediary image; for threading screw and threading edge dislocations in the c-plane wafer, fringes are clearly observed in section topography.

2) Though widely used as a defect characterization tool for SiC wafers, etching exhibits large limitations when applied to BPD density analysis since it 1) only reveals the defects that intersect the sample surface and 2) it wrongly considers the average length of BPDs as almost the same as the sample thickness. Therefore the value of BPD density obtained by etch pit counting is potentially very misleading. On the other hand, X-ray topography, by nature providing a true 3-D view of the overall defect distribution reveals all dislocations not only intersecting the surface but also lying inside the wafer. It gives more precise results when used in density assessment. The ratio of BPD density calculated from SXRT image (considered as representative of real density) to that from etch pits is larger than $1/\sin\theta$, where θ is the offcut angle of the wafer.

3) A mechanism of basal plane dislocation (BPD) multiplication named Hopping Frank-Read sources in 4H-SiC has been developed. These configurations result from a sequence of processes involving inter-conversion between non-screw oriented glissile BPDs, which intersect the slightly off-axis growth interface, and TEDs. These inter-conversion processes are brought about by step interactions on the growth interface. These processes repeat resulting in a dislocation comprising several glissile BPD segments on parallel basal planes interconnected by relatively sessile TED segments. Should such interconnected BPD and TED segments experience thermal stress whilst in the growth chamber, the glissile BPD segments would readily glide but would be pinned at their connection points to the relatively sessile TED segments leading to the operation of single ended Frank Read sources. Through such processes, BPDs appear to “hop” from one basal plane to another through what is termed here as a Hopping Frank-Read source mechanism. Moreover, the glissile BPD segments adopt <1-100> line directions demonstrating that such 30 degree orientations correspond to the Peierls valleys on the basal plane. This mechanism of BPD multiplication in 4H-SiC appears to be dominant.

4) **c** and **c**+**a** threading dislocations lead to the formation of stacking faults when deflected onto (0001); three types are discussed in this paper. (1) Simple Shockley Fault: Overgrowth of a **c** + **a** dislocation with a c-height step such that the Shockley partials associated with the **a** component of the deflected dislocation are located on slip planes displaced by the **c** component such that one becomes sessile and other glissile. (2) Simple Frank Fault: Overgrowth

of demi-steps associated with **c** dislocation. (3) Combination of 1 and 2, with additional **c** + **a** dislocations protruding onto the terrace between the two c/2 steps followed by postgrowth glide

5) A possible model for the expansion of rhombic-shaped Shockley type stacking faults bounded by Shockley partial dislocations has been presented which involves the operation of a double-ended Frank-Read partial dislocation source. The Shockley partials are postulated to dissociate from a segment of a prismatic dislocation which has cross-slipped onto the basal plane. The trailing partial of this cross-slipped segment is locked in position by the force exerted by an opposite sign Shockley present in a nearby segment of BPD. This enables the leading partial to expand leaving a double Shockley fault in its wake. Subsequently, the glide and cross-slip of the leading partial leads to a local transformation from 4H to 3C polytype via the mechanism postulated by Pirouz and Yang [69]. In the limit, this process leads to the formation of microscopic 3C inclusions which are large enough to diffract independently. The second possible model for the formation of rhombic-shape double Shockley faults is by the leading partials provided by the dissociation of basal plane half-loops nucleated from micropipes. More studies are required to analysis the origins of double-Shockley partials.

6) Prismatic slip of threading edge dislocations directly observed in axial slices, as most of the threading dislocations are not straight along [0001] direction, but curved towards the same direction. In the plane-view wafers, prismatic slip of threading edge dislocations are more easily to be observed in the vicinity of micropipes. Slip bands formed by glide of threading edge dislocation in the prismatic slip system <11-20> {-1100} during growth is observed. Some segments of TED loops adopt screw-orientation and then they will be able to cross-slip back to basal plane.

7) Observations indicate that a Matthews-Blakeslee type mechanism of relaxation occurs during homo-epitaxial growth of 4H-SiC. However, the mechanism appears to differ in some cases in that the source for the IDs does not initially intersect the substrate surface and simply get replicated into the epilayer. Short edge-oriented BPD segments located up to 100 microns below the substrate surface are forced to glide on the basal plane towards the interface under compression thermal stress. Having overshot the interface, they produce, opposite sign pairs of screw oriented BPDs which initially replicate into the epilayer, but once critical thickness is reached glide sideways creating IDs and HLAs. In another type of case, the surface intersections of a half loop of BPD, are initially converted to TEDs as the half-loop is drawn towards the interface by thermal stress. It again overshoots the interface, eventually inverting its shape and crossing into the epilayer, where it escapes through the surface producing two opposite sign, screw oriented BPD segments. These again initially replicate and then glide sideways in opposite directions once critical thickness has been reached forming IDs and HLAs.

It was also shown that HLA's can be generated from epilayer surface-nucleated half-loops of BPD, BPD half-loops generated from 3C inclusions in the epilayer, BPD half-loops produced from micropipes and from BPD half loops emanating from substrate/epilayer interface scratches. In addition, it was found that only those screw BPD segments with Burgers vectors parallel to the offcut direction appear to create HLAs.

The interfacial dislocation is composed by two immobile C-cores, while the basal plane segments of half-loop array are composed by two mobile Si-cores. As a result, during device operation or UVPL image, BPD segments of HLAs will dissociate into two inclined and two

vertical segments of mobile, Si-core, 30^{o} partials via electron-hole recombination enhanced dislocation glide, which will expand towards opposite direction and form Shockley faults on the basal plane, a phenomenon which leads to to lifetime limiting forward voltage drop. Meanwhile, the edge component of interfacial dislocation will not form stacking faults. Sometimes, the screw-oriented gliding segments of interfacial dislocations composed by one Si-core and one C-core are observed to form stacking faults.

Future work

(1) Distinguish threading dislocations with Burgers vector **c** or **c**+**a**. Although threading dislocations with Burgers vector **c** or **c**+**a** can be distinguished by X-ray topographs recorded from axial slices using $\boldsymbol{g} \cdot \boldsymbol{b}$ analysis, no systematic method has been developed so far to discriminate them in c-plane view wafers. Ray-tracing simulation based on the orientation contrast mechanism is one option but requires further investigation. Additionally, differentiating the influence of **c** or **c**+**a** threading dislocations on the performance of devices has not been reported in literature so far.

(2) Studies to eliminate 3C polytypes during 4H-SiC epilayer growth. Homoepitaxy growth is the basis for device fabrication and 3C polytypes are the most detrimental defects during 4H-SiC device operation. However, 3C polytypes are difficult to eliminate when growing thicker epilayers for high-power devices. It is also observed that 3C polytypes can nucleate along the upstep edge of the wafers, emanating many half-loop arrays from them that expand all the way to the center of the wafers. As we know, the BPD segments of HLAs can form Shockley faults which lower the breakdown voltage.

(3) In-situ study of annealing process to observe the behavior and the motion of dislocations. As mentioned in Chapter 10.4, the existence of compressive thermal stress in the center of the wafer during homoepitaxy growth can cause the formation of interfacial dislocations and half-loop arrays. In-situ studies can help determine the origin of the thermal stress and the magnitude of thermal stress gradient required for formation of interfacial dislocations and half-loop arrays.

(4) Measurement of lattice parameter changes across the facet. Facet is the area with high nitrogen doping compared with the rest of the wafer, an undesirable but unavoidable effect. It appears to not have much influence on dislocation densities inside and outside the facet. However, there are several reports of double Shockley stacking fault formation due to the high nitrogen doping. Therefore study of the lattice parameter changes across the facet is useful to predict the influence of high nitrogen doping in facet area on device performance.

(5) In chapter 6, the formation of star fault around the micropipe in heavily nitrogen-doped SiC substrate has been discussed. Two possible models have been suggested. However, the sources of double Shockley partials still requires further investigation.

Reference

[1] M. Bhatnagar and B. J. Baliga, Electron Devices, IEEE Transactions on **40** (3), 645 (1993).
[2] B. J. Baliga, Proceedings of the IEEE **82** (8), 1112 (1994).
[3] B. J. Baliga, Electron Devices, IEEE Transactions on **43** (10), 1717 (1996).
[4] A. Elasser and T. P. Chow, Proceedings of the IEEE **90** (6), 969 (2002).
[5] C. E. Weitzel, J. W. Palmour, C. H. Carter Jr, K. Moore, K. J. Nordquist, S. Allen, C. Thero and M. Bhatnagar, Electron Devices, IEEE Transactions on **43** (10), 1732 (1996).
[6] R. Trew, Proceedings of the IEEE **90** (6), 1032 (2002).
[7] P. G. Neudeck, R. S. Okojie and L.-Y. Chen, Proceedings of the IEEE **90** (6), 1065 (2002).
[8] A. S. Bakin, International journal of high speed electronics and systems **15** (04), 747 (2005).
[9] G. L. Harris, *Properties of silicon carbide*. (Iet, 1995).
[10] M. Dudley, X. R. Huang, W. Huang, A. Powell, S. Wang, P. Neudeck and M. Skowronski, Applied Physics Letters **75** (6), 784 (1999).
[11] P. G. Neudeck and J. A. Powell, Electron Device Letters, IEEE **15** (2), 63 (1994).
[12] M. Brady, M. Calus, J. R. Jenny, R. Leonard, D. Malta, S. G. Müller, A. R. Powell, V. F. Tsvetkov, R. Glass and C. H. Carter Jr, Materials Science Forum **457**, 3 (2004).
[13] M. Selder, L. Kadinski, F. Durst, T. Straubinger, P. Wellmann and D. Hofmann, Materials Science Forum **353-356**, 65 (2001).
[14] A. Samant and P. Pirouz, International Journal of Refractory Metals and Hard Materials **16** (4), 277 (1998).
[15] P. G. Neudeck, W. Huang and M. Dudley, Solid-State Electronics **42** (12), 2157 (1998).
[16] A. G. Acheson, British Patent, 17, 911 (1892).
[17] A. J. Lely, Ber, Dtsch. Keram. Ges **32**, 229 (1955).
[18] D. R. Hailton, "The growth of silicon carbide by sublimation" in *Silicon carbide. A High Temperature Semiconductor* (Pergamon, Oxford 1960), pp. 45.
[19] V. P. Novikov, Growth Cryst. **6**, 9 (1968).
[20] Y. M. Tairov and V. Tsvetkov, Journal of Crystal Growth **43** (2), 209 (1978).
[21] R. Yakimova and E. Janzén, Diamond and related materials **9** (3), 432 (2000).
[22] G.Dhanaraj, X. R. Huang, M. Dudley, V. Prasad and R. H. Ma, "Silicon carbide crystals-Part II: Process physics and modeling " in *Crystal Growth Technology*, edited by K. Byrappa and T. Ohachi (Springer, Berlin, Heidelberg, 2001), pp. 181.
[23] D. Nakamura, I. Gunjishima, S. Yamaguchi, T. Ito, A. Okamoto, H. Kondo, S. Onda and K. Takatori, Nature **430** (7003), 1009 (2004).
[24] B. K. Tanner and D. K. Bowen, Materials Science Reports **8** (8), 371 (1992).
[25] W.F.Berg, Naturwiss **19**, 391 (1931).
[26] C. S. Barrett, Trans. AIME, **161**, 15 (1945).
[27] N. Wooster and W. A. Wooster, Nature **155**, 786 (1945).
[28] A. Guinier and J. Tennevin, Acta Cryst. **2**, 133 (1949).
[29] A. Lang, Journal of Applied Physics **29** (3), 597 (1958).
[30] M. Hart, Journal of Applied Crystallography **8** (4), 436 (1975).
[31] B. Tanner, Progress in Crystal Growth and Characterization **1** (1), 23 (1977).
[32] D. K. Bowen and B. K. Tanner, *High resolution X-ray diffractometry and topography*. (CRC Press, 2005).
[33] A. Lang, Acta Crystallographica **12** (3), 249 (1959).
[34] B. Capelle and C. Malgrange, Journal of Applied Physics **53** (10), 6762 (1982).

[35] J. F. Petroff, Applications of x-ray topographic methods to materials science, 75 (1984).
[36] X. R. Huang, D. R. Black, A. T. Macrander, J. Maj, Y. Chen and M. Dudley, Applied Physics Letters **91** (23), 231903 (2007).
[37] W. H. Zachariasen, *Theory of X-ray Diffraction in Crystals*. (Courier Dover Publications, 2004).
[38] B. W. Batterman and H. Cole, Reviews of modern physics **36** (3), 681 (1964).
[39] P. Cloetens, W. Ludwig, J. Baruchel, J.-P. Guigay, P. Pernot-Rejmánková, M. Salomé-Pateyron, M. Schlenker, J.-Y. Buffière, E. Maire and G. Peix, Journal of Physics D: Applied Physics **32** (10A), A145 (1999).
[40] B. Tanner, *X-Ray and Neutron Dynamical Diffraction: Theory and Applications* (Plenum Press, New York, 1996), p.147.
[41] B. D. Cullity and S. R. Stock, *Elements of X-ray Diffraction*. (Pearson, 2001).
[42] P. M. Adams, (2003).
[43] E. Pearson, T. Takai, T. Halicioglu and W. A. Tiller, Journal of Crystal Growth **70** (1), 33 (1984).
[44] M. Syväjärvi, R. Yakimova and E. Janzén, Journal of The Electrochemical Society **147** (9), 3519 (2000).
[45] H. Wang, S. Sun, M. Dudley, S. Byrappa, F. Wu, B. Raghothamachar, G. Chung, E. K. Sanchez, S. G. Mueller, D. Hansen and M. J. Loboda, Journal of Electronic Materials **42** (5), 794 (2013).
[46] R. Kaplan and V. Bermudez, in *Properties of Silicon Carbide* (EMIS Datareview Series INSPEC ~ INSPEC, London, 1995), Vol. 13, p. 103.
[47] B. Tanner, *X-ray Diffraction Topography*. (Pergamon Press, Oxford, 1976), p.81.
[48] M. Dudley, X. Huang, W. Huang, A. Powell, S. Wang, P. Neudeck and M. Skowronski, Applied physics letters **75** (6), 784 (1999).
[49] X. Huang, M. Dudley, W. Vetter, W. Huang, W. Si and C. Carter Jr, Journal of applied crystallography **32** (3), 516 (1999).
[50] A.Authier, International summer school on X-ray Dynamic theory and topography **A72**, 17 (1975).
[51] P. G. Neudeck, in *The VLSI Handbook*, edited by W. K. Chen (CRC/IEEE, Roca Raton, FL, 2000).
[52] P. G. Neudeck, Materi. Sci. Forum **338-342**, 1161 (2000).
[53] S. G. Müller, M. Brady, A. Burk, H. M. Hobgood, J. Jenny, R. Leonard, D. Malta, A. Powell, J. Sumakeris and V. Tsvetkov, Superlattices and Microstructures **40** (4-6), 195 (2006).
[54] Q. Wahab, A. Ellison, A. Henry, E. Janzén, C. Hallin, J. Di Persio and R. Martinez, Applied Physics Letters **76** (19), 2725 (2000).
[55] R. Singh, Microelectronics Reliability **46** (5), 713 (2006).
[56] Y. Ishikawa, Y. Z. Yao, Y. Sugawara, K. Danno, H. Suzuki, Y. Kawai and N. Shibata, Materials Science Forum **717-720**, 367 (2012).
[57] Y. Chen, Defects structures in silicon carbide bulk crystals, epilayers and devices, Ph.D. Thesis, State University of New York at Stony Brook, 2008.
[58] A. Authier, in *Advanced in X-ray Analysis*, edited by J. B. N. a. G. R. Mallett (Plenum Press, New York, 1967), Vol. 10, p. 9.

[59] S. G. Müller, J. Sumakeris, M. Brady, R. Glass, H. M. Hobgood, J. Jenny, R. Leonard, D. Malta, M. Paisley and A. Powell, The European Physical Journal Applied Physics **27** (1-3), 29 (2004).
[60] F. Frank and W. Read Jr, Physical Review **79** (4), 722 (1950).
[61] A. Authier and A. Lang, Journal of Applied Physics **35** (6), 1956 (1964).
[62] J. Miltat and D. Bowen, physica status solidi (a) **3** (2), 431 (1970).
[63] M. Dudley, F. F. Wang, T. Fanning, G. Tolis, J. Wu and D. T. Hodul, Mater. Letts. **10**, 87 (1990).
[64] S. Ahmad, M. Ohtomo and R. Whitworth, Nature **319** (1986).
[65] D. Hull and D. J. Bacon, *Introduction to dislocations*. (Butterworth-Heinemann, 2001).
[66] Y. Chen, G. Dhanaraj, W. M. Vetter, R. H. Ma and M. Dudley, Materials science forum **556**, 231 (2007).
[67] J. Gilman, W. G. Johnston and G. Sears, Journal of Applied Physics **29** (5), 747 (1958).
[68] A. Authier and Y. Epelboin, physica status solidi (a) **41** (1), K9 (1977).
[69] M. Dudley, N. Zhang, Y. Zhang, B. Raghothamachar and E. K. Sanchez, Materials Science Forum **645-648**, 295 (2010).
[70] M. H. Hong, A. Samant and P. Pirouz, Philosophical Magazine A **80** (4), 919 (2000).
[71] P. Pirouz, J. Demenet and M. Hong, Philosophical Magazine A **81** (5), 1207 (2001).
[72] M. Skowronski, J. Q. Liu, W. M. Vetter, M. Dudley, C. Hallin and H. Lendenmann, Journal of Applied Physics **92** (8), 4699 (2002).
[73] H. Tsuchida, I. Kamata and M. Nagano, Journal of Crystal Growth **306** (2), 254 (2007).
[74] H. Fujiwara, T. Kimoto, T. Tojo and H. Matsunami, Applied Physics Letters **87** (5), 051912 (2005).
[75] S. Izumi, H. Tsuchida, I. Kamata and T. Tawara, Applied Physics Letters **86** (20), 202108 (2005).
[76] S. I. Maximenko, J. A. Freitas, P. B. Klein, A. Shrivastava and T. S. Sudarshan, Applied Physics Letters **94** (9), 092101 (2009).
[77] M. Benamara, X. Zhang, M. Skowronski, P. Ruterana, G. Nouet, J. J. Sumakeris, M. J. Paisley and M. J. O'Loughlin, Applied Physics Letters **86** (2), 021905 (2005).
[78] H. Chen, G. Wang, Y. Chen, X. Jia, J. Bai and M. Dudley, MRS Proceedings **911**, 0911 (2006).
[79] M. Dudley, H. H. Wang, F. Z. Wu, S. Y. Byrappa, B. Raghothamachar, G. Choi, E. K. Sanchez, D. M. Hansen, R. Drachev and S. G. Mueller, Materials Science Forum **679**, 269 (2011).
[80] X. R. Huang, M. Dudley, W. M. Vetter, W. Huang, S. Wang and C. H. Carter, Applied Physics Letters **74** (3), 353 (1999).
[81] F. Frank, Acta Crystallographica **4** (6), 497 (1951).
[82] J. Heindl, H. Strunk, V. Heydemann and G. Pensl, physica status solidi (a) **162** (1), 251 (1997).
[83] P. Krishna, S.-S. Jiang and A. Lang, Journal of crystal growth **71** (1), 41 (1985).
[84] W. M. Vetter and M. Dudley, Philosophical Magazine **86** (9), 1209 (2006).
[85] J. Heindl, W. Dorsch, H. Strunk, M. St G, R. Eckstein, D. Hofmann and A. Winnacker, Physical review letters **80** (4), 740 (1998).
[86] V. Presser, A. Loges and K. Nickel, Philosophical Magazine **88** (11), 1639 (2008).
[87] M. Skowronski and S. Ha, Journal of applied physics **99** (1), 011101 (2006).
[88] P. Pirouz and J. Yang, Ultramicroscopy **51** (1), 189 (1993).

[89] H. Tsuchida, I. Kamata and M. Nagano, Journal of Crystal Growth **310** (4), 757 (2008).
[90] M. Dudley, S. Byrappa, H. Wang, F. Wu, Y. Zhang, B. Raghothamachar, G. Choi, E. Sanchez, D. Hansen and R. Drachev, MRS Proceedings **1246**, 1246 (2010).
[91] A. Galeckas, J. Linnros and P. Pirouz, Applied physics letters **81** (5), 883 (2002).
[92] A. Lebedev, Semiconductors **33** (2), 107 (1999).
[93] B. Raghothamachar, M. Dudley and G. Dhanaraj, "X-Ray Topography Techniques for Defect Characterization of Crystals" in *Springer Handbook of Crystal Growth* (Springer, 2010), pp. 1425.
[94] M. Dudley, Y. Chen, X. R. Huang and R. H. Ma, Materials Science Forum **600-603**, 261 (2009).
[95] M.Dudley and X.Huang, Mater. Sci. Forum **338-342**, 431 (2000).
[96] M. Dudley, F. Wu, H. Wang, S. Byrappa, B. Raghothamachar, G. Choi, S. Sun, E. K. Sanchez, D. Hansen, R. Drachev, S. G. Mueller and M. J. Loboda, Applied Physics Letters **98** (23), 232110 (2011).
[97] F. Z. Wu, H. H. Wang, S. Y. Byrappa, B. Raghothamachar, M. Dudley, E. K. Sanchez, D. M. Hansen, R. Drachev, S. G. Mueller and M. J. Loboda, Materials Science Forum **717**, 343 (2012).
[98] F. Wu, H. Wang, S. Byrappa, B. Raghothamachar, M. Dudley, P. Wu, X. Xu and I. Zwieback, Journal of Electronic Materials **42** (5), 787 (2013).
[99] W. M. Vetter, Characterization of dislocation structures in silicon carbide single crystals, Thesis, Stony Brook University, 1999.
[100] J. Yang, Silicon carbide: Problems in crystal growth and polytypic transformation, Thesis, Case Western Reserve University, 1993.
[101] S. Ha, N. T. Nuhfer, G. S. Rohrer, M. De Graef and M. Skowronski, Journal of electronic materials **29** (7), L5 (2000).
[102] H. H. Wang, S. Y. Byrappa, F. Wu, B. Raghothamachar, M. Dudley, E. K. Sanchez, D. M. Hansen, R. Drachev, S. G. Mueller and M. J. Loboda, Materials Science Forum **717**, 327 (2012).
[103] B. Escaig, J. Phys. (paris) **29**, 225 (1968).
[104] P. Pirouz and P. M. Hazzledine, Scr. Met. **25**, 1167 (1991).
[105] P. Pirouz, M. Zhang, H. M. Hobgood, M. Lancin, J. Douin and B. Pichaud, Philosophical Magazine **86** (29-31), 4685 (2006).
[106] H. J. Chung, J. Q. Liu and M. Skowronski, Applied Physics Letters **81** (20), 3759 (2002).
[107] B. Skromme, K. Palle, C. Poweleit, L. Bryant, W. M. Vetter, M. Dudley, K. Moore and T. Gehoski, Materials Science Forum **389**, 455 (2002).
[108] T. A. Kuhr, J. Liu, H. J. Chung, M. Skowronski and F. Szmulowicz, Journal of Applied Physics **92** (10), 5863 (2002).
[109] D. Hull and D. J. Bacon, *Introduction to Dislocation*. (Oxford: Pergamon 1984).
[110] R. Stevens, Journal of Materials Science **7** (5), 517 (1972).
[111] P. Pirouz, Philosophical Magazine A **78** (3), 727 (1998).
[112] M. Brady, W. Brixius, G. Fechko, R. Glass, D. Henshall, J. R. Jenny, R. Leonard, D. Malta, S. G. Müller and V. F. Tsvetkov, Materials Science Forum **338**, 3 (2000).
[113] W. M. Vetter and M. Dudley, Journal of applied physics **96** (1), 348 (2004).
[114] S. Nishino, J. A. Powell and H. A. Will, Applied Physics Letters **42** (5), 460 (1983).
[115] I. H. Khan and A. J. Learn, Applied Physics Letters **15** (12), 410 (1969).

[116] F. R. Chien, S. R. Nutt, J. M. Carulli, N. Buchan, C. P. Beetz and W. S. Yoo, Journal of Materials Research **9** (08), 2086 (1994).
[117] A. R. Powell and L. B. Rowland, Proceedings of the IEEE **90** (6), 942 (2002).
[118] A. R. Powell, J. J. Sumakeris, R. T. Leonard, M. F. Brady, S. G. Müller, V. F. Tsvetkov, H. M. Hobgood, A. A. Burk, M. J. Paisley, R. C. Glass and C. H. Carter, MRS Online Proceedings Library **815**, null (2004).
[119] A. Schöner, "New Development in Hot Wall Vapor Phase Epitaxial Growth of Silicon Carbide" in *Silicon Carbide*, edited by W. J. Choyke, H. Matsunami and G. Pensl (Springer Berlin Heidelberg, 2004), pp. 229.
[120] V. Dmitriev, S. Rendakova, N. Kuznetsov, N. Savkina, A. Andreev, M. Rastegaeva, M. Mynbaeva and A. Morozov, Materials Science and Engineering: B **61–62** (0), 446 (1999).
[121] D. H. Hofmann and M. H. Müller, Materials Science and Engineering: B **61–62** (0), 29 (1999).
[122] R. Yakimova, M. Syväjärvi, T. Iakimov, H. Jacobsson, R. Råback, A. Vehanen and E. Janzén, Journal of Crystal Growth **217** (3), 255 (2000).
[123] T. H. S. Nakamura, T. Kimoto, T. Fuyuki, H. Matsunami, Materials Science Forum **338-342**, 201 (2000).
[124] S. N. T. Hatayama, K. Kurobe, T. Kimoto, T. Fuyuki, H. Matsunami, Materials Science Engine. B **61/62**, 135 (1999).
[125] J. Powell and D. Larkin, physica status solidi (b) **202** (1), 529 (1997).
[126] H. Matsunami and T. Kimoto, Materials Science and Engineering: R: Reports **20** (3), 125 (1997).
[127] A. W. R. Rupp, P. Friedrichs, D. Peters, R. Schorner, D. Stephani, Materials Science Forum **264-268**, 89 (1998).
[128] C. Sartel, J. M. Bluet, V. Soulière, I. El Harrouni, Y. Monteil, M. Mermoux and G. Guillot, Materials Science Forum **433**, 165 (2003).
[129] T. K. S. Nakamura, H. Matsunami, Mater. Sci. Forum **389-393**, 183 (2002).
[130] T. Kimoto, A. Itoh and H. Matsunami, physica status solidi (b) **202** (1), 247 (1997).
[131] O. Kordina, C. Hallin, A. Henry, J. Bergman, I. Ivanov, A. Ellison, N. T. Son and E. Janzén, physica status solidi (b) **202** (1), 321 (1997).
[132] R. Rupp, Y. N. Makarov, H. Behner and A. Wiedenhofer, physica status solidi (b) **202** (1), 281 (1997).
[133] A. Burk Jr, M. O'loughlin and H. Nordby Jr, Journal of crystal growth **200** (3), 458 (1999).
[134] H. Tsuchida, I. Kamata, T. Jikimoto and K. Izumi, Journal of crystal growth **237**, 1206 (2002).
[135] K. Fujihira, T. Kimoto and H. Matsunami, Materials Science Forum **433-436**, 161 (2003).
[136] M. Ito, L. Storasta and H. Tsuchida, Applied physics express **1** (1), 015001 (2008).
[137] Y. Ishida, T. Takahashi, H. Okumura, K. Arai and S. Yoshida, Materials Science Forum **600**, 119 (2009).
[138] F. La Via, G. Izzo, M. Mauceri, G. Pistone, G. Condorelli, L. Perdicaro, G. Abbondanza, L. Calcagno, G. Foti and D. Crippa, Journal of Crystal Growth **311** (1), 107 (2008).
[139] H. Pedersen, S. Leone, A. Henry, F. Beyer, V. Darakchieva and E. Janzén, Journal of crystal growth **307** (2), 334 (2007).
[140] P. Lu, J. Edgar, O. Glembocki, P. Klein, E. Glaser, J. Perrin and J. Chaudhuri, Journal of crystal growth **285** (4), 506 (2005).

[141] V. Heine, J. Am. Ceram. Soc. **1991**, 74 (1991).
[142] K. Shibahara, N. Kuroda, S. Nishino and H. Matsunami, Japanese journal of applied physics **26** (11A), L1815 (1987).
[143] H.-S. Kong, J. T. Glass and R. F. Davis, Journal of applied physics **64** (5), 2672 (1988).
[144] K. Kościewicz, W. Strupiński, D. Teklinska, K. Mazur, M. Tokarczyk, G. Kowalski and A. R. Olszyna, Materials Science Forum **679**, 95 (2011).
[145] Y. Ueoka, K. Shingu, H. Yano, T. Hatayama and T. Fuyuki, Japanese Journal of Applied Physics **51** (11R), 110201 (2012).
[146] S. S. J. Zhang, J. Mazzola, B. Tyrrell, G. Stewart, R. Stahlbush, J. Coldwell, P. Klein, M. Mazzola and J. Casady, Mater. Res. Soc. Symp. Proc. **1069-D07-10** (2008).
[147] T. Aigo, W. Ito, H. Tsuge, H. Yashiro, M. Katsuno, T. Fujimoto and W. Ohashi, Materials Science Forum **717**, 101 (2012).
[148] K. Tamura, C. Kudou, K. Masumoto, J. Nishio and K. Kojima, Materials Science Forum **778**, 214 (2014).
[149] L. Lilja, J. Hassan, E. Janzen and P. Bergman, Mater. Sci. Forum **778-780** 206 (2014).
[150] S. Monnoye, D. Turover and P. Vicente, "Surface preparation techniques for SiC wafers" in *Silicon Carbide* (Springer, 2004), pp. 699.
[151] J. Powell, J. Petit, J. Edgar, I. Jenkins, L. Matus, J. Yang, P. Pirouz, W. Choyke, L. Clemen and M. Yoganathan, Applied physics letters **59** (3), 333 (1991).
[152] A. Burk Jr and L. Rowland, Journal of crystal growth **167** (3), 586 (1996).
[153] F. D. H. Lendenmann, N. Johansson, R. Soderholm, P. A. Nilsson, J. P. Bergman and P. Skytt, Mater. Sci. Forum **353-356**, 727 (2001).
[154] H. Tsuchida, M. Ito, I. Kamata and M. Nagano, physica status solidi (b) **246** (7), 1553 (2009).
[155] H. H. Wang, F. Z. Wu, S. Y. Byrapa, Y. Yang, B. Raghothamachar, M. Dudley, G. Chung, J. Zhang, B. Thomas and E. K. Sanchez, Materials Science Forum **778**, 332 (2014).
[156] X. Zhang, S. Ha, M. Benamara, M. Skowronski, M. J. O'Loughlin and J. J. Sumakeris, Applied Physics Letters **85** (22), 5209 (2004).
[157] T. Okada, T. Kimoto, H. Noda, T. Ebisui, H. Matsunami and F. Inoko, Japanese Journal of Applied Physics **41** (Part 1, No. 11A), 6320 (2002).
[158] H. Jacobson, J. Bergman, C. Hallin, E. Janzén, T. Tuomi and H. Lendenmann, Journal of applied physics **95** (3), 1485 (2004).
[159] S. Ha, M. Skowronski and H. Lendenmann, Journal of applied physics **96** (1), 393 (2004).
[160] R. Stahlbush, M. Fatemi, J. Fedison, S. Arthur, L. Rowland and S. Wang, Journal of electronic materials **31** (5), 370 (2002).
[161] Z. Zhang, E. Moulton and T. S. Sudarshan, Applied Physics Letters **89** (8), 081910 (2006).
[162] Z. Zhang and T. Sudarshan, Applied Physics Letters **87** (15), 151913 (2005).
[163] B. L. VanMil, R. E. Stahlbush, R. L. Myers-Ward, K. K. Lew, C. R. Eddy and D. K. Gaskill, Journal of Vacuum Science & Technology B: Microelectronics and Nanometer Structures **26** (4), 1504 (2008).
[164] B. L. V. M. R. L. Myers-Ward, R. E. Stahlbush, S. L. Katz, J. M. McCrate, S. A. Kitt, C. R. Eddy, Jr., and D. K. Gaskill, Mater. Sci. Forum **105**, 615 (2009).
[165] R. L. M. W. R. E. Stahlbush, B. L. Vanmill, D. K. Gaskill, C. R. Eddy, Jr., Mater. Sci. Forum **271**, 645 (2010).
[166] H. Jacobson, J. Birch, C. Hallin, A. Henry, R. Yakimova, T. Tuomi, E. Janzén and U. Lindefelt, Applied Physics Letters **82** (21), 3689 (2003).

[167] X. Zhang, S. Ha, Y. Hanlumnyang, C. H. Chou, V. Rodriguez, M. Skowronski, J. J. Sumakeris, M. J. Paisley and M. J. O'Loughlin, Journal of Applied Physics **101** (5), 053517 (2007).
[168] X. Zhang, M. Skowronski, K. X. Liu, R. E. Stahlbush, J. J. Sumakeris, M. J. Paisley and M. J. O'Loughlin, Journal of Applied Physics **102** (9), 093520 (2007).
[169] J. W. Matthews, Journal of Vacuum Science and Technology **12** (1), 126 (1975).
[170] J. Matthews and A. Blakeslee, Journal of Crystal Growth **27**, 118 (1974).
[171] R. People and J. C. Bean, Applied Physics Letters **49** (4), 229 (1986).
[172] R. People and J. C. Bean, Applied Physics Letters **47** (3), 322 (1985).
[173] N. Zhang, Y. Chen, Y. Zhang, M. Dudley and R. E. Stahlbush, Applied Physics Letters **94** (12), 122108 (2009).
[174] H. Wang, F. Wu, M. Dudley, B. Raghothamachar, G. Chung, J. Zhang, B. Thomas, E. K. Sanchez, S. G. Mueller, D. Hansen and M. Loboda, Materials Science Forum **778-780**, 328 (2014).
[175] S. Sasaki, J. Suda and T. Kimoto, Materials Science Forum **717-720**, 481 (2012).
[176] Y. Chen, G. Dhanaraj, M. Dudley, H. Zhang, R. Ma, Y. Shishkin and S. E. Saddow, MRS Proceedings **911**, 0911 (2006).
[177] X. Zhang, T. Miyazawa and H. Tsuchida, Materials Science Forum **717-720**, 313 (2012).
[178] D. Chidambarrao, G. R. Srinivasan, B. Cunningham and C. S. Murthy, Applied Physics Letters **57** (10), 1001 (1990).
[179] B. Kallinger, P. Berwian, J. Friedrich, G. Müller, A.-D. Weber, E. Volz, G. Trachta, E. Spiecker and B. Thomas, Journal of Crystal Growth **349** (1), 43 (2012).
[180] G. Green, B. Tanner, S. Barnett, M. Emeny, A. Pitt, C. Whitehouse and G. Clark, Philosophical Magazine Letters **62** (3), 131 (1990).
[181] J. P. Hirth and J. Lothe. (Wiley, New York, 1982).
[182] A. Seeger, in *Dislocations and Mechanical Properties of Crystals*, edited by W. G. J. J. C. Fisher, R. Thomson, and T. Vreeland, Jr. (John Wiley & Sons Publication, New York, 1956), p. 252.
[183] H. Alexander and P. Haassen, J. Phys. (Paris) **40** (C6) (1979).
[184] S. Ha, H. Chung, N. Nuhfer and M. Skowronski, Journal of crystal growth **262** (1), 130 (2004).
[185] J. Q. Liu, H. J. Chung, T. Kuhr, Q. Li and M. Skowronski, Applied Physics Letters **80** (12), 2111 (2002).
[186] Y. Zhang, H. Chen, M. Dudley, Y. Zhang, J. Edgar, Y. Gong, S. Bakalova, M. Kuball, L. Zhang and D. Su, Mater. Res. Soc. Symp. Proc. **1307** (2011).